Development of Optical and Mechanical Techniques to Investigate Rheology and Adhesion in Biological and Biomimetic Systems

Von der Universität Bayreuth
zur Erlangung des Grades eines
Doktors der Naturwissenschaften (Dr. rer. nat.)
genehmigte Abhandlung

von

Wolfgang Groß
aus Marktredwitz

1. Gutachter: Prof. Dr. Holger Kress
2. Gutachter: Prof. Dr. Jürgen Köhler
3. Gutachter: Prof. Dr. Alexander Rohrbach

Tag der Einreichung: 19.07.2022
Tag des Kolloquiums: 22.01.2025

Abstract

Mechanical interactions between cells and their environment have a profound impact on many cellular functions. In our body, the stiffnesses of different types of tissues differ by multiple orders of magnitude. While brain is very soft, other kinds of tissue such as muscle or cartilage is considerably stiffer. Individual cells can exert forces on their environment in order to sense the rigidity of their environment and in turn, adapt their behavior accordingly. By now, it is well established that many cellular processes such as adhesion, migration, and morphogenesis are influenced by the mechanical properties of the cellular environment. A common model system to investigate the mechanical interactions between cells and their surrounding tissue are soft, biomimetic polymer substrates, which are typically polymerized in the form of thin films with different stiffnesses. Experiments, in which cells are allowed to adhere on the surface of such soft substrates have not only revealed that several processes such as cell migration, adhesion, and differentiation are influenced by the rigidity of the substrate. Such substrates can also provide an in-depth view into the dynamics of the mechanical machinery of individual cells, in particular the forces adherent cells exert on their environment. For all of those studies, precise methods to measure the elastic properties of such thin polymer films are necessary.

In the first experimental part of this work, a simple technique to measure the elastic modulus and the Poisson ratio of films with a thickness of a tenth of a millimeter is presented. Steel spheres with different radii were placed on such substrates, the indentation was measured with an inverted microscope and the interplay between the elastic properties and finite thickness effects was exploited to determine both elastic parameters in a single experiment. The technique was applied to four different materials, which are commonly used in such studies, namely polyacrylamide, porous polyacrylamide, poly-N-isopropylacrylamide, and polydimethylsiloxane. Furthermore, Monte-Carlo simulations were carried out to optimize the precision of future experiments.

Another cellular process, which is inherently governed by mechanical interactions, is the internalization of extracellular objects into cells. As one central part of our innate immune system, macrophages can engulf objects such as bacteria or whole cells in a process called phagocytosis by wrapping their membrane around the target. The protrusion of the membrane is driven by the polymerization of cortical actin, which is a central part of the cytoskeleton of macrophages located directly below the membrane. Thus, for a theoretical understanding of the process, knowledge of the cortical rheology during phagocytosis is necessary. However, there is only very limited data of the changes of the cortical rheology during cup formation available. In the experiments described in the second experimental part of this work, a technique based on blinking holographic optical traps to measure the viscoelastic properties of macrophages during phagocytosis is presented. As a model system, antibody-coated polystyrene particles were used as phagocytic targets and attached to the macrophages. After cell-particle contact, temporally modulated optical forces were exerted on the particles to mechanically probe the cells. The technique was demonstrated to be capable of resolving the viscoelastic properties of the macrophages as well as the temporal evolution of the cell-particle contact radius during the early phagocytic binding phase. This phase takes roughly 1 to 2 minutes and it was established, that cortical remodeling does not occur in a systematic manner during this phase. The setup was extended with a 3-dimensional feedback system to enable constant optical forces before, during, and after phagocytic cup formation. Furthermore, fluorescence microscopy was used to visualize the cortical dynamics and to identify the internalization process.

To quantify the cell-particle adhesion strength, which is presumably an important driver of the early phagocytic particle binding mechanism, a microfluidic device was designed and verified in the final experimental part of this work. To quantify the adhesion strength between hundreds of particles and cells simultaneously, the particles were sedimented on the cells and subsequently exposed to a shear flow. The binding and unbinding rates, the fraction of irreversible binding events,

and the number of particles remaining after the exertion of a hydrodynamic force of 50 pN were quantified as measures for the adhesion strength. For the study, nominally identical polystyrene particles were purchased from eight different manufacturers and it is demonstrated that the adhesion strength of those particles differed drastically, depending on the ζ-potential of the particles. Additionally, some particles were incubated in salt and freshwater to model environmental exposure of microplastic particles. This exposure goes along with the formation of an eco-corona on the surface of the particles, which also increased the cell-particle adhesion strength.

All three techniques developed in this work contribute to the understanding of the mechanical interplay between cells and their environment. In particular, the combination of all three techniques is a powerful tool set to unravel further details about the mechanics of phagocytosis in the near future. Interesting directions for future experiments to investigate the mechanics of phagocytosis are discussed in the final part of this work.

Zusammenfassung

Die mechanischen Interaktionen zwischen Zellen und ihrer Umgebung haben einen großen Einfluss auf viele zelluläre Funktionen. Die Steifigkeit verschiedener Gewebetypen in unserem Körper unterscheidet sich um mehrere Größenordnungen. Während das Gehirn sehr weich ist sind andere Gewebetypen, wie zum Beispiel Muskeln und Knorpel, deutlich härter. Einzelnen Zellen können Kräfte auf ihre Umgebung ausüben und so die Härte ihrer Umgebung abtasten und ihr Verhalten entsprechend anpassen. Ein typisches Modellsystem, mit dem die mechanische Interaktion zwischen Zellen und ihrem umgebenden Gewebe untersucht wird sind weiche, biomimetische Polymersubstrate. Diese Substrate werden typischerweise in Form von dünnen Schichten mit verschiedener Härte polymerisiert. Mit Experimenten mit adhärenten Zellen auf der Oberfläche solcher weichen Substrate wurde in der Vergangenheit gezeigt, dass verschiedene Prozesse wie zum Beispiel Zellmigration, Adhäsion und Differenzierung von der Härte des Substrats beeinflusst werden. Solche Substrate können auch einen detaillierten Blick in die Dynamik der zellulären krafterzeugenden Maschinerie eröffnen. Insbesondere können damit die Kräfte gemessen werden, die adhärente Zellen auf ihre Umgebung ausüben. Für solche Studien werden allerdings genaue Techniken benötigt, um die mechanischen Eigenschaften solcher dünnen Polymerschichten zu messen.

Im ersten experimentellen Teil dieser Arbeit wird eine Technik vorgestellt, mit der das Elastizitätsmodul und die Poissonzahl von dünnen Schichten mit einer Dicke von etwa einem Zehntel Millimeter bestimmt werden kann. Dazu wurden Stahlkugeln mit verschidenen Durchmessern auf solche Polymersubstrate gelegt und ihre Eindringtiefe mit einem invertierten Mikroskop vermessen. Unter Ausnutzung von Schichtdickeneffekten wurden dann beide Elastizitätsparameter bestimmt. Die Technik wurde auf vier verschiedene Materialien angewandt, die typischerweise in den beschriebenen Zellstudien verwendet werden. Dabei handelte es sich um Polyacrylamid, poröses Polyacrylamid, Poly-N-Isopropylacrylamid und Polydimethylsiloxan. Des Weiteren wurden Monte-Carlo Simulationen durchgeführt, um die Genauigkeit zukünftiger Experimente zu optimieren.

Die Internalisierung von extrazellulären Objekten ist ein weiterer Vorgang, der von mechanischen Interaktionen zwischen Zellen und ihrer Umgebung bestimmt wird. Ein zentraler Teil der angeborenen Immunantwort ist der Phagozytoseprozess, in dem Makrophagen extrazelluläre Objekte, beispielsweise Bakterien oder ganze Zellen umschlingen können, indem sie ihre Zellmembran um die Zielobjekte schieben. Der Membranvorschub wird durch die Polymerisation von kortikalem Aktin angetrieben, welches ein zentraler Teil des Zytoskeletts von Makrophagen ist. Für ein theoretisches Verständnis des Phagozytoseprozesses ist deswegen die Kenntnis der Rheologie des Kortex notwendig. Die Datenlage hierzu ist allerdings zum gegenwärtigen Stand sehr eingeschränkt. Im zweiten experimentellen Teil dieser Arbeit wird eine Technik basierende auf einer blinkenden holographischen optischen Pinzette vorgestellt, mit der sich die viskoelastischen Eigenschaften von Makrophagen während der Phagozytose messen lassen. Im verwendeten Modellsystem wurden mit Antikörpern beschichtete Polystyrolpartikel als Zielobjekte an die Zellmembran angeklebt. Nach dem der Kontakt zwischen Zelle und Partikel hergestellt war wurden zeitlich modulierte optische Kräfte auf die Partikel ausgeübt, um die Zellmechanik zu untersuchen. Mit dieser Technik wurden einerseits die viskoelastischen Eigenschaften und andererseits die zeitliche Entwicklung des Kontaktradius zwischen Partikel und Zelle während der anfänglichen Bindungsphase aufgelöst. Diese Phase dauert etwa 1 bis 2 Minuten. Weiterhin wurde gezeigt, dass während dieser Phase keine systematische Remodellierung des Kortex stattfindet. Das bestehende Setup wurde mit einer 3D-Feedbackschleife erweitert, sodass vor, während und nach der Phagozytose konstante optische Kräfte auf die Zielpartikel ausgeübt werden können. Zusätzlich wurden fluoreszmikroskopische Aufnahmen angefertigt, um die Dynamik des Kortex zu visualisieren und damit den Internalisierungsprozess zu identifizieren.

Um die Stärke der Adhäsion zwischen Zellen und Partikeln, die vermutlich für die Bindung während der frühen Phagozytose verantwortlich ist, zu quantifizieren wurde eine Mikrofluidikanlage entwickelt und validiert. Diese Anlage wird im letzten experimentellen Teil dieser Arbeit vorgestellt. Um die Adhäsionsstärke zwischen hunderten Partikeln und Zellen gleichzeitig zu quantifizieren wurde gewartet, bis die Partikel auf die Zellen sedimentiert waren. Anschließend wurden die Partikel einer Scherströmung ausgesetzt. Als Kenngrößen für die Adhäsionsstärke wurden An- und Abbinderate, der Anteil der irreversiblen Bindungsevents sowie die Anzahl der Partikel, die nach Ausübung von 50 pN hydrodynamischer Scherkraft adhärent blieben, definiert. In der Studie wurden nominell identische Partikel von acht verschiedenen Herstellern untersucht. Die Zell-Partikel-Adhäsionsstärke unterschied sich drastisch von Hersteller zu Hersteller, abhängig vom ζ-potential der Partikel. Zusäztlich zu den unbehandelten Partikeln wurden manche Partikel in Salz- und Süßwasser inkubiert um die Umweltexposition von Mikroplastikpartikel zu modellieren. Diese Umweltexposition führte zur Bildung einer Eco-Corona auf der Oberfläche der Partikel, die die Adhäsionsstärke zwischen Zellen und Partikeln erhöhte.

Alle drei Techniken, die im Rahmen dieser Arbeit entwickelt wurden, tragen zum Verständnis des mechanischen Zusammenspiels zwischen Zellen und ihrer Umgebung bei. Insbesondere stellt die Kombination aller drei Techniken eine vielseitige Plattform dar, um weitere Details zur Mechanik der Phagozytose zutage zu fördern. In dieser Hinsicht interessante, mögliche zukünftige Experimente werden im letzten Teil dieser Arbeit diskutiert.

Contents

1 Introduction: Biophysical Background

Evolution started at the dawn of life about 4 billion years ago[1] and only recently, a little more than 200.000 years ago, the 'homo sapiens' emerged[2], which, with today's best estimates, describes an accumulation of 10^{14} individual cells[3]. Judging from the number of possible permutations, it is obvious that the configuration of those cells is far from random. In fact, countless different cell types in the human body are organized in higher level systems to form different kinds of tissue, which in turn accumulate to organs, apparatuses, and ultimately make up our whole body. In their book 'The Ancestors Tale: A Pilgrimage to the Dawn of Life', Richard Dawkins and Yan Wong summarized in broad strokes what is known about the incredible journey evolution took to develop these complicated multi-level systems[4]. Early on, evolution figured out how to store and accumulate information to enable long term progress and only about 70 years ago, it was discovered that the main information storage in eukaryotic cells is a single molecule, the DNA[5]. Through a relentless process of optimization driven by success and failure, biological matter has accumulated information on how to metabolize chemical energy and use this energy to interact with its environment in a seemingly favorable manner. Today's knowledge suggests that human cells synthesize about 19.000 different proteins with the information encoded in their DNA[6]. Those proteins provide a multitude of basic functions, depending on their structure. For example, photoreceptor proteins such as photopsins can detect electromagnetic waves and ultimately enable vision[7]. Motor proteins such as myosins can generate forces to drive muscles[8] and mechanosensitive ion channels translate mechanical sound waves into chemical signals in our ears[9]. Other proteins catalyze chemical reactions and encode or detect biochemical signals. These proteins are used on the cellular and supercellular level to drive and coordinate functions such as proliferation, migration, adhesion, the detection of pathogens, or signal transduction. The functions of individual cells are then integrated in the above-mentioned organization levels to enable the shear endless number of options our body has to interact with our environment, either in a conscious or unconscious manner[10].

One example of such a complex system in our body is our immune system. When infected with a pathogen such as *Legionella pneumophila*, which causes Legionnaires' disease, our immune system detects and responds to the infection in order to protect the whole organism from uncontrolled bacterial growth. Upon infection with an unknown pathogen, the innate immune system can detect pathogen-associated molecular patterns, which are essential for the survival of many different pathogens. Dedicated cells of our immune system such as macrophages are for example equipped with specific receptor proteins to detect when flagellin, one of the main proteins forming bacterial flagella, enters their cytosol, indicating a virulent infection[11]. Upon detection, a set of responses of the innate immune system is triggered. Those include the secretion of chemokines to trigger the activation of other leukocytes and the secretion of cytokines, which trigger an inflammatory response in the neighboring tissue. The inflammation in turn leads to the recruitment of other immune cells like neutrophils, which migrate to the infection site[12]. Macrophages can also bind to, engulf and clear pathogens and subsequently trigger the activation of the adaptive immune system by presenting an antigen, i.e. a characteristic protein on the surface of the pathogen, to helper T lymphocytes. Through signaling proteins, T lymphocytes activate B lymphocytes, which, in a trial-and-error process termed V(D)J recombination, synthesize proteins called antibodies. These antibodies specifically bind to the antigen with a high affinity[10,13,14]. Furthermore, they can be recognized by professional phagocytes such as macrophages with dedicated membrane receptor

proteins, and the recognition leads to a more efficient clearance of pathogens marked with antibodies. In that way, reinfections with pathogens often lead to less severe disease and ultimately, better chances of survival[10].

Another example of such a complex system, which extends over many organization levels, are our skeletal muscles[15]. Inside our muscle cells, which are commonly referred to as muscle fibers, myosin II motor proteins and the cytoskeletal protein actin are organized in long, parallel filaments, and millions of those filaments are bundled together to form myofibrils[15]. The heads of the myosin motors bind to dedicated binding sites on the actin filaments[16]. Upon the arrival of a nerve stimulus, the action potential is transmitted to the cytoplasm of the muscle fibers by the influx of calcium ions through ion channels in the membrane, which ultimately triggers the activation of the myosin motors[15]. According to the sliding filament theory, myosin motor proteins exert forces in distinct power strokes upon the hydrolysis of adenosine triphosphate to adenosine diphosphate, siding the myosin filaments relative to the actin filaments and thus, contracting the myofibrils[17–19]. Each of the muscle fibers, which are approximately 100 µm in diameter and 1 cm in length, contain thousands of myofibrils[15]. A multitude of transmembrane proteins mechanically link the intracellular filaments to the extracellular matrix[20], which mediates cell-cell adhesion and ultimately enables the cooperation of many individual fibers in our muscles. Thousands of muscle fibers are organized together with connective tissue to form our muscles[15], which can generate forces of hundreds of newtons and contract by a few centimeters. The fact that the myosin motors, which ultimately enable these macroscopic functions, move along the actin filaments in distinct steps with a size of 11 nanometers and exert forces in the piconewton range[21] is unequivocal evidence of the complexity of the whole system which forms muscles.

This seemingly unlimited complexity of these biological systems has attracted a multitude of biologists, chemists, physicists and also engineers and material scientists who try to unearth more and more details about the fascinating processes evolution was creating and optimizing during the last 4 billion years. They all aim to retrace nature's steps along the path of evolution. The main goal of this work was to provide future scientists, who are willing to take some steps, with three walking sticks in the form of three experimental techniques. All three techniques are suitable to advance our understanding of the mechanical interface between cells and their environment, enabling the quantification of cellular forces, rheology, and adhesion. The techniques were applied to established biological and biomimetic model systems to demonstrate their practicability. Although the techniques are generally applicable to a wide range of different cell types, the cell experiments presented in this work focus on the investigation of the mechanics of the internalization of extracellular objects by cells, which is an inherent function of the above-mentioned innate immune system. In the following two sections 1.1 and 1.2 of this chapter, the biomechanical background of those techniques is established. In section 1.3, the techniques are briefly summarized.

1.1 Mechanobiology

1.1.1 Mechanotransduction

The fact that mechanical signals can heavily influence cellular functions has been well established in the past decades. It has become more and more apparent that the mechanical interactions between cells and their environment can have a profound impact on the behavior and function of individual cells and tissue. For example, cells have been shown to exert forces on their environment during adhesion[22,23], migration[24–26], and morphogenesis[27]. In many eucaryotic cell types, there is a thin, yet dense protein network consisting mainly of actin filaments referred to the actin cortex, which is located directly below the cellular membrane (fig. 1.1). Cells can generate contractile forces inside this network with myosin motors, which bind to two of these filaments, moving them relative to

each other[28–30]. A mechanical link between the intracellular actin network and the extracellular matrix (ECM) is established with transmembrane proteins such as integrins[31]. Integrins can couple to various ECM proteins, for example laminin[32], collagen[33], or fibronectin and can thus mediate cell-cell or cell-matrix interactions[34]. When they bind to fibronectin, integrins organize in distinct adhesion structures such as focal adhesions[29] or podosomes, in which integrins are mechanically coupled to actin filaments via linker proteins such as talin or vinculin[35,36]. Cells can thus transmit forces generated by myosin motors in the cortex to the ECM via these integrin-mediated mechanical interconnects.

It has also been shown that cells can in turn use these forces to sense the rigidity of the ECM[36–38]. One mechanism cells use to detect different ECM rigidities has recently been suggested to be mediated by two different integrin types. It was observed that fibronectin-integrin bonds have different binding and unbinding rates depending on the integrin type and the loading rate. Cells have been suggested to use these binding affinity differences to sense the rigidity of the ECM by exerting contractile forces on the ECM. A subsequent signaling pathway translates the differential mechanical signal generated by both integrins to a biochemical signal, a process generally referred to as mechanotransduction. The whole mechanism was conceptualized as the *molecular clutch* for mechanotransduction[39–43]. Further details about the mechanics of the cytoskeleton were previously reviewed, for example by Mofad[44], Fletcher and Mullins[45], and Tao et al.[46].

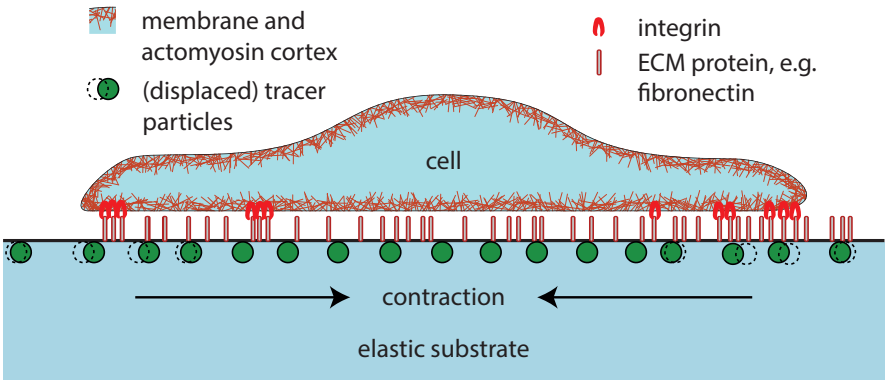

Figure 1.1: Cell adhesion and traction force microscopy. Cells are seeded on an elastic substrate with a stiffness in the same range as that of mammalian tissue. In order to facilitate cell adhesion, the substrates can be coated with a variety of ECM proteins such as fibronectin or collagen. These ECM protins bind to transmembrane receptors such as integrins, which cluster to form adhesion sites like focal adhesions or podosomes, mechanically linking the actomyosin cortex to the substrate. Thus, contractile forces exerted by myosin motors within the cortex can be transmitted to the substrate. Those forces can be measured with traction force microscopy, as they induce deformations, which can be detected with tiny fluorescent tracer particles embedded in the top substrate layer. Subsequent image analysis allows the reconstruction of the stresses the cells exert on the substrate. (Tracer particles and proteins not drawn to scale.)

The most common model system to study mechanotransduction are soft polymer substrates with tunable elastic properties. On order to mimic physiological environments, the elastic properties are typically chosen such that they lie within the physiological range. In mammals, this range does span multiple orders of magnitude. While brain is generally very soft as it has elastic moduli ranging from a few tens of Pa to about one hundred Pa, muscles are considerably stiffer as they have elastic moduli of about 10 kPa. The elastic modulus of cartilage is roughly 1 MPa[47–49]. In

order to facilitate cell adhesion on these soft substrates, their surface can be functionalized with ECM proteins like fibronectin[50,51]. Cellular behavior on these substrates is then be studied. Such experiments have revealed that a considerable number of cellular processes is influenced or directed by the mechanical properties of the environment of the cells and in particular, these processes are adapted when the ECM stiffness changes within the physiological range. For instance, gene expression and and stem cell differentiation have been shown to be influenced by mechanical clues[52,53]. Engler et al. showed that naive mesenchymal stem cells differentiate to neurons on soft substrates mimicking the stiffness of brain tissue, to myoblasts on substrates with a rigidity of muscles, and to osteoblasts on stiff substrates, which mimic collagenous bone[54]. Morphogenesis is also greatly influenced by matrix elasticity. For instance, myoblasts, fibroblasts, macrophages, osteoblasts and astrocytes have been shown to spread more the stiffer the substrate[55–60]. In contrast, neuron branches form faster[61] and in higher numbers[62] on soft substrates, which, interestingly, have approximately the same stiffness as brain. Such differences in the cellular morphology are typically also reflected by structural differences of the cytoskelton and in particular, the organization of filamentous actin differs, depending on the ECM rigidity. For instance, stress fibers, i.e. contractile actin bundles ranging through the whole cell[63] are abundant in fibroblasts adherent to rigid substrates and rare in fibroblasts adherent to soft substrates[64]. Another process which is strongly influenced by the rigidity of the environment is cell migration, which is faster on substates with medium stiffnesses and slower on very soft and very stiff substrates[37,65]. When experiencing a stiffness gradient, fibroblasts and epithelial cells have been shown to migrate towards stiffer regions in a process termed durotaxis, indicating that cells are able to sense stiffness gradients[55,66–69]. Even the internalization efficiency of extracellular objects into cells has been shown to depend on the stiffness of the target objects themselves and previous findings suggest that stiffer targets are taken up more efficiently than softer targets[70–75].

1.1.2 Cellular Force Generation

Experiments with such soft substrates have not only revealed that several processes such as migration, adhesion, and differentiation are influenced by the rigidity of the environment. The substrates can also provide an in-depth view into the dynamics of the mechanical machinery of individual cells, in particular the forces adherent cells exert on their environment. A common technique to measure these cellular forces is traction force microscopy (TFM). The method is outlined in figure 1.1. In TFM, the stiffness of the substrates is chosen soft enough such that the cells can deform it. In early studies, it was noticed that cellular forces exerted on the substrate surface induced wrinkles next to and below the cells[24,76]. Even though the wrinkles established that cells exert forces on their environment, quantification of these forces from the wrinkles is possible, but challenging[77,78]. This limitation was overcome in the mid 90s. Technological advances in digital image acquisition and computational power enabled the development of modern TFM, with which the cellular stresses can be quantified in a spatially and temporally resolved manner. In order to do so, fluorescent tracer particles were embedded in the top layer of the substrates. Those particles enabled the visualization of the deformation field in a more accessible manner[25]. In modern TFM, the positions of the tracers are detected and tracked with automated particle detection and tracking routines to quantify the deformation field. The substrate is mathematically modeled as a linear elastic half space, to which cellular stresses are applied at the top surface. These stresses can then be reconstructed with the Green's function describing the stress-strain relationship of the substrate[79]. While early reconstruction algorithms were rather slow, modern technological and computational advances have enabled almost real time reconstruction speeds[51,80,81]. While earlier work achieved resolutions of a few micrometers, which is sufficient enough to resolve the coarse stress fields of eukaryotic cells, modern implementations using differently-colored tracer particles

have almost reached the Abbe diffraction limit, resolving individual adhesion sites of eucaryotic cells[81,82] and the stress fields of individual bacteria with a size of only a couple of micrometers[83]. Since its development, TFM has revealed interesting details about cellular force generation. For example, it is by now well established that cellular forces exerted on the ECM are mainly generated by contractions of the actomyosin machinery[30,84–86]. TFM has also revealed the critical role of focal adhesions[87–89] and the respective integrin-binding proteins of the ECM in cellular force generation[90,91]. Furthermore, the spatial organization of traction forces has been investigated, relating cell morphology and traction force generation[23,63,90,92]. During cell migration, an analysis of the force field has revealed that the forces are exerted on the ECM in a quasi-periodic manner and that the temporal and spatial evolution of the force field can be used to define different stages of the motility cycle[80,83,84,93,94]. Aside from single cell studies, TFM has also revealed collective phenomena such as cooperative force generation during collective migration of bacteria[83] as well as mechanical cell-to-cell communication[95].

1.2 Uptake of Extracellular Objects: An Inherently Mechanical Process

1.2.1 Internalization Mechanisms

Another process, which is inherently governed by mechanical interactions, is the internalization of extracellular objects into cells. While multiple distinct internalization mechanisms such as phagocytosis or macropinocytosis have been identified[96], all of those mechanisms share some similarities. All of them start with the initial contact between the target and the membrane. Typically, ligands on the target surface bind to membrane receptors, and those binding events initiate intracellular signaling cascades. Although the signaling cascades differ between different uptake mechanisms[97], they all ultimately lead to the polymerization of actin filaments, which drive membrane protrusions to wrap the target, forming an endosome[96,98,99]. Large objects with a diameter of a few micrometers such as large bacteria[100,101], apoptotic or dead cells[102–105], and large microplastic particles[106] can be taken up by phagocytosis and some cells can even engulf objects which are larger than $20\,\mu m$[107]. In contrast, objects smaller than a micrometer such as macromolecules and viruses are typically taken up by receptor-mediated endocytosis[108]. Macropinocytosis is biologically rather similar to receptor-mediated endocytosis and is often referred to as the uptake of liquids[96,98,108]. However, also nanoparticles can be taken up by macropinocytosis[109,110].

All of these uptake mechanisms play significant roles in innate and adaptive immunity[96,108], but also in tissue homeostatis and repair[111–113]. In the case of phagocytosis for example, Elie Metchnikoff was the first to realize this significance, and for this reason, he is considered to be the father of innate immunity today[114,115]. For his discoveries, Metchnikoff was awarded the Nobel Prize in 1908.

Cells capable of phagocytic uptake can be divided into two categories, namely professional and non-professional phagocytes[116]. On the one hand, professional phagocytes such as neutrophils, monocytes, and monocyte-derived as well as tissue-resident macrophages are specifically dedicated to the elimination of different pathogens. As such, they are equipped with a wide range of specific transmembrane receptors to detect and internalize different targets with high specificity. Professional phagocytes also present antigens to other lymphocytes and thus critically contribute to adaptive immunity.[116–118] Non-professional phagocytes such as fibroblasts, dendritic cells, and epithelial cells are also capable of performing phagocytosis. Those cells, however, have a much more limited scope and engulf targets more slowly and less efficiently[118].

1.2.2 Phagocytic Uptake

Phagocytosis is a highly involved process and its coordination is orchestrated by a sequence of biochemical reactions. It can be conceptualized into four different stages. Those stages are summarized in figure 1.2. Further details, especially about the involved biochemical processes, can be found in the referenced publications in this section.

The process of phagocytosis starts with the binding of an opsonized target to the membrane. The binding process and subsequent receptor activation (fig. 1.2A), are discussed in section 1.2.2.1. In section 1.2.2.2, the mechanics of the wrapping of the target in a tight membrane protrusion termed the phagocytic cup are recapitulated (fig. 1.2B). The subsequent closure of the cup to form an intracellular vacuole termed the phagosome (fig. 1.2C) is summarized in section 1.2.2.3. Section 1.2.2.4 discusses the subsequent intracellular transport of the phagosome and its acidification, leading to the degradation of the target (fig. 1.2D).

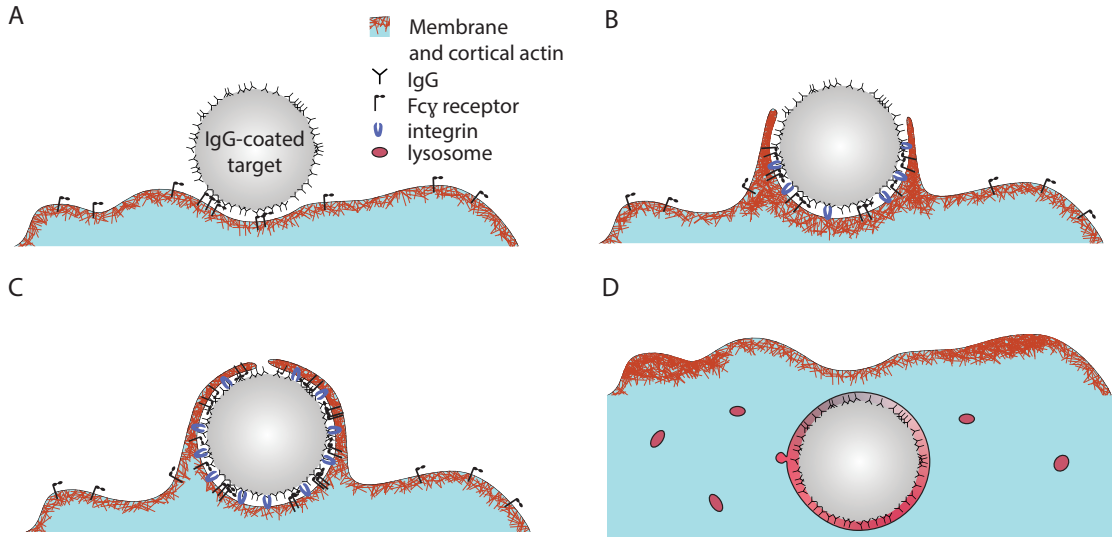

Figure 1.2: Individual stages of particle uptake. (A) After an IgG-coated target, e.g. a bacterium or an apoptotic cell comes into contact with the membrane of a phagocyte, more and more IgG antibodies bind to Fcγ receptors in the membrane. Subsequent receptor clustering and signal integration eventually lead to (B) a localized protrusion of the membrane around the particle, which is driven by actin polymerization, shaping the so-called phagocytic cup. The protrusion is likely mechanically anchored to the target by integrin bonds, which form behind the leading edge. (C) After cup closure, (D) the vesicle matures through fusion with lysosomes, which is accompanied by the acidification of the vesicle. The target is ultimately degraded. (Proteins not drawn to scale.)

1.2.2.1 Binding and Receptor Activation

During the first phase of phagocytosis, the target binds to the cell membrane (fig. 1.2A). In the process, the target can be biochemically detected with antibodies bound to its surface, to induce opsonic phagocytosis. In mammels, five different classes of such antibodies exist, namely IgA, IgD, IgE, IgG, and IgM. In the blood, IgG is abundantly distributed as part of the adaptive immune response. The y-shaped protein consists of two identical antigen binding sites, which serve to

inactivate antigens by binding to epitopes, specific binding regions on the antigen. As IgG has two identical epitope binding sites, IgG can cross-link antigens to form large complexes. These complexes become increasingly less soluble and precipitate, inactivating the antigen[10]. Aside from inactivation of antigens, IgG can also initiate phagocytic uptake of antigen-coated targets. On the tail end of the antibody, the Fcγ binding region can bind to Fcγ membrane receptors (FcγR) of phagocytes. Both IgG and Fcγ exist in different subtypes, which differ in their binding affinity to the respective binding partners. A detailed review about these subtypes of IgG and FcγR was published by Nimmerjahn and Ravetch in 2008[119].

Aside from antibodies, opsonic phagocytosis can also be triggered by the binding of fibronectin to integrin[99,103,120,121]. Overviews of additional phagocytosis-triggering ligand-receptor pairs were published by Freeman and Grinstein[122] and Gordon[123]. In contrast to the uptake-enhancing opsonins described above, specific ligands can also decrease phagocytic uptake efficiency. For example, CD47 is upregulated in many cancer cell lines and serves as a phagocytosis inhibitor, preventing macrophages from clearing leukemia and tumor cells. Inactivation of CD47 has been shown to lead to tumor cell elimination by phagocytic uptake[124,125].

As phagocytic receptors are typically activated upon opsonin binding and clustering, opsonins must be tightly packed on the target and the receptors must be free to diffuse within the membrane for activation. Diffusion of transmembrane proteins is however impeded by the meshwork of cortical actin directly below the membrane[126–130]. Therefore, depolymerizaton of cortical actin increases the mobility of membrane receptors and ultimately enhances FcγR clustering in the membrane[131,132]. This was conceptualized in the picket-fence model for phagocytosis[122,133]. In this regard, macrophages which exhibit dynamic remodeling of the cortex, e.g. visible by active membrane ruffling, are primed for enhanced receptor clustering and uptake. Such an activated state of the cortex of macrophages can for example be induced by stimulation with chemokines or toll-like receptor ligands[134].

1.2.2.2 Phagoytic Cup Formation

Upon receptor activation, an intracellular signaling cascade is triggered, which ultimately leads to the polymerization of cortical actin[97,99]. This polymerization drives the protrusion of the membrane around the target (fig. 1.2B). Typically, the protrusion is tightly localized around the target[72,135]. The structure is therefore also referred to as the 'phagocytic cup'. The polymerization of actin is initiated by the recruitment of nucleation-promoting factors. Those include, for example, formin, which promotes the elongation of existing filaments and the nucleation of new filaments.[136] Another nucleation-promoting factor, which has been shown to be recruited to the cup is Arp2/3, which initiates the polymerization of branched actin filaments[122,135,137]. Furthermore, it has been hypothesized that the subsequent binding of IgG to FcγR is necessary to continuously promote the protrusion of the cup formation around the target in a zipper-like manner[96,138]. In contrast, the picture for integrin-mediated phagocytosis is less clear. While earlier work suggested that the targets rather sink into the cytosol[96,139,140], tight cup formation was observed in macrophages in recent studies[72,141].

Although the precise mechanics of the cup formation of both pathways are still under fierce debate[142], important progress was made during the last five years. A recent study by Jaumouille et al. showed that both inhibition of formin with SMIFH2 and inhibition of Arp2/3 with CK-666 impeded phagocytic efficiency in integrin-mediated phagocytosis, suggesting that both formin- and Arp2/3-dependent polymerization drive cup formation. Using fluorescence imaging, they showed that a dense, branched Arp2/3 mediated actin network drove membrane protrusion, while a formin-mediated actin network promoted integrin-dependent coupling to the particle surface behind the leading edge[72]. Jaumouille et al. found that the speed of the leading edge of the cup is linked

to the degree to which the formin-mediated actin network is mechanically coupled to the target. Furthermore, they suggested that this coupling is bolstered by an integrin-mediated molecular clutch, which regulates the protrusion speed. When the clutch is engaged, actin retrograde flow is impeded or even stopped, increasing the protrusion speed of the cup. In contrast, when the clutch is disengaged, actin retrograde flow slows down the protrusion of the membrane, counteracting actin polymerization at the leading edge. The clutch can supposedly be reinforced by the recruitment of vinculin, proposing a promising explanation for the observed mechanosensitivity of phagocytosis mentioned in section 1.1[72,143].

Until recently, integrin- and FcγR-mediated phagocytosis were thought to be different mechanisms. However, the discovery of this molecular clutch mechanism in integrin-mediated phagocytosis has also interesting implications for the cup formation in FcγR-mediated phagocytosis. In FcγR-mediated phagocytosis, the importance of integrin-mediated adhesion sites is more and more recognized[143]. Firstly, it was observed long ago that integrin adhesion-site associated proteins such as talin and vinculin are recruited to FcγR-mediated phagocytic cups[140,144]. Secondly, integrin inactivation lead to reduced phagocytic uptake efficiency[145] and finally, it was observed that integrins are activated in the vicinity of engaged FcγR receptors. It was therefore proposed that integrins are supposedly required in the zipper mechanism to bridge the space between opsonins on the target surface[145]. Studies with inhomogeneously coated janus particles support this idea. However, the gaps between the antibodies must not be too large as the uptake efficiency decreased, the smaller the opsonized area on the particle was[146].

Together, these findings promote the idea, that the mechanical aspects of cup protrusion in integrin- and FcγR-mediated phagocytosis may not be all that different. Integrin binding may be involved in both pathways and may mediate affinity to the target in order to ensure tight wrapping. In this view, instead of establishing a mechanical link between target and phagocyte, opsonin binding to membrane receptors such as FcγR may rather increase specificity to the target[145]. This hypothesis is also supported by the fact that no mechanical linker proteins between FcγR and actin are known, rendering the observed mechanosensitivity of FcγR-mediated phagocytosis difficult to explain[70,74,142].

1.2.2.3 Cup Constriction and Closure

When the whole target is fully wrapped, the membrane closes to form a vesicle, which is commonly termed *phagosome*. By now, it is established that mechanical constriction of the cup occurs. This is especially the case during the late stages, when most of the target is already engulfed. Experiments with soft target particles[75] have recently demonstrated in a convincing manner that this constriction is mediated by myosin-II motors. The constriction occurs at the leading edge of the cup and appears to be orchestrated in a 'purse string' manner, ensuring a tight fit of the leading edge to the target[75,147,148]. The membrane scission event, which eventually closes the cup, is extremely difficult to capture, especially with fixed cells and thus, probably the least studied stage of phagocytosis[149]. To date, it is known that recruitment of the membrane-remodelling GTPase dynamin2[150] to the tip of the cup is associated with the membrane scission event to form the phagosome. However, the precise role of dynamin2 remains subject for further research[151]. The phagosome formation is also accompanied by the depolymerization of actin inside the cup, mechanically decoupling the phagosome from the cortex. However, although some details about the biochemical regulators are known, the decoupling mechanism is also poorly understood[152].

1.2.2.4 Phagosome Maturation

After the detachment from the cortex, the phagosome matures as it is transported to the nucleus via microtubules. Recently, Keller et al. showed that the transport efficiency to the nucleus is size dependent and larger phagosomes with a size of 3 µm were transported more efficiently by dynein motors. In contrast, smaller phagosomes with a size of 1 µm were transported in a more erratic manner, suggesting a possible sorting mechanism for phagosomes[153,154]. During the transport to the nucleus, the phagosome acidifies as it fuses with lysosomes to ultimately become a phagolysosome[152]. In the process, the proton-pumping transmembrane protein V-ATPase is accumulated in the phagosomal membrane and the phagosome acidifies[152,155]. Inside the phagolysosome, the pH can drop to values as low as 4.5[152]. Phagolysosomes also contain many hydrolytic enzymes such as proteases, lysozymes, and lipases as well as other microbicidal components such as reactive oxygen species which degrade the phagocytic target[149,152]. Further biochemical details on the maturing process, especially on the transition from the phagosome to the phagolysosome have been reviewed by Rosales Uribe-Querol as well as Levin et al.[149,152].

1.3 Outline of this Thesis

For the above-mentioned studies on mechanotransduction and cellular force generation, precise knowledge of the elastic properties of the used substrates is crucial so that different physiological environments can be mimicked in a controlled manner. Knowledge of the elastic modulus and the Poisson ratio is especially critical for TFM studies, as both parameters are required to calculate the stress field. The substrates are typically polymerized in-house in the form of thin polymer films with a thickness of a few tens of micrometers. As the elastic properties of such films greatly depend on the precise polymerization protocols, in-house methods are necessary to measure their elastic properties. While various methods to determine the elastic modulus are available, techniques to measure the Poisson ratio of thin films are scarce. In chapter 2 of this work, a method to measure the elastic properties termed the *steel sphere method* was advanced to allow the simultaneous measurement of both the elastic modulus and the Poisson ratio of such films. In the technique, steel spheres with a diameter of roughly one millimeter were placed on the surface of the films and the elastic properties of the films were derived from the indentation depth. In the first experimental part of chapter 2, thin hydrophilic films were investigated. The techniques were adapted to hydrophobic films in the second part of chapter 2. Methods to optimize the reconstruction precision are presented in the third part of chapter 2.

Furthermore, two techniques to study the mechanics of the early phase of the phagocytic binding process were developed. As a model system for phagocytosis, the interactions between murine macrophages and polystyrene particles as phagocytic targets were investigated.

The technique presented in chapter 3 is based on holographic optical tweezers, which offer the possibility to selectively bring individual particles into contact with the membrane of the phagocyte. Optical forces were exerted on the phagocytic target in a periodic manner. In the first experimental part of this chapter, the step response of the phagocyte was measured to resolve its viscoelastic properties and the cell-target adhesion dynamics. An extension of the technique is presented in the second experimental part of chapter 3. The setup was extended such that it enabled the direct visualization of the phagocytic cup formation in the fluorescence channel, while simultaneously resolving the viscoelastic properties of the cells.

In chapter 4, a shear flow essay is developed to investigate cell-particle interactions. The technique enables the quantification of the cell-particle adhesion strength for large ensembles of particles simultaneously. In the first experimental part of chapter 4, polystyrene particles purchased from different manufacturers were characterized. The design and the hydrodynamic characterization of

the flow chamber is presented in the second experimental part of chapter 4. The cell-particle and coverslip-particle adhesion were characterized in the third experimental part of chapter 4.

In the final chapter 5 of this work, additional experiments are discussed. The chapter focuses on experiments to investigate the mechanics of phagocytosis and other endocytic pathways.

2 A Technique to Simultaneously Measure of the Young's Modulus and the Poisson Ratio of Thin Biomimetic Films

The methods and results described in this chapter are in part based on work described in the author's master's thesis[156]. In this work, the methods were improved and a novel algorithm to reconstruct the elastic modulus and the Poisson ratio was developed. The methods to characterize polyacrylamide films described in the author's masters thesis were adapted to a wider range of materials, namely porous polyacrylamide, poly(N-isopropylacrylamide), and polydimethylsiloxane. Some of the measurements on polydimethylsiloxane films were carried out by Rebecca Benelli. Furthermore, simulations were carried out to investigate how different experimental parameters contribute to the measurement accuracy. Many of the methods and results presented in this chapter were published in the following two research articles:

- *'Simultaneous measurement of the Young's modulus and the Poisson ratio of thin elastic layers' (W. Gross and H. Kress, Soft Matter, 2017)[157]*
- *'Optimization of experimental parameters for the mechanical characterization of thin elastic films' (W. Gross and H. Kress, Journal of Physics Communications, 2019)[158]*

2.1 Thin Film Rheology in the Field of Mechanotransduction

As established in chapter 1, a common technique to study mechanotransduction is to place cells on polymer films with a stiffness in the same range as that of mammalian tissue. This range spans multiple orders of magnitude and ranges from a few tens of Pa to about roughly 1 MPa[47–49]. Consequently, biomimetic materials with a wide range of stiffnesses have to be produced to be able to mechanically mimic the physiological environment of cells. In most studies, polymers are used as their stiffness can be tuned by changing details of the polymerization reaction. These polymer films are typically produced in-house and thus, their properties have to be characterized *in situ*. In this section, different suitable polymer types are introduced and the literature on available film characterization methods is reviewed.

2.1.1 Biocompatible Polymers

The most commonly used polymer for such mechanotransduction studies is probably polyacrylamide (PAA)[51,54,58,81,83,159–163]. PAA is an elastic hydrogel, which can be polymerized in situ in any desired geometry. The gel is formed by polymerization of an aqueous monomer solution containing acrylamide (AA), which forms linear chains upon polymerization and N,N'-methylenebisacrylamide (BIS) which forms cross links between these chains. The gel's stiffness depends on the concentrations of AA and BIS. Finally, the surface of PAA gels can be coated with various ECM proteins such as fibronectin to facilitate cell adhesion and to model different biochemical environments[50,81].

A polymer with similar chemistry is poly-N-isopropylacrylamide (PNIPA). PNIPA can be polymerized in a similar manner to PAA, exchanging AA for N-isopropylacrylamide (NIPA)[164,165]. Below the so-called lower critical solution temperature (LCST), PNIPA is markedly hydrated and has optical and elastic properties very similar to those of PAA. In contrast to PAA, PNIPA undergoes a phase transition at around 32 °C. The phase transition point depends on various parameters e.g. on the precise monomer concentrations and the pH[165–169]. This phase transition coincides with a volume loss as a large amount of water is released from the hydrogel upon heating[166,169]. It also coincides with a change of the elastic properties as PNIPA is considerably stiffer above the LCST than below[166,170,171]. Temperature-resolved measurements have shown that the phase transition does not happen at a precise temperature. Instead, the transition happens in a temperature interval of a few °C[166,170,171]. PNIPA is commonly used in cell experiments and in tissue engineering due to these temperature-dependent properties. Above the LCST, PNIPA facilitates cell spreading, growth, and adhesion at 37 °C[168,172,173]. When the temperature is lowered below the LCST, cells detach from PNIPA. For instance, this can be used to produce cell sheets consisting of an intact cell monolayer[174].

Another polymer which is commonly used is polydimethylsiloxane (PDMS)[49,51,175–177]. PDMS is an elastomer which is commonly shipped in the form of a polymer base (silicon oil) and a curing agent. The curing agent is used to cross link the base, forming an elastic material[178,179]. Depending on the base-to-curing agent ratio, the elastomer's elastic properties can be tuned to various stiffnesses in the physiological range[175,178]. In contrast to PAA and PNIPA, PDMS is hydrophobic. Hence, the polymer does not have to be stored in an aqueous solution, which simplifies the handling[51,179].

PAA, PNIPA and PDMS are all biocompatible, nontoxic, and transparent elastic polymers which can be crafted in the shape of thin films with tunable stiffnesses for cell and tissue experiments. The polymerization is typically done in the laboratories to account for special needs of the respective experiment. For example, in TFM, fluorescent particles can be embedded near the upper film surface during polymerization to visualize and measure the deformation field when cells exert traction stresses on the top layer of the film (fig. 1.1)[37,50,81–83]. The stiffnesses of all of those materials are highly dependent on the monomer concentrations and consequently, they can be tuned to suit the precise needs of the experiment[50,175,176,178,180–182]. However, care has to be taken because polymerization protocol details such as polymerization temperature and duration can change the elastic properties of the polymerized material[180,183,184]. For hydrogels such as PAA, the swelling ratio, which depends for example on salt[185–187] and crosslinker concentrations[74] can also alter the elastic properties. Furthermore, dissolved oxygen in the monomer solution can also alter the elastic properties of the final polymer[50,81]. All of those influences make comparisons between literature results difficult, highlighting the fact that *in-situ* techniques are necessary to mechanically characterize the materials. In fact, in the vast majority of the studies cited in this section, in-house techniques were used to measure the polymer's elastic properties with a variety of different methods. An overview over the used techniques is given in the next section.

2.1.2 Established Techniques for Polymer Characterization

In order to measure the elastic modulus of macroscopic polymer samples, tension tests are suitable[56,65]. Aside from tensile strain, the materials can also be probed either by shear[180] or by compression[74,188]. Probably the most common procedure to measure the elastic modulus of such polymers is to compress the material with an indenter and to measure the indentation depth as a function of the indentation force. Theoretical descriptions of the indentation problem are available for different indenter shapes. Among the most commonly used shapes are spherical[50,188–192], cylindrical[193,194], and pyramidal[195,196] geometries. A suitable technique is, for example, atomic force

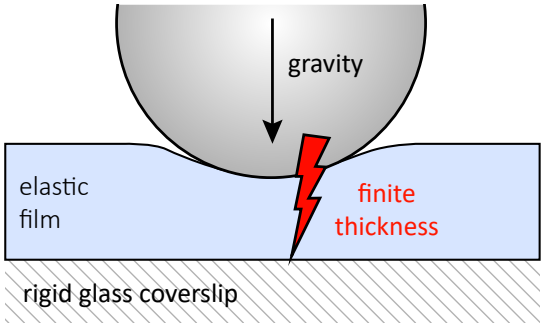

Figure 2.1: Finite thickness effects in indentation experiments. When an elastic film with finite thickness is probed with an indenter and the deformation field's size is approximately equal to the film thickness, the rigid glass substrate can lead to an overestimation of the film's stiffness if finite thickness effects are not accounted for.

microscopy. In atomic force microscopy, an indenter is attached to a cantilever and the cantilever itself is attached to a precise positioning system, which is used to control indentation depth and force. The indentation force is determined by the deflection of the cantilever[188,196,197]. Another technique to achieve well-controlled indentation forces is the so-called steel sphere method, in which steel spheres are placed on the surface of the sample. These spheres sink into the sample due to their gravitational force. The elastic properties are then determined by measuring the spheres' indentation depths[50,55,191].

In all of those indentation experiments, finite thickness effects should either be avoided or accounted for when thin samples are probed. In case a soft sample is bound to a hard substrate, e.g. a thin elastic film, which adheres to the surface of a coverslip (fig. 2.1), finite thickness effects can lead to an overestimation of the elastic modulus. These finite thickness effects have to be accounted for, when the size of the lateral and therefore also the size of the axial deformation field is not considerably smaller than the film thickness[190,194]. For this reason, an elastic film can be considered to be 'thin' in indentation experiments whenever the contact radius of the indentation region is approximately of the same size or smaller than the film thickness.

The measurement of the Poisson ratio of such materials is, however, a relatively difficult task and techniques to simultaneously measure the elastic modulus and the Poisson ratio are scarce. Techniques to measure both elastic parameters include micropipette aspiration[198], macroscopic compression tests[199], and magnetic microneedles[200]. Furthermore, it has been shown that the elastic modulus and the Poisson ratio of a thin film can be determined from indentation experiments by deforming the film with a cylindrical indenter with a diameter of approximately the same size as the film[193,194,201]. Cylindrical and pyramidal indenters do, however, have certain downsides compared to spherical indenters. It is e.g. critical that the sample is indented perpendicular to its surface. Furthermore, nonlinear effects can occur, especially near the edge of the indenter where the deformations are relatively large.

All of those methods described above to determine the Poisson ratio of thin elastic films require specialized equipment, which is not necessary for mechanotransduction studies. In particular, some measurement setups require macroscopic samples, which are incompatible with the inverted microscopes and high NA-objectives used for the cell studies[175]. As the elastic properties of PAA, PNIPA and PDMS are, as described above, sensitive to the precise polymerization conditions, this approach to calibrate thin films may not always be valid. In case critical parameters differ during the polymerization of a thin samples compared to the polymerization of a thick samples,

the polymers' elastic properties can differ. This can happen due to subtle effects e.g. due to a different temperature distribution inside the samples during curing, which can arise due to an exothermic polymerization reaction[74,183]. Some studies even relied on literature data for the Poisson ratio[90,202–204] or assumed that the material is incompressible[159,199,205], even though the Poisson ratios reported for PAA vary from 0.24-0.5[51,188,196,199,200,206–209]. In the Hertzian model, in which a hard sphere with radius R is pushed into a linear elastic half space with a given force F, the half space's elastic modulus E is given by[189]

$$E = \frac{3\left(1-\nu^2\right)F}{4\left(R\delta^3\right)^{0.5}}. \tag{2.1}$$

Here, δ is the indentation depth. Hence, the difference between the assumption of a Poisson ratio of 0.24 and 0.50 affects the resulting elastic modulus by a factor of $\left(1-0.24^2\right)/\left(1-0.50^2\right) = 1.3$ or 30 %. It has also been shown that, in TFM, the cellular stress field reconstruction on thin PAA films is greatly influenced by the Poisson ratio of the film and in turn, the apparent substrate stiffness felt by cells on the films is also greatly influenced by the Poisson ratio of the film[210], highlighting the need for easy to use *in situ* techniques to measure the elastic properties of thin films with a stiffness in the physiological range.

2.1.3 Simultaneous Measurement of the Elastic Modulus and the Poisson Ratio

In this chapter, an experimentally simple technique to determine the elastic modulus and the Poisson ratio of such thin films is presented. The technique is based on the classical steel sphere method[50,55,191], however, the interplay between the elastic properties and finite thickness effects is exploited to determine both elastic parameters in a single experiment[190,193,194]. Steel spheres with radii R between 200 and 500 µm were placed on linear elastic films with thicknesses h ranging from 30 to 170 µm. The indentation region was imaged with an inverted microscope to measure the indentation depth $\delta\left(h,R\right)$. The elastic modulus E and the Poisson ratio ν were reconstructed using an analytical *ab-initio* solution of the spherical contact problem developed by Dimitriadis et al., which takes finite thickness effects into account[190]. The technique was applied to four different materials, namely PAA, porous PAA, PNIPA, and PDMS, which all had different elastic properties inside the physiological range. While PAA and PNIPA films were polymerized in a custom protocol, PDMS films were commercially acquired.

The general methods to apply the technique are developed on the basis of thin PAA and PNIPA films in section 2.2. In section 2.3, the methods are adapted to PDMS films, which are hydrophobic and therefore, they adhere to the spheres. Among other difficulties, the adhesion between the films and the indenter introduces a hysteresis, i.e. the indenter sticks to the film as the indenter is removed. A method to mitigate adhesion effects between PDMS and the steel spheres is also presented in section 2.3. In the next section 2.4, simulated indentation experiments were used to assess the technique's precision. Using these simulations, guidelines to achieve a high precision at a minimal workload are presented in section 2.4. A overview of the prerequisites, of all the methods and the limitations of the technique developed in this chapter is given in the final section 2.5 of this chapter.

2.2 Characterization of Thin Hydrophilic Films

2.2.1 Polyacrylamide Hydrogel Polymerization

2.2.1.1 Coverslip Cleaning and Activation

This section describes the preparation of the coverslips, which were used as a hard substrate for PAA and PNIPA hydrogels. Since PAA hydrogels only weakly adhere to untreated glass coverslips, the coverslips were chemically treated. The treatment is used to covalently bind the coverslips to the hydrogels[159]. A detailed version of this protocol is given in appendix 6.1.1.

Rectangular coverslips (40x22 mm, # 1, Glaswarenfabrik Karl Hecht, Sondheim v. d. Rhön, Germany) were placed in custom-built coverslip holders. They were cleaned by sonication for 10 min in 0.2 M EDTA, 10 % w/v hydrogen chloride, and 1 % v/v 7X-O-Matic (MP Biomedicals, Germany, Eschwege, Germany) or a freshly prepared 1 % w/v Alconox (Alconox, White Plains, NY, USA) solution. The coverslips were cleaned in purified, deionized water (MilliQ) and dried with canned air after each sonication step. In the following steps, no differences between coverslips treated with 7X-O-Matic and Alconox were observed. Cleaned coverslips were stored in 90 % ethanol for at most three months.

Activation was done according to a long-established protocol[50,81,159,211], which is summarized in fig. 2.2. Since some parts of this protocol are time critical, each step was done with three coverslips at a time. In this and all following protocols, all liquid volumes were measured with pipettes (Pipetman P2, P10, P200, and P1000, Gilson, Middleton, Wisconsin, USA). All solids were weighed with a laboratory balance (ATL-124-I, Acculab, New York, USA). 12 µl of 0.1 M

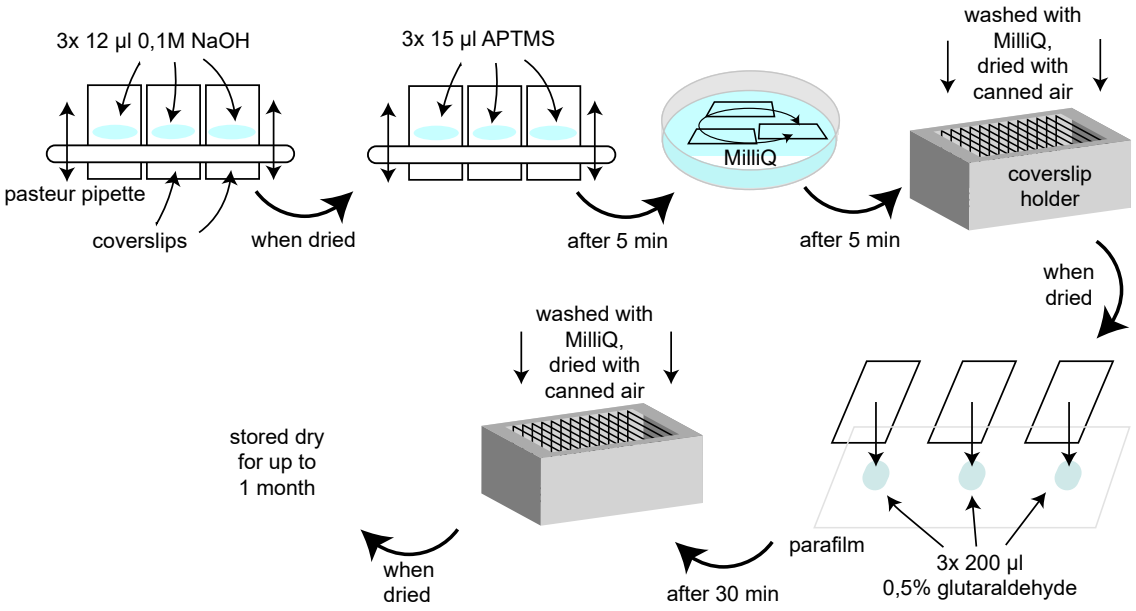

Figure 2.2: Coverslip activation protocol. 44x22 mm-sized coverslips were activated with NaOH, 3-APTMS and glutaraldehyde. The coating facilitates covalent binding of polyacrylamide hydrogels. A detailed description of this protocol is provided in the main text in section 2.2.1.1.

NaOH were spread on each coverslip by rolling a pasteur pipette over the top of each coverslip. The coverslips were air-dried and 15 µl of (3-aminopropyl)trimethoxysilane (3-APTMS, Sigma-Aldrich, St Louis, MO, USA) were spread on each coverslip and allowed to covalently bind to the glass coverslip[211] for 5 min. Care was taken not to dry the coverslips longer than 5 min as a fully dried hard layer of 3-APTMS can not be washed away reliably with the subsequent protocol. The coverslips were then washed in MilliQ water in petri dishes for 5 min under gentle agitation and subsequently transferred to the coverslip holders, where they were washed with running MilliQ water twice with a short interim incubation time. This process ensured that unbound 3-APTMS was properly removed, which would have lead to reddish remainders on the coverslip. The coverslips were dried with canned air and the surfaces coated with 3-APTMS were incubated on a drop of 0.5 % glutaraldehyde solution (prepared from 8 % stock solution, Sigma-Aldrich). Care was taken that the whole coverslip surface was covered properly with liquid. The coverslips were then transferred to the coverslip holders, washed in MilliQ water three times and dried with canned air. Drying the coverslips with canned air ensured that no drying spots were left on the coverslips. As the coating was invisible, the non-activated coverslip sides were marked with a tiny capital 'L' to avoid confusion. The coverslips were stored together with desiccant beads (Neolab Migge, Heidelberg, Germany) at room temperature in a container sealed with parafilm for up to one month. If necessary, any dust was removed with MilliQ water and canned air directly prior to use.

Small, round coverslips with a diameter of 15 mm (Menzel-Gläser, Braunschweig, Germany) were used to achieve flat top surfaces on PAA and PNIPA films. They were coated hydrophobically with RainX (Krako Car Care International) according to the manufacturers protocol to facilitate easy detachment after the polymerization process. The coverslips were briefly soaked in RainX and allowed to air-dry. Excess RainX was removed with cleaning tissue and dust was removed with canned air.

2.2.1.2 Polymerization of Polyacrylamide Films and Springs

Thin PAA films were prepared according to well established polymerization protocols[50,65,81,159,161]. A detailed version of the protocol used in this work is given in the appendix (section 6.1.2). Briefly, monomer solutions of 3 % w/v and 10 % w/v AA (from 40 % w/v stock solution, Sigma Aldrich, molecular weight 71 u) and 0.03, 0.06, and 0.10 % w/v BIS (from 2 % w/v stock solution, Sigma-Aldrich, molecular weight 154 u) as a crosslinker were prepared in phosphate buffered saline (1xPBS, 0.2 g/l KCl, 8 g l^{-1} NaCl, 1.44 g l^{-1} Na_2HPO_4, 0.24 g l^{-1} KH_2PO4 in MilliQ water). N,N,N',N'-Tetramethylethylenediamine (TEMED; Thermo Fisher Scientific, Waltham, MA) was added at a concentration of 1/2000 v/v as a catalyst. Tracer particles (FluoSpheres, carboxylate-modified polystyrene microspheres, Thermo Fisher Scientific #F8811, diameter 0.2 µm, Ex/Em: 505/515 nm, stock concentration 4.5×10^{12} particles/ml, density $\rho_{PS} = 1.055\,g/cm^2$) were briefly sonicated, and vortexed to minimize particle clustering. The stock particle solution was added at a concentration of 0.51 % v/v. An aqueous 10 % ammonium-persulfate (APS; Thermo Fisher Scientific) solution was always prepared directly prior to polymerization and stocks of APS were stored in N_2 atmosphere. The free-radical polymerization[212] was started with the addition of 1/200 v/v of APS solution.

The process to polymerize hydrogel layers with a thickness of a few tens of micrometers is summarized in figure 2.3. For every hydrogel, 15 µl of monomer solution were pipetted onto the RainX-coated side of a round coverslip. A rectangular coverslip was lowered carefully from above with the activated surface facing downwards until contact to the solution was established. The configuration was suspended between two Pasteur pipettes and the solution was polymerized at room temperature for two hours. In order to avoid evaporation at the films' edges, which could alter the monomer concentrations in an uncontrolled manner and which was shown to cause wrin-

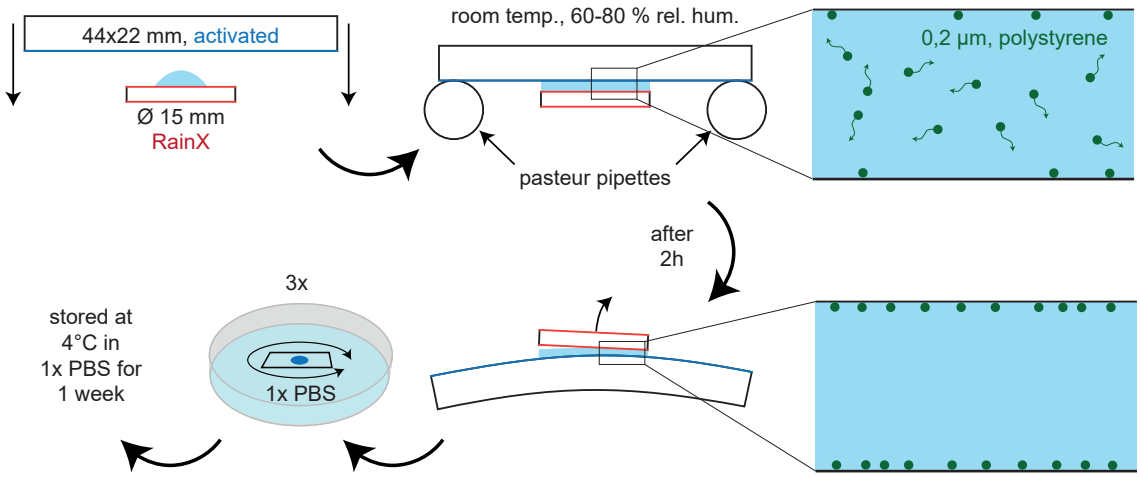

Figure 2.3: Polymerization of thin polyacrylamide films. Thin PAA hydrogel films were polymerized from freshly prepared monomer solutions between a large rectangular coverslip and a small RainX-coated coverslip. In the early stages of polymerization, fluorescent tracer particles diffused through the liquid and got stuck on both coverslips (sec. 2.2.1.3), forming two flat layers which could be easily detected with fluorescence microscopy. After 2 h of polymerization, the hydrophobic coverslip was removed with forceps. The PAA hydrogels were washed in 1xPBS and subsequently stored in 1xPBS in the fridge at 4 °C for up to one week.

kling at the films' edges[156], the setup was covered with a plastic box, which provided 60 to 80 % relative humidity. After the polymerization, the activated coverslip was slightly bent until the hydrophobically coated round coverslip detached from the hydrogel. The round coverslip was carefully removed with forceps and the hydrogels were washed three times in 1xPBS to remove any leftover monomers, TEMED and APS and thus, to stop the polymerization reaction.

Porous PAA films were polymerized as outlined in figure 2.4 by adding $CaCO_3$ powder with a particle size of 1 to 3 µm to the monomer solution at concentrations of 3, 10, and 20 % v/v. The films were slightly turbid and had a whitish appearance after polymerization, which was to be expected as the particles were slightly larger than the wavelength of visible light. The particles were dissolved in 1 % HCl for 1.5 h under gentle agitation after the polymerization was finished. Higher HCl concentrations lead to detachment of the films from the coverslip as the CO_2 formed too quickly and led to bloating. The porous hydrogels were fully transparent after the treatment with HCl, indicating $CaCO_3$ was fully dissolved and that CO_2 had been fully replaced by 1xPBS. The pores were also not visible with the microscope, indicating that the refractive index of 1xPBS and PAA were very similar. This observation is consistent with literature[74]. For this reason, it was not possible to measure the pores' size inside the films. It is, however, reasonable to assume that they had approximately the same size as the $CaCO_3$ powder particles (1 to 3 µm).

Macroscopic PAA springs with a length of about 20 cm were polymerized for control experiments. Polymerization was carried out inside 5 ml plastic pipettes which had an inner diameter of 6 mm. After two hours of polymerization, the plastic pipettes were carefully broken with a hammer and the springs were removed. No damage was observed on the springs.

Similarly, temperature-responsive PNIPA films were polymerized by substituting AA with NIPA (Sigma-Aldrich, molecular weight 113 u). Monomer solutions of 10 % w/v NIPA, 0.1 % w/v BIS, 0.51 % v/v fluorescent tracer particles were prepared in 1xPBS. The polymerization of PNIPA films took a lot longer compared to the AA films under similar conditions. For this reason, the

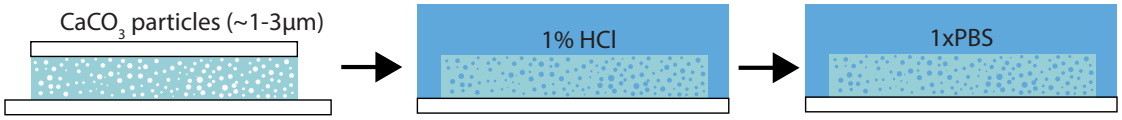

Figure 2.4: Polymerization of porous PAA films. Thin layers of porous PAA were polymerized by adding $CaCO_3$ particles with a diameter of 1-3 µm to the monomer solution. After polymerization, the films were immersed in 1 % HCl to dissolve the $CaCO_3$. The films were then washed excessively in 1xPBS to remove the HCl.

concentrations of TEMED and APS were doubled to 1/1000 v/v and 1/100 respectively. Additionally, the monomer solution was degassed in a desiccator for 45 minutes prior to polymerization. Degassing removes dissolved oxygen from the solution, which is known to affect the polymerization efficiency[50]. As the PNIPA films were a lot thinner than the films polymerized with AA, 50 µl of monomer solution were used for each gel for polymerization and thickness was controlled with two stainless steel spacers with a thickness of 50 µm positioned on each side of the liquid droplet. Furthermore, the polymerization was carried out in N_2 atmosphere for 3 h.

In order to prevent osmotic swelling after gelation, both the films and the springs were stored immersed in 1xPBS in the fridge at 4 °C for up to one week after polymerization[81]. The protocol's reproducability was validated previously[156]. With the described protocol, the films' thickness and its upper surface angle can not be controlled well. Although this could be achieved with spacers, a fine control of the thickness profile for PAA films was not necessary for the experiments presented in this work. Instead, the variability of the film thickness even proved to be beneficial as described in the following sections. When films with a well defined thickness are to be be produced, the precise details of the swelling behavior have to be taken into account[185,186].

2.2.1.3 Tracer Particle Distribution in Thin Films

The tracer particles' size was chosen to be small enough such that they do not sediment during polymerization. The buoyancy-corrected gravitational force acting on the tracer particles is given by:

$$F_{\text{grav}} = \Delta\rho g V \tag{2.2}$$

$$= g\left(\rho_{\text{PS}} - \rho_{\text{sol}}\right)\frac{4}{3}\pi R^3. \tag{2.3}$$

ρ_{PS} is the density of the polystyrene particles, ρ_{sol} is the monomer solution's density, $g = 9.81\,\text{m/s}^2$ is the gravitational constant, and R is the particle radius. During sedimentation, the hydrodynamic drag force F_{Stokes} on the particle is given by Stokes' law

$$F_{\text{Stokes}} = 6\pi\eta_{\text{sol}} R v \tag{2.4}$$

where η_{sol} is the solution's (time dependent) dynamic viscosity, which, during polymerization, was likely always equal to or larger than the viscosity of water $\eta_{\text{w}} = 1\,\text{mPas}$ at room temperature[213]. $v = \Delta z/\Delta t$ is the particles' sedimentation velocity. In equilibrium, $F_{\text{grav}} = F_{\text{Stokes}}$ must be satisfied. Therefore, assuming that, during polymerization, the solution's viscosity is always above the viscosity of water $\eta_{\text{w}} = 1 \times 10^{-3}\,\text{Pas}$ at room temperature and that the solution's density is

not lower than the density of water $\rho_w = 1.0 \times 10^3\,\mathrm{kg/m^3}$, the particles sediment the most by

$$\Delta z_{sed} < \frac{2g\,(\rho_{PS} - \rho_w)\,R^2}{9\eta_w}\Delta t \tag{2.5}$$

$$\approx 4\,\mu m \tag{2.6}$$

during two hours of polymerization time, which is a lot smaller than the typical film height. The particles' diffusion constant D is given by the Stokes-Einstein relation

$$D = \frac{k_B T}{6\pi\eta_{sol} R},$$

where k_B is the Boltzman constant and T is the temperature. Using the same assumptions as described above, the vertical displacement caused by diffusion can be estimated by the square root of the mean squared displacement (MSD) in one dimension:

$$\Delta z_{diff} \approx \sqrt{MSD} \tag{2.7}$$

$$= \sqrt{2D\Delta t} \tag{2.8}$$

$$< \sqrt{\frac{k_B T}{3\pi\eta_w R}\Delta t} \tag{2.9}$$

$$= 175\,\mu m \tag{2.10}$$

which is a lot larger than Δz_{sed} and also larger than the typical hydrogel height. Therefore, the tracer particles' final distribution was likely dominated by diffusion. When the hydrogels were polymerized without the addition of 1xPBS, the carboxylated tracer particles were evenly distributed throughout the gel after the polymerization. In contrast, the particles adhered to both glass surfaces and formed two plain layers when the polymerization was carried out in 1xPBS, which is preferable, since the particle monolayers could be used to easily identify the hydrogel surfaces. Since changes in the saline concentrations changed the particles' adhesion behavior, it is likely that electrostatic interactions mediated the adhesion between the particles and the coverslips. A more detailed analysis of these adhesion effects, including the behavior of different particle types is given in chapter 4.

2.2.2 Imaging and Data Evaluation

The setup used for imaging is summarized in figure 2.5. Imaging was performed on an inverted, motorized microscope (Nikon Eclipse Ti-E; Nikon, Tokyo, Japan), which was equipped with a 60x water immersion objective (CFI Plan Apo IR 60x WI, Lambda-S Series, NA=1.27; Nikon) and a 40x water immersion objective (CFI Apo LWD 40x WI, Lambda-S series, NA=1.15; Nikon) as well as with two objectives with a lower magnification (10x, CFI Plan Fluor DL 10x, NA=0.45, Nikon; 20x, CFI S Plan Fluor ELWD ADM 20xC, NA=0.3, Nikon). The microscope is fitted with a brightfield illumination lamp for transmission microscopy (grey beam path in fig. 2.5). Both water immersion objectives also support differential interference contrast microscopy (DIC), which is suitable to resolve local changes of the refractive index in the sample. This is for example useful to image thin cell filaments[214]. To use DIC microscopy, a DIC polarizer, two Wollaston prisms and a DIC analyzer were inserted into the beam path. Fluorescence illumination was provided by a mercury lamp (Nikon Intensilight C-HGFI; Nikon). In order to visualize the tracer particles, a fluorescence filter cube (GFP-LP; excitation wavelength: 460 - 500 nm, blue beam path in fig. 2.5; dichroic mirror wavelength: 505 nm; emission long pass filter wavelength 510 nm, green

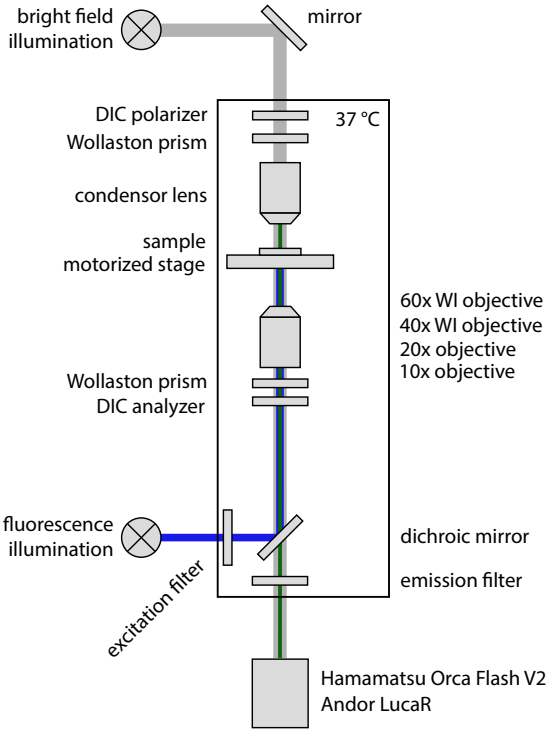

Figure 2.5: Optical setup used for the steel sphere experiments. The Nikon Eclipse Ti-E microscope was equipped with a bright field illumination lamp for transmission microscopy (gray beam path). Aditionally, fluorescence microscopy with various filters is possible (excitation light path: blue, emission light path: green). A detailed description of this figure is provided in the main text in section 2.2.2.

beam path in fig. 2.5; Nikon) was inserted into the beam path. Image acquisition was mainly done with an electron multiplying charge coupled device camera (EMCCD; Andor Luca R; 14 bit; sensor area size: 8 mm × 8 mm; Andor Technology, Belfast, Northern Ireland). Some of the measurements were captured with a complementary metal-oxide-semiconductor camera (CMOS; OrcaFlash4.0 V2; Hamamatsu Phontonics, Hamamatsu, Japan), because it had a larger sensor area of 13.3 mm × 13.3 mm and thus, enabled measurements with a larger field of view. Both the cameras and the microscope were controlled by the software NIS-Elements Advanced Research (Nikon). A custom-built incubation chamber, which enclosed the majority of the microscope including the microscopy stage and the objectives, was used to incubate the samples at temperatures above room temperature[156,215]. The incubation chamber enabled temperature stability of ±0.2 °C inside the sample[156]. Further details about the setup were described by K. Berghoff and S. Keller recently[154,216].

The coverslips with thin hydrogel layers were glued to aluminium coverslip holders with vacuum grease (fig. 2.7A) and the gels were immersed in 1xPBS. Small chrome steel spheres (density $\rho_s = (7.76 \pm 0.15)\,\mathrm{g/cm}$, grade 10, IHSD-Klarmann, Bamberg, Germany) with nominal radii of $R = 200, 250, 300, 350, 400,$ and $500\,\mu\mathrm{m}$ were used as indenters. They were cleaned with 70 % ethanol and placed on the gels. Their cleanliness was checked with bright field imaging and

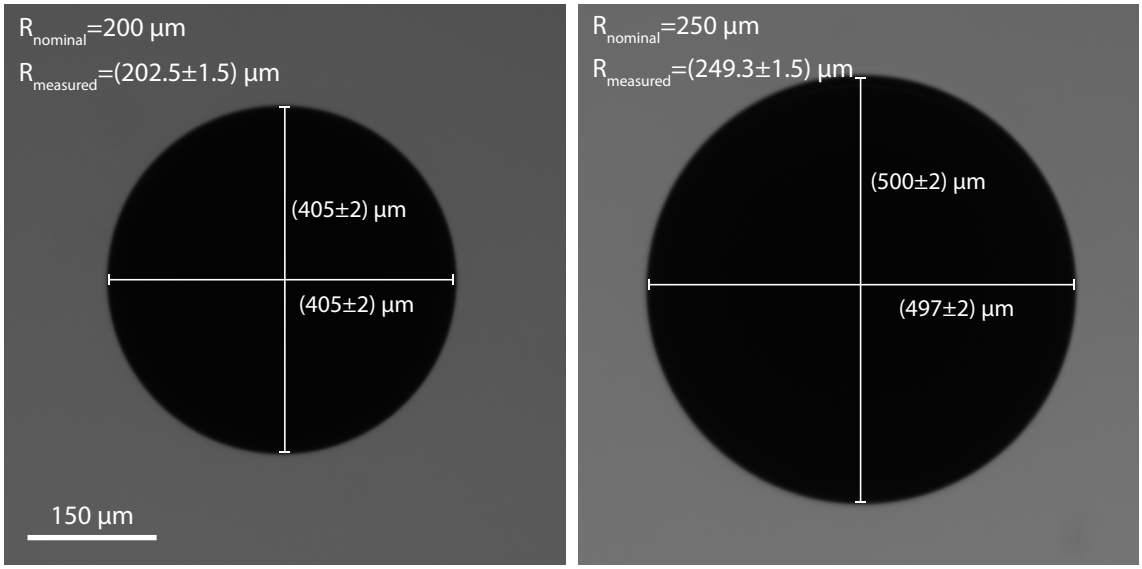

Figure 2.6: Images of two steel spheres. The images of the spheres with nominal radii of 200 and 250 µm were captured with the 10x objective. The spheres' dimensions were measured by two independent diameter measurements respectively.

their radii were measured (fig. 2.6). Deviations from the nominal radius above 1.5 % were never detected, and the eccentricities were typically below $\sqrt{1 - 1/1.01^2} = 0.14$. This high symmetry was essential, as the uncertainty of the sphere radius was one of the major contributors to the error of the whole method. The sphere radius error was estimated to be 1.5 µm by comparing the two independent sphere diameter measurements along both lateral directions through the sphere center, accounting for the spheres' eccentricity (fig. 2.6). When the sample was slightly tilted, the spheres rolled on the films' surfaces and adhesion between spheres and PAA and PNIPA films was not noticeable. The chamber was sealed with a second glass coverslip to avoid evaporation and optical distortions induced by the curved water-air interface. The system was then placed on the microscope stage. For the PNIPA film, the incubation chamber was heated to (30.0 ± 0.2) °C 1 h before the experiment and the PNIPA sample was incubated in the chamber for 15 minutes prior to the acquisition of the first data point.

Every sphere was placed at 10 to 30 different locations on the gel with a small magnet, which enabled measurements at different gel heights h. Depending on the contact radius between the spheres and the film (fig. 2.8A), the objective was chosen such that the whole contact region fits well within a single image. The microscope software also supports the acquisition of larger images by automatically moving the motorized stage. However, these acquisition modes were found to be too inaccurate for this application. Whenever possible, the 60x water immersion objective was used, which was typically possible when smaller spheres were used. The film height was measured at every location by focusing on fluorescent particle layers z_1 and z_2 located at the top and at the bottom film layers (fig. 2.7B). The height $h = z_1 - z_2$ varied between 30 - 175 µm throughout all films. The z-position of the gel surface could be measured in a very precise manner by exploiting the fact that the particles are brightest when they were perfectly in focus. Thus, the correct focal planes could be reliably and reproducibly identified via the histogram of the live image while adjusting the objective's z-position. The error of the height $s_\mathrm{h} = 1 - 1.5$ µm was roughly estimated by repeated measurements.

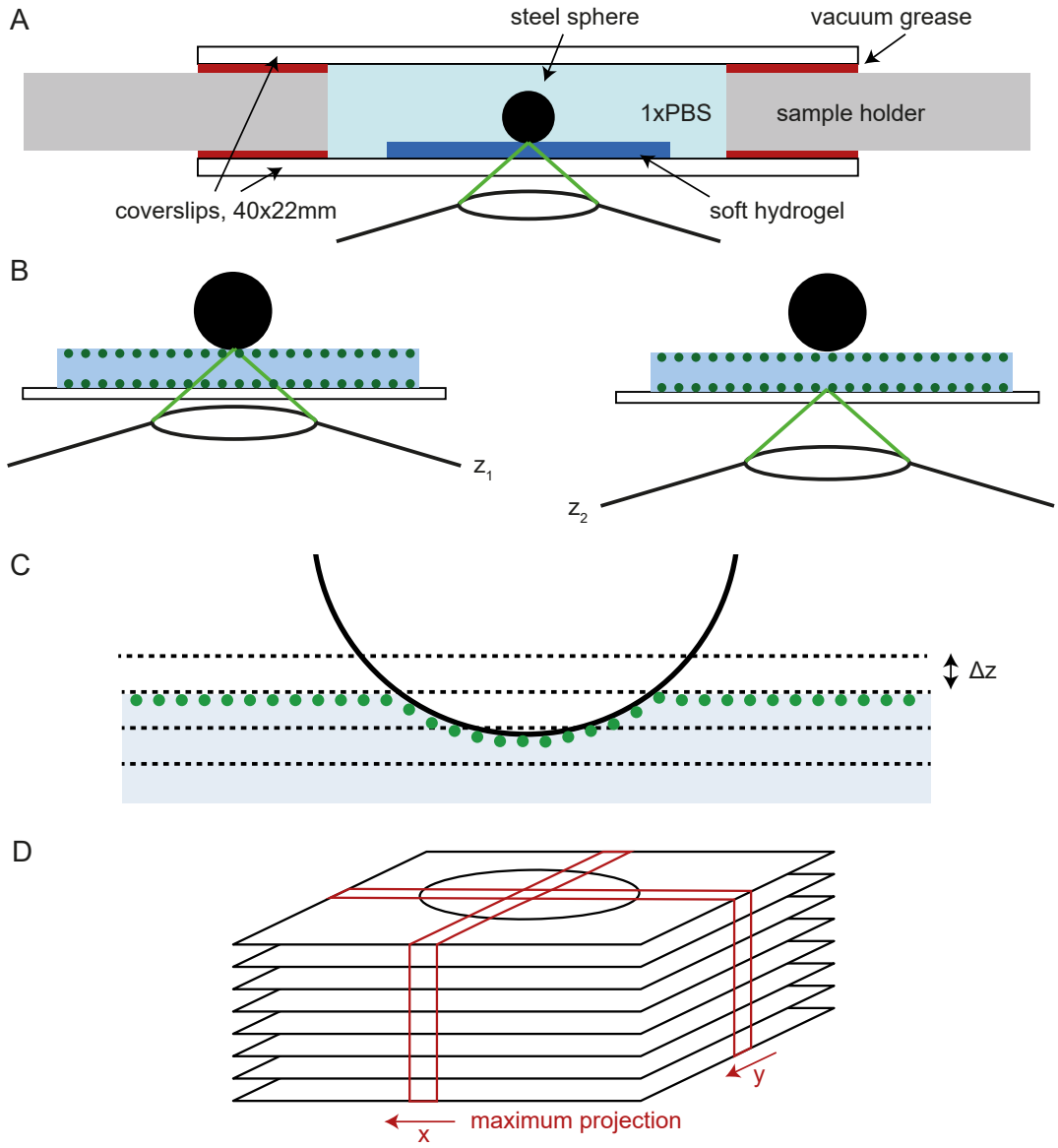

Figure 2.7: Steel sphere method data acquisition. (A) The coverslip with the hydrogel was glued to an aluminium coverslip holder with vacuum grease. The hydrogel was immersed in 1xPBS to prevent the sample from drying out. Steel spheres of different radii were placed on the gels. The system was sealed with a second coverslip and imaged with a 40x or a 60x water immersion objective. (B) The hydrogels' height $h = z_1 - z_2$ was measured by focusing on the tracer particle layers at the top and at the bottom. (C) The indentation cap was imaged by focusing on different planes with an axial distance of $\Delta z = 0.2\,\mu\text{m}$. (D) Two side views of the indentation region were created via maximum projection of a subsection of the whole stack located at the indentation cap's center. Panels (A), (B), and (C) were adapted from the author's master's thesis[156] and Gross and Kress, Soft Matter, 2017[157].

In general, if the immersion medium's refractive index and that of the sample differ, the difference between both motor positions is not equal to the distance between both focal planes[51]. When hydrogels were imaged, there was no need to correct for any refraction index mismatch between the immersion medium and the hydrogel since the refractive indices of water, 1xPBS[217] and PAA[74,218] differ by only about 1.5 %. Below the LCST at 30 °C, this holds also true for PNIPA[219]. Note that the refractive index of PNIPA does increase to about 1.4 at 36 °C[219].

In order to determine the indentation depth δ, fluorescence images of the deformed tracer particle layer were captured in different focal planes starting from a few micrometers below to a few micrometers above the indentation cap (fig. 2.7C). The axial distance of $\Delta z = 0.2\,\mu m$ was chosen to be smaller than the axial optical resolution to maximize the measurement's precision[220].

For every stack, two side views through the indentation cup's center were created with Fiji ImageJ[221] along both lateral directions (fig. 2.7D). In case the indentation cap's radius was only slightly smaller than the camera's field of view, the whole stack was rotated by 45° beforehand to optimize the visibility of the undeformed surface next to the indentation cap. The width of the substacks was chosen to be large enough to include a sufficient number of particles. However, the width had to be a lot smaller than the indentation cap's diameter, such that the generated side views only included particles located near the indentation cap's center. Typically, depending on the size of the indentation cap, two substacks with a width of a few micrometers were evaluated and a maximum projection through each substack was generated to simplify data evaluation.

A typical example of such a side view is shown in figure 2.8A. The hydrogel's deformed upper surface was located where the lowest tracer particle layer visible in figure 2.8A was located. In most measurements, the contact region was completely located below the gel's undeformed surface level. Mirror images of the particles were visible where the sphere did not touch the film. In these locations, the sphere surface was located in the middle between the particles and the particles' mirror images. Occasionally, particles adhered to the sphere surface. These particles were observed centered in-between the hydrogel surface and the mirror images of the tracer particles in the film surface (fig. 2.8A, red arrow).

The indentation depth was determined by measuring the radius of the spherical cap x below the undeformed upper film surface level far away from the sphere (fig. 2.8A). The Pythagorean theorem

$$x^2 + (R - \delta)^2 = R^2$$

was used to derive the indentation depth δ:

$$\delta = R \left[1 - \sqrt{1 - \frac{x^2}{R^2}} \right].$$

δ was measured along the x and the y direction (fig. 2.7D). Both values were averaged to reduce the measurement error. Typically, measurements along both lateral axes deviated by about $s_\delta = 0.2$ to 0.4 µm. The direct measurement of the indentation depth δ using the motor positions as in the height measurement would have been far less reliable.

Since the coverslips used for hydrogel preparation were coated to form a covalent bond between glass and PAA (sec. 2.2.1.1), it is reasonable to assume that a no-slip boundary condition at the bottom of the hydrogel is suitable. This assumption was validated by imaging the complete hydrogel once with the steel sphere on top (fig. 2.8 B, blue color) and once after the steel sphere was removed (fig. 2.8 B, red color). The corresponding side views are overlaid in fig. 2.8B. Firstly, the comparison of both data sets shows that no deformation could be detected at the bottom of the hydrogel, indicating that the hydrogel was properly bound to the glass substrate. Secondly, the deformation at the top surface was mostly confined to the contact region and fully reversible.

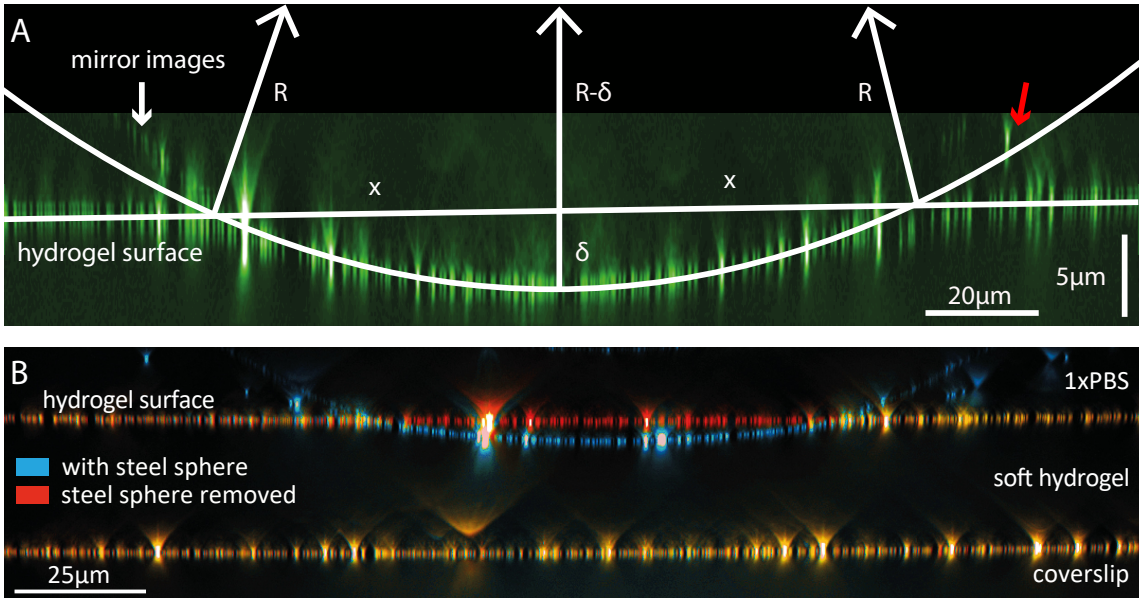

Figure 2.8: Side views of the indentation region on PAA films. (A) A steel sphere with radius $R = 400\,\mu m$ is indenting a soft PAA hydrogel with 10 % AA and 0.1 % BIS (false color). The radius x of the spherical cap was measured to calculate the indentation depth δ. Light from the tracer particles was reflected from the sphere surface, and mirror images appeared (white arrow). Occasionally, tracer particles detached from the gel and stuck to the sphere (red arrow). The images of these particles were located centered between the hydrogel surface and the mirror images. Note that the scale in the vertical and in the horizontal direction is different. (B) Comparison of the tracer particle layers at the top and the bottom hydrogel surfaces before (blue, false color) and after (red) a steel sphere with a radius of $R = 249\,\mu m$ was removed from the hydrogel surface. The hydrogel had a height of $h = 25\,\mu m$. Particles, which did not move as the sphere was removed, are shown in orange. Figure adapted from the author's master's thesis[156] and Gross and Kress, Soft Matter, 2017[157].

After the sphere was removed, no deviation from a flat top surface could be detected, which was in line with a fully elastic deformation.

In thicker regions, diffusion of the particles during polymerization had not been fast enough and not all particles had reached the top and bottom layer until polymerization was finished (sec. 2.2.1.3). In the experiments, this happened mostly in films which were thicker than 70 µm. Such thick films could, however, be used to visualize the deformation field inside the film. Likewise, the film could also be polymerized without 1xPBS to visualize the indentation region. Without 1xPBS, the tracer particles were observed to not stick to the coverslips during polymerization.

Figure 2.9 shows side views of the indentation region, imaged at a position with a thickness of about 105 µm. Spheres with different radii were used to visualize the different deformation fields. For every sphere, one image stack was acquired with the sphere lying on top of the film (red) and the other one was acquired after the sphere was removed (blue). The indentation cap was considerably deeper, the larger the sphere radius was. The displacements were also larger for larger spheres and they were mainly centered directly below the steel sphere and were mainly directed along the z-axis.

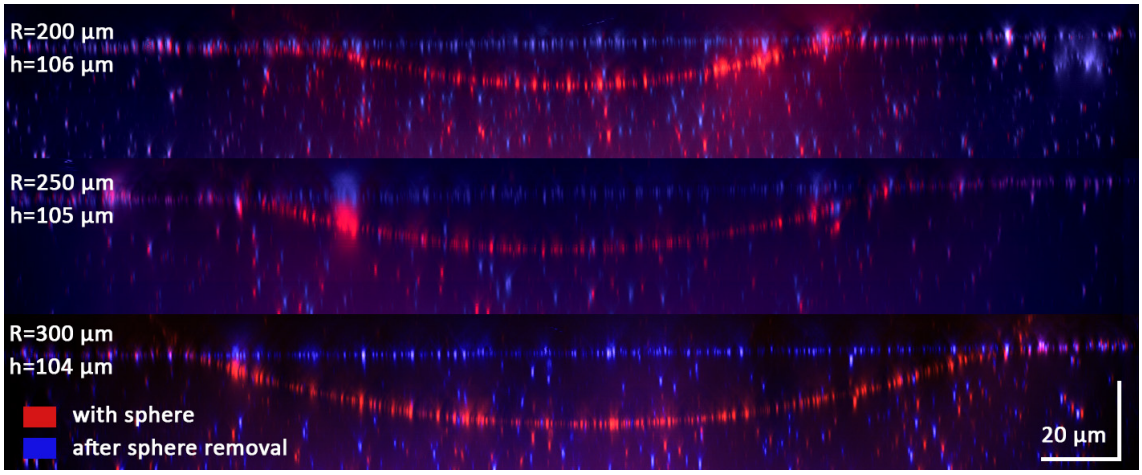

Figure 2.9: Visualization of the deformation field inside a PAA film for sphere radii of 200 µm**,** 250 µm**, and** 300 µm**.** The images were acquired on a film with 3 % AA and 0.1 % BIS. One image stack was acquired with the sphere lying on top of the film (red, false color) and one was acquired after the sphere was removed (blue). The film thickness was comparable in all three measurements. Note that the films moved slightly when the sphere was removed. Therefore, not all particles were visible in both images.

2.2.3 Finite Layer Thickness Model

The datapoints $\delta(R,h)$ were evaluated with a model developed by Dimitriadis et al. in 2002, which takes finite thickness effects into account[190]. The model is an *ab initio* extension of the Hertzian solution (eq. 2.1) for a hard sphere indenting an isotropic and homogeneous film with height h, which is deformed within the linear elastic regime[189]. The model corrects for finite film thickness effects, i.e. compared to the case of an elastic half space the spheres sink in less due to the hard coverslip at the bottom of the film. The elastic modulus E of a thin film is given by[190]

$$E = \frac{3\left(1-\nu^2\right)F}{4\left(R\delta^3\right)^{0.5}}\,\frac{1}{C}, \tag{2.11}$$

where the correction factor C given by

$$C = 1 - \frac{2\alpha_0}{\pi}\chi + \frac{4\alpha_0^2}{\pi^2}\chi^2 - \frac{8}{\pi^3}\left(\alpha_0^3 + \frac{4\pi^2\beta_0}{15}\right)\chi^3 + \frac{16\alpha_0}{\pi^4}\left(\alpha_0^3 + \frac{3\pi^2\,\beta_0}{5}\right)\chi^4 \tag{2.12}$$

accounts for finite thickness effects. ν is the Poissson ratio of the hydrogel, and F is the indentation force acting on the sphere. In the experiment, F is given by the difference between the sphere's gravitational force and the corresponding buoyancy force in 1xPBS:

$$F = \frac{4}{3}R^3\pi g\left(\rho_\mathrm{S} - \rho_\mathrm{PBS}\right). \tag{2.13}$$

Here, g is the gravitational acceleration and ρ_PBS is the density of 1xPBS. Using the spheres' nominal radii, which were 200, 250, 300, 350, 400, and 500 µm, the nominal indentation forces of the spheres used in this work were 2.22, 4.34, 7.50, 11.9, 17.8, and 34.7 µN respectively. Sphere radii were always measured directly before the indentation experiments. Consequently, the radii

measured before each experiment were used to calculate the indentation forces. The dimensionless parameter

$$\chi = \frac{\sqrt{R\delta}}{h} \tag{2.14}$$

is the fraction of the Herzian contact radius $(R\delta)^{0.5}$ and the film thickness h[190]. In case of $\chi = 0$, the Hertzian solution for an infinitely thick film is recovered. Therefore, finite thickness effects have to be accounted for whenever the contact radius is not considerably smaller than the layer thickness h. In this case, the correction factor C is larger than 1. The Taylor series given in equation 2.12 converges for values $0 \leq \chi \leq 1$, and thus, equation 2.11 is only valid in this range[190]. Since the film height h was inhomogeneous in the experiments, the indentation force was not perfectly pointed perpendicular to the surface. However, thickness inhomogeneities never exceeded 70 µm, which corresponded to an angle of 89.7° given the films' diameter of 15 mm. This effect was therefore neglected.

As no displacements at the bottom of the hydrogel were detected (fig 2.8 B, orange color), the no-slip boundary condition was considered to be suitable. In this case, α_0 and β_0 in eq. 2.12 are given by[190]

$$\alpha_0 = -\frac{1.287 - 1.4678\nu + 1.3442\nu^2}{1-\nu} \tag{2.15}$$

and

$$\beta_0 = \frac{0.6387 - 1.0277\nu + 1.5164\nu^2}{1-\nu}. \tag{2.16}$$

In case of an infinitely thick, homogeneous film ($\chi = 0$; $E, \nu = const$), the term $F/\left(R\delta^3\right)^{0.5}$ in equation 2.11 is invariant when different sphere radii R are used. Therefore, only the fraction $E/\left(1-\nu^2\right)$ can be recovered and a supplementary experiment is necessary to determine either E or ν independently. In practice, the common choice is to assume that the material is almost incompressible[51,222] or to use macroscopic methods to determine the Poisson ratio[56,206]. So far, the equation 2.11 has only been used to determine the elastic modulus of thin layers. However, C depends on the Poisson ratio and the contact geometry (fig. 2.10 A, B) and thus, both E and ν can be measured by varying the contact geometry in the range $0 \leq \chi \leq 1$ and fitting equation 2.11 to the measured indentation data $\delta(R, h)$ as it has been pointed out by Dimitriadis et al.[190]. The influence of the film's finite thickness described by the correction factor C strongly depends on the Poisson ratio near $\nu = 0.5$. In general, the higher the Poisson ratio (fig. 2.10 A) and the higher χ (fig. 2.10 B), the stronger the influence of finite thickness effects. Hence, the reconstruction of E and ν is most accurate when the material is nearly incompressible. C is very flat below $\nu = 0.3$, especially near $\nu = 0$ for all values of χ. Therefore, it is neither practical to analyze films with a Poisson ratio smaller than 0.3 with the methods demonstrated in this work nor is it possible to discriminate auxetic ($\nu < 0$) from non-auxetic, isotropic materials using equation 2.11. However, such materials are rare as most materials have a positive Poisson ratio[223].

In this work, multiple sphere radii between 200 and 500 µm were placed on films, of which the thickness varied roughly from 30 to 175 µm. The spheres sank a few micrometers into the film. With these parameters, χ varied in the range $0.15 \leq \chi \leq 1$ in the experiments, depending on the condition.

2.2.4 Reconstruction of the Rheological Parameters and Error Analysis

The measured indentation depths $d(h, R)$ for PAA films with different concentrations of AA, BIS, NIPA and for porous PAA films polymerized with $CaCO_3$ are shown in figure 2.11. Panels A-D show the data of PAA films polymerized with different concentrations of AA and BIS. The data

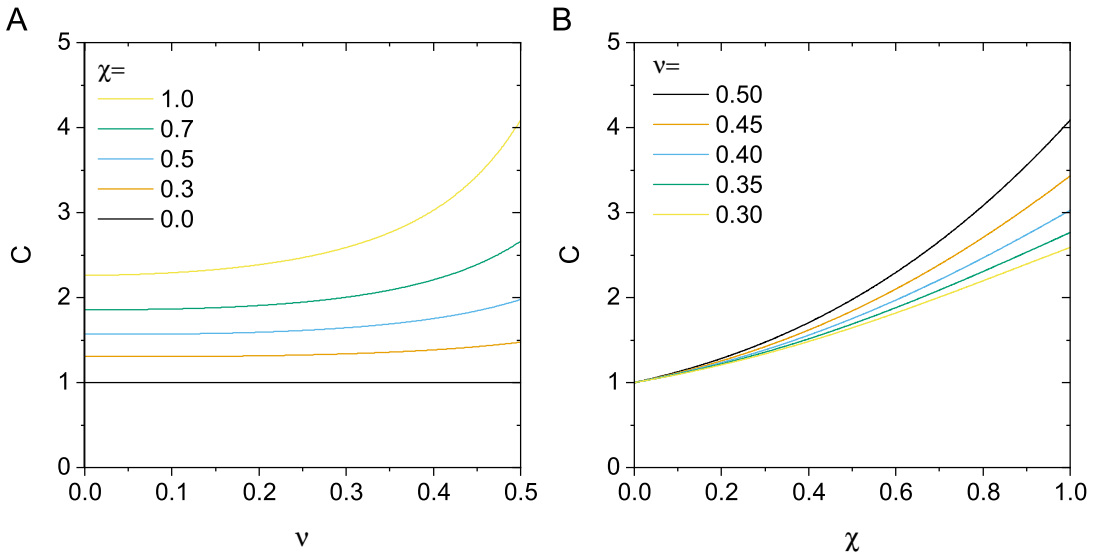

Figure 2.10: Finite thickness correction factor. (A) $C(\nu)$ for different contact geometries χ. Panel adapted from Gross and Kress, Soft Matter, 2017[157]. (B) $C(\chi)$ for different poisson values ν. Panel adapted from Gross and Kress, Journal of Physics Communications, 2019[158]. The curves in both panels were calculated with equations 2.12, 2.15, and 2.16.

of porous PAA films polymerized with 10 % w/v AA and 0.1 % BIS and with 3 % v/v, 10 % and 20 % $CaCO_3$ is shown in panels E-G. The data of the PNIPA film polymerized with 10 % NIPA and 0.1 % BIS, which was measured at 30 °C, is plotted in panel H.

In many cases, the indentation depth at a given sphere radius increased with increasing film height, indicating that the finite thickness effect was relevant in the tested conditions. The indentation depth also increased with increasing sphere radius, i.e. larger spheres sank deeper into the film. This was to be expected as it can be seen from the special case of $C = 1$ regarding equation 2.11. In case of $C = 1$, i.e. the Herzian case of an infinitely thick film, $\delta \propto R^{5/3}$ at a given elastic modulus and at a given Poisson ratio.

The elastic modulus E and the Poisson ratio ν for a data set $\{\delta_\mathrm{i}, h_\mathrm{i}, R_\mathrm{i}\}$ measured on a thin film were determined with the following, iterative algorithm: Poisson values between 0 and 0.6 with a step size of 0.001 were used to calculate an average elastic modulus for every measured data set $\{\delta_\mathrm{i}, h_\mathrm{i}, R_\mathrm{i}\}$ using equation 2.11:

$$E = < E\left(\{\delta_\mathrm{i}, h_\mathrm{i}, R_\mathrm{i}\}, \rho_\mathrm{S}, \rho_\mathrm{PBS}; \nu\right) >_\mathrm{i}$$

For every pair of E and ν, equation 2.11 was used to calculate the expected indentation depths $\delta_{\mathrm{i,exp}}(h_\mathrm{i}, R_\mathrm{i}, E, \nu)$, numerically solving equation 2.11 with the Euler method for δ. The optimal pair of E and ν was defined as the pair, for which the total standard deviation of δ was lowest:

$$\sum_\mathrm{i} \left(\delta_\mathrm{i} - \delta_{\mathrm{i,exp}}\right)^2 \rightarrow \min.$$

The algorithm was implemented in Java.

The errors of E and ν were mainly caused by measurement errors of δ, h, and R. In order to get an estimate for the reconstruction accuracy of E and ν, a Monte-Carlo approach was used. A

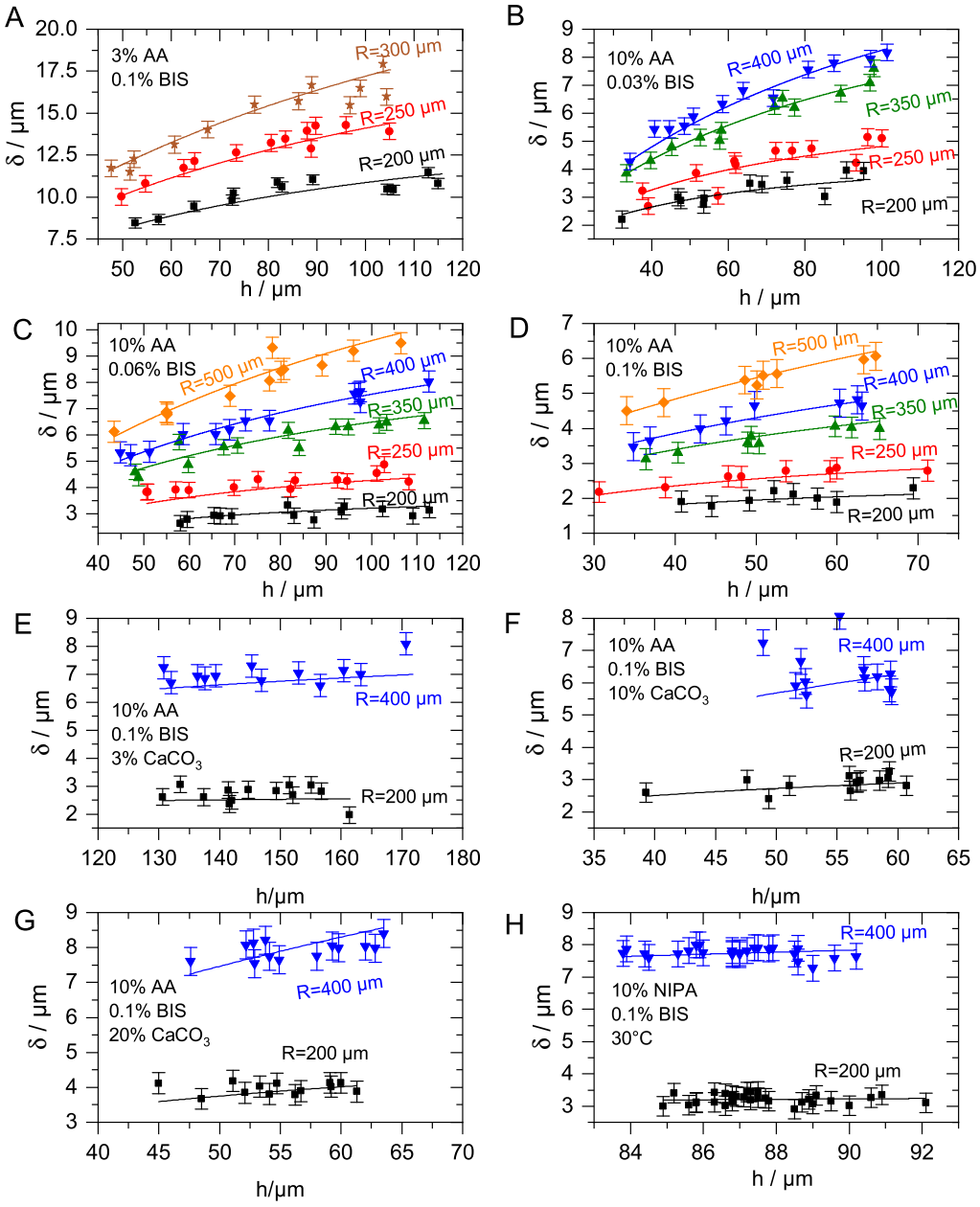

Figure 2.11: Indentation depth $\delta(h)$ of steel spheres on different PAA and PNIPA films. The respective concentrations are denoted on the left side of each panel. Every symbol denotes one measurement conducted as shown in fig. 2.8B. Error bars were estimated by comparing the deviations of δ between both lateral directions (fig. 2.7 D). Solid lines were calculated by solving equation 2.11 for δ with the reconstructed values of E and ν given in table 2.1. The concentrations of AA, BIS and NIPA are given in % w/v and the concentration of $CaCO_3$ is given in % v/v. Panels B, C, D and H were adapted from Gross and Kress, Soft Matter, 2017[157]. The data in panels C and D were measured during the author's master's project and the reconstruction of the elastic parameters was updated to the methods described in this thesis[156].

comprehensive description of the approach was published by Press et al.[224]. In every experimental data set, every data point $(\delta_\mathrm{i}, h_\mathrm{i}, R_\mathrm{i})$ was randomized by sampling from a normal distribution with a mean value equal to the measured value and a standard deviation equal to the respective uncertainty. A total of 10 000 randomized data sets was generated for every experimental data set $\{\delta_\mathrm{i}, h_\mathrm{i}, R_\mathrm{i}\}$ and a pair of E and ν was determined for each of the 10 000 generated data set as described above.

For the data set obtained on the film polymerized with 10 %AA and 0.06 % BIS (fig. 2.11C), the resulting distributions of the rheological parameters E and ν obtained from the 10 000 generated data sets are exemplarily shown in fig. 2.12 A. Both distribution functions were fitted with an asymmetrical Gaussian peak function defined by

$$p(x) = \begin{cases} A \exp \frac{(-x-\mu)^2}{2\sigma_\mathrm{l}^2} & x < 0 \\ A \exp \frac{(-x-\mu)^2}{2\sigma_\mathrm{u}^2}, & x \geq 0 \end{cases} \tag{2.17}$$

where μ is the mean value of E or ν respectively and σ_l and σ_u are the corresponding standard deviations, indicating the error of the reconstruction. In the following, the reconstruction results of E and ν are reported in the form $\mu^{+\sigma_\mathrm{u}}_{-\sigma_\mathrm{l}}$. Whenever the distribution was nearly symmetrical, i.e. when σ_u and σ_l deviated by less than a factor of two, the average of both standard deviations is reported: $\mu \pm (\sigma_\mathrm{u} + \sigma_\mathrm{l})/2$. In the case of the PAA film polymerized with 10 %AA and 0.06 % BIS, the reconstruction yielded $E = (11.7 \pm 0.7)\,\mathrm{kPa}$ and $\nu = 0.48 \pm 0.02$.

On films with a lower Poisson ratio, i.e. in a condition where the resolution of the method is worse, the reconstructed distribution functions were structurally different. This was for example the case for the PNIPA film polymerized with 10 % NIPA and 0.1 % BIS. Due to the minima of $C(\nu)$ near $C = 0$ (fig. 2.10A), some of the reconstructions yielded $\nu \approx 0$. Those reconstructions appeared as a distinctive peak in the distribution function (fig. 2.12B, blue). This peak could be reproduced by simulating a comparable indentation data set on a hypothetical film with $E_0 = 15\,\mathrm{kPa}$ and $\nu_0 = 0.3$, which is indented by two steel spheres with radii of 200 and 500 µm. In order to simulate the indentation depths δ, equation 2.11 was solved numerically for δ. Gaussian noise was added to δ, h, and R similar to the experimental noise (fig. 2.13A) and the reconstruction algorithm described above was applied. The resulting distribution functions of the reconstructed rheological parameters of the simulated film with $E_0 = 15\,\mathrm{kPa}$ and $\nu_0 = 0.3$ are shown in figure 2.13B. The distribution was similar to the distribution obtained from the measured data (fig. 2.12B). In particular, both peaks near $\nu = 0$ (blue in both figures) and $\nu = 0.3$ (red in both figures) are visible. Furthermore, 50 data sets with $E_0 = 15\,\mathrm{kPa}$ and $\nu_0 = 0.5$ were simulated and the reconstructions with $\nu > 0.05$ yielded $E = (15.4 \pm 1.3)\,\mathrm{kPa}$ and $\nu = 0.29 \pm 0.05$, which was in excellent agreement with the ground truth values E_0 and ν_0 used for the simulations. Therefore, the peak near $\nu = 0$ is an inherent property of equation 2.11, which comes to light due to measurement noise. Thus, all reconstructions of the experimental data yielding $\nu < 0.05$ were dismissed before fitting equation 2.17 to the distributions plotted in figure 2.12B. The reconstruction yielded $E = \left(15.1^{+1.2}_{-1.5}\right)\mathrm{kPa}$ and $\nu = 0.33^{+0.05}_{-0.11}$ for the PNIPA film.

For every condition, both rheological parameters were used to predict the indentation depth $\delta(h, R; E, \nu)$ by solving equation 2.11 numerically for δ. These theoretical predictions are shown in figure 2.11 as solid lines. The predictions are in excellent agreement with the measured data $\delta(h, R)$ indicating that the model is valid in all tested conditions. The reconstructed numerical values of E and ν for all data sets shown in figure 2.11 are reported in section 2.2.6.

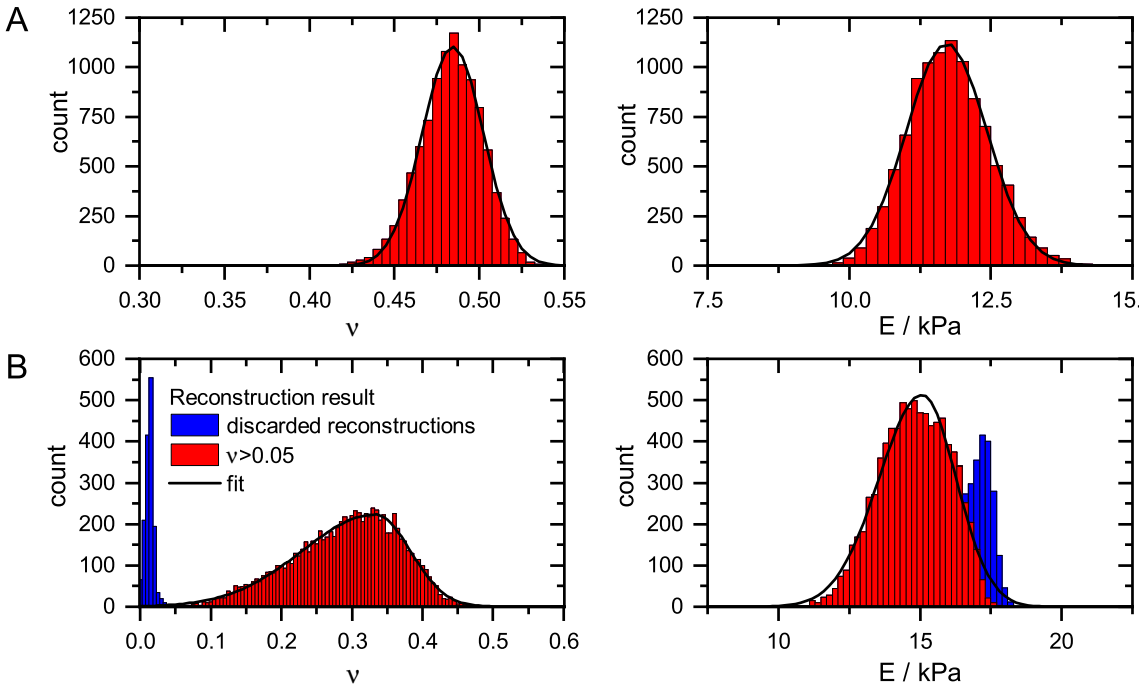

Figure 2.12: Distributions of E and ν generated by the reconstruction algorithm. The distributions for the samples with (A) 10 % AA, 0.06 % BIS and (B) 10 % NIPA, 0.1 % BIS were fitted with the asymmetric normal distribution given by equation 2.17. In panel B, some of the reconstructions yielded $\nu < 0.05$. These reconstructions were discarded (blue) and the remaining distribution (red) was fitted with equation 2.17 to determine the mean value and the reconstruction errors. Figure adapted from Gross and Kress, Soft Matter, 2017[157].

2.2.5 Control Experiments with Macroscopic Springs

Control experiments with macroscopic PAA springs were carried out as described previously[156]. Macroscopic springs were suspended 5 cm in front of millimeter paper (fig. 2.14 A). The millimeter paper was glued to a piece of cardboard and aligned with a level. As the wet springs were very slippery, they were wrapped in a piece of tissue at the top and suspended with a fold back clip (fig. 2.14 B). A thin wire was pierced through the spring to suspend small brass weights with masses between 1 and 10 g to mechanically load the springs (fig. 2.14 A, C). In between measurements, it was verified that the spring returned to its original, unloaded length between measurements with different weights to exclude any nonlinear effects. All springs were also checked for fissures, especially near the wires and the suspension before, during and after the measurements. In no case, any damage could be observed. The elongations of the springs at different loads were imaged with a digital camera, which was placed approximately 3 m away from the spring to minimize parallax (fig. 2.14C). It was observed that the springs became slightly shorter with time. This happened presumably because the liquid film at the surface evaporated during the measurements. In order to prevent any influence of these evaporation effects, the springs were reimmersed in 1xPBS regularly between the measurements.

The elongation of a loaded linearly elastic spring is given by Hooke's law

$$\sigma = E\epsilon, \tag{2.18}$$

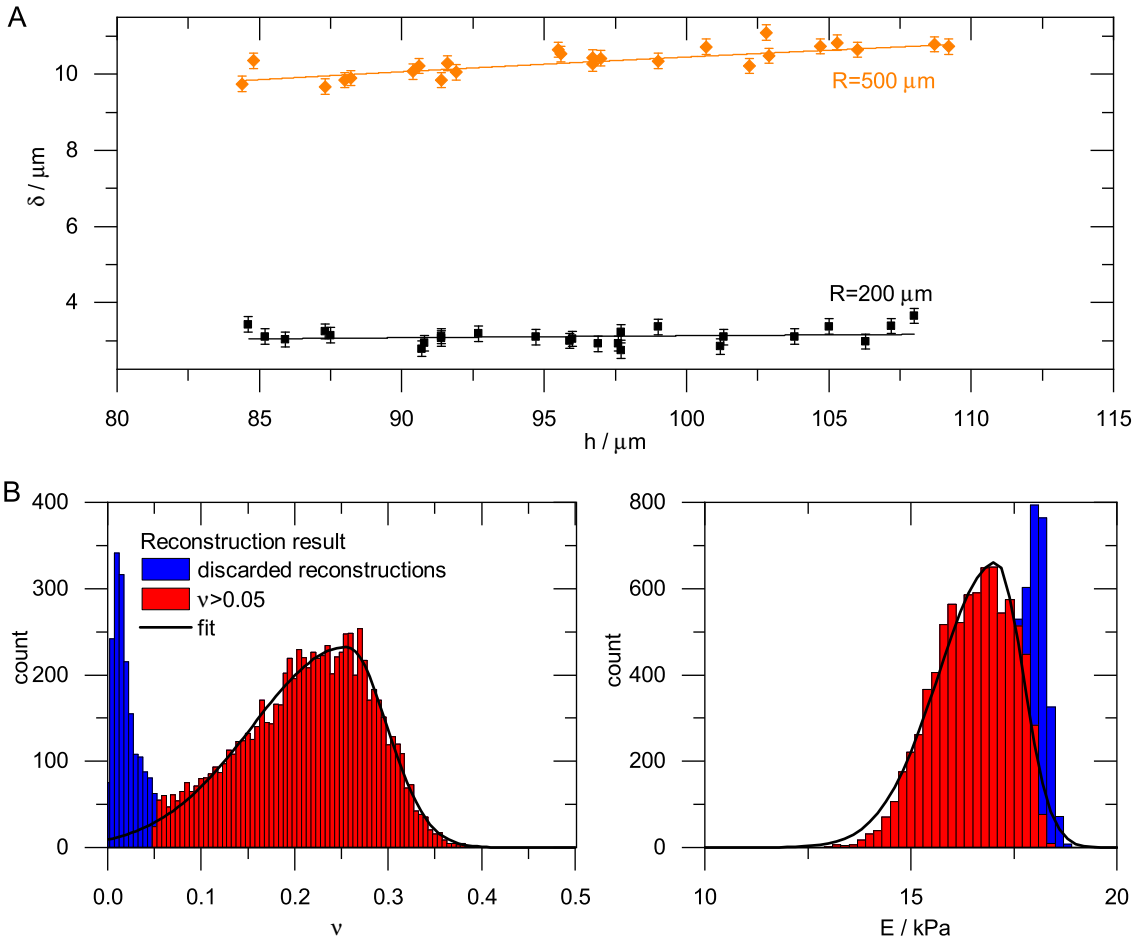

Figure 2.13: Distributions of E and ν generated with simulated data. (A) Simulated indentation depth for a film with $E = 15\,\mathrm{kPa}$ and $\nu = 0.3$. Error bars denote the standard deviation used to simulate experimental noise. Solid lines were obtained by numerically solving equation 2.11 for δ. (B) Distribution functions of the reconstructed Poisson ratios and the reconstructed elastic moduli. Figure adapted from Gross and Kress, Soft Matter, 2017.[157].

where the stress $\sigma = F/A$ is given by the force F per cross-sectional area A and the relative elongation $\epsilon = \Delta L/L_0$ is defined as the elongation ΔL divided by the spring's undeformed length L_0 (fig. 2.14 A). L_0 was measured with an error of 1 cm with a metal ruler with the spring lying horizontally on the workbench. The uncertainty of L_0 was mainly given by the suspension point, which was difficult to define. As the suspended springs were deformed by their own weight m_0 by a length ΔL_0 and by the brass weights m at the bottom by a length ΔL, the stress in the spring depended on the vertical position z with the highest stress located at the top and the lowest stress located at the bottom of the spring. In this case, the total elongation ΔL_{tot} of the spring can be

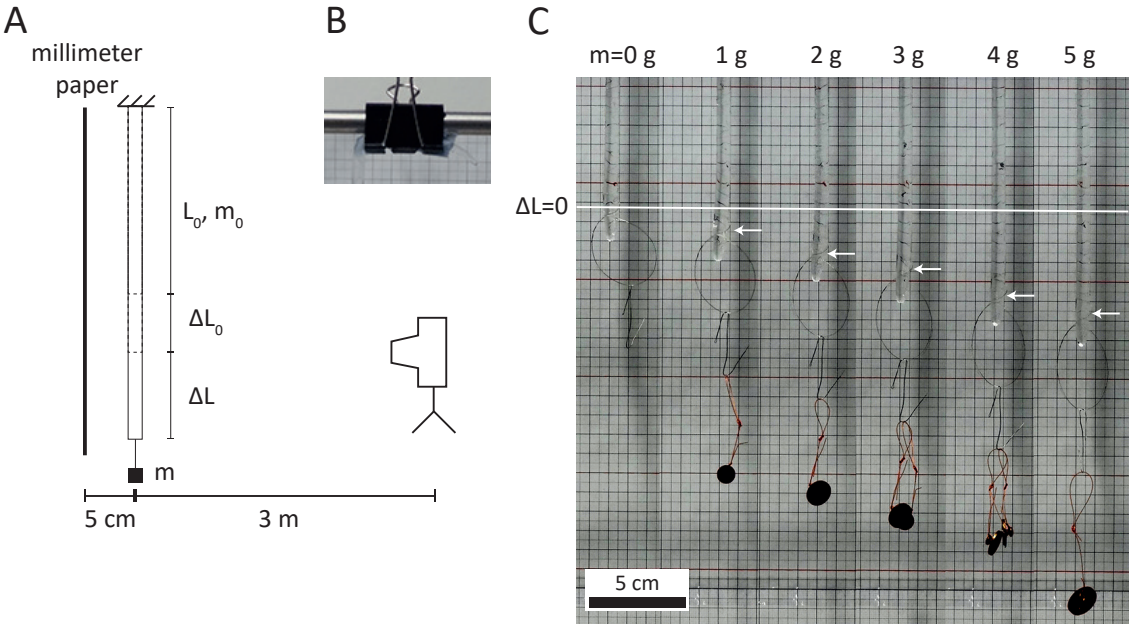

Figure 2.14: Bulk tensile experiments. (A) Sketch of the setup used to measure the elastic modulus of a macroscopic PAA spring. The spring was suspended in front of millimeter paper and loaded with brass weights. Images of the deformed spring were captured with a digital camera, which was placed on a tripod located 3 m away from the spring. (B) Detailed image of the suspension. The PAA spring was wrapped with tissue and fixed to a bar with a fold back clip. The spring is difficult to see as PAA is almost completely transparent. (C) 6 exemplary images of a suspended PAA spring polymerized with 10 % AA and 0.03 % BIS. The spring was loaded with different brass weights with mass m. The uppermost position of the wire used to suspend the weights at $m = 0$ was used as a reference to measure ΔL (white line). This wire position is marked with white arrows in all images with attached weights. The contrast in panels B and C was increased nonlinearly to enhance the visibility of the almost fully transparent springs.

derived from equation 2.18:

$$\Delta L_{\mathrm{tot}} = \Delta L + \Delta L_0 = \int_0^{L_0} \mathrm{d}\left(\Delta \mathrm{L}\right) \tag{2.19}$$

$$= \frac{1}{AE} \int_0^{L_0} F\left(z\right) \mathrm{d}z \tag{2.20}$$

$$= \frac{g}{AE} \int_0^{L_0} \mathrm{d}z \left[m + m_0 \left(1 - \frac{z}{L_0} \right) \right] \tag{2.21}$$

$$= \frac{g L_0}{AE} \left(\frac{m_0}{2} + m \right). \tag{2.22}$$

The first term in equation 2.22 describes the deformation ΔL_0 due to the spring's own weight, while the deformation due to the brass weight ΔL is given by the second term. Since equation 2.18 is linear, the elastic modulus can be calculated independently from the spring's own weight

$$E = \frac{L_0 g m_0}{2A\Delta L_0} \tag{2.23}$$

and the mass of the brass weights at the bottom

$$E = \frac{L_0 g m}{A \Delta L}. \tag{2.24}$$

For all springs used in this work, the determination of the elastic modulus with equation 2.24 was more exact than with 2.23 and was thus used in this work. In equation 2.24, the stress applied due to the gravitational force of m can be identified as:

$$\sigma_\mathrm{m} = \frac{g m}{A}. \tag{2.25}$$

The cross-section area $A = (28 \pm 4)\,\mathrm{mm}$ was estimated from the radius of the syringe used during polymerization and the mass of the brass weights m was measured with was measured with a laboratory balance (ATL-124-I; Acculab). The spring's relative elongation due to the brass weight can also be identified in equation 2.24:

$$\epsilon_\mathrm{m} = \frac{\Delta L}{L_0}. \tag{2.26}$$

In the experiment, ΔL was defined as the z-position change of the bottom wire as the weight was attached (fig. 2.14 A, C). ΔL was measured with a precision of about 1.5 mm. The errors of σ_m and ϵ_m were calculated with gaussian error propagation considering the errors of A, L_0 and ΔL. The corresponding version of Hooke's law can be derived by combining equations 2.24, 2.25 and 2.26:

$$\sigma_\mathrm{m} = E\,\epsilon_\mathrm{m}. \tag{2.27}$$

In order to determine the springs' elastic modulus, the measured values $\sigma(\epsilon)$ were fitted with equation 2.27 (fig. 2.15). The error of E was estimated with a Monte-Carlo approach similar to the methods described in section 2.2.4 considering the errors of ϵ and σ.

Softer springs polymerized with 3 % AA and 0.1 % BIS, which had an elastic modulus of $(1.3 \pm 0.3)\,\mathrm{kPa}$[225], were only capable of supporting their own weight up to a length of about $L_0 \approx 15$ to 20 cm. Thus, to avoid irreversible, nonlinear deformations of such softer springs, it is advisable to consider using shorter springs and to use the deformation due to the spring's own weight to measure E. Such an approach was described by Alexander Ochs[225].

2.2.6 Elastic Properties of Polyacrylamide and Poly-N-Isopropylacrylamide

The results of the steel sphere experiments and the results of the macroscopic tensile tests are summarized in table 2.1 and in figure 2.16. Comparing the results of PAA films with different concentrations of AA and BIS, it was found that the elastic modulus increased both with increasing concentrations of AA and BIS. In detail, at a BIS concentration of 0.10 %, the elastic modulus increased from $(1.50 \pm 0.06)\,\mathrm{kPa}$ to $(23.3 \pm 2.8)\,\mathrm{kPa}$ as the AA concentration was increased from 3 to 10 % w/v. Similarly, the elastic modulus also increased as a function of the BIS concentration at a constant AA concentration of 10 % w/v. At a BIS concentration of 0.03 % w/v, the elastic modulus was measured to be $(8.8 \pm 0.7)\,\mathrm{kPa}$ and it increased to $(23.3 \pm 2.8)\,\mathrm{kPa}$ at a BIS concentration of 0.10 % w/v. These results were cross-checked with the macroscopic spring method which yielded similar results. Within the margin of error, the results from both experiments were similar, even though the geometry of both experiments was completely different and the length scale at which the stresses were applied differed by two orders of magnitude. Porous PAA films polymerized with $CaCO_3$ particles were softer the higher the concentration of $CaCO_3$ used during polymerization. All porous PAA films were polymerized at an AA concentration of 10 % w/v and a

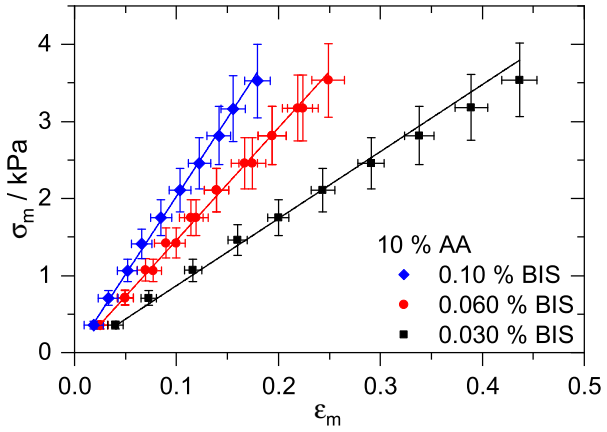

Figure 2.15: Stress-strain curves for different PAA springs. The stress σ_m (ϵ_m) of macroscopic springs polymerized with 10 % AA and different BIS concentrations. In order to determine the elastic modulus given by the slope of the curves, Hooke's law (equ. 2.27) was fitted to the data (solid lines). Figure adapted from Gross and Kress, Soft Matter, 2017[157]. The data of the spring polymerized with 10 % AA and 0.06 % BIS were measured during the author's master's project[156] and reevaluated in this work. In this work, the elastic modulus was determined by fitting Hooke's law to the raw data.

AA / % w/v	NIPA / % w/v	BIS / % w/v	$CaCO_3$ / % v/v	E/kPa (steel sphere)	ν (steel sphere)	E/kPa (spring)
3	0	0.10	0	1.50 ± 0.06	0.45 ± 0.01	1.3 ± 0.3*
10	0	0.03	0	8.8 ± 0.7	0.53 ± 0.02	8.4 ± 0.6
10	0	0.06	0	11.7 ± 0.7**	0.48 ± 0.02**	14.5 ± 1.2**
10	0	0.10	0	23.3 ± 2.8**	0.42 ± 0.04**	20.1 ± 1.6
10	0	0.10	3	18.9 ± 3.3	$0.48^{+0.06}_{-0.15}$	
10	0	0.10	10	11.5 ± 1.8	$0.46^{+0.03}_{-0.06}$	
10	0	0.10	20	6.3 ± 0.7	$0.47^{+0.03}_{-0.02}$	
0	10	0.10	0	$15.1^{+1.2}_{-1.5}$	$0.33^{+0.05}_{-0.11}$	

Table 2.1: **Elastic moduli E and Poisson ratios of different kinds of PAA and PNIPA gels.** Elastic moduli and Poisson ratios of thin PAA films were determined with the steel sphere method. The elastic moduli of macroscopic springs were measured with bulk tensile tests. The PNIPA film was measured at 30 °C, which was slightly below the LCST. All other experiments were conducted at room temperature. The errors were calculated as described in sections 2.2.4 and 2.2.5. The value marked with one asterisk was determined by Alexander Ochs[225]. Results marked with two asterisks are based on raw data, which were acquired during the author's master's project[156].

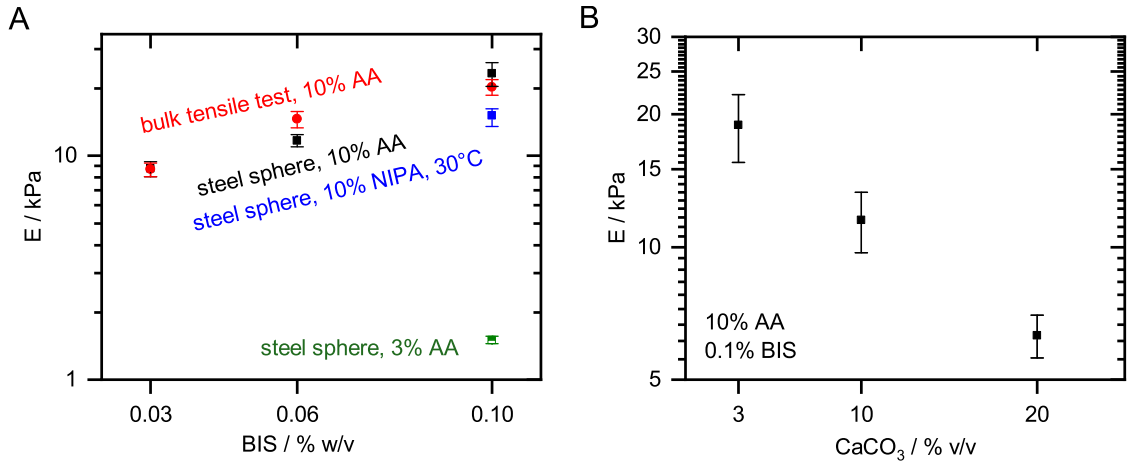

Figure 2.16: Elastic modulus E of different hydrophilic films and springs. (A) Elastic modulus of PAA and PNIPA films as a function of the BIS concentration measured with the steel sphere method and bulk tensile tests. The PNIPA film was measured at 30 °C, which was slightly below the LCST. All other experiments were conducted at room temperature. (B) Elastic modulus as a function of the $CaCO_3$ concentration measured with the steel sphere method. The error bars were calculated as described in sections 2.2.4 and 2.2.5. The numerical values are given in table 2.1. Panel A adapted from Gross and Kress, Soft Matter, 2017[157].

BIS concentration of 0.10 % w/v. The films' elastic moduli decreased from (23.3 ± 2.8) kPa without $CaCO_3$ to (18.9 ± 3.3) kPa at a $CaCO_3$ concentration of 3 % v/v. At 10 and 20 % v/v, the elastic modulus decreased further to (11.5 ± 1.8) kPa and (6.3 ± 0.7) kPa respectively.

The PAA films' Poisson ratios varied slightly from 0.53 ± 0.02 at 10 % w/v AA and 0.03 % w/v BIS to 0.42 ± 0.04 at 10 % w/v AA and 0.10 % w/v BIS at room temperature. The film polymerized with 3 % w/v AA and 0.1 percent w/v BIS had a Poisson ratio of 0.45 ± 0.10 at room temperature. Interestingly, the Poisson ratios of the porous films polymerized with 10 % w/v AA, 0.1 % w/v BIS and $CaCO_3$ were similar to those of the PAA samples polymerized without $CaCO_3$. The Poisson ratio varied around 0.47 at 3, 10 and 20 % v/v $CaCO_3$ and was thus independent of the $CaCO_3$ concentration.

In contrast to the AA films, the steel sphere measurements of the film polymerized with 10 % w/v NIPA and 0.10 % BIS were done at 30 °C, which was slightly below the LCST. In these conditions, the film's elastic modulus was measured to be $(15.1^{+1.2}_{-1.5})$ kPa which was comparable to that of the film polymerized with 10 % w/v AA and 0.06 % BIS. The PNIPA film's Poisson ratio was measured to be $0.33^{+0.05}_{-0.11}$, which was significantly lower than the Poisson ratio of all other films.

2.2.7 Discussion

In the steel sphere experiments conducted on PAA and PNIPA films, an excellent agreement between the measured $\delta(h)$ and the model from Dimitriadis et al. (eq. 2.11) was achieved in all cases (fig. 2.11). Barely any deviations from the model predictions were observed, indicating that the films behaved like homogeneous, linear elastic layers. The strains in the steel sphere method can roughly be approximated by δ/h. However, this approximation overestimates the strain near the coverslip and underestimates the strain directly below the sphere. In the experiments presented in this work, δ/h ranged from about 1 % to about 20 %, depending on the sphere radius, the

film thickness and the monomer concentrations (fig. 2.11). In the macroscopic tension tests, the imposed strains were even higher and ranged from a few percent up to 44 %, depending on the film type (fig. 2.15). even for such large deformations, the films behaved like linearly elastic solids (fig. 2.15). The fact that PAA films behave like linearly elastic solids is commonly known. For example, Engler et al. did not even find nonlinear effects in PAA gels for deformations of up to 80 %[196].

The elastic moduli obtained by the steel sphere method with non-porous films were validated with the macroscopic tensile tests. The results of E from both techniques, and in particular the results for very soft gels (steel sphere: $E = (1.50 \pm 0.06)\,\mathrm{kPa}$, macroscopic: $E_{\mathrm{macrocopic}} = (1.3 \pm 0.3)\,\mathrm{kPA}$) but also for stiff gels (steel sphere: $E = (23.3 \pm 2.8)\,\mathrm{kPa}$, macroscopic: $E = (20.1 \pm 1.6)\,\mathrm{kPa}$) agreed well with each other, covering the full range of tested stiffnesses. This also held true for all stiffnesses tested in between. Theoretically, the spring's diameter d is expected to contract laterally by Δd according to[51]

$$\nu = -\frac{\Delta d/d}{\Delta L/L_0}. \tag{2.28}$$

At a relative elongation of $\Delta L/L_0 = 40\,\%$, which was about the highest value of ϵ_{m} in the experiments, the diameter of an incompressible spring with $\nu = 0.5$ is therefore expected to contract by 20 % or about 1 mm, which was not resolvable. However, the Poisson ratio and the elastic modulus are not independent in the steel sphere reconstruction. Individual reconstructions, which yielded a low Poisson ratio also yielded a high elastic modulus and vice versa (fig. 2.12). Therefore, the validation of E with the bulk tensile tests also verified the results of ν.

The length scales at which the forces were applied and thus also the size of the deformation fields inside the material differed by more than two orders of magnitude between both techniques. The diameters of the indentation caps in the steel sphere measurements were typically in the range of a few tens of micrometers and ranged up to about 200 µm, which amounts to contact areas of roughly up to $30 \times 10^3\,\mu\mathrm{m}^2$ (fig. 2.9). In contrast, the macroscopic cylinders were larger and they had diameters of 3 mm, with a cross sectional area of $28\,\mathrm{mm}^2$. In the steel sphere experiments, the forces exerted by the spheres ranged from about 2 µN to 35 µN and the macroscopic springs were loaded with forces ranging from 1 to 10 mN. The strains in both techniques were, however, comparable as discussed above.

By now, it is well established that the elastic modulus of PAA hydrogels is higher the higher the BIS concentration[50,65,74,196,207,226]. This was also observed in this work. At an AA concentration of 10 % w/v, the elastic modulus increased nearly linearly from $(8.8 \pm 0.7)\,\mathrm{kPa}$ at 3 % w/v BIS to $(23.3 \pm 2.8)\,\mathrm{kPa}$ at 0.1 % BIS, which is to be expected when the probability of any BIS molecule forming an effective cross link in the polymer network does not change[226]. In experiments performed at 10 % w/v AA, the ratios of the concentrations of AA to BIS molecules used during polymerization ranged from 220 (0.1 % w/v BIS) to 720 (0.03 % BIS). Since AA molecules far outnumbered BIS molecules during the reaction in all cases, it is plausible that the probability of a BIS molecule forming an independent effective cross link in the network does not depend on the BIS concentration in this regime. At an AA concentration of 12 % w/v, this linear scaling has been observed for far higher BIS concentrations of up to 0.6 % w/v BIS by macroscopic measurements with a shear rheometer[226]. Similarly, it was observed down to cross linker concentrations of 0.01 % w/v of BIS at a concentration of 7.5 %[226]. Engler et al. found nearly linear scaling with the cross linker concentration for AA concentrations of 3, 5, and 10 % w/v, ranging from 0.03 to to 0.3 % w/v of BIS[196]. The measured elastic modulus was also lower the lower the concentration of AA. This has been observed previously, e.g. by Yeung et al.[226], Engler et al.[196], Kraning-Rush et al.[50], and also in recent work by Vorselen et al., who investigated soft PAA microparticles[74].

Interestingly, the PNIPA film polymerized with 10 % NIPA and 0.1 % BIS had a considerably lower elastic modulus of $15.1^{+1.2}_{-1.5}\,\mathrm{kPa}$ than the film polymerized with 10 % AA at the same BIS con-

centration, which had an elastic modulus of (23.3 ± 2.8) kPa. This is in line with the macroscopic observation that the PNIPA films polymerized slower at identical AA concentrations under otherwise similar polymerization conditions. Even though the PNIPA monomer solution was degassed for 45 min and the APS and TEMED concentrations were doubled to speed up the polymerization process, it appears as if the polymerization reaction had possibly not completely finished. A decreased polymerization efficiency of NIPA under these conditions or a lower fraction of BIS molecules forming an effective cross link inside the PNIPA network compared to the PAA film are, among others, further possible explanations.

However, comparing results of the elastic modulii to results obtained in previous studies is not easily possible as the stiffnesses of polymerized PAA and PNIPA depend on various details of the polymerization process. For example, differences in the polymerization time, the polymerization temperature, the concentrations of APS and TEMED and the amount of dissolved oxygen in the monomer solution can affect the polymerization efficiency and thus also the stiffness of the polymerized films[50,164,180]. In this work, these critical parameters were not changed between experiments. Care was taken not to introduce bubbles inside the monomer solutions, both in the prepared samples and in the stock solutions. Furthermore, the polymerization temperatures were kept at room temperature between 20 °C and 22 °C and the polymerization was done in a custom built humidifying chamber to prevent evaporation. For instance, reasonably good agreement was observed with the results obtained by Dembo and Wang, who measured 6.2 kPa at 10 % w/v AA and 0.03 % BIS ((8.8 ± 0.7) kPA in this work)[159] and also with the work by Boudou et al., who measured about (25 ± 5) kPa at 10 % w/v AA and 0.1 % w/v BIS with micropipette aspiration ((23.3 ± 2.8) kPa)[207].

The measured Poisson ratios all indicate that the PAA films were almost incompressible, with values ranging from 0.42 ± 0.04 to 0.53 ± 0.02, increasing slightly with increasing cross linker concentration. As the Poisson ratio of linearly elastic materials must be below 0.50[223,227] and as the measured Poisson ratios of all other films was below 0.5, it is likely that statistical measurement errors caused this deviation. The films' Poisson ratio is a measure of the material's volume change under stress or strain. The fact that all other measured Poisson ratios of PAA films were close to 0.5 and often indistinguishable from 0.5 indicates that, if at all, very little water was squeezed out of those films in the indentation experiments[188]. The results are in good agreement with recent literature. For example, Boudou et al. reported values of about 0.47 for PAA films with different AA and BIS concentrations[207]. Engler et al. determined Poisson ratios of 0.4 to 0.45 with macroscopic tension tests[196] and Maskarinec et al. reported a value of 0.48 to 0.50 measured with macroscopic compression tests[199]. Recently, a technique in which bulk modulus measurements based on osmotic pressure was combined with atomic force microscopy measurements to determine the Poisson ratio of small PAA particles with a diameter of a few micrometers by Vorselen et al.[74] and values between 0.42 ± 0.02 and 0.44 ± 0.01 were determined, depending on the crosslinker concentrations used during polymerization. Interestingly, the PNIPA film polymerized with 10 % w/v NIPA and 0.1 % w/v BIS, which was measured at a temperature of 30 °C slightly below the LCST, had a Poisson ratio of $0.33^{+0.05}_{-0.11}$ and was thus far away from incompressibility, indicating that water was squeezed out of the film during the indentation experiments. This result is also in good agreement with literature[166,170,171,223].

The results obtained for the porous PAA films with 10 % w/v AA and 0.1 % BIS are quite interesting. Firstly, no considerable deviations from linearly elastic, homogeneous solids could be detected. This is in line with the fact that the $CaCO_3$ particles had a diameter between 1 and 3 µm. For example, the smallest Hertzian contact radii were observed on the film polymerized with 3 % v/v $CaCO_3$. Those were approximately $\sqrt{R\delta} \approx \sqrt{200 * 3}$µm ≈ 24 µm large (see also fig. 2.11E), which is supposedly about one order of magnitude larger than the pores. Thus, in the lateral direction, the samples appeared to be homogeneous as multiple pores and parts of PAA are

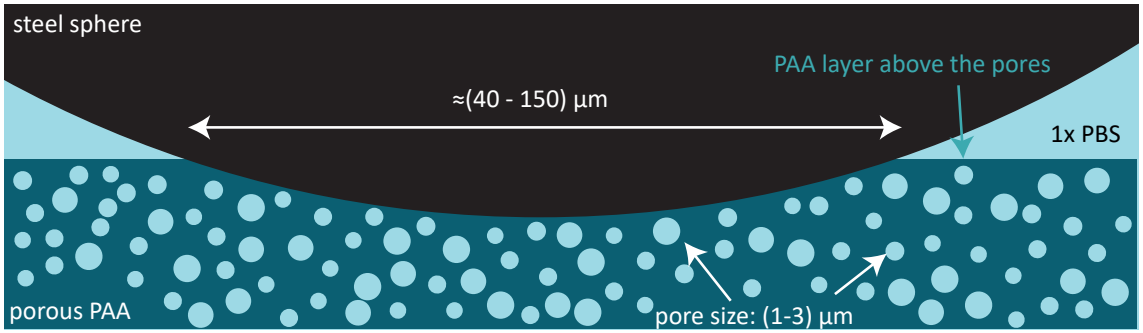

Figure 2.17: Length scales during the steel sphere experiments of porous polyacrylamide films. The pores with a size of presumeably 1 to 3 µm were most likely evenly distributed inside the films. The deformation field was larger than the pore size and consequently, the films appeared to be homogeneous when probed with spherical indenters larger than the pore size.

probed at the same time in one measurement. An illustration of the length scales involved is shown in fig. 2.17. Only for a few data points and thus in only a few regions of the film, the spheres sank deeper into the film than expected (fig. 2.11 E, F). It is likely that aggregates of $CaCO_3$ caused these localized inhomogeneities.

What is more surprising is the fact that the data of the porous films were self-consistent, indicating that the material was homogenous (fig. 2.11E, F, G). $CaCO_3$ has a density of about $2.7\,\mathrm{g/cmm}^3$[213]. From equation 2.6, it follows that even small $CaCO_3$ particles with a radius of 1 µm sediment with a velocity of about $1\,\mu\mathrm{m\,s}^{-1}$ in a solution, which has same viscosity as water. Thus, they should fall through such a liquid layer with a height of 100 µm in about 100 s, which is a lot shorter than the PAA polymerization time. Although the solution's viscosity certainly increased with time after the addition of APS, the macroscopic viscosity only appeared to increase after tens of minutes (tested by stirring the polymerizing solution with a pipette tip and by aspiration of the polymerizing solution into a pipette tip). Typically, the formation of an elastic gel seemed to happen very late during the polymerization process (laboratory observation). As the films were inverted during polymerization, the density of pores at the top should consequently be higher than at the bottom of the film and the film should also be stiffer at the bottom and softer at the top. However, this was not observed in the experiments. For example, the steel sphere with a radius of 400 µm indented the film polymerized with 3 % v/v $CaCO_3$ by $\approx$ 7 µm in a location where the film thickness was $\approx$ 150 µm. This amounts to a Hertzian contact radius of $\approx$ 50 µm. In contrast, the sphere with $R = 200\,\mu\mathrm{m}$ sank $\approx 4\,\mu\mathrm{m}$ into the film, which amounts to a Hertzian contact radius of 28 µm. Considering the fact that the dimensions of the deformation field in the axial and lateral directions are approximately equal[190,194], the fact the the data of both spheres agreed very well with the prediction for $\delta(R, h)$ given by equation 2.11 indicates that the samples were also homogeneous in the axial direction (fig. 2.11 E, F, G). One possible explanation for this seemingly contradictory result is based on the reaction kinetics of the PAA polymerization. It has been suggested that polymerization is not necessarily a homogeneous process but rather a process in which microgelation can happen and only in the final gel, these microgels are interconnected by rather loose crosslinks[228]. In case these microgels adhered to the $CaCO_3$ particles, it is possible that the effective hydrodynamic radius of the particles increased without any macroscopically visible gelation. Furthermore, it is also possible that the formation of an early, loose network structure was already strong enough to support the weight of the $CaCO_3$ particles and thus, prevented the

sedimentation. A more detailed analysis of the gelation process and the final particle distribution inside such films may bring clarification and has the potential to elucidate interesting details about the reaction kinetics leading up to the formation of the hydrogels, which are not necessarily visible via macroscopic viscosity measurements during polymerization.

The elastic modulus of porous PAA films decreased from $(23.3 \pm 2.8)\,\mathrm{kPa}$ for the film without any pores to $(6.3 \pm 0.7)\,\mathrm{kPa}$ for a film with 20 % v/v $CaCO_3$, which indicates that the internal structure of the films was considerably weakened by the pores. At the same concentrations, the Poisson ratio did not change within the margin of error. Consequently, it appears that even for 20 % v/v of $CaCO_3$, the pores inside the film were not sufficiently interconnected to allow water to be squeezed out of the films. However, when the films were immersed in 1 % HCl to dissolve the $CaCO_3$, emerging CO_2 outgassed fully as no holes were visible inside the film and thus, the medium was optically homogeneous and the holes' refractive index was very close to or identical to that of the gels. Otherwise CO_2 bubbles inside the film would lead to diffraction at the interface between air and gel and the films would have had a turbid appearance.

2.3 Characterization of Hydrophobic Polydimethylsiloxane Films

2.3.1 Film Geometry and Labelling with Tracer Particles

In this section, the steel sphere method is applied to PDMS. PDMS films were not custom made but a commerically available product was bought (ibidi μ-Dish 35mm, high ESS, ibidi, Gräfelding, Germany). The slides consisted of a glass supports, which were coated with a thin PDMS films. The films typically had a thickness of about 100 µm. In contrast to the self-made PAA and PNIPA films, these films were not coated with tracer particles out-of-the-box. In order to label the surface for the steel sphere method, the tracer particle stock dispersion (FluoSpheres, carboxylate-modified polystyrene microspheres, Thermo Fisher Scientific #F8811, diameter 0.2 µm, Ex/Em: 505/515 nm, stock concentration 4.5×10^{12} particles/ml, density $\rho_{\mathrm{PS}} = 1.055\,\mathrm{g/cm^2}$) was diluted in 1xPBS or deionized water at a concentration of approximately 1/1000 and the PDMS films were immersed in the dispersion for 10 min. The tracer particles adhered to the films' surfaces. The bottom layer of the films could not be labeled with tracer particles. In order to measure the film height, DIC microscopy was used after the sphere was removed, which enabled the visualization of small dust particles at the interface between the PDMS and the glass bottom. The tracer particles at the top surface were also clearly visible with DIC microscopy and thus, the method shown in fig. 2.7B was adapted to DIC microscopy.

2.3.2 Correction of the Refractive Index Mismatch

The refractive index of PDMS $n_{\mathrm{PDMS}} = 1.42$ (manufacturer's data, Style et al. report a value of ≈ 1.4 for silicone[51]) is considerably higher than the refractive index of water $n_{\mathrm{w}} = 1.33$[217]. Since there was a mismatch between the refractive index of the immersion medium n_{im} and the refractive index of the sample n_{s}, the film thickness h is different than the difference of the z-positions $\Delta z_{\mathrm{motor}}$ of the motor driving the objective. This had to be accounted for when the film thickness was measured by focussing on the top and bottom film surfaces. The relation between h and $\Delta z_{\mathrm{motor}}$ can be derived from ray optics and it is given by[51,229]

$$h = \Delta z_{\mathrm{motor}} \frac{n_{\mathrm{s}}}{n_{\mathrm{im}}}. \tag{2.29}$$

This relation was validated by coating two coverslips with fluorescent tracer particles as described above. One coverslip was glued to an aluminium holder and the second coverslip was tilted using

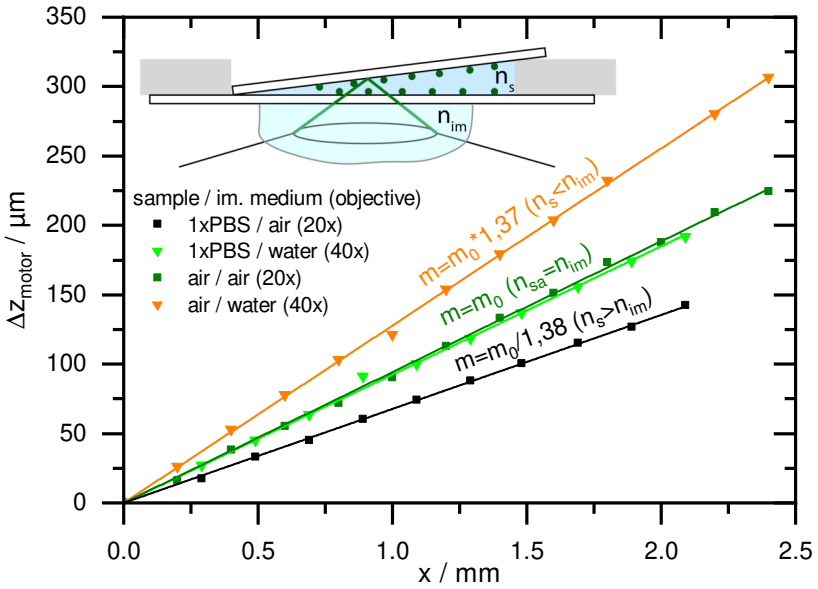

Figure 2.18: Z-axis calibration experiment. Two coverslips coated with fluorescent tracer particles were aligned in a wedge-like geometry on an aluminium holder. The difference of the motor positions $\Delta z_{\mathrm{motor}}$ driving the objective was measured as a function of the lateral stage position x. As a sample, the wedge was filled with air and 1xPBS and the slope m was measured by focusing on the particles with the 20x objective (no water immersion) and with the 40x water immersion objective.

an aluminium holder as a spacer on one side (fig. 2.18 inset). The slope m of the tilted coverslip was filled with either air or 1xPBS and imaged with the 20x objective (no water immersion) and the 40x objective (water immersion). In case of $n_{\mathrm{s}} = n_{\mathrm{im}}$, the slope $m \equiv m_0$ was identical independent of the sample (fig. 2.18, green curves). In this case, the angle between the coverslips was $\arctan(m_0) = 5.3°$, which was in good agreement with the value of 5.0° determined with a micrometer gauge. When 1xPBS was used as a sample and the 20x objective was used, the measured slope was lower than m_0 by a factor of 1/1.38, which was close to the theoretical value of $1/1.34$[217] (fig. 2.18, black curve). Thus, the sample thickness was underestimated when the sample's refractive index was higher than that of the immersion medium. When the coverslip wedge was filled with air and the 40x water immersion objective was used, the measured slope was higher than m_0 by a factor of 1.37 (fig. 2.18, orange curve). Consequently, the sample thickness was overestimated when the refractive index of the sample was lower than that of the immersion medium. The difference of about 4 % presumably arose since equation 2.29 is derived from ray optics, assuming small incidence angels. Equation 2.29 was used to calculate the thickness h of PDMS films, which amounts to a correction of about 7 %.

2.3.3 Hydrophobicity and Adhesion

When a steel sphere was placed on the PDMS films as shown in figure 2.7A, the interaction between the films and the steel spheres was widely different compared to PAA and PNIPA films. It was observed that the steel spheres adhered to the film surfaces when the films were immersed in 1xPBS, i.e. they were not rolling freely and in some cases, it was even difficult to detach the spheres from

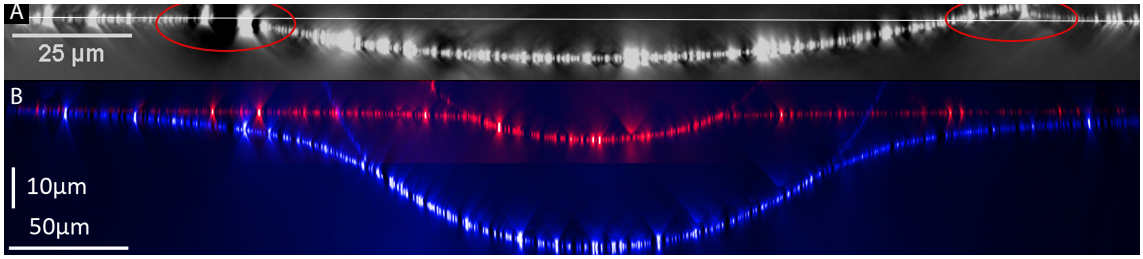

Figure 2.19: Side views of the indentation region of PDMS films. (A) A sphere with a radius of 350 µm immersed in 1xPBS indented a PDMS film with a thickness of 104 µm with a nominal elastic modulus of 15 kPa. The white line indicates the surface level of the film. The contact geometry was asymmetric, since the PDMS film was visibly pulled upwards on the right side towards the sphere surface, which did not happen at the left side (red circles). (B) The contact geometry of spheres immersed in oil (red) and 10 % TritonX (blue) indenting PDMS films with a nominal elastic modulus of 1.5 kPa formed a contact layer similar to the geometry observed with PAA (fig. 2.8, 2.9) and PNIPA films. Both films were (122 ± 1) µm thick below the sphere. The measurement in oil was carried out by Rebecca Benelli.

the film with a permanent magnet. In many cases, the PDMS film was visibly pulled upwards even above levels higher than the film surface far away from the indentation region (fig. 2.19A). This did not happen symmetrically around the edge of the indentation cap. In the example shown in fig. 2.19A, the film was only pulled upwards on the right side and no such adhesion effects could be resolved on the left side (red circles). Most likely, these asymmetric adhesion effects occurred as the spheres were dropped on the surface of the films in an uncontrolled manner. Furthermore, the indentation depth δ measured in 1xPBS varied drastically at a given sphere radius and at a given film thickness and thus, the reconstruction of E and ν described for PAA and PNIPA films was not possible.

Previously, it was observed that the wetting angle between water and PDMS can be altered upon the addition of a nonionic surfactant such as Triton X-100[230]. For this reason, oil (ÖlP3, Pfeiffer Vacuum GmbH, Asslar, density $\rho_{\text{oil}} = (768 \pm 8)\,\text{kg/m}^3$; measured by Rebecca Benelli) or a 10 % solution of Triton X-100 (VWR, Radnor, PA, USA, density $\rho_{10\,\%\text{TritonX}-100} = (980 \pm 10)\,\text{kg/m}^3$; measured by Rebecca Benelli), which is a nonionic surfactant, was used instead of 1xPBS to immerse the steel spheres. When immersed in oil or 10 % Triton X-100, the spheres rolled freely on the film surface and they were easy to remove with a permanent magnet. In both immersion media, the contact geometry between the sphere and the PDMS (fig. 2.19B) was comparable to the contact geometry of PAA in 1xPBS (fig. 2.8, 2.9). It is therefore reasonable to assume that the adhesion between the sphere and the film was significantly reduced in oil and 10 % Triton X-100 compared to 1xPBS.

2.3.4 Elastic Properties of PDMS Films

Even though the adhesion effects could be mitigated and the obtained data appeared to be self consistent, the stiffness of different PDMS film batches shipped by Ibidi with nominally the same elastic modulus still varied drastically. An example of a sphere with a radius of $R = 200\,\mu\text{m}$ indenting two films from different batches is shown in fig. 2.19B. Both films had a nominal elastic modulus of 1.5 kPa and a steel sphere with a radius of $R = 200\,\mu\text{m}$ was positioned in locations where the films were $h = (122 \pm 1)\,\mu\text{m}$ thick. On one film, the sphere sank $\delta = (6.8 \pm 0.2)\,\mu\text{m}$ into the film (fig. 2.19B, red) and on the other film, the sphere sank $\delta = (36.6 \pm 0.5)\,\mu\text{m}$ into the film (fig.

2.19B, blue), which, assuming incompressibility, amounts to elastic moduli of (3.60 ± 0.83) kPa and (150 ± 30) Pa according to equation 2.11.

In order to exclude that the film had a heterogeneous stiffness, a total of 20 measurements at different positions on the first film yielded indentation depths between 6.5 and 7.6 µm and 5 independent measurements on the second film yielded indentation depths between 34 and 38 µm while both films had a thickness between 98 and 122 µm. Therefore, the measurements on both films were repeatable and the differences can neither be explained by heterogeneities in one of the films nor by differences in their thickness.

A second hypothesis for these observed batch-to-batch differences was that the PDMS films swell in oil and thus become softer. However, this could be excluded by measurements of Rebecca Benelli. She incubated PDMS films with and without oil for 5 hours respectively and found that the films' thickness changed by less than 3 %, indicating that the films swell, if at all, only slightly over an extended period of time. Secondly, the films were immersed in oil for the first time directly before the acquisition of the first data point $\delta(h)$. In case continuous swelling had influenced the indentation experiments, the films elasticity could have changed with time. Typically, the imaging of about 10 data points took 60 min and the films were immersed in oil and Triton X-100 for multiple hours. During this time, no significant softening or stiffening was observed. Thirdly, one would expect that swollen films are either all softer or all stiffer than unswollen films. As it was the case in the examples described above, some films had elastic moduli larger than their nominal values and some had elastic moduli lower than their nominal values. Similar differences were observed for other batches and different nominal stiffnesses. Consequently, the discrepancies between the calculated and the nominal elastic moduli can most likely be attributed to the films' elastic properties themselves and they were most likely related to an irreproducible manufacturing process. For this reason, only the data of three PDMS films are presented below to illustrate that the method is generally also applicable to hydrophobic materials with the adaptations described above. All three films were immersed in 10 % Triton X-100.

The measured indentation depths are shown in figure 2.20 as a function of the film thickness. On those films with a rather homogeneous thickness (fig. 2.20 A,B), the indentation depth $\delta(h, R)$ was in good agreement with the model of Dimitriadis et al.[190] (eq. 2.11), indicating that the films behaved like homogeneous, linear elastic solids. The elastic modulus E and the Poisson ratio ν could be reconstructed as described in section 2.2.4. However, the elastic moduli deviated from the nominal elastic moduli. While the film with a nominal elastic modulus of 6.5 kPa was slightly softer ($E = (5.5 \pm 0.5)$ kPa) than its nominal value the film with a nominal elastic modulus of 15 kPa was considerably softer than its nominal value and had an elastic modulus of (6.3 ± 0.5) kPa, highlighting the need for in situ methods to calibrate thin films. Both films had a Poisson ratio of 0.46 ± 0.03. In contrast, on the film, which had an inhomogeneous thickness, the indentation depth increased in regions where the film was thinner (fig. 2.20C). This was also reflected by the fact that the elastic modulus calculated from equation 2.11 decreased as a function of h (fig. 2.20D). To calculate E, the assumption that the film was incompressible ($\nu = 0.50$[51]) was made. However, the data was, self-consistent, i.e. the measured elastic modulus $E(h)$ was identical for all tested sphere radii at a given film thickness. The results for E and ν are summarized in table 2.2.

2.3.5 Discussion

The method was adapted to PDMS films in this section. In contrast to hydrophilic PAA and PNIPA films, hydrophobic PDMS showed pronounced adhesion effects when imaged in 1xPBS and the film-sphere contact region was not even radially symmetrical. Parts of the film were pulled upwards near the edge of the contact region (fig. 2.19), indicating that there was strong adhesion between sphere and film. Presumeably, the asymmetric contact geometry was, at least in part,

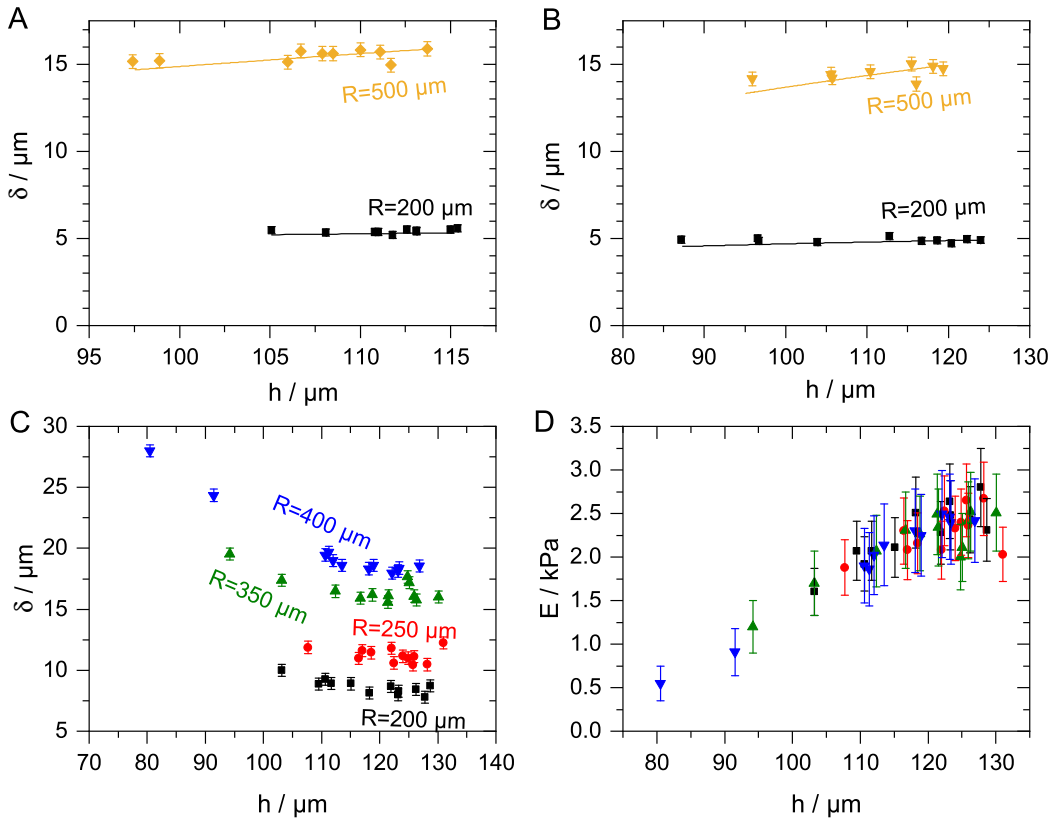

Figure 2.20: Results of the steel sphere method on PDMS films immersed in 10 % Triton X-100. (A), (B), (C) Indentation depth as a function of the film thickness for PDMS films from different batches. The films had nominal elastic moduli of of 6.5 kPa (A) and 15 kPa (B,C). Error bars were estimated by comparing the deviations of δ between both lateral directions (fig. 2.7 D). Solid lines in panels A) and B) were calculated by solving eq. 2.11 for δ with the reconstructed values given in table 2.2. (D) Elastic modulus as a function of the film thickness calculated from every data point in panel C using equation 2.11 with the assumption that the film was incompressible ($\nu = 0.50$[51]). The error bars were calculated from the errors of R, δ, and h by Gaussian error propagation. The elastic modulus did depend on the layer thickness, indicating that the film was inhomogeneously stiff. The data in panels A and B were acquired by Rebecca Benelli.

also determined by the uncontrolled falling motion of the sphere as it was positioned with the magnet. After the spheres falling motion was stopped by the film, the sphere most likely indented the film deeper than the equilibrium position and subsequently, the film stuck to the sphere surface, leading to hysteresis effects. In conjunction with that, the spheres did not roll on the film, further bolstering the fact that adhesion effects were not negligible. A likely explanation of this behavior is that in contrast to PAA and PNIPA films, PDMS is hydrophobic and thus, an increased contact area between the spheres and PDMS was energetically more favorable. Theoretical work has been done to account for such adhesion effects during indentation experiments. In 1971, Johnson et al. published a theory extending the Hertzian contact problem to account for attractive forces in the contact region, describing the experimentally observed hysteresis effects associated with adhesion.

The theory was, at the time, applied to the contact between a rubber sphere and a rubber flat as well as a gelatine sphere pushed onto a perspex flat[231]. Recently, the theory was extended to account for solid surface tension, which can be dominant on length scales of a few micrometers and below, e.g. when silica spheres are pushed into a PDMS film[232,233]. However, in the experiments discussed here, the spheres dropped in a non-reproducible and asymmetric manner. Consequently, due to the hysteresis, the contact geometries were also asymmetrical. Thus, the data of PDMS films immersed in 1xPBS was not evaluated and the experimental system had to be adapted to mitigate these adhesion effects. No adhesion effects were observed when the spheres were immersed in oil or Triton X-100.

Even though the PDMS films issued by ibidi were most likely not cured in a reproducible manner, the steel sphere method yielded consistent results on films which had homogeneous elastic properties, when immersed in Triton X-100 (fig. 2.20 A,B). As it was the case with the PAA and PNIPA samples, the measured indentation depth $\delta(h, R)$ was in good agreement with equation 2.11 and thus, those films behaved like linear elastic solids. In particular, the reconstructed Poisson ratios were close to 0.5 and they were in very good agreement with the literature[51,176,234]. However, the absolute values were not in agreement with the nominal values provided by the manufacturer. This can be seen from the raw data as well as from the reconstructed values of E and ν. As it can be seen from figures 2.20 A and B, the measured values of $\delta(R, h)$ of both films with nominally different elastic moduli were rather similar. For example, both on the film with a nominal elastic modulus of $E = 6.5\,\mathrm{kPa}$ and on the film with a nominal elastic modulus of 15 kPa, the sphere with a radius of 500 µm indented the film with a thickness of 90 to 120 µm by about 15 µm. Solving equation 2.11 for $\delta(R = 500\,\mu\mathrm{m}, h = 110\,\mu\mathrm{m}; E = 15\,\mathrm{kPa}, \nu = 0.5)$ yields $\delta \approx 9\,\mu\mathrm{m}$, which is far lower than the experimentally determined values of $\delta \approx (15.0 \pm 0.4)\,\mu\mathrm{m}$. Thus, the elastic modulus of the film was indeed far lower than its nominal value.

Possible reasons for those discrepancies can only be speculated about. The calibration carried out by the company was not performed on thin films and instead, thick macroscopic samples with a thickness of a few millimeters were prepared and indented with a flat punch with a diameter of 4 mm as described by Ulbricht et al.[176] (information by the manufacturer). According to the manufacturer, this did yield consistent results even when different batches were probed. A possible hint for the discrepancies is provided by the data of the film with the inhomogeneous thickness

E / kPa (nominal)	$\delta(h, R)$	E / kPa (steel sphere)	ν (steel sphere)
6.5	fig. 2.20 A	5.5 ± 0.5*	0.46 ± 0.03*
15	fig. 2.20 B	6.3 ± 0.5*	0.46 ± 0.03*
15	fig. 2.20 C	fig. 2.20 D	0.50**

Table 2.2: **Elastic moduli E and Poisson ratios ν of different PDMS films.** The elastic moduli and the Poisson ratios of thin PDMS films were determined with the steel sphere method from the indentation data $\delta(h, R)$ presented in figure 2.20. All experiments were conducted at room temperature and in 10 % Triton X-100. All films were ordered from ibidi and shipped in separate batches. The errors were calculated as described in section 2.2.4. The values marked with an asterisk are based on measurements by Rebecca Benelli. The third film presumably had a heterogeneous elastic modulus (fig. 2.20D) and thus, the Poisson ratio could not be determined. The assumption was made that the film was incompressible (two asterisks)[51]. None of the nominal elastic moduli matched the measured elastic moduli within the margin of error.

shown in figure 2.20 C and D. As adhesion effects should be independent of the film thickness (and were generally not noticed when measuring in Triton X-100), they can not explain the observed increased indentation depth at lower film thicknesses. However, the elastic modulus measured with four different sphere radii appeared to be consistent at any given film thickness. The measured elastic modulus of the film was considerably lower in thinner regions and high in thicker regions of the film. Given the fact that the spheres even sank deeper into the film in thinner regions, it is unlikely that adhesion effects caused this effect, as those should be independent of the film thickness. The fact that the measured elastic modulus was consistent for multiple spheres with different radii which all had different indentation depths excludes that optical distortions could have caused the effect. It is however possible that these inhomogeneities were not noticed in the macroscopic characterization experiments carried out by the manufacturer, as those experiments probed larger samples on a length scale of a few millimeters and not the thin films themselves (information by the manufacturer).

2.4 Optimization of the Reconstruction Precision

The uncertainties of the elastic parameters obtained by the steel sphere method in sections 2.2 and 2.3 varied from one measurement to the next (tab. 2.1), depending on the experimental conditions. The errors of the elastic modulus varied from 4 % (3 % AA, 0.1 % BIS) to 17 % (10 % AA, 0.1 % BIS, 3 % $CaCO_3$) and the errors of the Poisson ratio varied from 0.01 (3 % AA, 0.1 % BIS) to 0.1 (10 % AA, 0.1 % BIS, 3 % $CaCO_3$). Consider for example the film with 10 % w/v AA and 0.03 % BIS, which had an elastic modulus of (8.8 ± 0.7) kPa and was incompressible ($\nu = 0.53 \pm 0.02$). The elastic modulus was reconstruced based on 47 data points distributed over 4 sphere radii ranging from 200 to 400 µm (fig. 2.11). The error of the elastic modulus was about 8 % and the error of the Poisson ratio was 0.02. Interestingly, on the PDMS film, which had very similar elastic properties ($E = (6.3 \pm 0.5)$ kPa, $\nu = 0.46 \pm 0.03$), data was measured using only two spheres with radii of 200 and 500 µm and a total of only $N = 17$ data points. However, the reconstruction accuracy was very similar. With this observation in mind, the question arises how different measurement parameters can be optimized to minimize measurement errors.

In this section, the conditions in which the reconstruction is most accurate will be investigated to provide guidelines for future experiments to tune the parameters such that the accuracy is maximized. In particular, the size, density, and number of the spheres, the film thickness, as well as the number of data points can be altered to optimize the accuracy of the method. For this, a bootstrapping approach was used. Indentation experiments were simulated using equation 2.11, noise was added to the critical parameters of the experiment, i.e. sphere radius, indentation depth, and film thickness and the elastic properties were reconstructed with the algorithm described in section 2.2.4.

2.4.1 Simulation of Indentation Data and Reconstruction Data

The details of the algorithm are summarized in figure 2.21. Below, the term 'condition' summarizes the critical parameters used to simulate the indentation data, namely the true elastic modulus E_0 and the true Poisson ratio ν_0 of the film, the thickness range $h_{\min}$ and $h_{\max}$, the number of data points N per measurement, the sphere radii R, and their density ρ_S. 50 independent measurements were simulated for every condition. Every measurement consists of N independent data points. If not stated otherwise, the sphere density was set to the density of steel (AISI 420C, $\rho_S = (7.76 \pm 0.15)\,\mathrm{g/cm^3}$, sec. 2.2.2). For stiff films with an elastic modulus of 50 kPa, it is however useful to use spheres with a higher density. In this case, the density of gold $\rho_S = 19.3\,\mathrm{g/cm^3}$ was

also used in the simulations[213]. Thus, the indentation forces of the gold spheres were roughly three times higher than those of the steel spheres. The total number of data points N was distributed evenly over all sphere radii used in the measurement. The film properties were chosen as follows. For the ground truth elastic modulus, values of $E_0 = 1$, 3, 5, 15 and 50 kPa were used. For the ground truth Poisson ratio, values of $\nu_0 = 0.3$ and 0.5 were used. The film thickness h of every data point was chosen randomly between $h_{\min}$ and $h_{\max}$. In order to account for measurement errors, R, δ, and h were randomized by adding normally distributed noise with a standard deviation similar to the experimental errors (unless stated otherwise): $s_{\mathrm{R}} = 1.5\,\mu\mathrm{m}$, $s_\delta = 0.2\,\mu\mathrm{m}$, and $s_{\mathrm{h}} = 1.5\,\mu\mathrm{m}$. A total of 50 data sets $\delta_{\mathrm{i}}, h_{\mathrm{i}}, R_{\mathrm{i}}$ was simulated for every condition.

The algorithm described in section 2.2.4 was then used to reconstruct the elastic modulus $E^{+s_{\mathrm{E}}}_{-s_{\mathrm{E}}}$ and the Poisson ratio $\nu^{+s_\nu}_{-s_\nu}$ together with their respective errors in all of the 50 simulated data sets with 1000 generated, randomized data sets per simulated data set to determine the reconstruction uncertainties (sec. 2.2.4). If the reconstruction of any of the 50 simulated data sets failed (i.e. the algorithm described in section 2.2.4 did not converge), the whole condition was considered to be not reconstructable. If all 50 reconstructions succeeded, the averaged errors $< s_{\mathrm{E}} >=< s^+_{\mathrm{E}} + s^-_{\mathrm{E}} > /2$ and $< s_\nu >=< s^+_\nu + s^-_\nu > /2$ were used as a measure of the precision of the steel sphere method in this particular condition. Unless stated otherwise, the method yielded the ground truth values E_0 and ν_0 within the margin of error in all conditions.

2.4.2 Validation of the Bootstrapping Approach

At first, it was validated that the experimental uncertainties could be reproduced by the simulations described above. In order to do this, the reconstruction uncertainties of two experimentally measured data sets were compared to the reconstruction uncertainties determined by the simulation of indentation data sets in a similar condition.

First, a condition similar to the PAA film data set with 10 % AA and 0.06 % BIS (fig. 2.11C and tab. 2.1) was simulated. For the simulation, a film with a thickness of $h = 55$ to 120 µm, an elastic modulus of $E_0 = 11.7$ kPa, and a Poisson ratio of $\nu_0 = 0.48$ were used. Of all the experimentally acquired data points, 60 data points $\delta\,(h)$ were randomly selected. The used spheres in this data set had radii of 200, 250, 350, 400, and 500 µm.

The second condition was chosen to be similar to the experimental PNIPA film data set (10 % NIPA, 0.1 % BIS, fig. 2.11H and tab. 2.1), which consisted of 50 data points. The simulation was carried out at a thickness of $h = 90\,\mu\mathrm{m}$, an elastic modulus of $E_0 = 15.1$ kPa and a Poisson ratio of $\nu_0 = 0.33$, and the film was indented with steel spheres with nominal radii of 200 and 400 µm. The experimental uncertainties of the indentation depth were $s_\delta = 0.3\,\mu\mathrm{m}$ for spheres with radii $R \leq 350\,\mu\mathrm{m}$ and $s_\delta = 0.4\,\mu\mathrm{m}$ for spheres with radii of 400 and 500 µm.

The conditions were chosen firstly because the Poisson ratio of both films in the the experiment was widely different (PAA: $\nu = 0.48 \pm 0.02$, PNIPA: $\nu = 0.33^{0.05}_{-0.11}$). Secondly, the PAA film was a film with an inhomogeneous thickness, while the PNIPA film had a homogeneous thickness of about 90 µm. Lastly, the PAA data set was acquired with 5 spheres while the PNIPA data set was acquired with only two spheres. Both experimental data sets were split into data sets with fewer, yet independent data points with an equal number of data points per sphere. For example, the PAA data set which contained $N = 60$ data points distributed over 5 spheres could be split into 6 independent data sets, each containing $N = 2$ data points per sphere.

The average reconstruction uncertainties are plotted as a function of N in figure 2.22. In both conditions, the reconstruction uncertainties derived from experimental and simulated data sets were in excellent agreement with each other, independent of the number of data points N used per reconstruction. Therefore, it can be concluded that the simulations conducted as described in section 2.4.1 are a suitable tool to predict the reconstruction uncertainties of experimental data

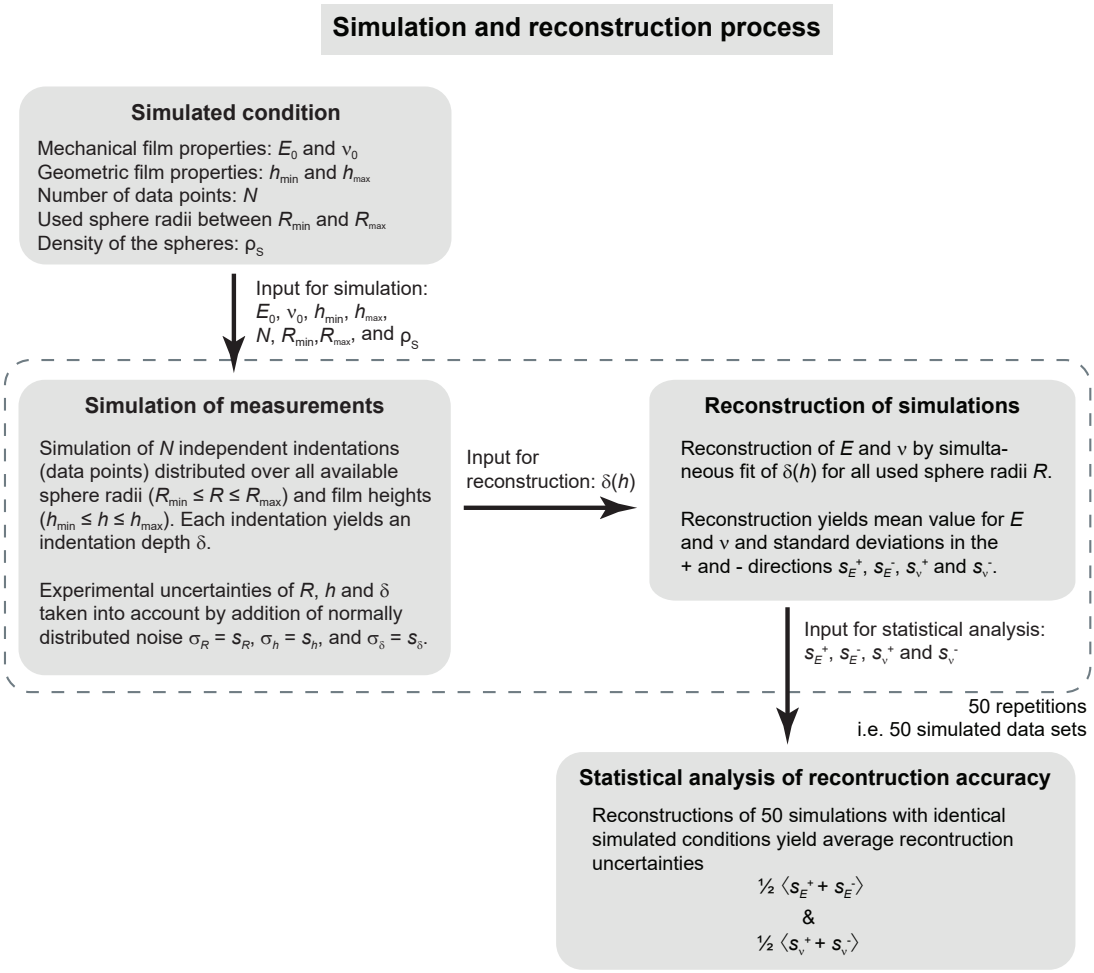

Figure 2.21: Algorithm used to predict the reconstruction uncertainty. Figure adapted from Gross and Kress, Journal of Physics Communications, 2019[158].

sets.

2.4.3 Choice of Data Point Count

As indicated by the results in section 2.4.2, the reconstruction accuracy does improve with larger N, i.e. higher workload. However, from the experimental results, it can be seen that good accuracy can be achieved with relatively low workload and especially the use of more than two sphere radii does not appear to be necessary. It is therefore interesting to investigate how many data points should reasonably be acquired to balance workload and accuracy and whether a desired accuracy can be achieved at all with a given set of sphere radii and a certain film parameter set defined by h, E_0, and ν_0. Therefore, the indentation of two spheres with radii of 200 and 500 µm into films with an elastic modulus $E_0 = 15\,\mathrm{kPa}$ and Poisson ratios of 0.3, 0.4, and 0.5 was simulated for two different film types.

The first type consisted of films with a homogenous thickness h. The film thickness was chosen

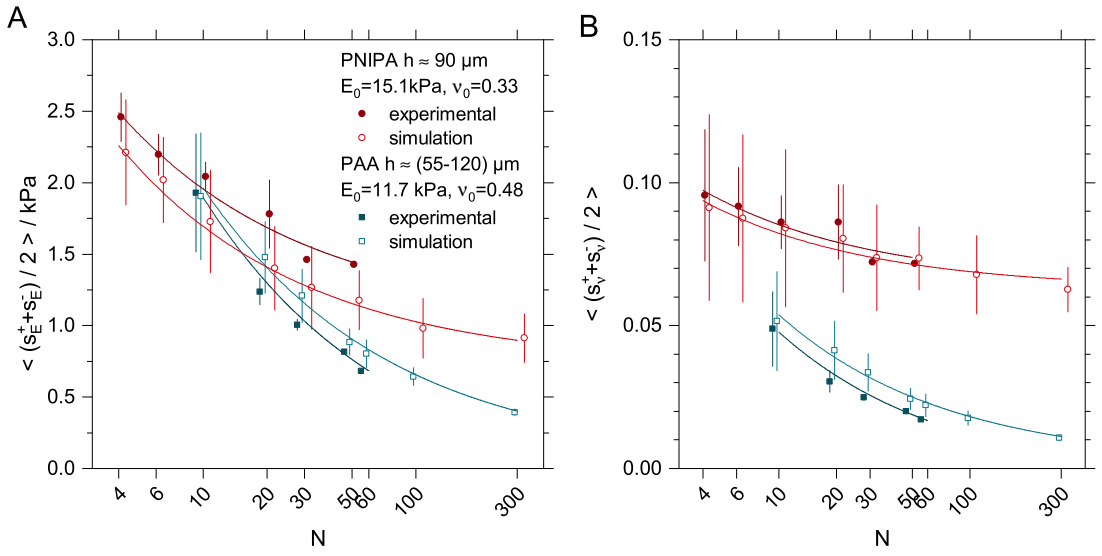

Figure 2.22: Validation of the reconstruction accuracy. Comparison of the average experimental (filled symbols) and simulated simulated (open symbols) reconstruction uncertainties of (A) E and (B) ν and as a function of N. The experimental PAA film data set containing 10 % AA and 0.06 % BIS (blue curves) with a high Poisson ratio of 0.48 and the PNIPA film data set containing 50 data points (10 % NIPA, 0.1 % BIS) with a low Poisson ratio of 0.33 (red curves) were used (fig. 2.11 C, H and tab. 2.1). The values of N denoted by the labels of the abscissa is equal to the number of data points used for every reconstruction. The data points were slightly offset to the side along the abscissa for better visibility. The error bars denote the standard deviation of the reconstruction uncertainty for every condition, calculated with all repetitions. Solid lines are a guide to the eye. Figure adapted from Gross and Kress, Journal of Physics Communications, 2019[158].

such that a maximally wide range of contact geometries was tested, i.e. the range of χ values was maximal. In this case, the contrast of the finite thickness correction factor was largest (fig. 2.10) and therefore, the reconstruction of E and ν was as accurate as possible. Furthermore, the film thickness h was chosen such that the indentation of the largest sphere in the thinnest film region corresponded to $\chi\left(R = 500\,\mu\text{m}, h = h_{\text{min}}, \delta\left(R, h\right)\right) = 1$. For example, in case of a film with $h = 54\,\mu\text{m}$, $\nu_0 = 0.5$ and $E_0 = 15\,\text{kPa}$, a sphere with $R = 200\,\mu\text{m}$ is expected to indent the film by $\delta = 2.5\,\mu\text{m}$ (eq. 2.11), in which case $\chi \approx 0.4$ (eq. 2.14). In contrast, a sphere with a larger radius of 500 µm indents the surface of the film by $\delta = 5.8\,\mu\text{m}$, which corresponds to $\chi \approx 1$. Thicknesses lower than h correspond to $\chi > 1$, for which the series in equation 2.12 does not converge[190] and thus, equation 2.11 can not be used. It is important to note that in the simulations, the film thickness was matched to the sphere radii. If this is not an option in practice, the sphere radius can analogously be matched to the film thickness.

As a second type, films with an inhomgenous thickness between h_{min} and $h_{\text{max}} = 500\,\mu\text{m}$ were chosen. On these films, χ is different for any given sphere radius. At the lower end at $h = h_{\text{max}}$, the finite thickness correction is almost negligible and $\chi < 0.2$ for both spheres in all conditions. At $\chi < 0.2$, the finite thickness correction only slightly depended on the Poisson ratio (fig. 2.10). Such a contact geometry is similar to the Herzian case of an infinitely thick film and in this case, only E or ν can be resolved. Therefore, the small differences in contrast between the different conditions

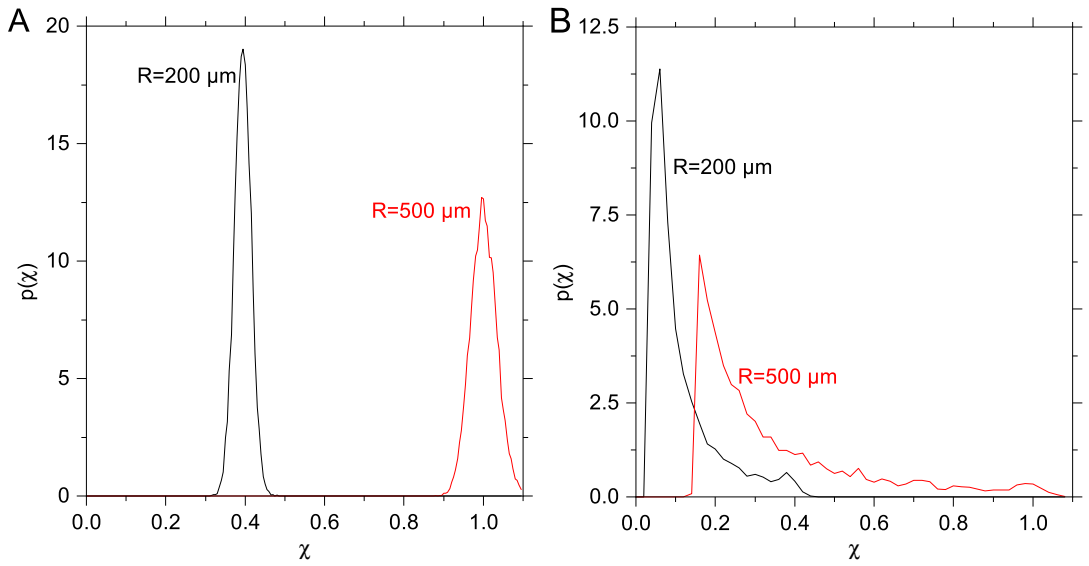

Figure 2.23: Simulated normalized distribution functions $p(\chi)$ on films with $E_0 = 15\,\mathrm{kPa}$ and $\nu = 0.5$. The films in panel A had a homogeneous thickness of $h = 54\,\mu\mathrm{m}$ while the films in panel B had an inhomogeneous thickness of $h_{\min} = 54\,\mu\mathrm{m} < h < 500\,\mu\mathrm{m} = h_{\max}$. The distributions were calculated according to the conditions described in section 2.4.3. Noise was added to δ, h and R. Figure originally published in Gross and Kress, Journal of Physics Communications, 2019[158].

induced by the choice of an identical $h_{\max}$ were considered to be negligible for the sake of this analysis. $h_{\min}$ was chosen such that $\chi(R = 500\,\mu\mathrm{m}, h = h_{\min}, \delta(R,h)) = 1$ as described above for the films with a homogenous thickness. In all conditions with films with an inhomogeneous thickness, all N data points were distributed evenly in the range $h_{\min} - h_{\max}$. The resulting normalized probability distribution functions $p(\chi)$ of the values of χ on both film types at $\nu_0 = 0.5$ are shown in figure 2.23.

Simulations with the conditions described above were carried out with $N = 4$, 6, 10, 30, 60, 100, and 300 data points. The reconstruction uncertanties in these conditions were determined as described in section 2.4.1 and they are shown in figure 2.24. Interestingly, the reconstruction accuracy of the elastic modulus was better on films with an inhomogeneous thickness and did not depend on the Poisson ratio (fig. 2.24 A, blue curves). On films with a homogeneous thickness, the reconstruction of E was far less accurate than on inhomogeneously thick films and depended on the Poisson ratio (fig. 2.24 A, red curves). The reconstruction uncertainties of the elastic modulus were lower on films with a lower Poisson ratio. The reconstruction of ν was generally more accurate the higher the Poisson ratio of the films. This was the case on films with a homogeneous (fig. 2.24B, red curves) and on films with an inhomogeneous thickness (fig. 2.24B, blue curves). However, in contrast to the elastic modulus, the reconstruction accuracy of ν improved only slightly on films with an inhomogeneous thickness.

In general, the reconstruction uncertainty of both E and ν was lower when more data points were used per reconstruction. Practically, a choice between $N = 20$ and $N = 60$ data points appears to be a good compromise between workload and accuracy in all conditions. In case of $N = 60$, the uncertainties had dropped considerably and the reconstruction uncertainties did not decrease by a big margin as N was increased above 60. If only the elastic modulus is to be determined with

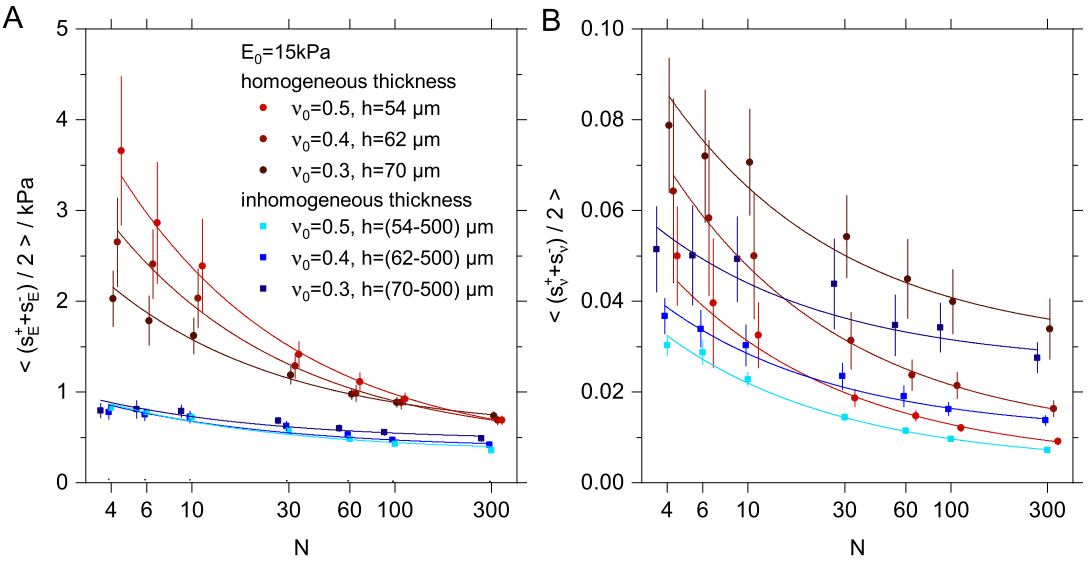

Figure 2.24: Simulated reconstruction uncertainties of (A) the elastic modulus and (B) the Poisson ratio as a function of the number of data points N. Films with an elastic modulus of $E_0 = 15\,\mathrm{kPa}$ and Poisson ratios of $\nu = 0.5$, 0.4, and 0.3 and a homogeneous (red symbols) as well as an inhomogeneous thickness (blue symbols). The data belong to the labels at the abscissa and were offset slightly for better visibility. Solid lines are a guide to the eye. The error bars represent the standard deviation of the reconstruction uncertainties, calculated with all 50 repetitions. Figure adapted from Gross and Kress, Journal of Physics Communications, 2019[158].

a high precision, the choice of a film with an inhomogeneous thickness is optimal. In this case, a small number of data points $N < 10$ is enough to achieve a reconstruction uncertainty of about $0.7\,\mathrm{kPa}/15\,\mathrm{kPa} \approx 5\,\%$, which may be sufficient depending on the application.

2.4.4 Choice of Sphere Radius, Count and Density

The sphere choice also impacts the reconstruction accuracy. While the indentation depth δ of a very small sphere will be below the resolution limit, a sphere, which is too large, will sink in too deep to satisfy the theoretical limit $\chi \leq 1$, which is equivalent to $\delta \leq h^2/R$.

With these limitations in mind, the use of up to 5 sphere radii of $R = 200$, 250, 350, 400, and 500 µm is discussed below. According to the results shown in section 2.4.3, 60 data points were distributed evenly over all spheres used in the simulation. The film properties were chosen as follows. The elastic modulus was varied in the range between $E_0 = 1$ and 50 kPa and two Poisson ratios of $\nu = 0.3$ and 0.5 were tested. For inhomogeneously thick films, the upper boundary was chosen to be $h_{\mathrm{max}} = 500\,\mu\mathrm{m}$ and the lower boundary h_{min} was chosen such that $\chi \approx 1$ for the largest sphere. Homogeneously thick films had a thickness of h_{min} (sec. 2.4.3).

The reconstruction uncertainty was quite different on films with a homogeneous thickness and on films with an inhomogeneous thickness. On homogeneously thick films, the reconstruction of the film's elastic properties was only possible, when more than one sphere was used. Otherwise, the contact geometry is not varied within the experiment (i.e. χ is identical for all data points and thus, C is also identical). As a consequence, two spheres must be used to be able to reconstruct

both E and ν. Even then, the choice of sphere radii used per experiment had a major impact on the reconstruction accuracy (fig. 2.25). In all tested conditions, the use of all 5 sphere radii was among the most accurate ones, independent of E_0. Both on compressible and on incompressible films, the reconstruction accuracy degraded when only larger spheres were used and was least precise, when two spheres with radii of 400 and 500 µm were used. In all cases, the reconstruction uncertainties of both E and ν nearly doubled when the disadvantageous set of sphere radii of 400 and 500 µm was used compared to the set of 250 and 500 µm. This can presumably be attributed to the fact that the range of χ which was covered was far smaller in the first case. From figure 2.26 A, it can be seen that in case of $E_0 = 1$ kPa and $\nu_0 = 0.5$, the range of χ covered by the experiment was different in both cases ($0.75 \leq \chi \leq 1$ for $R = 400$ and 500 µm and $0.35 \leq \chi \leq 1$ for $R = 200$ and 500 µm). The optimal sphere radius set to determine E was also nearly optimal to reconstruct ν and vice versa.

The situation is different when a film with an inhomogeneous thickness is available. In this case a single sphere radius can cover a range of different contact geometries and the reconstruction is generally possible when only one sphere is used. The simulations results are shown in figure 2.27. The reconstruction uncertainties of E and ν were generally lowest when only one large sphere with a radius of 500 µm was used and highest, when only a relatively small sphere radius of 200 µm was used. This was the case both on incompressible films (fig. 2.27 A, B) and on films with $\nu_0 = 0.3$ (fig. 2.27 C, D). The reconstruction uncertainty varied drastically depending on the precise condition. For example, at $E_0 = 15$ kPa and $\nu_0 = 0.5$, the reconstruction accuracy of E was about 2 % when a single sphere radius of 500 µm was used and increased to 11 % at a sphere radius of 200 µm, which is a 5.5-fold increase. Likewise, the reconstruction uncertainty of ν increased from 0.008 to 0.06, which amounts to a 7.5-fold increase. Reconstruction was not even possible in some cases on very stiff films with 15 and 50 kPa, when only a single, small steel sphere was used (fig. 2.27). The utilization of multiple sphere radii yielded similar results for all radii combinations. The errors were approximately double as high as in the best case of a single, large sphere with $R = 500$ µm. Thus, the utilization of multiple sphere radii on films with an inhomogeneous thickness even degrades accuracy. Firstly, this can be attributed to the fact that here, one sphere can cover a wide range of contact geometries, described by the parameter χ (fig. 2.26 B). For example, in case of $E_0 = 1$ kPa and $\nu_0 = 0.5$, the range of χ covered by a sphere with $R = 200$ µm is $0.1 \leq \chi \leq 0.4$ and at $R = 500$ µm the range is a lot larger ($0.32 \leq \chi \leq 1$). Secondly, the values of χ covered by small spheres is also lower compared to larger spheres and thus, smaller spheres offer less resolution since the correction factor C does only slightly depend on the Poisson ratio in this range of χ-values (fig. 2.10 A, B). Therefore, it is not beneficial to use small spheres, since the indentation error s_δ is relatively large and resolution degrades.

In general, the reconstruction uncertainty of both E and ν was smaller the lower E_0 and the reconstruction of ν was less precise on compressible films than on incompressible films (fig. 2.25 and 2.27). Comparing the results in detail, at $\nu_0 = 0.5$ and 0.3, the reconstruction uncertainties of E were similar on soft films with $E_0 = 1$, 3, and 5 kPa and $\nu_0 = 0.3$ and 0.5 with a given set of sphere radii (fig. 2.25 and 2.27 A, C) with values roughly between 1 and 10 % for E and between 0.002 and 0.08 for ν, depending on the condition. The stiffer the films, the more the reconstruction uncertainty of E increased. In the extreme, reconstruction was not even possible on films with $E_0 = 50$ kPa, $\nu_0 = 0.5$ and a homogeneous thickness with any of the used steel sphere radius combinations. The reconstruction even failed when only a single, small sphere was used on films with an inhomogeneous thickness. Likewise, The reconstruction was also not possible at $E_0 = 50$ kPa and $\nu_0 = 0.5$ when only a single steel sphere with a radius of 200 and 250 µm was used. Similarly, reconstruction was also not possible on compressible films with $E_0 = 15$ and 50 kPa and $\nu_0 = 0.3$ with steel spheres with radii of 200 and 250 µm, and in case of $E_0 = 50$ kPa with a single sphere with a radius of 350 µm. Yet, reconstruction was possible in all of these cases, when spheres

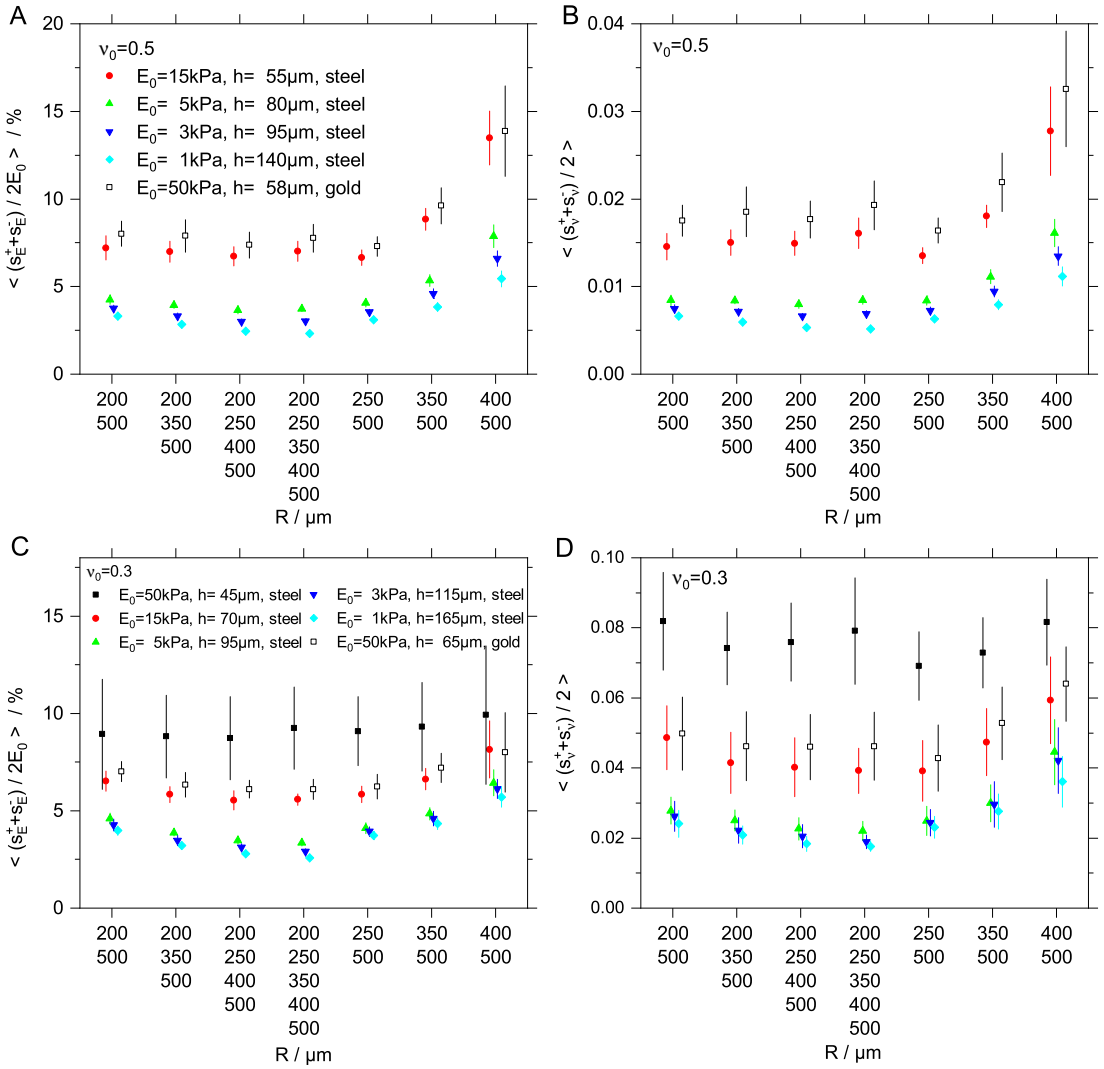

Figure 2.25: Simulated reconstruction uncertainties on films with a homogeneous thickness as a function of the used sphere radii. Reconstruction uncertainties of (A, C) E and of (B, D) ν were calculated for (A, B) $\nu_0 = 0.5$ and (C, D) $\nu_0 = 0.3$ and various elastic moduli E_0. The reconstruction of E and ν of films with $E_0 = 50\,\mathrm{kPa}$ and $\nu_0 = 0.5$ was not possible with any of the tested steel sphere combinations. However, reconstruction was possible when spheres with the density of gold were used (open symbols in panels A and B) or on films with $\nu_0 = 0.3$ (open symbols in panels C and D). $N = 60$ data points were used for every independent simulated data set. Error bars represent the standard deviation of the reconstruction uncertainties calculated with all 50 simulated data sets. Figure adapted from Gross and Kress, Journal of Physics Communications, 2019[158].

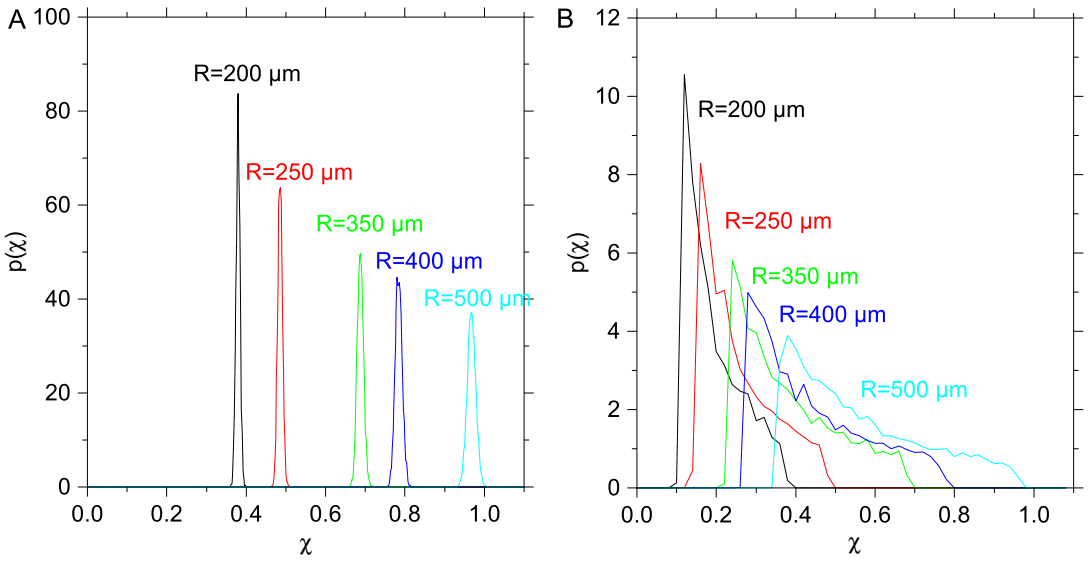

Figure 2.26: Simulated normalized distribution functions $p(\chi)$ of the contact geometry χ. The simulations were carried out on films with $E_0 = 1\,\mathrm{kPa}$, $\nu_0 = 0.5$ and (A) a homogeneous thickness of $h = 140\,\mu\mathrm{m}$ as well as (B) and inhomogeneous thickness of $140\,\mu\mathrm{m} \leq h \leq 500\,\mu\mathrm{m}$. The underlying data is identical to the data from (A) figure 2.25 and (B) figure 2.27. Figure adapted from Gross and Kress, Journal of Physics Communications, 2019[158].

with the density of gold were used instead (fig. 2.25 and 2.27).

This dependence of the reconstruction accuracy on E_0 can most likely be attributed to the fact that the indentations on soft films are generally deeper. For example, in case of an incompressible film with $E = 50\,\mathrm{kPa}$ and a homogeneous thickness of $55\,\mu\mathrm{m}$ (fig. 2.25 A, B), a steel sphere with a radius of $200\,\mu\mathrm{m}$ is expected to indent the film by $\delta \approx 1.2\,\mu\mathrm{m}$. Thus, the relative error of the indentation is about $0.2\,\mu\mathrm{m}/1.2\,\mu\mathrm{m} = 17\,\%$. In contrast, when gold spheres with a higher indentation force are used, the indentation depth increases to $2.5\,\mu\mathrm{m}$ and the reconstruction became possible with uncertainties of approximately the same size as in the case in which a film with $E_0 = 15\,\mathrm{kPa}$ is probed with a steel sphere of the same radius. This appears to be plausible since the fraction $E/(\rho_{\mathrm{sphere}} - \rho_{PBS})$ is similar in both cases (eq. 2.11 and 2.13).

Even with the optimal set of spheres, reconstruction uncertainties of both E and ν were also considerably lower on films with an inhomogeneous thickness compared to films with a homogeneous thickness. For example, the elastic modulus of an incompressible film with an elastic modulus of $E_0 = 1\,\mathrm{kPa}$ and a homogeneous thickness could be determined with an uncertainty of $2.3\,\%$, when all five spheres were used (fig. 2.25 A). On a film with an inhomogeneous thickness, the uncertainty was only $1.0\,\%$ (fig. 2.27) which was less than half of the value of a film with a homogeneous thickness. Likewise, the error of the Poisson ratio drops from 0.005 to 0.001, which is a five-fold decrease. A similar behavior was found in many of the other conditions and the reconstruction on a film with an homogeneous thickness was never better than on a film with a homogeneous thickness.

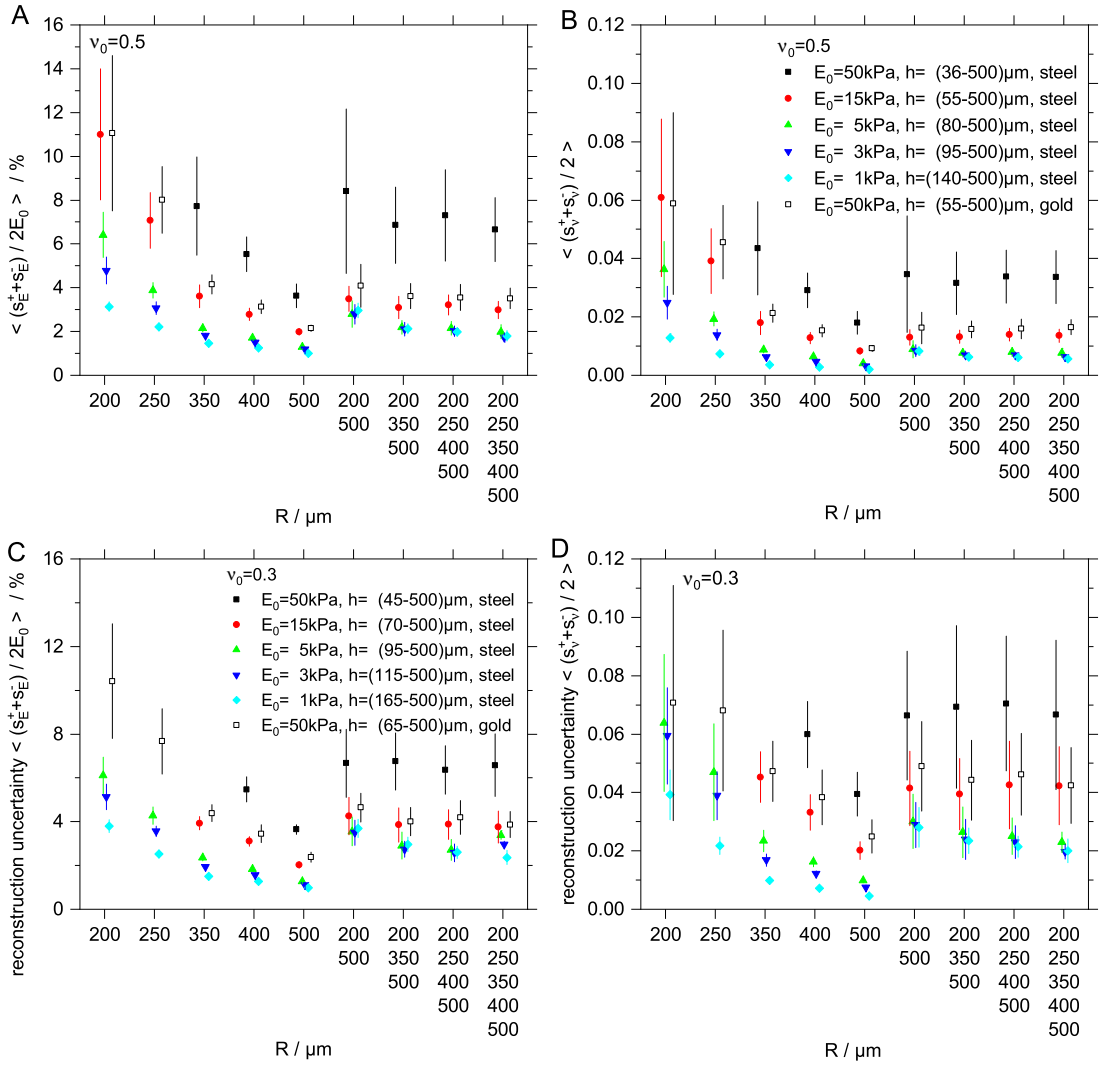

Figure 2.27: Simulated reconstruction uncertainties of films with an inhomogeneous thickness as a function of the used sphere radii. The reconstruction uncertainties of (A, C) E and of (B, D) ν were calculated with (A, B) $\nu_0 = 0.5$ and (C, D) $\nu_0 = 0.3$ and various elastic moduli E_0 as a function of the used sphere radii. The reconstruction of E and ν of films with $E_0 = 50\,\mathrm{kPa}$ and $\nu_0 = 0.5$ was not possible when only a single steel sphere with a radius of 200 and 250 µm was used. Similarly, the reconstruction was also not possible on compressible films with $E_0 = 15$ and 50 kPa and $\nu_0 = 0.3$ with steel spheres with radii of 200 and 250 µm, and in case of $E_0 = 50\,\mathrm{kPa}$ with a single sphere with a radius of 350 µm. However, the reconstruction was possible in those cases, when spheres with the density of gold were used (open symbols). $N = 60$ data points were used for every independent simulated data set. The error bars represent the standard deviation of the reconstruction uncertainties calculated with all 50 simulated data sets. Figure adapted from Gross and Kress, Journal of Physics Communications, 2019[158].

2.4.5 Discussion

As demonstrated in section 2.4.3, reconstruction uncertainties of E and ν in the experiments could be reproduced with simulated indentation data, considering the errors of R, δ and h (fig. 2.22). This demonstrates that the experimental errors are well understood and that the bootstrapping approach is suitable to predict the precision of the real experiments. The simulation results show that there are some general boundary conditions, which have to be considered to optimize the method's precision, namely the number of data points, the choice of the spheres and the interplay between the spheres and the finite layer thickness effects. With the experimental errors of the methods and the setup used in this work, it was demonstrated that the acquisition of more than 60 data points only marginally improved the precision of the reconstruction in all tested conditions (fig. 2.24). Instead of increasing the number of data points N beyond 60, the method greatly profited from a smart data point distribution, which covers a wide range of χ values and therefore also a wide range of contact geometries. In particular, the method is most sensitive in the range $0.4 < \chi < 1$, which is the range in which finite thickness effects greatly influence the indentation (fig. 2.10) and therefore, it is most important to cover this range in the experiments to resolve both E and ν accurately. The sphere radius and their density as well as the layer thickness should be kept in a range such that the indentation depth can be well resolved by the setup.

A summary of the suggested workflow that can be deduced from the simulation results is given in figure 2.28. Firstly, with the experimental methods described in this work and with the precisions achieved to measure δ, h and R, the reconstruction of E and ν was possible when the fraction of $E/\left(\rho_{\mathrm{S}} - \rho_{\mathrm{PBS}}\right)$ was smaller than $2.7\,\mathrm{m}^2/\mathrm{s}^2$ and the reconstruction was more accurate, the smaller $E/\left(\rho_{\mathrm{sphere}} - \rho_{\mathrm{PBS}}\right)$. The material choice for the sphere is therefore crucial to achieve good accuracy and a bad choice can even make the reconstruction impossible if the ensuing indentation depths can not be resolved accurately enough. This could for example be observed when the indentation of small spheres was simulated on stiff films with a relatively high elastic modulus of $E_0 = 50\,\mathrm{kPa}$. Since it is the aim of the experiments to measure the elastic modulus, the elastic modulus is not known beforehand. In order to mitigate this, it is beneficial to estimate the elastic modulus and the Poisson ratio with preliminary experiments or literature search, and to make a final choice for the sphere density ρ_{S} based on those estimates. Another option is to adapt the methods to a different setup, in which the indentation force and consequently also the indentation geometry can be varied at a given sphere radius and a given film height in a controlled manner. For instance, this is possible with an atomic force microscope[235] or with macroscopic setups as described e.g. by Ulbricht et al.[176] or Jacot et al.[204].

The simulations also suggest that the use of a film with an inhomogenous thickness can be beneficial. On the one hand, the reconstruction on such films was possible with only a single sphere radius and on the other hand, the simulations suggested that the reconstruction accuracy was even enhanced compared to the use of a film with a homogeneous thickness, which has to be probed with at least two spheres. Yet, in all simulated conditions, the use of a film with an inhomogeneous thickness in conjunction with a large sphere was never worse at a given E_0 and a given ν_0. The reconstruction of the elastic parameters from simulated indentations was most accurate, when a single sphere was used and when the radius of the sphere was matched to the thickness profile of the film. Consequently, a film with an inhomogeneous thickness should be probed with a single sphere if feasible as it can provide considerably better accuracy without significant experimental downsides.

However, the feasible thickness range might be limited by experimental constraints. Firstly, the working distance of the objective has to be large enough to image the top surface of the film to measure δ and h. This is especially the case for high NA objectives, which enable good resolution. The working distance of these objectives is typically on the order of at most a few

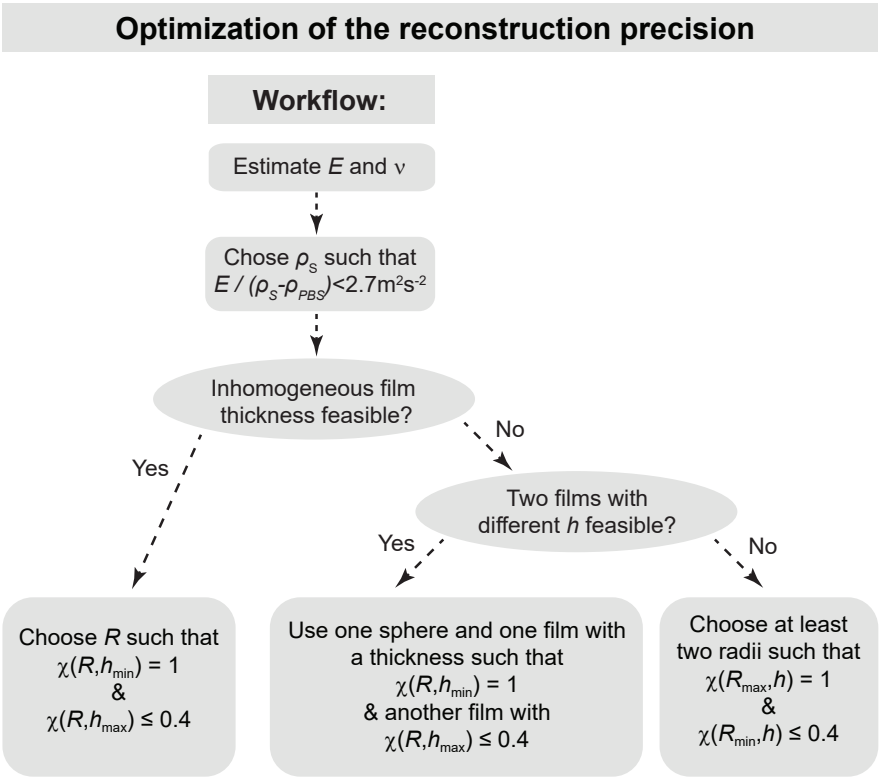

Figure 2.28: Guidelines for the choice of measurement parameters to optimize reconstruction accuracy of the elastic parameters. The parameters, i.e. sphere density and their radii as well as the thickness profile of the film should be chosen such that the indentation depth can be well resolved. Furthermore, the parameters should be chosen such that the contact geometry is varied in a wide range covering $0.4 \leq \chi \leq 1$. A detailed discussion of the parameter choice is given in section 2.4.5. Figure adapted from Gross and Kress, Journal of Physics Communications, 2019[158].

hundred micrometers. Secondly, films with an inhomogeneous thickness have a surface, which is inevitably tilted relative to the horizon. In the experiments presented in this work, the PAA and PNIPA films were about 15 mm in diameter and their thickness varied by at most 70 µm. Even though the fact that the indentation force was not oriented perfectly perpendicular to the film surface was negligible as the surface angle was only about 0.3° relative to the horizon, it was still observed that the spheres sometimes rolled slightly on the surface of PAA films due to gravity. Therefore, measurements on films with an even more titled surface may be impractical. In this case, as a possible workaround two films with different thicknesses but with otherwise identical elastic properties can be used. As a balanced choice, the maximum film thickness should be chosen such that $\chi(R, h_{\max}) \approx 0.4$ since below $\chi = 0.4$, the finite thickness contrast between different Poisson ratios only slightly increases (fig. 2.10 B) and consequently, the use of thicker films is less beneficial. On the other hand, the sphere radius and the minimal film thickness should be chosen such that $\chi(R_{\max}, h_{\min}) \approx 1$, which is roughly the theoretical limit for which the sum in equation 2.12 converges[190]. In the experiments in this work, different sphere radii were tested on every film and the radius was increased until $\chi(R_{\max}, h_{\min}) \approx 1$ was observed.

In case only a film with an almost homogeneous thickness distribution is available as it was the case for the PDMS films in this work (fig. 2.20 A and B), the use of multiple sphere radii is the only option to resolve both E and ν. In this case, a large sphere should be chosen such that $\chi(R_{\max}, h) \approx 1$. The smallest sphere should be chosen small enough to yield $\chi(R_{\min}, h) \approx 0.4$ for best results. In this χ-range, the correction factor C depends significanly on the Poisson ratio and thus, both E and ν can be resolved (eq. 2.12, fig. 2.10). However, as smaller spheres also sink less deep into the film, the radius should be chosen large enough such that the indentation depth can still be resolved accurately. Yet, multiple sphere radii can still be used in all conditions. When multiple radii are used, the number of different indentation geometries, which are tested is increased. As the indentation depth does depend on the sphere radius and the layer thickness, a comparison of the measured indentation depth $\delta(R, h)$ to the prediction from equation 2.11 is a good consistency check as it can be seen in figures 2.11 and 2.20. This was also the reason why multiple sphere radii were used in this work, even though the use of a single sphere with the same amount of data points would have possibly yielded more accurate results. For example, deviations from the model can occur when the film is not tested within the linear elastic regime, when the film's elastic properties are heterogeneous or when adhesion effects between the indenter and the film occur. Those effects have to be dealt with differently. Possible options are e.g. the use of a different model which accounts for nonlinear effects[191] or adhesion[231,235]. The approach taken in this work to mitigate adhesion effects by immersing the indentation region in a suitable liquid is also possible (sec. 2.3.3).

2.5 Summary of the Steel Sphere Technique

In this chapter, the steel sphere method, which is commonly used to characterize thin films with a stiffness in the range of cells and tissue[50,202,236] was advanced to allow the simultaneous reconstruction of the elastic modulus and the Poisson ratio. In this section, the main findings are revisited to summarize the technique presented in this chapter. An graphical overview of this section is provided in figure 2.29. In this work, the method was applied to four different film systems, namely PAA, porous PAA, PNIPA and PDMS. All tested films had stiffnesses in the same range as that of mammalian tissue. In general, when an infinitely thick film is indented by a spherical, hard punch, the fraction $E/\left(1-\nu^2\right)$ is constant, no matter which experimental parameters are varied (eq. 2.11, $\chi = 0$). The technique presented here is based on the fact that this is not the case when the film thickness is finite and comparable to the size of the contact region between the film and the indenter. When a film with a finite thickness is probed, the interplay between the film's compressibility and the contact geometry allows the simultaneous determination of both E and ν (sec. 2.2.4)[190,193,194].

The methods presented in this work rely on a theory which is an ab initio extension of the Hertzian solution for the indentation problem of a sphere indenting an elastic half space[189] and which takes finite thickness effects into account[190]. The model is valid when five major conditions are met. Firstly, the model is valid for thin films which are bound to a rigid substrate. This was the case for all films investigated in this work (sec 2.2.1.1 and 2.2.2). In case the film is not bound to the substrate, Dimitriadis et al. also provide an alternative solution[190]. Secondly, the model also assumes that the film is linearly elastic and homogeneous (sec. 2.2.3). It is important to note that the material must only be homogeneous on the length scale of the contact radius. If the samples are probed on longer length scales, i.e. on length scales larger than the dimension of the inhomogeneities, the elastic response of the whole film may still be in line with that of a homogeneous elastic material. As an example of such a material, porous PAA films were investigated (sec. 2.2.6). On the contrary, if the length scale of the inhomogeneities is larger than the

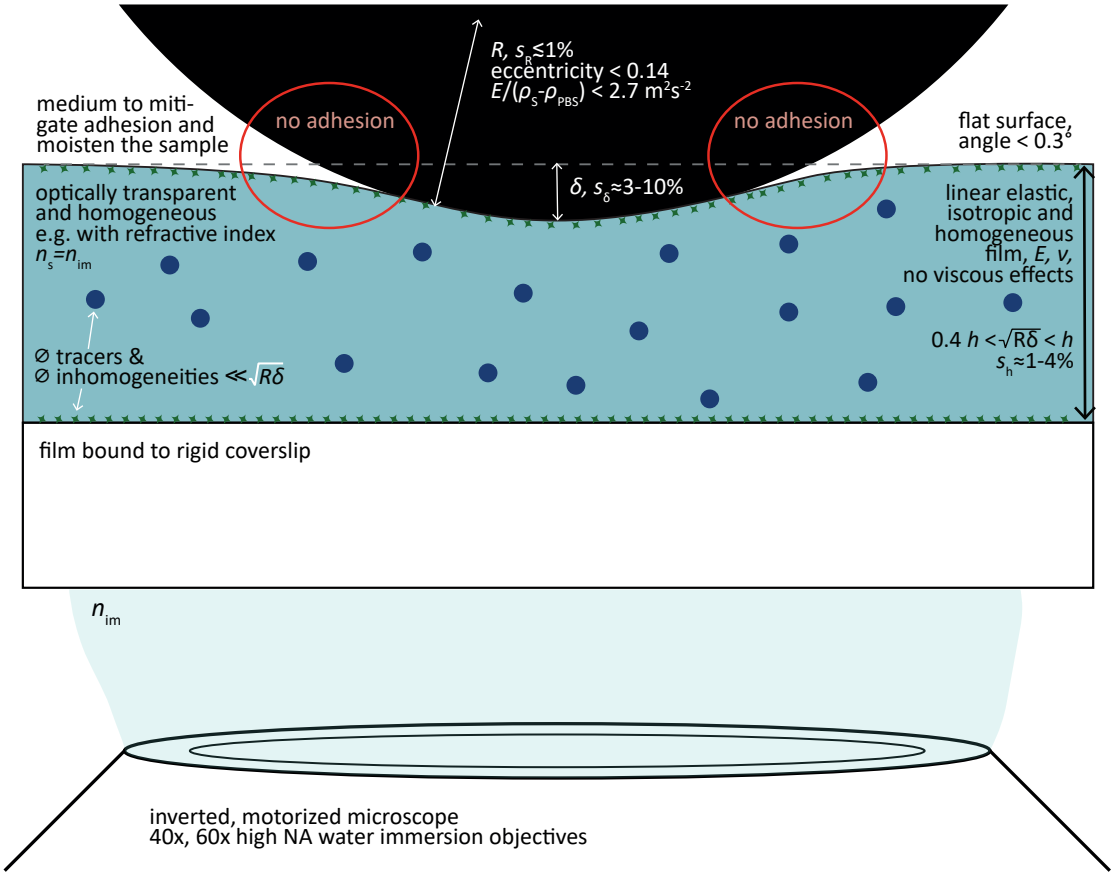

Figure 2.29: Methods and requirements to apply the steel sphere method. The figure summarizes the main findings of sections 2.2, 2.3, and 2.4. A detailed discussion of this figure is provided in section 2.5.

dimension of the deformation field, the material response can still be locally in line with the model as it was observed for inhomogeneous PDMS films (sec. 2.3.4). Thirdly, viscous contributions in the elastic response of the probed material must be negligible. While viscous contributions were not observed in any of the four model systems studied in this chapter, this is not necessarily the case for biological samples. In contrast, the rheological response of cells and tissue contains both elastic and viscous contributions when probed on the time scale of a few seconds[49,237]. For such viscoelastic samples, the steel sphere method is not suitable. The time required to acquire an image stack capturing the indentation cap was typically on the order of 1 to 2 minutes, depending on the number of images required and, as a consequence, the indentation depth would change during data acquisition. A technique to characterize the rheology of such viscoelastic samples is presented in chapter 3 of this work. Fourthly, the model by Dimitriadis et al.[190] also does not account for adhesion. In case the indenter sticks to the film, care should be taken and the model is most likely not applicable. This is in particular the case if hysteresis effects are observed. While PAA and PNIPA did not adhere to the spheres when immersed in 1xPBS, PDMS films immersed in 1xPBS were very sticky and the adhesion effects were even visible at the edge of the indentation region. The edge of the indentation cap was asymmetric and the film was locally pulled upwards above

the film surface level next to the contact region. However, the experimental conditions can be adapted to mitigate those effects, e.g. by immersing the indendation region in a different medium. If PDMS is probed, oil or an aqueous solution containing tensides such as Triton X-100 can be used instead of 1xPBS. This way, adhesion effects could be mitigated in the PDMS system as demonstrated in section 2.3.3. Fifthly, the model is only valid in the range $0 \leq \chi \leq 1$, which is mathematically identical to the fact that the Herzian contact radius $\sqrt{R\delta}$ must not be larger than the layer thickness.

In general, it must be noted that the reconstruction requires a precise measurement of δ, which, in this work, was measured with an error of about 3 to 10 % depending on the condition. The layer thicknesses were measured with relative errors below 4 % and the errors of the sphere radii were below 1 %. The eccentricity of the spheres must not be too high to accurately determine the indentation force. Although the ensuing inconsistencies of the weight of the spheres could be mitigated by dedicated measurements, knowledge of the local sphere radius in the contact region is crucial to accurately determine the finite thickness correction factor $C(\chi)$ and is consequently crucial for the reconstruction of E and ν. Therefore, spheres with a high eccentricity and locally different curvature radii should not be used. Although a detailed analysis of this requirement was not done in this work, spheres with an eccentricity of typically below 0.14 were demonstrated to be suitable.

In this work, the resolution to measure those critical parameters was accomplished with high NA water immersion objectives. Different layers in the sample were identified by changing the focal plane. Importantly, if the refractive index of the film does not match the refractive index of the immersion medium between the objective and the sample, this mismatch has to be corrected when measuring axial distances (sec. 2.3.2). In order to measure the indentation depth, the film surfaces can be labeled with fluorescent markers to avoid any ambiguity (sec. 2.2.2 and 2.3.1). However, when the sphere is placed on top of the film, the indentation cap can only be imaged from the bottom and transmission microscopy is therefore not applicable. Thus, an inverted microscope is required, which is the only equipment necessary to employ the technique. It is highly beneficial if the microscope is motorized to automate the acquisition of the z-stack. The film thickness can, however, also be measured after the sphere is removed and after the film has relaxed to its undeformed state. In this work, images of the relaxed film surface were captured to verify that the films were reversibly deformed, i.e. they were only deformed within the elastic regime (sec. 2.2.2). In order to measure the film thickness, techniques such as DIC or brightfield microscopy can also be a viable option if the bottom of the film can not be labeled with fluorescent markers (sec. 2.3.1). However, both techniques to measure the thickness and the indentation depth presented in this work require the film to be optically transparent and homogeneous, as inhomogeneities would introduce aberrations when imaging through such thick samples. This would effectively render the imaging of the upper film surfaces impossible.

In summary, sufficiently small errors for δ, h, and R are required to resolve both E and ν. With the precision achieved in this work, the errors of E and ν were about about $s_{\mathrm{E}} \approx 10\,\%$ and $s_\nu \approx 0.01$ to 0.1 respectively, depending on the condition. Further accuracy improvements may be possible if three dimensional particle detection is used to detect the indentation cap. This approach would allow the analysis of the full indentation region[202,232], while the procedures used in this work only used the information from two cross sections (sec. 2.2.2). Similarly, the whole film could be labeled with a fluorescent dye and imaged with confocal microscopy to implement an automatic analysis routine[238].

Reconstruction accuracy was discussed in detail with measured and simulated indentation data in section 2.4 and it was demonstrated that, aside from the experimental limitations given by the setup, a careful choice of sphere radii and their density as well as the film thickness profile can be highly beneficial to increase the reconstruction precision. In particular, simulations indicated that

it is important to cover a wide range of indentation geometries in the range between $0.4 \leq \chi \leq 1$, which can either be achieved by an inhomogeneous film thickness or by placing differently-sized spheres on the film. As the indentation depth is generally given by the film's elastic properties and its thickness as well as the sphere radius and density, the choice of the spheres is limited by the film's elastic properties and the availability of high quality spheres with a particular radius or density can be an issue. In this case, an adaptation of the technique to a different setup can be a viable option. In particular, a setup in which a spherical indenter is attached to a translation stage and to a force sensor, either in the form of an atomic force microscope or in the form of a macroscopic device is promising. This way the contact geometry $\chi(\delta, R, h)$ could be varied at a fixed indentation radius and at a fixed film thickness and, theoretically, also allow the reconstruction of E and ν from a single, continuous indentation curve. Consequently, this would also speed up the data acquisition and the analysis.

3 Cell Rheology and Cell-Particle Contact Dynamics during Phagocytic Binding

In this chapter, a novel technique based on blinking holographic optical tweezers to investigate the rheology of macrophages during phagocytosis is presented. The first experimental part of the project described in section 3.3 was done in cooperation with Konrad Berghoff. In this part of the project, the rheology of the cells as well as the early binding kinetics between a phagocytic target particles and macrophages were measured. The experiments were carried out by Konrad Berghoff[216]. The experimental part is briefly summarized in this work for clarity. Further details of the experimental methods, especially about the holographic optical tweezers setup, were published by Konrad Berghoff[216]. This work focuses on the data analysis and the modeling of the cellular rheology as well as the resolution of the early contact dynamics between the particle and the cell. In contrast to the elastic systems, which were characterized in chapter 2, the rheology of cells is of a viscoelastic nature. Therefore, the theory was adapted to account for viscoelastic effects. Many of the methods and results presented in this section were published in the following research article:

'Using Blinking Optical Tweezers to Study Cell Rheology During Initial Cell-Particle Contact' (K. Berghoff, W. Gross, M. Eisentraut, and H. Kress, Biophysical Journal, 2021)[239]

In the second experimental part of this chapter, improved experiments are described, which allow prolonged measurements during phagocytic uptake. Those measurements allow the simultaneous visualization of the cytoskeleton as well as the measurement of the cellular rheology. For those measurements, a preliminary data analysis is presented.

If not stated otherwise, all mathematical symbols are redefined in this chapter.

3.1 Phagocytic Uptake Mechanics

As described in chapter 1, the uptake of extracellular objects is an inherently mechanical process. Firstly, depolymerization of the actin cortex below the cell membrane has been hypothesized to enable receptor diffusion in the membrane, which ultimately leads to receptor-opsonin binding and receptor clustering, initiating the uptake. Secondly, during cup formation, the actin cytoskeleton is also crucial as its polymerization drives the protrusion of the membrane. Finally, after cup closure, the decoupling of the phagosome from the cortex enables the subsequent transport to the nucleus and the transition from the phagosome to the phagolysosome, which goes along with it. Most of what is known today about the remodeling of the cytoskeleton during phagocytosis is qualitative and mechanical information is lacking. In this section, the current state of knowledge, i.e. current mechanical models of phagocytic cup formation are reviewed. Furthermore, multiple techniques to acquire mechanical data suitable to feed those models are presented.

3.1.1 Mechanical Modeling of the Phagocytic Cup

Until today, a unified model of cup formation is lacking and modeling is still in its infancy[240]. The phase which is probably best understood from a mechanical point of view is the formation of the phagocytic cup around a spherical target. The theoretical model which is most commonly applied is the zipper model[241–244], in which a thin protrusion zippers around the target. Mechanical contact is made via distinct adhesion sites. In 2016, Richards and Endres were able to extend the model for non-spherical targets[245]. They reproduced experimental results, demonstrating that slightly oblate sphereoids are internalized faster than spheres and that the internalization of highly elongated objects such as rods is far slower[246–248]. Additionally, an easier model system, in which cells are seeded on an opsonized substrate, has been used to simplify the geometry. Using such an approach, Francis et al. were recently able to theoretically verify that active protrusion occurs at the leading edge while purely adhesive, passive spreading was incompatible with the spreading dynamics observed in the experiments[244]. Comprehensive summaries about the current theoretical understanding of the cup formation were published by Richards and Endres[249] and Richards[240].

Although it is well established that for example target stiffness[70,71,74,250], shape[246,247,251,252], size[106,249,253], and opsonization[146,254,255] influence phagocytosis efficiency, it has not been possible to predict the uptake probability, dynamics and shape of the phagocytic cup in a unified manner, in part, because experimental data about the mechanical properties of the cells during phagocytosis is currently very limited and only very few techniques to measure the elastic properties are available[242,256,257]. Instead, most of the knowledge of the mechanics of phagosome formation is based on imaging techniques, localizing fluorescently labeled proteins to visualize the binding of IgG to FcγR[132], the signaling cascades[99,258–260], and the subsequent reorganization of actin[261–263], which ultimately drives the formation of the phagocytic cup.

3.1.2 Techniques to Measure the Mechanics of the Phagocytic Cup

In general, the number of suitable techniques to measure the elastic properties of the cortex during phagocytosis is limited and the techniques, which are available, have certain downsides. For example, Nelsen et al.[264] showed that the combination of an atomic force microscope together with a volumetric light sheet system can be used to measure cellular forces exerted on the target. An IgG-coated particle was glued to a cantilever and the particle was attached to the membrane of a macrophage. The forces exerted on the particle during uptake were measured by detecting the deformation of the cantilever. Those forces were then correlated with the polymerization of cortical actin, which was visualized in the fluorescence channel[264]. This technique could be adapted to also yield the elastic properties of the cortex during phagocytosis by deliberately pushing the particle into the cell. The approach is however rather tedious as all particles have to be laboriously glued to a cantilever. Furthermore, due to the cantilever, the cup closure, the decoupling from the membrane, and the subsequent transport to the nucleus can not be captured with an atomic force microscope.

A micropipette approach was used by Herant et al. to resolve the cellular mechanical properties during phagocytosis[256]. Neutropils were aspirated during phagocytosis to show that cortical tension did not rise during the early phase of cup formation and only during the later stages, cortical tension rose. Furthermore, they inferred that cortical tension rose more during neutrophil aspiration than during phagocytosis at similar surface area increases, suggesting that excess membrane is provided in response to phagocytic signaling[242,256,265]. The mechanical data provided by this micropipette approach, however, reflects the properties of the whole cell and is therefore only of limited use for modeling as actin polymerization occurs locally inside the cup.

The most direct approach taken so far to measure the cellular elastic properties during phago-

cytosis was presented by Irmscher et al., who measured cortical stiffness during phagocytic cup formation with magnetic twisting cytometry[257,266]. Tiny fluorescent tracer particles were attached to the surface of opsonized ferromagnetic target particles. A rotating magnetic field was generated to exert a torque on the particle and the rotations were detected by tracking the tracer particles on the surface of the opsonized target particle. The rotational stiffness increased during cup formation, dropped off steeply and stabilized at a lower level after cup formation[257]. However, the technique does not provide any control over the attachment process and is thus also rather tedious from an experimental point of view.

An indirect approach to quantify the role of cortical actin can be taken by adding the mycotoxin cytochalasin D (CytoD) before initiation of phagocytosis. CytoD is known to bind to the barbed or fast-growing end of actin filaments and thus, it inhibits the elongation of existing actin filaments[267,268]. As a consequence, the cortex of treated cells is softer[269]. An ensemble of opsonized particles is typically sedimented on ice to reduce phagocytic activity. After sedimentation, the samples are heated up to 37 °C and the cells are allowed to engulf the particles for a defined amount of time. The sample is then fixed and the number of internalized particles can, for example, be quantified with confocal or electron microscopy. In studies using this technique, it is commonly found that the inhibition of actin polymerization with CytoD impedes uptake efficiency[216,270,271]. However, because the uptake process itself is typically not visualized, the specific uptake pathways may also be unclear. Furthermore, even with the assumption that only phagocytosis occurs and that all other endocytic uptake pathways are inactive, the precise mechanism why phagocytosis is impeded is difficult or even impossible to identify with fixed samples. Even though it is likely that cup formation is impeded under the influence of CytoD, counteracting effects such as an increased receptor mobility due to the depolymerized cortical actin structure may also be at play.

3.1.3 Using Holographic Optical Tweezers to Study the Mechanics of Phagocytosis

The lack of data is thus also reflected by a lack of techniques suitable to resolve the cellular rheology during phagocytosis. In this chapter, a new technique is presented which is designed to overcome these limitations. The technique is based on optical tweezers. In general, optical tweezers consist of a focused infrared laser beam, which acts as trap for dielectric particles. Optical tweezers were originally invented by Arthur Ashkin[272] and revolutionized the field of biophysics as forces of a few pN can be exerted on micrometer-sized particles. The particle position can be simultaneously measured with nanometer accuracy[273]. To steer the trap or even generate multiple traps, a diffractive optical element can be introduced into the beam path[274–276]. Those traps are called holographic optical traps[277].

In the experiments described in this chapter, holographic optical tweezers were used to resolve the viscoelastic properties of the cells by exerting variable optical forces on the target. Holographic optical traps can be used to precisely position the target in the sample, and thus precise control over the attachment process is possible. As optical forces can be exerted on the particle without any mechanical contact to the particle, the whole phagocytic process from the initial binding phase to the transport to the nucleus can be captured. The technique does not rely on any fluorescent markers glued to the target particle, which greatly simplifies data analysis and image processing. Instead, fluorescence microscopy can be used to visualize proteins and in particular actin to visualize the formation of the phagocytic cup. This is crucial as the visualization of the phagocytic cup is difficult with transmission microscopy alone. Typical phagocytic model systems rely on polystyrene particles as targets, which have a refractive index of $n = 1.6$[278]. In such a system, thin phagocytic cups are even difficult to visualize with contrast-enhancing microscopy techniques such as differential interference contrast microscopy as the refractive index

of the particles is typically a lot higher than that of the cells and than that of the medium. Thus, the contrast generated by the cell is relatively small compared to the contrast generated by the particles and cup formation is not resolvable.

In the next section 3.2, the concept of optical tweezers is briefly introduced. In section 3.3, the setup and the blinking trap experiments performed by Konrad Berghoff are briefly described, with which the early contact mechanics were accessible. These experiments were built upon to prolong the measurements until cup formation. In section 3.4, the corresponding methods and early mechanical data acquired during the cup formation are presented. In the final section 3.5 of this chapter, the findings of both experimental parts are summarized to review the possibilities of the technique.

3.2 Optical Tweezers

Optical forces can be exerted on a dielectric particle as momentum is transferred from photons to the particle. In the following, only the case that the refractive index of the particle is higher than that of the surrounding medium is discussed. In this case, in a highly focused laser beam, these forces are oriented such that the particle is generally trapped slightly behind the focus[279]. Conceptually, these forces can be split into two components. The scattering force is oriented in the direction of light propagation. When photons hit the particle, they are scattered in all directions and, in case the imaginary part of the dielectric constant is larger than 0, some photons are absorbed. Thus, momentum is transferred from the photons to the particle and if the particle and the beam are collimated and symmetric, the corresponding forces cancel out in all directions except along the optical axis. In everyday light conditions, the scattering force is dominant. The scattering force is for example used for spacecraft propulsion by solar sails. To hold a particle in position, a counteracting force is necessary. This so-called gradient force arises in a focused laser beam, when light is refracted at the interface between the particle and the surrounding medium[273].

There are two edge cases, in which a simple theory to describe the optical forces exists. When the particle radius R is a lot smaller than the laser wavelength λ, i.e. $R \ll \lambda$, Raleigh scattering theory is applicable. In this case, the scattering force F_{scat} is[273,280]

$$F_{\mathrm{scatt}} = \frac{I_0 \sigma n_{\mathrm{m}}}{c}, \tag{3.1}$$

where I_0 is the laser light intensity, n_{m} is the refractive index of the medium and c is the speed of light. The scattering cross section σ is given by[273,280]

$$\sigma = \frac{128\pi^5 R^6}{3\lambda^4} \left(\frac{m^2 - 1}{m^2 + 2} \right)^2 . \tag{3.2}$$

Here, $m = n_{\mathrm{p}}/n_{\mathrm{m}}$ is the relation between the refractive index of the medium n_{m} and that of the particle n_{p}. The scattering force is oriented such that it points along the propagation direction of the incident light and it is proportional to the intensity of the incident light. The gradient force F_{grad} arises as the dielectric particle is polarized in the inhomogeneous field and it is given by[273,280]

$$F_{\mathrm{grad}} = \frac{2\pi\alpha}{c n_{\mathrm{m}}^2} \nabla I_0. \tag{3.3}$$

Here, the polarizability α is

$$\alpha = n_{\mathrm{m}}^2 R^3 \left(\frac{m^2 - 1}{m^2 + 2} \right). \tag{3.4}$$

The gradient force is thus proportional to the intensity gradient. Therefore, in order to generate a stiff optical force in a microscopic sample, an objective with a high numerical aperture has to be used.

In case $R \gg \lambda$, the optical force can be derived from ray optics. This case is illustrated in analogy to Nieminen et al. in figure 3.1[281]. For illustration purposes, two isolated rays of a Gaussian beam are illustrated. Their respective gradient forces F_1 and F_2 are illustrated in figure 3.1. In case the bead is positioned in front of the focus, the ray are diffracted such that the beam is less collimated after the particle (fig. 3.1A). Thus, forward momentum was transferred to the particle and the gradient force is oriented in the direction of propagation. In case the bead is positioned after the focus, the beam is collimated by the particle and the photons gain forward momentum (fig. 3.1B). Thus, the gradient force is oriented such that the particle is pushed rearwards into the focus by the gradient force. In case the particle is positioned to the left of the beam center (fig. 3.1C), ray number 2 is more intense. Beam number 2 is deflected to the left and thus, the particle is pushed to the right towards the focus by the gradient force. The opposite is true when the particle is deflected to the right (fig. 3.1D). In this case, the gradient force is oriented to the left and the particle is again pushed towards the focus. In summary, in all four cases, the gradient force is oriented such that it points towards the focus. Additionally, the scattering force acts on the particle and it is oriented in the direction of beam propagation. Thus, the equilibrium position of the trap is located slightly above the focus with the geometry illustrated in figure 3.1.

Whenever the wavelength and the particle radius are approximately equal, neither of those approaches is valid[273]. Instead, a more complicated electromagnetic examination of the problem is needed. In this case, the linear trap stiffness $k = \mathrm{d}F_{\mathrm{opt}}/\mathrm{dx}$, i.e. the spatial derivative of the optical force F_{opt}, depends on the particle radius and on the refractive index of the medium and that of the particle in a highly nonlinear manner[273,281–284]. The practical approach in this case is to measure the optical forces experimentally. The most common technique to measure the force profile, i.e. the optical force as a function of the distance from the equilibrium position. The particle is deflected and the relaxation velocity is measured. In equilibrium, Stokes drag is equal to the optical force. Thus, the instantaneous particle velocity can be used to quantify the optical forces[273,285,286].

Since their invention by Ashkin in the 1970s[272], optical tweezers have been shown to be a versatile tool for micromanipulation and to study micromechanics. Forces on the order of pN to nN can be generated with optical traps. Optical tweezers are a valuable tool to study single molecule mechanics. For example, the mechanics of the unfolding of DNA[287,288] or proteins[289] has been studied with optical forces by attaching the probed molecules to trapped particles. Optical tweezers have also proven useful to unravel the step sizes and stall forces of motor proteins such as myosin[290], kinesin[291] or dynein[292], which are typically on the order of nanometers and piconewtons, depending on the precise motor type.

Furthermore, optical tweezers have also been used to study the mechanics and the behavior of whole cells. For example, optical tweezers were used to measure the forces the flagellated parasite *Leishmania amazonensis* can generate during chemotaxis[293]. Similarly, trapped particles can be loaded with chemicals to stimulate chemotaxis[294] and thermal heating of the particle can be used to stimulate thermotaxis in neutrophils[295]. Furthermore, Suresh et al. attached two particles to red blood cells infected with the malaria parasite *Plasmodium falciparum* to resolve stiffness changes upon infection[296] and Balland et al. quantified the viscoelastic properties of myoblasts and epithelial cells using optical tweezers[297].

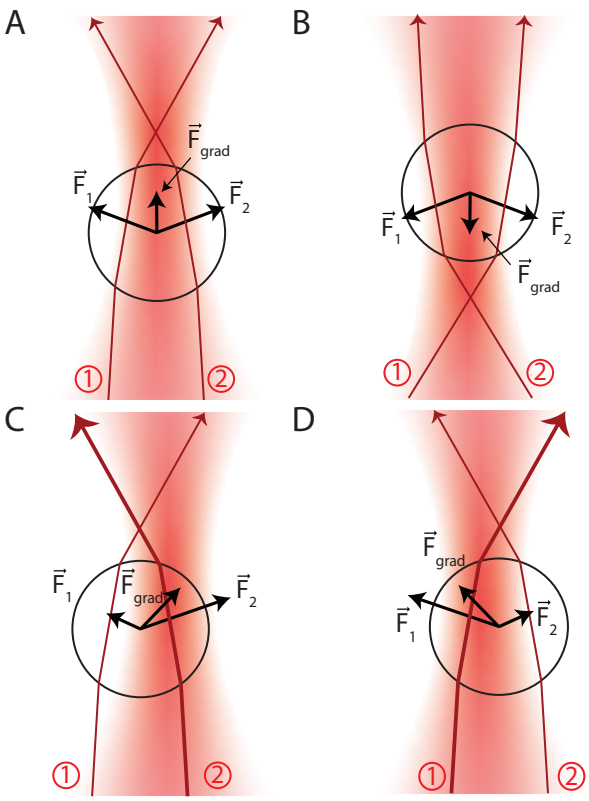

Figure 3.1: The principle of optical trapping. When $R \gg \lambda$, ray optics can be used to derive the optical forces on the particle. The particle is always pulled towards the focus, no matter whether it is positioned (A) before, (B) after, (C) to the left, or (D) to the right of the focus. A description of this figure is provided in the main text in section 3.2.

3.3 Blinking Trap Experiments During the Early Phagocytic Binding

In this section, a technique to measure the viscoelastic properties of macrophages during early phagocytic binding is presented. The technique is based on blinking holographic optical traps and it is designed to resolve cortical stiffness changes and cell-target binding kinetics during early phagocytic binding. As a model system, IgG-coated particles were trapped and attached to murine J774 macrophages (fig. 3.2A). This model system is one of the most-studied systems for FcγR-mediated phagocytosis[141,298–304]. As the cells were stronger than the trap, the particles were pulled out of the trap center position after attachment by a distance $\vec{\rho}$, exerting an optical force F_{HOT} on the particle when the laser was turned on (fig. 3.2B). The viscoelastic step response of the particle was measured by continuously turning the trap on and off to generate a blinking optical trap (fig. 3.2B, C). The particle position was imaged with a high speed camera and the trajectory was analyzed to obtain the elastic properties of the macrophages during the process. Typically, the particles were fully pulled out of the optical trap after 1 to 3 min (fig. 3.2D). As phagocytic cup formation itself typically started minutes after the binding process, the rheological data obtained by this method is limited to the early binding phase. In some experiments, the

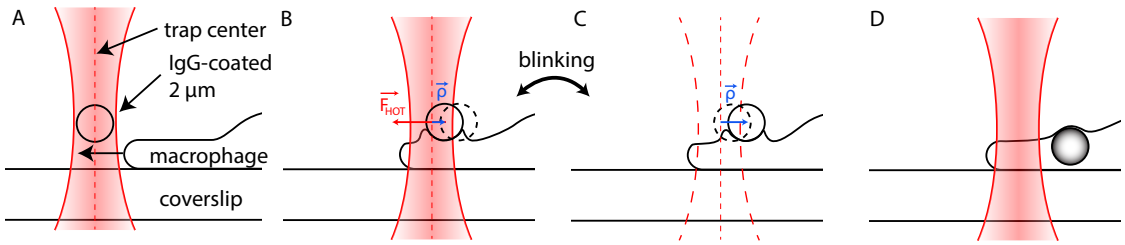

Figure 3.2: Sketch of the blinking trap experiments to investigate the early binding dynamics. (A) An optical trap was used to attach an IgG-coated polystyrene particle to the cell membrane to initiate cell-particle contact. (B, C) Cellular forces mediated by cell-particle adhesion pulled the particle away from the equilibrium position of the optical trap. The distance from the trap center position is given by $\rho(t)$ (blue). The trap at the particle's position is turned on and off, modulating the optical force F_{HOT} (red) exerted on the particle. (D) The particles were typically pulled out of the optical trap after 1 to 3 minutes. Figure adapted from Berghoff et al., Biophysical Journal, 2021[239].

fungal toxin cytochalasin D (CytoD) was used to disturb the cytoskeleton in order to verify that the technique is suitable to resolve the cortical mechanics. In the following sections 3.3.1.1 to 3.3.1.6, the experimental methods are briefly described. In sections 3.3.1.7 to 3.3.1.9, the data analysis implemented in this work is presented. The results, i.e. the resolved time dependence of the contact radius between the cell and the particle as well as the viscoelastic properties of the macrophages are presented in section 3.3.2 and discussed in section 3.3.3.

3.3.1 Methods

3.3.1.1 Cell Culture

The blinking holographic optical tweezers experiments were carried out with the murine macrophage cell line J774 (generous gift from Maximiliano Gutierrez, The Francis Crick Institute, London, Great Britain and purchased from DSMZ, Braunschweig, Germany). To visualize the cortex of the macrophages at different concentrations of cytoD, Lifeact-GFP[305] transfected J774 macrophages (generous gift from Alexander Rohrbach and Rebecca Michiels, Freiburg, Germany) were used. The cells were cultured in Dulbecco's modified Eagle's Medium (Gibco, Carlsbad, California, USA) supplemented with 4 mmol/l Glucose (Gibco), 10 % fetal calf serum (FCS, Biochrom, Berlin, Germany), 5 % penicillin-streptomycin (10×10^3 units/ml penicillin, 10×10^3 µg/ml streptomycin; Gibco), and 5 % glutamine (Thermo Fisher Scientific, Braunschweig, Germany). The cells were cultured under standard cell culture conditions (37 °C, 5 %, CO_2 atmosphere, ≈ 93 % relative air humidity) in T-25 cell culture flasks (Corning, Corning, New-York, USA) and passaged three times a week. For passaging, the old medium was removed, the cells were scraped off of the bottom flask surfaces and the cells were resuspended in fresh medium. For cell experiments, cells suspended in fresh medium were seeded on coverslips (e.g. # 1, diameter 16 mm, Menzel Gläser, Braunschweig, Germany) and cultured under standard cell culture conditions for 24-48 h before the experiments. The cells were tested against mycoplasm infection regularly.

3.3.1.2 Microparticles and Microparticle Functionalization

White carboxylated polystyrene particles with a diameter of 2 µm (refractive index $n = 1.6$[278], micromer COOH, micromod, Rostock, Germany) were used as phagocytic targets. 200 µl of stock

particle dispersion was coated with murine primary IgG antibodies (Merck Millipore, Darmstadt, Germany) according to a passive adsorption protocol established by Steve Keller who published a detailed version of the functionalization protocol[154]. Briefly, the stock particle dispersion was washed three times in 2-(N-morpholino)ethanesulfonic acid (25 mM, pH 6, Sigma-Aldrich, Saint-Louis, Missouri, USA) by centrifugation (2000 g, room temperature). After the last washing step, the particles were suspended in 1 ml of MES.

IgG was thawed on ice and enough IgG was added to the particle dispersion to achieve a maximum of 200 % surface opsonization with IgG, taking the stock particle concentration into account. For every particle batch, the precise precise amount of IgG was calculated assuming that the molecular mass of IgG is 150×10^3 u[306] and that the geometrical radius of IgG is equal to its hydrodynamic radius of 6.4 nm[307]. The particles were incubated in the IgG solution for 24 h under gentle agitation at room temperature and subsequently washed three times in Dulbecco's phosphate-buffered saline (DPBS, Gibco). The coated particles were stored in a storage buffer (0.1 mol/l PBS, 0.1 % glycine, pH 7.2, Lonza, Basel) at 4 °C for up to a few months. The IgG coating was validated with secondary antibody staining[216].

3.3.1.3 Live Cell Imaging

Holographic optical trapping experiments were carried out with the inverted, motorized microscope Nikon Eclipse Ti-E, which was also used in the experiments described in chapter 2 (see sec. 2.2.2). The most important optical parts of the microscope used for imaging during the blinking experiments are summarized in figure 3.3. For all experiments described in this section, the 60x water immersion objective (CFI Plan Apo IR 60xWI, NA = 1.27, Nikon) was used. The sample was placed on the motorized microscopy stage, which was controlled by the microscope's internal controller. The incubation chamber enclosing the main parts of the microscope was heated to (37.0 ± 0.2) °C before all live cell experiments. The microscope was equipped with a bright field illumination lamp used for transmission microscopy (gray beam path). Bright field transmission microscopy was used to measure the position of the target particle with a high speed camera (IDT Nx4-S2, Imaging Solutions, Eningen unter Achalm, Germany).

Differential interference contrast microscopy images were acquired simultaneously to monitor cell morphology and behavior. Therefore, two Wollaston prisms and a DIC polarizer were inserted into the beam path (gray beam path in fig. 3.3). DIC images were acquired with the Andor LucaR or the Andor iXon Ultra 897 camera. To achieve the DIC effect only on the Andor cameras, the DIC analyzer was positioned in the dual camera port directly before the Andor cameras. The generation of the holographic optical traps is described in section 3.3.1.4. Further details about the configuration of the hardware during the experiments are described in section 3.3.1.6, where the precise implementation of the blinking experiments is presented.

3.3.1.4 Holographic Optical Trapping

The laser beam path to generate the holographic optical traps was described in great detail by Adal Sabri[308], Konrad Berghoff[216] and Steve Keller[154]. The main aspects of the setup are briefly revisited in this section. Holographic optical traps were generated with an ytterbium fiber laser (IPG YLM-5-LP-SC; continuous wave; IPG Laser, Burbach, Germany) with a central wavelength of $\lambda = 1064$ nm (red beam path in fig. 3.3). This wavelength is commonly chosen for optical tweezers as cells are nearly transparent in the near-infrared wavelength regime, and thus, only little photodamage is induced[216,309]. The laser was operated at a constant output power of 3 W in all experiments[216]. The polarized laser beam was run through a Faraday insulator in order to protect the laser from back reflections, a waveplate to adjust the polarization and a beam

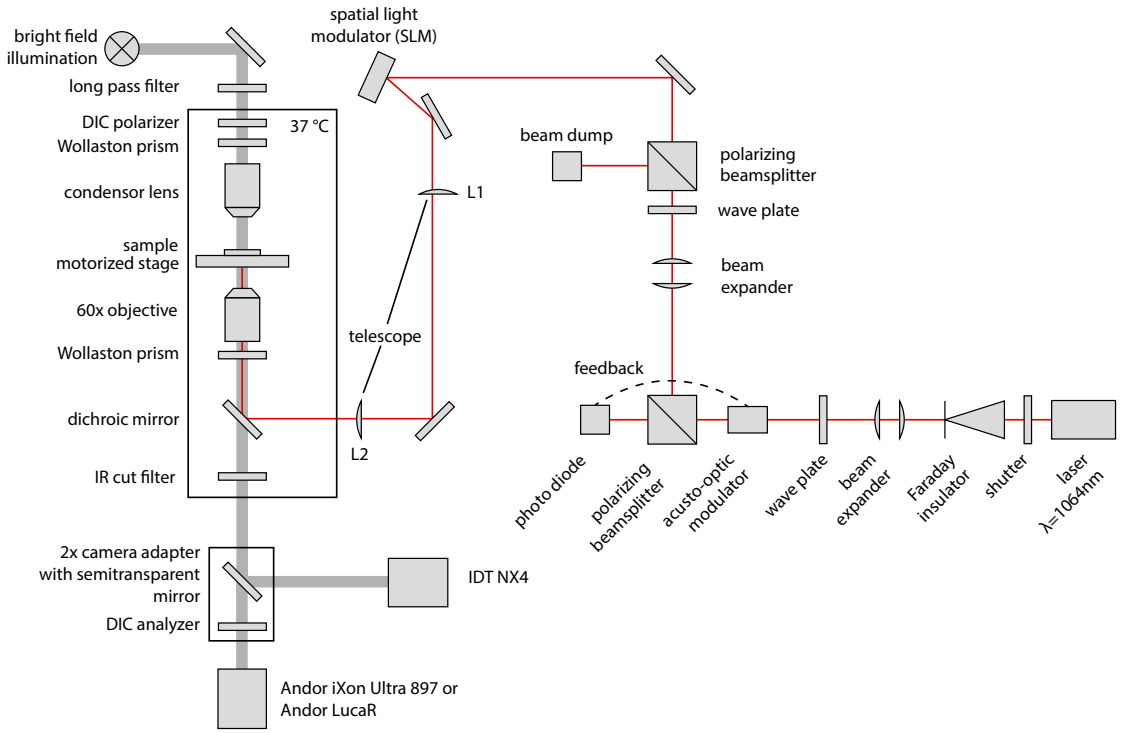

Figure 3.3: Optical Setup used for the Blinking Experiments. The Nikon Eclipse Ti-E microscope was equipped with a bright field illumination lamp used for transmission and DIC microscopy (gray beam path). The holographic optical trap was generated with an infrared laser beam with a wavelength of 1064 nm (red). An IR cut filter was used to block laser light reflected in the sample from reaching the camera sensors. A detailed description of the imaging setup is provided in the main text in section 3.3.1.3 and the laser beam path used to generate the optical traps is described in section 3.3.1.4.

expander to adjust the beam diameter. The laser power in the sample plane was stabilized with a feedback loop (NoiseEater, TEM Messtechnik, Hannover), in which the laser power was measured with a photo diode and adjusted to a constant level with an acousto-optic modulator. Laser power stability was validated by K. Berghoff[216]. The collimated beam was run through a beam expander, which was adjusted to fully illuminate the display of the SLM. The laser power in the back focal plane of the objective was controlled with a second wave plate and a polarizing beam splitter.

The holographic optical traps were generated with an SLM (NS XY Phase Series, P512-1064; 512 px × 512 px, display size 7.68 mm × 7.68 mm Meadowlark Optics, Colorado, USA). The SLM was used to spatially modulate the phase of the incident, collimated laser beam in the range $0 \leq \Delta\phi \leq 2\pi$. An SLM is essentially a spatially resolved wave plate, in which the index of refraction of the slow extraordinary axis can be electronically controlled for every pixel. This is achieved with nematic liquid crystals inside the display, which are reoriented as voltage is applied to the pixels by the SLM controller[216]. As only the extraordinary optical axis of the SLM can be controlled, the polarized beam splitter in front of the SLM was oriented such that the beam was polarized along the extraordinary axis of the SLM. On the driver level, the voltage to orient the nematic liquid crystals was adjusted upon the transfer of a 16 bit 512x512px image, the so-called

phase mask, to the SLM controller containing the phase information for every pixel.

The SLM plane was then projected into the back focal plane of the objective with a telescope consisting of two lenses L1 and L2 in 4-f configuration. In this configuration, a phase modulation in the SLM plane results in an amplitude modulation in the corresponding Fourier plane, which was the sample plane in this lens configuration[216]. This relationship can be used to generate and steer multiple optical traps in the sample plane by changing the phase pattern on the SLM. The beam path was aligned such that a single trap was generated in the center of the sample plane (0^{th} order) after a homogeneous gray image (i.e. no spatial phase modulation) had been transferred to the SLM. The amplitude in the sample plane can be modulated by transferring an inhomogeneous phase mask to the SLM. In this work, this method was used to modulate the power directed to an optical trap offset from the 0^{th} order. In general, a single trap can be generated at a distance d from the 0^{th} order when a blazed grating is displayed on the SLM. An example of such a grating is shown in section 3.3.1.6. With the setup shown in figure 3.3, d is given by[216,308]

$$d = f_{\text{MO}} \frac{f_1}{f_2} \cdot \tan\left(\arcsin\left(\frac{\lambda}{2\Lambda}\right)\right). \tag{3.5}$$

Here, f_{MO} is the focal length of the microscope objective, f_1 and f_2 are the focal lengths of the lenses L1 and L2, λ is the wavelength of the laser beam, and Λ is the periodicity of the blazed grating displayed on the SLM. In the following, this trap is referred to as the 1^{st} order. The corresponding phase mask was generated with the *Gratings and Lenses* algorithm[216,310,311]. As f_{MO} is not provided by Nikon, the effective focal length $f_{\text{MO}} f_1/f_2$ was calibrated to be $(4506 \pm 8)\,\mu\text{m}$. Details on the calibration and the derivation of equation 3.5 were provided by A. Sabri[308] and K. Berghoff[216].

3.3.1.5 Trap Calibration in Glycerol

In the cell experiments, the 1^{st} order trap was used for micromanipulation. In general, the stiffness of this trap for a given particle was fully defined by the total laser power reflected from the SLM (which was proportional to the laser power in the sample plane), the trap geometry, i.e. the phase image displayed on the SLM, the objective, and the refractive index of the medium. Therefore, to reproduce a certain trap stiffness, the laser power reflected from the SLM was measured with a power meter (PM100D; Thorlabs, Newton, New Jersey, United States) equipped with a thermal power sensor head (S310C; Thorlabs) at the start of each measurement session. The trap geometry was reproduced by setting the same phase mask on the SLM display in all experiments and the same particle type was used in all experiments (2 µm; refractive index $n = 1.6$; Micromer COOH, Micromod). This combination of parameters is subsequently referred to as a *trap configuration*. Not all of the laser power reflected by the SLM was directed to a single optical trap in the sample plane for several reasons. Firstly, the transmission of the 60x objective was about 70 % in the infrared regime[216]. Secondly, the resolution and size of the SLM display were finite and thus, not the full intensity of the beam can be directed to the 1^{st}-order. Thirdly, the lenses and gratings algorithm used to generate the optical traps assumed a homogeneous illumination of the SLM display. However, the illumination in the experiment was slightly inhomogeneous due to the Gaussian profile of the incident beam[216]. Finally, the beam diameter was adjusted by the telescope (lenses F1 and F2 in fig. 3.3) such that the beam was slightly wider than the objective's entrance pupil to optimize the trapping efficiency[273,312,313]. Therefore, the stiffness of any optical trap generated in the sample plane had to be calibrated and could not be derived from scattering theory. As the cells pulled the particles completely out of the trap during the experiments, a technique to calibrate the full force profile $F_{\text{opt}}(x, y)$ was required.

A suitable technique to measure the full force profile is the drag force method[273,285,286], which was used to calibrate the optical trap. The particles were immersed in an aqueous glycerol (Grüssing, Filsum, Germany) dispersion with a concentration of 73.6 % v/v. Glycerol was used in this project to slow down the relaxation process into the optical trap. As the refractive index of pure glycerol is about 1.5[213] and as such, different from the refractive index of the immersion medium, the optical trapping forces determined here are only a coarse approximation for the trapping forces exerted on the particles during the cell experiments. A detailed discussion about the implications of this issue for the cell experiments is provided in section 3.3.3. A technique to calibrate the optical trap in water is provided in section 3.4.1.4.

The force measurements were carried out at 37 °C. At this temperature the viscosity of the glycerol solution η is 19.3 mPas[314]. A particle was trapped in the 1st order trap 3 µm above the coverslip and the trap was turned off. Then, the microscope stage was moved laterally by 2.5 µm in the $+x$ and $-x$ directions. The trap was turned on again and the relaxation of the particle towards the trap center position was recorded with the IDT NX4-S2 high speed camera at a frame rate of 1 kHz. The particle trajectory was tracked with a custom-written MATLAB (MATLAB R2018a; The MathWorks, Natick, MA, USA) algorithm based on the fast template matching algorithm published by Lewis in 1995[315]. The tracking algorithm compares a small, manually chosen reference image of the particle in the first frame I_{ref} with all subsequent images I_{vid} by calculating the normalized 2D cross correlation image[316] CC of I_{ref} and I_{vid} (fig. 3.4). The cross correlation image peaks at the position where I_{vid} is most similar to I_{ref}. This peak was detected with a custom peak detection routine published by Style et al.[51] and fitted with a 2D Gaussian function of the form

$$f(x,y) = A \exp\left(\left(\frac{x-\mu_{\mathrm{x}}}{\sigma}\right)^2 + \left(\frac{y-\mu_{\mathrm{y}}}{\sigma}\right)^2\right) + B. \tag{3.6}$$

Here, A is the local amplitude of the cross correlation function, B is the offset and σ is the width of the peak, indicating the precision of the detection. The fitted peak positions $(\mu_{\mathrm{x}}, \mu_{\mathrm{y}})$ of the cross correlation function were used as the new particle position. The tracking algorithm achieved a localization accuracy of a few nanometers relative to the first frame in the video, depending on the input data[153,216].

In case of low Reynolds numbers, inertia can be neglected when the particle density is similar to the density of water, which was the case during the experiments[317,318]. The optical force during the relaxation was therefore only balanced by hydrodynamic drag at any point in time[285,286]. The measurements were carried out at a small distance $h = 3\,\mu\mathrm{m}$ above the coverslip relative to the particle radius $R = 1\,\mu\mathrm{m}$. In this case, the hydrodynamic force and also the optical force on the particle is given by[273,319–321]

$$F_{\mathrm{opt}} = 6\pi\eta\gamma R v, \tag{3.7}$$

where v is the instantaneous particle velocity and η is the viscosity of the glycerol solution. The dimensionless parameter γ corrects for the increased drag due to the influence of the nearby coverslip[319,320]:

$$\gamma = \left[1 - \frac{9}{16}\frac{r}{h} + \frac{1}{8}\left(\frac{r}{h}\right)^3 - \frac{45}{256}\left(\frac{r}{h}\right)^4 - \frac{1}{16}\left(\frac{r}{h}\right)^5\right]^{-1}. \tag{3.8}$$

The trap coordinate system was chosen such that the point $(x, y) = (0, 0)$ was equal to the trap's equilibrium position, which was equal to the averaged particle position after relaxation. The force profiles of three different trap configurations along the x-axis are shown in figure 3.5. The measurements were repeated by deflecting the particle in the $+y$ and $-y$ direction.

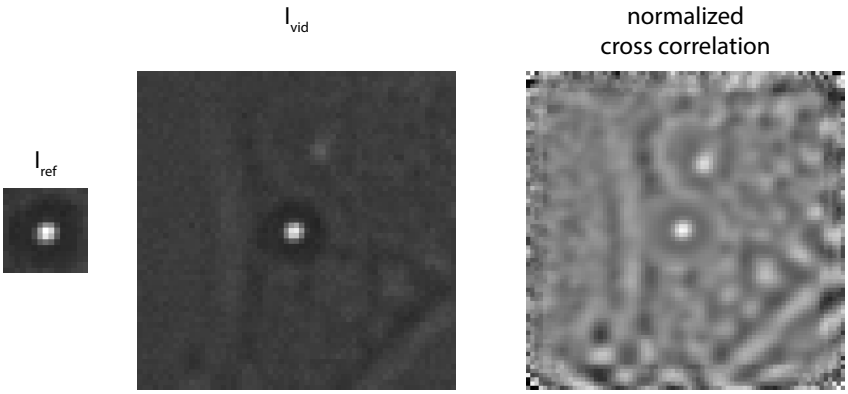

Figure 3.4: Principle of the cross correlation tracking algorithm. The reference image I_{ref} is compared to every subsequent image in the video I_{vid} by calculating the normalized 2D cross correlation function. The cross correlation function peaks at the position where I_{vid} and I_{ref} are most similar.

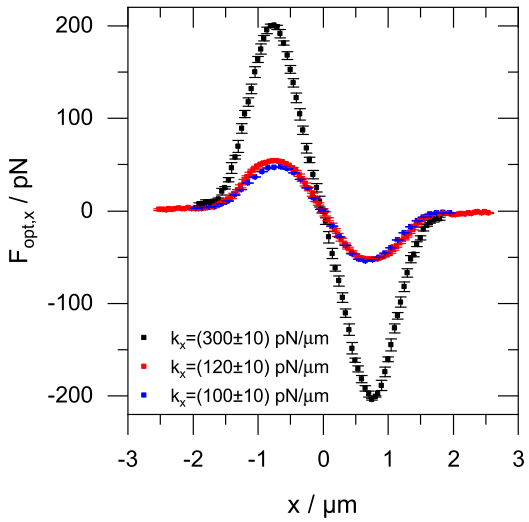

Figure 3.5: Results of the trap calibration with the drag force method along the x-axis. 2 µm-sized polystyrene particles were dispersed in an aqueous glycerol solution with a concentration of 73.5 % v/v and trapped in the 1$^{\mathrm{st}}$ order optical trap. The relaxation into the trap was recorded at a frame rate of 1000 Hz and tracked with the cross correlation tracker. Linear functions were fitted to the linear regime near the trap center to determine the trap stiffnesses in three different trap configurations: $k_{\mathrm{x}} = \mathrm{d}F_{\mathrm{opt,x}}/\mathrm{dx} = (300 \pm 10)\,\mathrm{pN/\mu m}$, $(120 \pm 10)\,\mathrm{pN/\mu m}$, and $(100 \pm 10)\,\mathrm{pN/\mu m}$. Error bars denote the standard deviation of the measured forces in intervals of $\Delta x = 50\,\mathrm{nm}$. Figure adapted from Berghoff et al., Biophysical Journal, 2021[239].

3.3.1.6 Blinking Trap Experiments

Directly before the blinking trap experiments, the coverslips together with the adherent cells were washed in DPBS, glued to aluminium holders with vacuum grease (Karasilon paste; Kurt Obermeier, Bad Berleburg, Germany) and immersed in minimal essential medium (Gibco) supplemented with 5 % HEPES (Gibco) as a pH buffer[322] together with 1 % penicillin-streptomycin (Gibco). Furthermore, IgG-coated particles with a diameter of 2 µm (sec. 3.3.1.2) were added at a concentration of typically 5×10^7 /ml. The aluminium holder was sealed with a second coverslip to prevent evaporation during the experiments and to avoid optical distortions, which would arise due to the surface curvature of the medium. The sample was placed on the stage of the Eclipse Ti-E microscope (sec. 3.3.1.3 and fig. 3.3). In some experiments, CytoD (Sigma Aldrich Chemie, München, Germany) was added to the imaging medium to inhibit the polymerization of filamentous actin. The cells were incubated at concentrations of $c_{\mathrm{CytoD}} = 1\,\mu\mathrm{M}$ and $c_{\mathrm{CytoD}} = 5\,\mu\mathrm{M}$ for at least 15 minutes before the experiments.

The blinking experiments were carried out as illustrated in figure 3.2. An IgG-coated polystyrene particle was trapped in one of the 1$^{\mathrm{st}}$ order traps calibrated in section 3.3.1.5, which was located a few micrometers away from the 0$^{\mathrm{th}}$ order. The phase mask displayed on the SLM in the Fourier plane used to generate to such a 1$^{\mathrm{st}}$ order trap is shown in figure 3.6A. Then, the camera fans and the incubation chamber fan were turned off to minimize vibrations.

Two time series of the binding process were captured simultaneously. The particle position was recorded with bright field microscopy with the Nx4-S2 camera capturing images at a high frame rate of 500 Hz or 1000 Hz. The high speed data was used to measure the viscoelastic properties of the cells. A frame rate of 500 Hz was found to be sufficient to resolve the particle dynamics upon force modulation. In order to monitor the cell shape and viability, DIC images were acquired with the Andor LucaR or Andor iXon Ultra 897 cameras with a far lower frame rate of 1 to 10 Hz, which was fast enough to capture the dynamics of the cell.

Then, the particle was carefully attached to the cell (fig. 3.6B). The step response of the cell was measured after the inital binding as follows. The supply voltage of the SLM display was turned off to disable the phase modulation in the Fourier plane (fig. 3.6C). In this configuration, the 1$^{\mathrm{st}}$ order trap was turned off and the laser intensity was directed to the 0$^{\mathrm{th}}$ order (fig. 3.6D). As the 1$^{\mathrm{st}}$ order trap was switched off, the particle relaxed away the trap center. This relaxation was, however, not necessarily directed towards the nucleus as the particles fluctuated randomly inside the trap (fig. 3.7). 2 s later, the 1$^{\mathrm{st}}$ order trap was turned on again by reenabling the supply voltage of the SLM display (fig. 3.6A,B). The particle was subsequently pulled towards the trap center again. This blinking process was repeated until the cell had ultimately pulled the particle out of the trap. Thus, the blinking frequency was 0.25 Hz and the optical force F_{HOT} exerted on the particle was also modulated with a frequency of 0.25 Hz.

A montage of DIC images captured during a blinking experiment is shown in figure 3.7. Eventually, the particles were pulled out of the optical trap by the cell. There was, however, a big variance between measurements. While some particles left the optical trap after 1 min, other particles were far slower and stayed inside the trap for multiple minutes. The typical time scale was about 3 min for untreated cells.

The particle positions were tracked in the high speed images as described in section 3.3.1.5. When the particles were not bound to the membrane and diffusing in the optical trap, the particles appeared in all four quadrants defined by the x and y axes of the coordinate system within short time intervals. After particle binding, these fluctuations quickly reduced and the particles were dragged away from the trap center position. Hence, the attachment time was defined as the time at which the particle had not appeared in all four quadrants for eight consecutive seconds for the first time. The precision of the attachment time point can therefore be roughly estimated to be

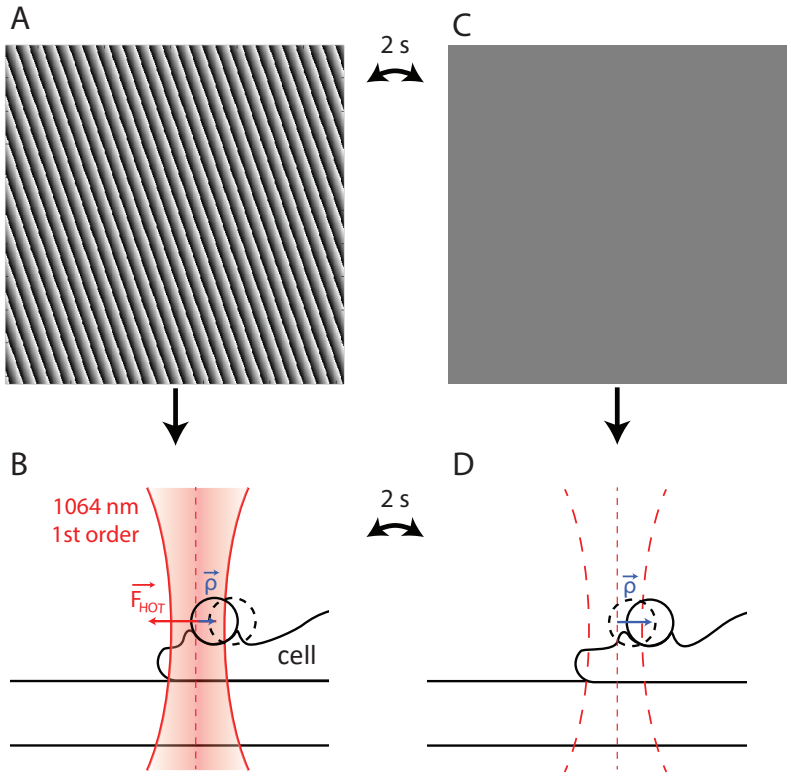

Figure 3.6: Implementation of the blinking experiments. (A) The phase mask displayed on the SLM in the Fourier plane used to generate the 1st order optical trap. Black regions indicate areas with no phase modulation and white regions indicate areas with a phase modulation of almost 2π. Gray values indicate phases in between 0 and 2π (linear scaling)[308]. (B) The corresponding trap was used to exert optical forces F_{HOT} on the particle attached to the macrophage. (C) To apply the blinking, the 1st order trap was switched off by disabling the supply voltage of the SLM display. (D) In the sample plane, the laser intensity was directed to the 0^{th} order trap and no optical force was exerted on the particle. The particle relaxed away from the trap center position. 2 s after the trap had been switched off, the 1st order trap was switched on again (A,B) and the particle relaxed towards the trap center position. Again, 2 s later, the trap was switched off (panels C and D). This blinking process was repeated to modulate the optical forces with a frequency of 0.25 Hz. The optical force exerted by the holographic optical trap as a function of time during this process is given by equation 3.19. Panels B and D adapted from Berghoff et al., Biophysical Journal, 2021[239].

8 s. Without exception, the time t is given relative to this attachment time in the rest of this chapter. The average particle position before attachment was defined as the equilibrium position of the optical trap $(x, y) = (0, 0)$. The radial distance ρ from the trap center is given by

$$\rho\,(t) = \sqrt{x\,(t)^2 + y\,(t)^2}. \tag{3.9}$$

A typical particle trajectory $\rho(t)$ is shown in figure 3.8. Generally, $\rho\,(t)$ increased during the measurement on a time scale of about a minute, as the particle was gradually pulled out of the optical trap (fig. 3.7). In the trajectory, the modulation due to the blinking trap is clearly visible.

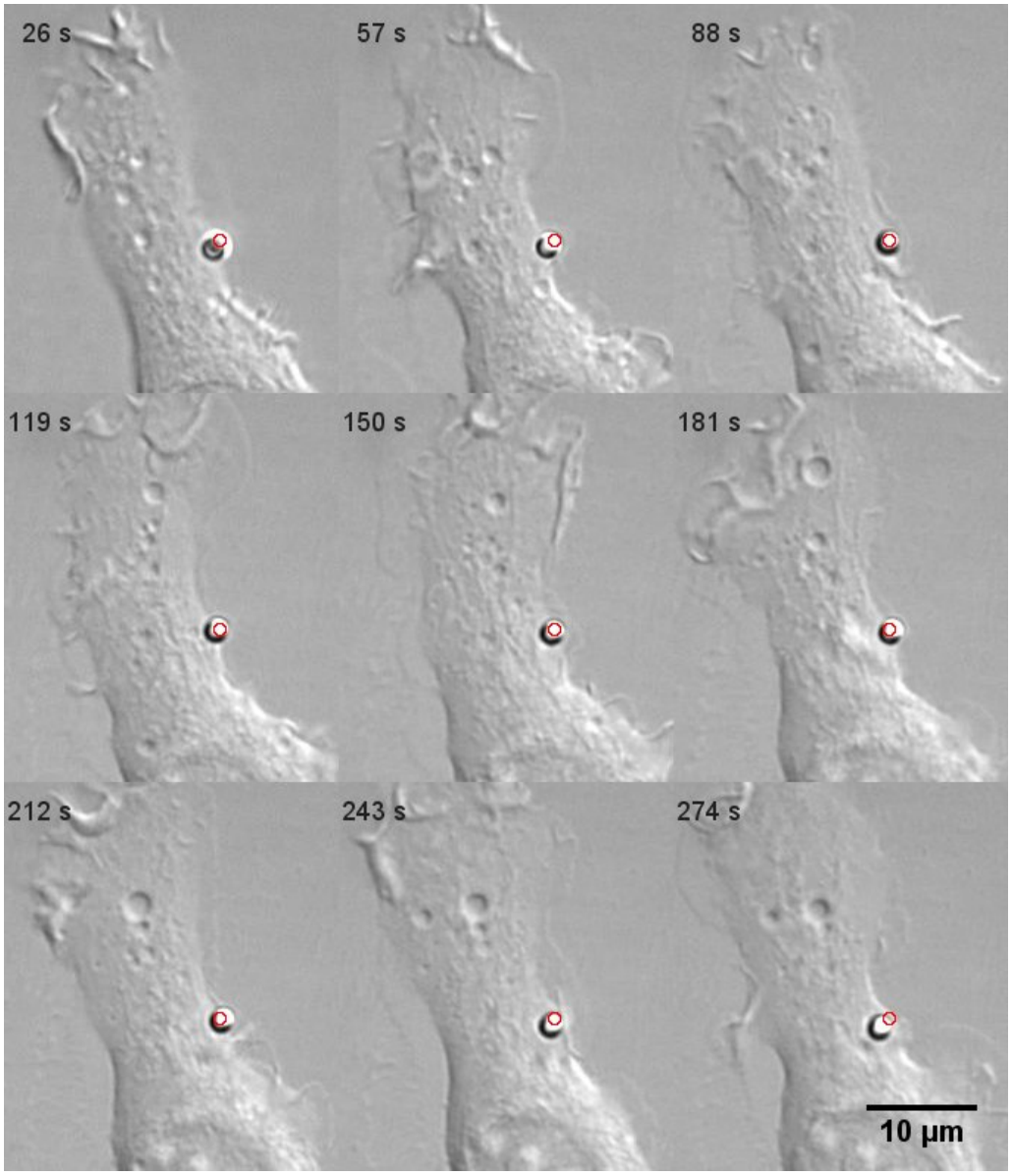

Figure 3.7: DIC images acquired during a blinking experiment with a J774 macrophage without CytoD. Time is given relative to the attachment time. The cell was very active and the membrane ruffled, especially on the lamellipodium at the top. The nucleus is visible at the bottom. The position of the 1st order trap is highlighted with a red circle. The particle moved apparently randomly inside the optical trap and was eventually pulled out of the trap after about 4.5 min. The time is given relative to the attachment time (sec. 3.3.1.6).

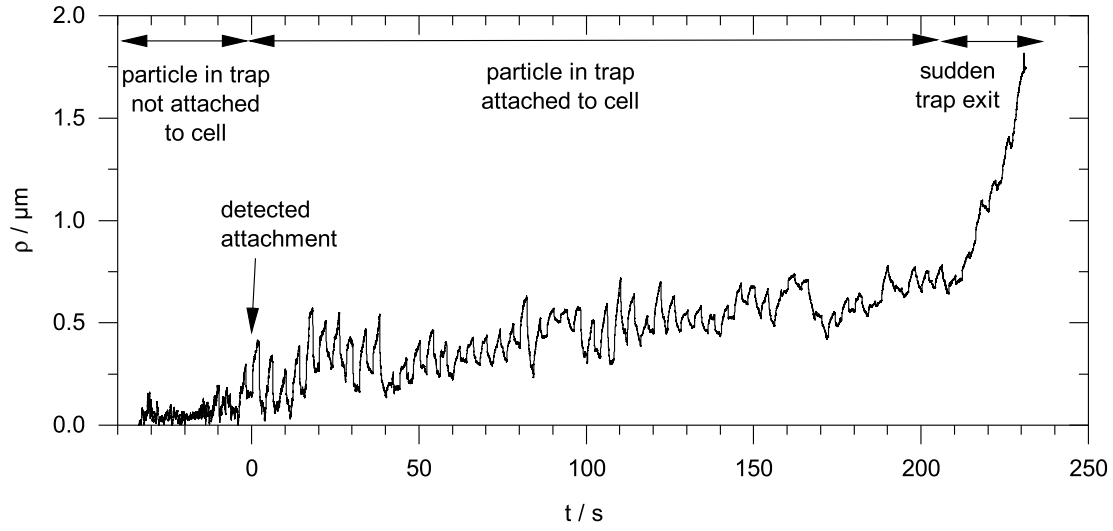

Figure 3.8: Typical particle trajectory during a blinking experiment. The time is given relative to the attachment time point (black arrow). The modulation of the optical force lead to periodic increases and decreases of $\rho(t)$ with a frequency of 0.25 Hz. After the attachment and during the blinking phase, the particle was subsequently pulled away from the trap center. ρ did however not always increase monotonically. Transport back to the trap center and also pause phases were observed (fig. 3.7). Figure adapted from Berghoff et al., Biophysical Journal, 2021[239].

$\rho(t)$ decreased after the trap was turned on and it increased after the trap was turned off. However, there was no experimental time synchronization between the switching time of the trap and the high speed data available. Therefore, the switching times of the trap had to be detected in the post analysis in order to obtain the cellular rheology from $\rho(t)$. The corresponding methods are described in the next section.

3.3.1.7 Blinking Event Detection

A custom written routine was developed in MATLAB to detect the individual blinking events in the particle trajectories (fig. 3.9A). The radial component of the particle velocity $\mathrm{d}\rho/\mathrm{dt}$ (fig. 3.9B, black curve) was filtered with a sharp, normalized band pass filter with a frequency of 0.25 Hz to isolate the blinking modulation (fig. 3.9B, yellow curve). The filter was designed such that it retained the sign of $\mathrm{d}\rho/\mathrm{dt}$, which allowed the distinction of those time points, at which the laser was turned on, from those, when the laser was turned off. Next, a custom-written peak finder was applied to detect the time points, at which the absolute value of the velocity was highest. These time points were located in the middle of the rising and falling edges of $\rho(t)$ (fig 3.9 A and B, closed symbols). Starting from these time points of highest velocity, the unfiltered radial velocity was backtracked until the sign of the unfiltered velocity had changed last. These time points t_0 were defined as the start of the blinking events (fig. 3.9 A and B, open symbols). The corresponding radial distance $\rho_0 = \rho(t_0)$ is subsequently referred to as the offset of a blinking event.

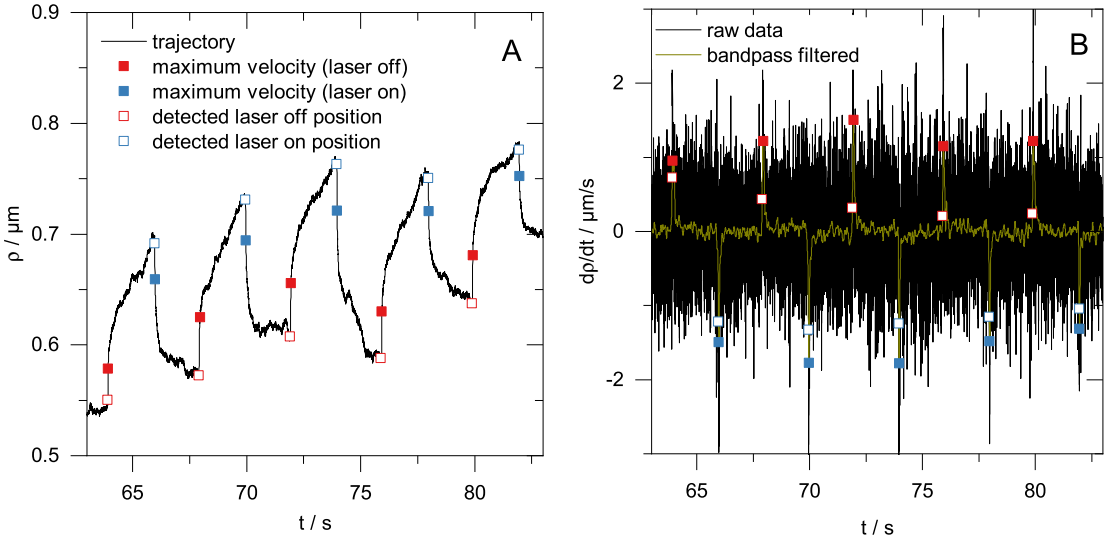

Figure 3.9: Automated detection of individual blinking events. (A) The particle trajectory $\rho(t)$ was (B) derived with respect to time to calculate the instantaneous velocity $\mathrm{d}\rho/\mathrm{dt}$. The blinking signal was isolated by filtering the velocity with a sharp band pass filter with a frequency of 0.25 Hz (B, yellow curve). The time points with the highest filtered velocity (closed symbols) were used as starting points to backtrack to the time points at which the laser was turned on or off (open symbols). These time points were defined as the points at which the sign of the unfiltered velocity had changed last before a velocity peak. The corresponding positions were defined as the blinking event offsets ρ_0. Figure adapted from Berghoff et al., Biophysical Journal, 2021[239].

3.3.1.8 Mechanical Modeling of the Blinking Events

In this section, the theory to derive the viscoelastic properties of the cells from the experimental data is established. In contrast to elastic systems, in which stress and strain are related by Hooke's law (eq. 2.18) and in which the stress is fully defined by the current strain at all times, viscoelastic systems such as cells have an inherent memory. This implies that all stresses σ applied to a viscoelastic system in the past generally have an influence on the current strain ϵ. Mathematically, this memory effect can be described by the tensile creep response $J(t)$[323–325]:

$$\epsilon(t) = \int_{-\infty}^{t} \mathrm{d}t' J(t-t') \frac{\mathrm{d}\sigma(t')}{\mathrm{d}t'}. \tag{3.10}$$

In the early 2000s, it was established that the viscoelastic response of cells can not be modeled with a finite number of spring-dashpod elements. In other words, the viscoelastic response of cells can not be characterized by distinct time scales[237]. Instead, Fabry et al.[326] were the first to show that $J(t)$ of cells can be described by a scale free power law of the form[237,326,327]

$$J(t) = j_0 \left(\frac{t}{\tau_0}\right)^{\beta}. \tag{3.11}$$

Here, j_0 is the tensile creep compliance. β is the material's power law exponent, which describes the relation between elastic and viscous contributions. τ_0 is an arbitrary time normalization constant,

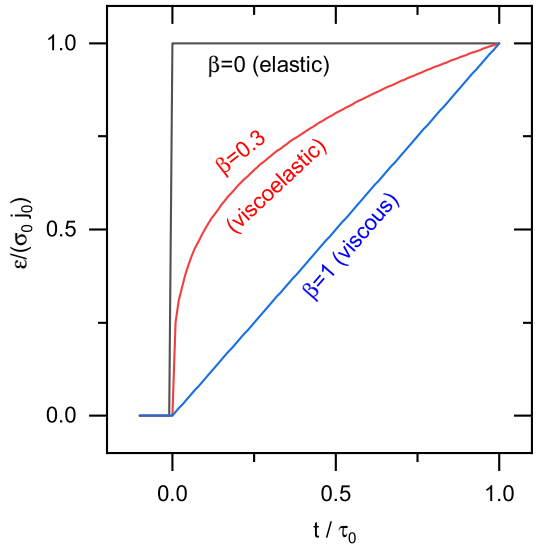

Figure 3.10: Step response of viscoelastic materials with different power law exponents β. $\epsilon(t)$ was calculated with equation 3.13. Figure drawn according to Kollmannsberger and Fabry[237].

which is typically set to 1 s[327]. The model described by equations 3.10 and 3.11 extends Hookes law (eq. 2.18) such that it can describe purely viscous materials, purely elastic materials, and viscoelastic materials. This can be illustrated as follows. Assume that the stress exerted on such a system jumps to a finite value σ_0 instantly at $t = 0$. Such a jump can be described by the Heaviside function $\Theta(t)$:

$$\sigma(t) = \sigma_0 \Theta(t). \tag{3.12}$$

Inserting equation 3.12 into equation 3.10 yields the step response of the system:

$$\epsilon(t) = \begin{cases} 0 & t \leq 0 \\ \sigma_0 \, j_0 \left(\frac{t}{\tau_0}\right)^{\beta} & t > 0. \end{cases} \tag{3.13}$$

In figure 3.10, the normalized step response is plotted for different values of β. In case of $\beta = 1$, the material is purely viscous and the strain increases with a constant velocity. In case of $\beta = 0$, the material is purely elastic and equation 3.10 simplifies to Hooke's law (eq. 2.18). In this case, the strain jumps to a constant value and the compliance j_0 is the inverse of the elastic modulus E (eq. 3.13 and 2.18). For $0 < \beta < 1$, the system's response contains both elastic and viscous contributions. Near $t = 0$, the initial curve slope is infinitely high for $\beta < 1$ (eq. 3.13 and fig. 3.10). This reflects the fact that the initial system response is purely elastic and viscous effects only slow down the response when the velocity is already larger than 0.

In the blinking experiments, two forces, i.e. the optical force F_{HOT} exerted by the holographic optical trap and the cellular force F_{cell} acted on the particle. The total stress σ on the particle is therefore given by

$$\sigma(t) = \frac{F_{\mathrm{HOT}}(t) + F_{\mathrm{cell}}(t)}{A(t)}. \tag{3.14}$$

Here, A is the contact area between the cell and the particle. Inserting equations 3.11 and 3.14 into equation 3.10, the strain ϵ becomes

$$\epsilon(t) = \int_{-\infty}^{t} \mathrm{d}t' j_0 \frac{(t-t')^{\beta}}{t_0^{\beta}} \frac{\mathrm{d}}{\mathrm{d}t'} \left(\frac{F_{\mathrm{HOT}}(t') + F_{\mathrm{cell}}(t')}{A(t')} \right). \tag{3.15}$$

Equation 3.15 can be simplified with a few assumptions. Firstly, the background drift of $\rho(t)$ was likely caused by the cellular forces F_{cell} exerted on the particle. As these forces were unknown, the background drift could not be used to gain information about the viscoelastic properties of the cell. Secondly, the direction of the background motion appeared to change on a time scale of 10 or more seconds, which was slower than the time scale of the blinking modulation (fig. 3.8). Thus, the assumption was made that during a short time period after trap switching, F_{cell} did not change. Furthermore, it was assumed that the viscoelastic properties of the cells and the contact radius did not change on the time scale of a blinking event:

$$\frac{\mathrm{d}j_0}{\mathrm{d}t'} = 0, \quad \frac{\mathrm{d}\beta}{\mathrm{d}t'} = 0, \quad \frac{\mathrm{d}A}{\mathrm{d}t'} = 0, \quad \frac{\mathrm{d}F_{\mathrm{cell}}}{\mathrm{d}t'} = 0, \tag{3.16}$$

To keep the errors induced by these assumptions low, only the first 500 ms of every blinking event were used for data evaluation. Furthermore, assuming that the influence of all previously applied forces was negligible, the change of the strain during one blinking event simplifies to:

$$\Delta\epsilon(\tau) = \frac{j_0}{A} \int_0^{\tau} \mathrm{d}\tau' \frac{(\tau-\tau')^{\beta}}{\tau_0^{\beta}} \frac{\mathrm{d}F_{\mathrm{HOT}}(\tau')}{\mathrm{d}\tau'}. \tag{3.17}$$

Here $\tau = t - t_0$ is the time since the blinking event started.

The force exerted by the holographic optical trap during a blinking event was modeled with the following two considerations. Firstly, since the particle positions were not necessarily located on the axes of the coordinate system, the calibration profiles along the x and y axes were combined to estimate the optical force F_{opt} at a random position (x, y). To account for slight asymmetries in the trap geometry of typically a few percent, $F_{\mathrm{opt}}(x, y)$ was estimated with

$$F_{\mathrm{opt}}(x, y) = \sqrt{F_{\mathrm{opt,x}}^2 + F_{\mathrm{opt,y}}^2}, \tag{3.18}$$

accounting for the quasi-Gaussian profile of the beam. The z displacement was not considered in the data evaluation, although the particles sometimes moved considerably along the axial direction. This can for example be seen as the particle images in figure 3.7 at $t = 26\,\mathrm{s}$ and $t = 57\,\mathrm{s}$ are considerably different. In this regard, the actual optical forces were lower than estimated by equation 3.18. The consequences of this omission are discussed in section 3.3.3. The optical force $F_{\mathrm{opt}}(x, y)$ was assumed to always be directed towards the equilibrium position. Secondly, the time required for the particles to relax towards the trap center position was on the order of a few tens of milliseconds, depending on the condition. This relaxation time was similar to the characteristic switching time of the SLM τ_{SLM}, i.e. the time required until a new phase pattern was established on the display. Therefore, the rise and fall times of the intensity of the 1$^{\mathrm{st}}$ order trap had to be accounted for in the data evaluation. K. Berghoff validated that the rise and fall of the intensity of the 1$^{\mathrm{st}}$ order was well described by an exponential relationship with a characteristic switching time τ_{SLM} of 17 ms, which was in line with the manufacturers specification[216]. Consequently, the optical force exerted on the particle during blinking was given by

$$F_{\mathrm{HOT}}(\tau) = F_{\mathrm{opt}}(\rho(\tau)) \begin{cases} \mathrm{e}^{-\tau/\tau_{\mathrm{SLM}}} & \text{laser switched off at } \tau = 0 \\ 1 - \mathrm{e}^{-\tau/\tau_{\mathrm{SLM}}} & \text{laser switched on at } \tau = 0. \end{cases} \tag{3.19}$$

Inserting equation 3.19 into equation 3.17 yields:

$$\Delta\epsilon\left(\tau\right)=\frac{j_0}{A}\int_0^\tau \mathrm{d}\tau'\frac{\left(\tau-\tau'\right)^\beta}{\tau_0^\beta}\frac{\mathrm{d}}{\mathrm{d}\tau'}F_{\mathrm{opt}}\left(\tau'\right)\begin{cases}\mathrm{e}^{-\tau'/\tau_{\mathrm{SLM}}} & \text{laser switched off at } \tau'=0\\ 1-\mathrm{e}^{-\tau'/\tau_{\mathrm{SLM}}} & \text{laser switched on at } \tau'=0.\end{cases} \tag{3.20}$$

The contact area $A=\pi r^2$ was modeled to be roughly circular with a contact radius r. To estimate the strain, a coarse approximation of the depth of the deformation field was used. An analogy is found in the steel sphere experiments presented in chapter 2, where the finite layer thickness h influenced the indentation depth $\delta(h)$ of the spheres, when the contact radius and the layer thickness were approximately equal. Therefore, the depth and the lateral size of the deformation field, which was roughly equal to the contact radius, were approximately equal in those experiments. In analogy to those observations, the depth of the deformation field in the blinking experiments presented here was also modeled to be roughly equal to the contact radius r. Consequently, the change of the strain $\Delta\epsilon=\Delta\rho/r$ was estimated by the change of ρ since the start of the blinking event $\Delta\rho=\rho-\rho_0$, divided by the depth of the deformation field, which was approximated by r. The same assumption was, for example, suggested by Kollmannsberger et al.[327]. Thus, the spatial resolution of the experiment is approximately given by the contact radius and the volume of the probed region is roughly equal to r^3. With these assumptions, $\Delta\rho\left(\tau\right)$ can be derived:

$$\Delta\rho\left(\tau\right)=\alpha\int_0^\tau \mathrm{d}\tau'\frac{\left(\tau-\tau'\right)^\beta}{\tau_0^\beta}\frac{\mathrm{d}}{\mathrm{d}\tau'}F_{\mathrm{opt}}\left(\tau'\right)\begin{cases}\mathrm{e}^{-\tau'/\tau_{\mathrm{SLM}}} & \text{laser switched off at } \tau'=0\\ 1-\mathrm{e}^{-\tau'/\tau_{\mathrm{SLM}}} & \text{laser switched on at } \tau'=0.\end{cases} \tag{3.21}$$

α is the blinking amplitude

$$\alpha=\frac{j_0}{\pi r}. \tag{3.22}$$

Thus, the blinking amplitude was a function of the cellular compliance j_0 and the contact radius r between the particle and the cell. As the contact radius could not be determined from the DIC images, both contributions could not be separated in a single experiment. Instead, the experiments described above were repeated with different trap stiffnesses and different concentrations of CytoD to isolate both effects. The corresponding model is presented in the results section 3.3.2.1.

In the derivation above, the cellular forces were neglected. However, the background drift possibly caused by such forces was clearly visible in the particle trajectories. In the derivation given above, the cellular response should, in general be symmetric, i.e. the absolute values of $\Delta\rho$ induced by force jumps of $\pm\Delta F_{\mathrm{opt}}$ should be symmetrical. The background drift, possibly caused by the cellular forces, however, reduced this symmetry as $\rho\left(t\right)$ gradually increased during the experiments. Therefore, the background drift was subtracted to isolate the displacement $\Delta\rho_{\mathrm{corr}}$ caused by the optical force alone. The background drift was quantified by fitting a shape preserving cubic spline (fig. 3.11, red curve) to the blinking event offsets $\rho_0(\tau=0)$ of those blinking events, when the laser was turned off (fig. 3.9, red open squares). The spline was then subtracted from the raw data to yield ρ_{corr} (fig. 3.11, blue curve). Changes of ρ_{corr} were thus considered to be solely caused by changes of the optical force:

$$\Delta\rho_{\mathrm{corr}}\left(\tau\right)=\alpha\int_0^\tau \mathrm{d}\tau'\frac{\left(\tau-\tau'\right)^\beta}{\tau_0^\beta}\frac{\mathrm{d}}{\mathrm{d}\tau'}F_{\mathrm{opt}}\left(\tau'\right)\begin{cases}\mathrm{e}^{-\tau'/\tau_{\mathrm{SLM}}} & \text{laser switched off at } \tau'=0\\ 1-\mathrm{e}^{-\tau'/\tau_{\mathrm{SLM}}} & \text{laser switched on at } \tau'=0.\end{cases} \tag{3.23}$$

Equation 3.23 was fitted numerically to $\Delta\rho_{\mathrm{corr}}\left(t\right)$ (fig. 3.11, blue curve) of every blinking event to obtain the blinking amplitude α and the power law exponent β. The optical force F_{opt} was derived from the unprocessed particle position using equation 3.18 and the trap calibration curves discussed in section 3.3.1.5.

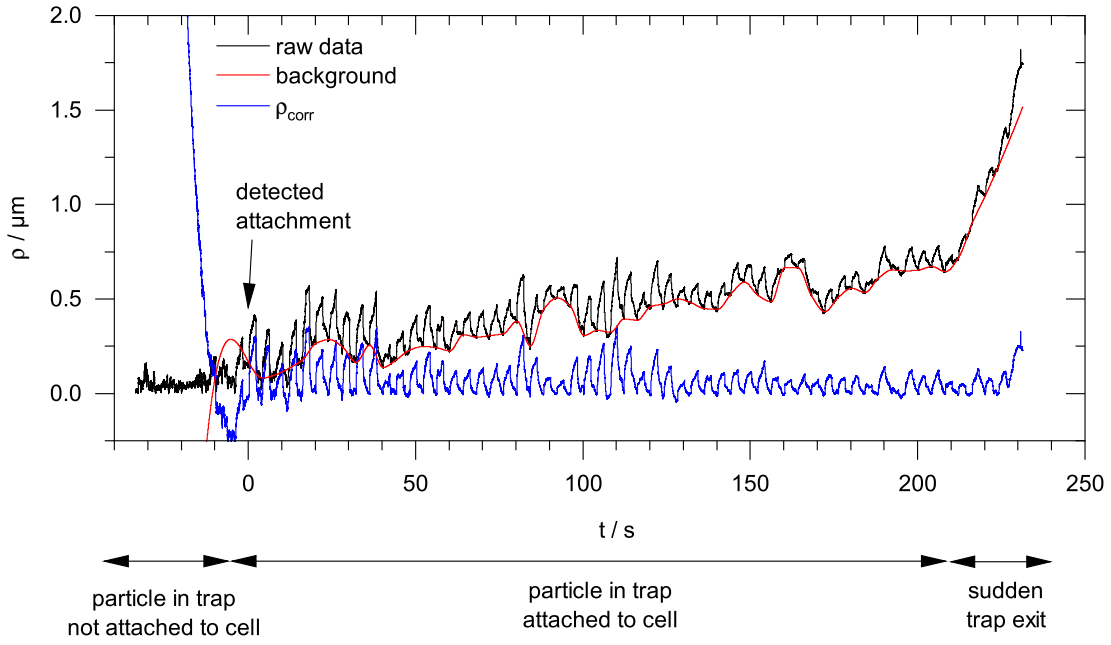

Figure 3.11: Background drift correction during the blinking experiments. The time is given relative to the attachment time point (black arrow). After the attachment and during the blinking phase, the particle was subsequently pulled away from the trap center. ρ did however not always increase monotonically. Transport back to the trap center and also pause phases were observed (fig. 3.7), which can likely be attributed to cellular forces acting on the particle. The background was quantified by fitting a cubic shape-preserving spline to the blinking event offsets ρ_0, at which the laser was turned off (red curve, see main text and fig. 3.9, red open squares). The corrected curve ρ_{corr} is shown in blue. Figure adapted from Berghoff et al., Biophysical Journal, 2021[239].

In some of the blinking events, the drift could not be fully corrected and the fit results were not plausible. Fits which did not yield a positive amplitude and fits, which yielded a power law exponent outside the range $0 \leq \beta \leq 1$ were discarded. Furthermore, fitted functions $\Delta\rho_{\mathrm{fit}}$, which deviated strongly from the measured data, i.e.

$$1 - \frac{\left\langle \left(\Delta\rho_{\mathrm{fit,i}} - \Delta\rho_{\mathrm{corr,i}}\right)^2 \right\rangle}{\left\langle \left(\Delta\rho_{\mathrm{corr,i}} - \langle\Delta\rho_{\mathrm{corr,i}}\rangle\right)^2 \right\rangle} < 0.8 \tag{3.24}$$

were also discarded. Here, $\langle ... \rangle$ denotes the mean value of all data points indexed by i. In most of those discarded cases, the drift changed drastically during one event and could not be corrected for with the fitted spline.

Examples of fitted functions are shown in figure 3.12. The fits of equation 3.23 were generally in very good agreement with the experimental data. The ideal step response of a viscoelastic system with $J(t)$ given by equation 3.11 has an infinitely high slope near $\tau = 0$ for $\beta < 1$ (eq. 3.13 and fig. 3.10). This was not observed in the experiment. The initial slope of $\Delta\rho_{\mathrm{corr}}$ was instead dominated by the switching time of the SLM τ_{SLM}, which was corrected for by the numerical fit of equation 3.23. The results for ρ_0, α, and β obtained from multiple cells were pooled and averaged over

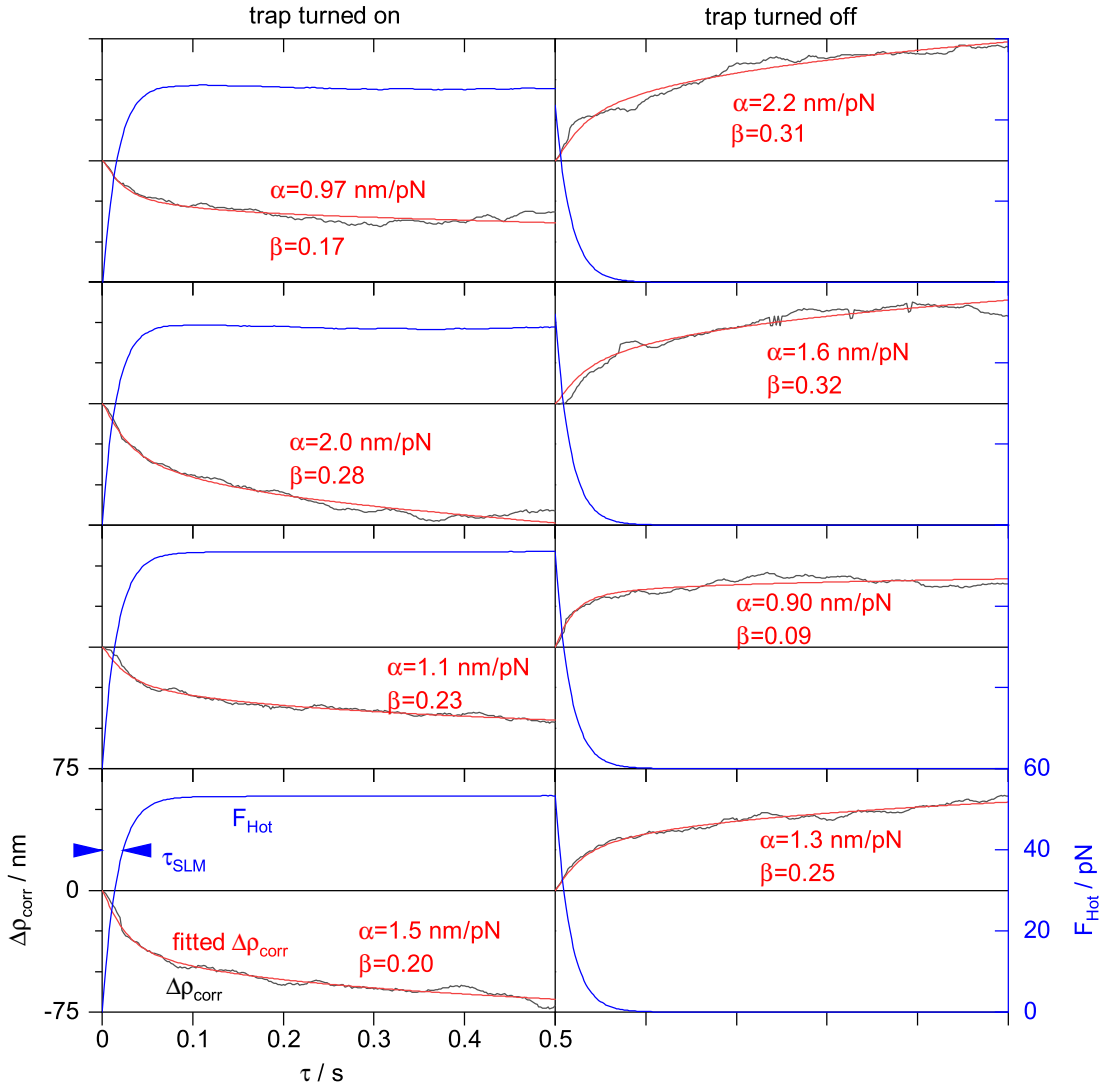

Figure 3.12: Fits of the creep response function to the blinking data. Equation 3.23 (red) was fitted to $\Delta\rho_{\mathrm{corr}}(\tau)$ (black). $\Delta\rho_{\mathrm{corr}}$ changed suddenly upon changes of the optical force F_{HOT}. When the trap was turned on, $\Delta\rho_{\mathrm{corr}}$ decreased (left column) and when the trap was turned off, $\Delta\rho_{\mathrm{corr}}$ increased (right column). Equation 3.23 was in very good agreement with the experimental data, especially near $\tau = 0$, where the influence of the switching time of the SLM τ_{SLM} was high.

intervals of 20 s to reduce noise and to eliminate cell-to-cell variations. The results are presented in section 3.3.2.1.

		$\rho_0(t) = A + B\,t$		$\beta(t) = C + D\,t$		
k/ pN µm^{-1}	c_{CytoD}/ µM	A/ µm	B / µm min^{-1}	C	D/ 1×10^{-3} min^{-1}	j_0/ kPa^{-1}
300 ± 10	0	0.46 ± 0.02	0.28 ± 0.02	0.25 ± 0.01	-25 ± 10	2.8 ± 0.5
120 ± 10	0	0.44 ± 0.02	0.18 ± 0.01	0.28 ± 0.01	-29 ± 5	7.9 ± 0.8
100 ± 10	0	0.28 ± 0.01	0.25 ± 0.01	0.28 ± 0.01	-27 ± 6	9.5 ± 1.0
100 ± 10	1	0.40 ± 0.02	0.14 ± 0.01	0.29 ± 0.01	-3 ± 5	8.7 ± 0.8
100 ± 10	5	0.26 ± 0.02	0.06 ± 0.01	0.44 ± 0.02	-10 ± 5	20.0 ± 0.6

Table 3.1: **Results of the blinking experiments.** Blinking event offset $\rho_0(t)$, power law exponent $\beta(t)$ and cellular compliance j_0 of macrophages measured after the binding of an IgG-coated particle with a diameter of 2 µm. The measurement was carried out for three optical trap stiffnesses k and for various concentrations of CytoD c_{CytoD}. The errors were determined with Monte-Carlo simulations, considering the errors of the averaged data points in figure 3.13.

3.3.1.9 Fixed Cytochalasin D Treated Cells

CytoD was used to disrupt the actin cytoskeleton of the cells. In order to visualize the influence of CytoD on the cortical actin, Lifeact-GFP transfected J774 macrophages were treated with CytoD at concentrations of $c_{\mathrm{CytoD}} = 1\,\mu\mathrm{M}$ and $c_{\mathrm{CytodD}} = 5\,\mu\mathrm{M}$ for 30 min and fixed in 4 % paraformaldehyde for 15 min. Fluoromount-G (Thermo Fisher Scientific) was used to mount the coverslips to object slides. The cells were imaged with an electron multiplying charge-coupled device camera (Evolve 512; Photometrics, Tucson, Arizona, USA) mounted on a DMI 6000 microscope (Leica SD AF; Leica, Wetzlar, Germany), which was equipped with a confocal spinning disc unit (CSU-X1; Yokogawa, Musashino, Japan). Analogous control experiments were conducted without CytoD ($c_{\mathrm{cytoD}} = 0\,\mu\mathrm{M}$). Confocal images of the corex are shown in section 3.3.2.2.

3.3.2 Results

3.3.2.1 Cell and Contact Mechanics During the Early Binding Phase

Blinking experiments without CytoD were carried out with three different trap stiffnesses ($k = 300\,\mathrm{pN\,\mu m^{-1}}$, $k = 120\,\mathrm{pN\,\mu m^{-1}}$, $k = 100\,\mathrm{pN\,\mu m^{-1}}$). At a trap stiffness of $100\,\mathrm{pN\,\mu m^{-1}}$, cells treated with a low concentration of CytoD ($c_{\mathrm{cytoD}} = 1\,\mu\mathrm{M}$) and cells treated with a high concentration of CytoD ($c_{\mathrm{cytoD}} = 5\,\mu\mathrm{M}$) were also probed with the blinking holographic optical tweezers setup.

As already stated in section 3.3.1.6, the blinking event offsets $\rho_0(t)$ varied from experiment to experiment. When averaged over multiple trajectories, the blinking event offsets ρ_0 increased monotonically with time for all three trap stiffnesses (fig. 3.13A). A linear function was fitted to $\rho_0(t)$ to quantify the average radial velocity, with which the particles left the optical trap (tab. 3.1). For the three trap stiffnesses, these radial velocities were very similar for untreated cells and ranged between $(0.18 \pm 0.01)\,\mu\mathrm{m\,min^{-1}}$ ($k = 120\,\mathrm{pN\,\mu m^{-1}}$) and $(0.28 \pm 0.02)\,\mu\mathrm{m\,min^{-1}}$ ($k = 300\,\mathrm{pN\,\mu m^{-1}}$). The fact that the highest velocity was found for the stiffest trap indicates that the cellular forces pulling the particle out of the trap were not influenced by the trapping laser. Even at a low CytoD concentration of $c_{\mathrm{cytoD}} = 1\,\mu\mathrm{M}$, ρ_0 increased with a velocity of $\mathrm{d}\rho_0/\mathrm{dt} = 0.14\,\mu\mathrm{m\,s^{-1}}$, which was slightly slower than in all untreated conditions. Cells treated with $c_{\mathrm{cytoD}} = 5\,\mu\mathrm{M}$ pulled the particles considerably slower out of the trap center position. The radial velocity was $\mathrm{d}\rho_0/\mathrm{dt} = (0.06 \pm 0.01)\,\mu\mathrm{m\,s^{-1}}$.

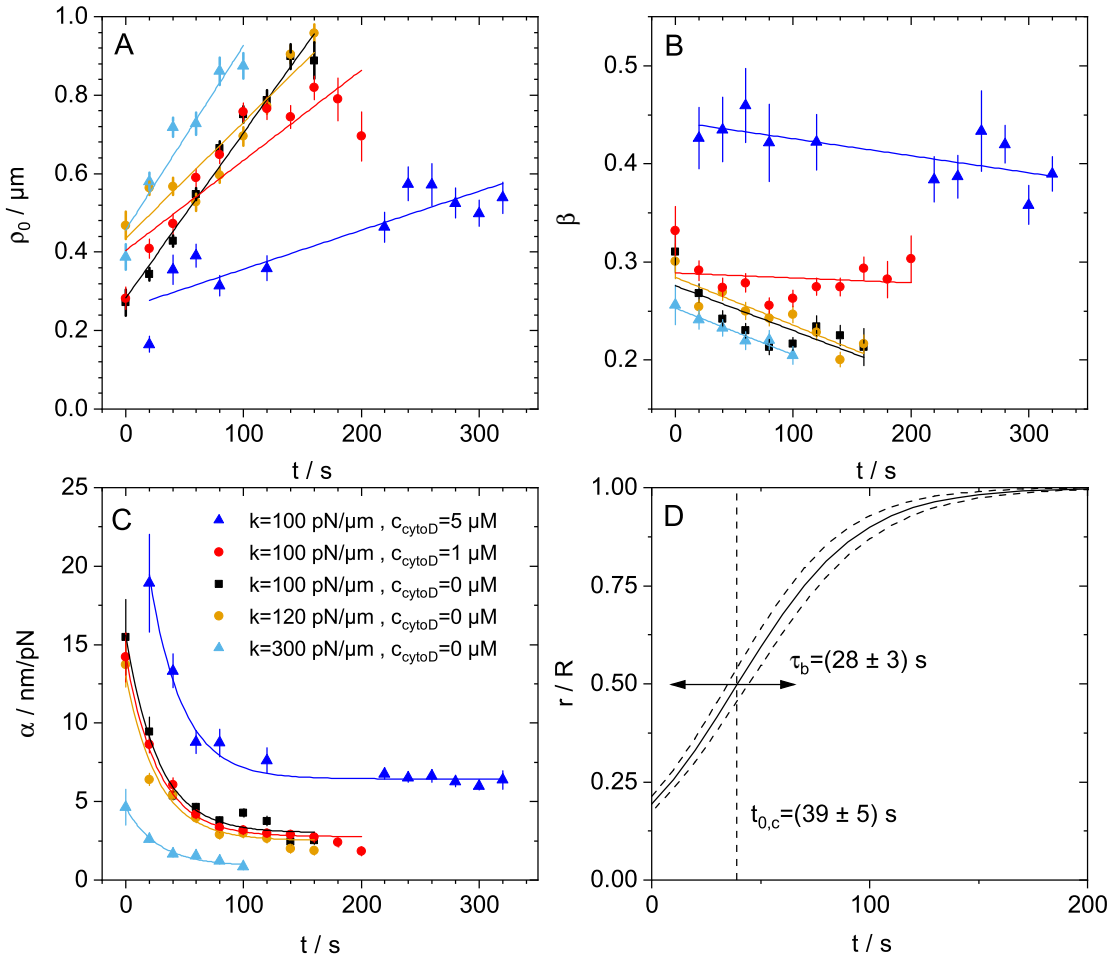

Figure 3.13: Results of the blinking experiments. (A) Blinking event offset ρ_0, (B) power law exponent β , and (C) the blinking amplitude α as a function of the time after attachment for different conditions. The data was acquired from N trajectories ($c_{\mathrm{cytoD}} = 0\,\mu\mathrm{M}$: $k = 300\,\mathrm{pN/\mu m}$: $N = 18$, $k = 120\,\mathrm{pN/\mu m}$: $N = 47$, $k = 100\,\mathrm{pN/\mu m}$: $N = 16$; $c_{\mathrm{cytoD}} = 1\,\mu\mathrm{M}$: $N = 17$; $c_{\mathrm{cytoD}} = 5\,\mu\mathrm{M}$: $N = 5$). The data were pooled in intervals of 20 s and every data point represents at least 15 individual blinking events. Error bars represent the standard error of mean. Linear functions were fitted to (A) $\rho_0\,(t)$ and (B) $\beta\,(t)$ to quantify the temporal evolution. The fit parameters are shown in table 3.1. (C) The amplitudes of all conditions were fitted simultaneously with equations 3.22 and 3.25 with $t_{0,\mathrm{c}}$, τ_{b} and the five compliances j_0 as the only free parameters. R was assumed to be 1 µm and $\mathrm{d}j_0/\mathrm{dt}$ was assumed to be 0. The fitted values of j_0 are given in table 3.1 and the fitted contact radius $r\,(t)$ is shown in panel D. The relative errors of r were determined from the experimental errors of α with Monte-Carlo simulations and they were on the order of 4 %. The error bars in panels A, B, and C represent the standard error of mean. Figure adapted from Berghoff et al., Biophysical Journal, 2021[239].

The power law exponents β of untreated cells were on the order of 0.2-0.3 and decreased slightly with time at rates between $(-0.027 \pm 0.001)\,\mathrm{min}^{-1}$ ($k = 100\,\mathrm{pN\,\mu m}^{-1}$) and $(-0.029 \pm 0.005)\,\mathrm{min}^{-1}$ ($k = 100\,\mathrm{pN\,\mu m}^{-1}$), indicating that the cellular response was slightly more elastic at the end of the experiments. Cells treated with a low CytoD concentration of 1 µM were slightly more viscous and their response did not become more elastic with time. β stayed relatively constant with values slightly below 0.3. However, at a high concentration of 5 µM of CytoD, the macrophages were far more viscous and the power law exponent was about 0.4 to 0.45.

The blinking amplitudes α dropped considerably as a function of time in all conditions and at the end of the experiments 3 to 4 min after the attachment, the amplitude had typically dropped to about 1/5 of its original value, seemingly converging to a constant value (fig. 3.13C). This effect was also observed in the majority of the individual trajectories $\rho\,(t)$ where the particle displacement was generally largest at the beginning of the experiment (fig. 3.11), even though the forces were low as the blinking event offsets ρ_0 were small compared to the trap size (fig. 3.5 and 3.13A).

As α is a function of the compliance j_0 and of the contact radius r (eq. 3.22), both parameters could theoretically cause the observed decrease of the cellular compliance. Firstly, it is possible that the cells' compliance j_0 decreased with time. Such a decrease of the compliance could have been caused by the polymerization of cortical actin, possibly initiated by the binding of IgG to FcγR. However, a similarly strong time dependence was not observed in the power law exponent β, which is also mediated by the cortical structure. Furthermore, the time scale, at which the amplitude decreased was identical in all tested conditions, especially at $c_{\mathrm{cytoD}} = 5\,\mu\mathrm{M}$. At this CytoD concentration, actin polymerization should be considerably slowed down compared to the untreated conditions. Thus, it appears unlikely that a significant and reproducible remodeling of cortical actin happened during the early binding phase. This hypothesis is also supported by experiments conducted with Lifeact-GFP transfected macrophages. The data presented in section 3.4.2.1 demonstrates that the actin density below the target does not increase systematically directly after cell-particle contact. Instead, actin polymerized in a quasi-periodic manner with an unstable frequency of roughly 40 s. As the blinking amplitudes presented here represent an average of multiple cells, it it highly unlikely that the decrease of the amplitude was caused by a reproducible, structural change of the cortex.

As the time scale of the process was independent of the CytoD concentration, it is far more likely that the process which caused the decrease of the amplitude is solely related to membrane proteins or the membrane itself. In this regard, the second possible explanation that the cell-particle contact radius r increased appears to be highly likely. As $t = 0$ was the attachment time point, time dependent changes of the amplitude in the early phase of the experiments certainly reflected an increase of $r\,(t)$. Such an increase could for example be mediated by the binding of IgG to FcγR^{328}. As the amplitudes seemingly converged to a constant value at the end of the experiments, $r\,(t)$ was modeled with a sigmoidal function.

$$r\,(t) = \frac{R}{1 + \exp\left(-\frac{t - t_{0,c}}{\tau_b}\right)} \tag{3.25}$$

The binding process was thus characterized with one characteristic length scale and two characteristic time scales. First, the assumption was made that the contact radius converged to the particle radius $R = 1\,\mu\mathrm{m}$ for $t \to \infty$ in all conditions. The first time scale $t_{0,\mathrm{c}}$ is the duration until the contact radius had reached 50 % of its final value and the second time scale τ_{b} is the duration of the binding dynamics. For example a high τ_{b} describes a slow binding process and vice versa.

To determine the creep compliances j_0, $t_{0,\mathrm{c}}$ and τ_{b}, the amplitude $\alpha\,(r\,(t))$ (eq. 3.23 and 3.25) was fitted to the experimental results for all five conditions simultaneously. The fits are shown in figure 3.13C and the creep compliances j_0 are summarized in table 3.1. The cells' compli-

ances decreased with increasing trap stiffness, i.e. with higher forces. Cells probed with the trap with $(100 \pm 10)\,\mathrm{pN/\mu m}$ had a compliance of $j_0 = (9.5 \pm 1.0)\,\mathrm{kPa^{-1}}$. j_0 decreased slightly to $(7.9 \pm 0.8)\,\mathrm{kPa^{-1}}$ at $k = (120 \pm 10)\,\mathrm{pN/\mu m}$ and decreased considerably to $(2.8 \pm 0.5)\,\mathrm{kPa^{-1}}$ at $k = (300 \pm 10)\,\mathrm{pN/\mu m}$. At a low CytoD concentration of 1 µM, the measured compliance was $(8.7 \pm 0.8)\,\mathrm{kPa^{-1}}$, which is, considering the margin of errors, an insignificant change compared to the untreated condition. However, at a high CytoD concentration of 5 µM, the cells' compliance had increased considerably compared to the untreated case and was measured to be $j_0 = (20.0 \pm 0.6)\,\mathrm{kPa^{-1}}$.

The fitted contact radius

$$r(t) = \frac{R}{1 + \exp\left[-\frac{t-(39\pm5)\,\mathrm{s}}{28\pm3}\right]}. \tag{3.26}$$

is shown in figure 3.13D. The relative error of $r(t)$ was determined from the standard errors of mean of α with Monte-Carlo simulations and it was on the order of 4 %. Note that this error does not account for the uncertainty of the convergence point R, which could theoretically also be smaller than 1 µm. The time scale of the initial binding process was $\tau_\mathrm{b} = (28 \pm 3)\,\mathrm{s}$ and about 2 min after the attachment, the initial binding process came to a halt. $t_{0,\mathrm{c}} = (39 \pm 5)\,\mathrm{s}$ after the initial contact, the contact radius had reached 50 % of its final value, which was assumed to the particle radius R. As the contact area scales with r^2, the contact area reached 50 % of its final extent about 1 min after the initial contact was made. Interestingly, the model predicts that the contact radius had already reached $\approx 20\,\%$ of its final value at $t = 0$. This was most likely caused by the definition of the attachment time point, which had an accuracy of about 8 s (sec. 3.3.1.7).

3.3.2.2 Influence of CytoD on the Cortical Structure

In order to probe whether the measured fluidification and the increased compliance of the cells at $c_\mathrm{cytoD} = 5\,\mu\mathrm{M}$ is reflected by changes in the cortical structure, Lifeact-GFP transfected cells were treated with 1 µM and 5 µM and fixed with PFA (sec. 3.3.1.9). Confocal imaging revealed that the cortical texture of cells treated with a high concentration of CytoD was significantly different from untreated cells. While untreated cells had discernible F-actin filaments with a length of a few micrometers, the filaments were a lot shorter in cells treated with 1 µM of CytoD. No such structures were visible in cells treated with 5 µM of CytoD (fig. 3.14). This was also reflected by the observation of K. Berghoff that the cells treated with 1 µM of CytoD showed far less membrane ruffling than untreated cells and cells treated with 5 µM did not show membrane ruffling at all[239]. Blebbing, which happens when the link between the cortex and the membrane is cleaved[329], was not observed even at $c_\mathrm{CytoD} = 5\,\mu\mathrm{m}$, indicating that parts of the cortex were still intact.

3.3.3 Discussion

In this section, a technique to measure the viscoelastic parameters of cells with blinking holographic optical tweezers was developed. The viscoelasticity of the cells was described with soft glassy rheology[237,297,330], and good agreement between the model and the experimental results was observed. The technique was demonstrated to be capable of resolving the temporal evolution of the contact radius $r(t)$, the creep compliance j_0, and the power law exponent β with a temporal resolution of about 20 s. $r(t)$ and j_0 were determined by analyzing the blinking amplitude α.

As CytoD decreases the polymerization rate of actin[267,268], the experiments with CytoD-treated cells established that the cellular viscoelastic response measured with blinking experiments was, at least in part, mediated by filamentous actin. While the effects of a low CytoD concentration of $c_\mathrm{cytoD} = 1\,\mu\mathrm{M}$ on j_0 and β were relatively minor, both on the cortical structure and on the viscoelastic parameters, a high concentration of $c_\mathrm{cytoD} = 5\,\mu\mathrm{M}$ had a considerable effect. Firstly,

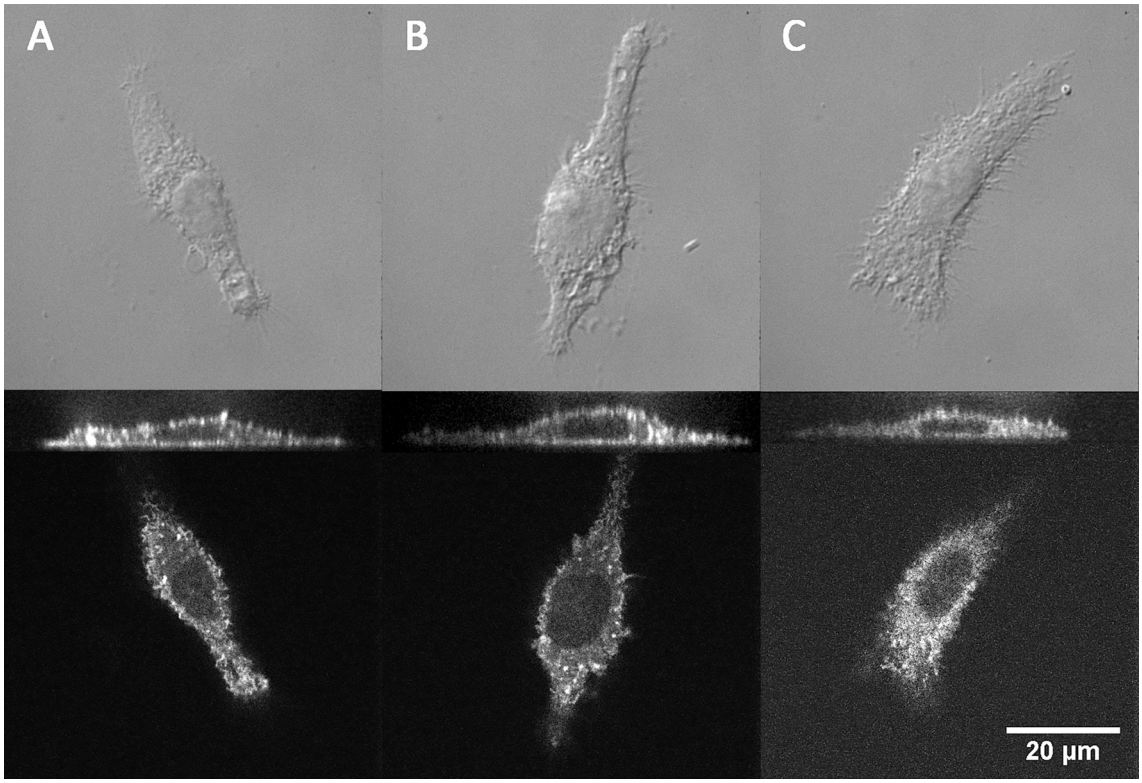

Figure 3.14: Influence of CytoD on the cortical structure. DIC images of Lifeact-GFP transfected macrophages (top row) and the corresponding confocal fluorescence images showing the cortical F-actin structure (middle and bottom row) at CytoD concentrations of (A) $c_{\mathrm{cytoD}} = 0\,\mu\mathrm{M}$, (B) $c_{\mathrm{cytoD}} = 1\,\mu\mathrm{M}$, and (C) $c_{\mathrm{CytoD}} = 5\,\mu\mathrm{M}$. While filamentous structures forming the cell cortex are clearly visible directly below the membrane at $c_{\mathrm{cytoD}} = 0\,\mu\mathrm{M}$, the size of and density of cortical actin filaments was slightly decreased at $c_{\mathrm{cytoD}} = 1\,\mu\mathrm{M}$. At a concentration of $5\,\mu\mathrm{M}$, the distribution of F-actin below the cell membrane was without any discernible structure. The macrophages did not form any stress fibers. Figure adapted from Berghoff et al., Biophysical Journal, 2021[239].

the cortical structure was significantly different from that of untreated cells and no actin filaments with a length of a few micrometers were visible at the cortex as it was the case for untreated cells (fig. 3.14). Furthermore, the compliance j_0 increased approximately twofold from $(9.5 \pm 1.0)\,\mathrm{kPa}^{-1}$ to $20.0\,\mathrm{kPa}^{-1}$. β increased from about 0.2-0.3 to 0.4, indicating that the probed parts of the cell became considerably more viscous upon the addition of CytoD. Such an increase of the compliance and fluidization upon the addition of CytoD has been observed previously. For example, Cai et al. used an atomic force microscope and showed that the power law exponent of mouse fibroblasts increased from 0.32 to 0.37 upon treatment with $c_{\mathrm{cytoD}} = 2\,\mu\mathrm{M}$[330]. This can most likely be attributed to the fact that the structure of the cortex was considerably less dense under the influence of CytoD. In particular, the length of the actin filaments in the cortex was observed to be smaller than the size of the sphere at $c_{\mathrm{CytoD}} = 5\,\mu\mathrm{M}$ with the confocal images. The rheological situation in this case is very similar to the hard tracer particles embedded in the films probed with the steel spheres in section 2. Those tracer particles do not influence the stress strain relationship when the probing length scale is considerably larger than the size of the particles. Thus, such short

actin filaments are not deformed but rather displaced when a force acts on the probe.

In all tested conditions and in particular for cells treated with a high concentration of CytoD, the characteristic timescale at which the blinking amplitude α decreased was about 30 s, which was reflected by the fact that the same sigmoidal function $r(t)$ explained the full time dependence of $\alpha(t)$ (fig. 3.13C). As this timescale, in contrast to the altered viscoelastic parameters, was also not affected by the high CytoD concentration, is appears unlikely that remodeling of cortical actin caused the decrease of the amplitudes, especially considering the fact that cortical actin was highly depolymerized at $c_{\mathrm{CytoD}} = 5\,\mu\mathrm{M}$. Furthermore, no indication was found that the cellular compliance j_0 changed systematically after particle binding. Consequently, it also appears unlikely that the binding of IgG to FcγR initiated a reproducible depolymerization of cortical actin during the first minutes after particle attachment. Such a localized remodeling in the early phase after particle binding was also not observed in the experiments conducted with the Lifeact-GFP transfected macrophages (sec. 3.4.2.1). It is, however, likely that the contact radius increased in a monotonic manner due to the adhesion between the particle and the cell, which could have been mediated by either unspecific binding, specific binding of membrane receptors to proteins in the medium, which adhered to the particle surface, or specific binding of IgG to FcγR. It is also possible that dedicated adhesion sites such as podosomes or focal adhesions formed on the particle surface. However, as these adhesion sites mechanically couple the ECM to the cortex (sec. 1.1), and as the adhesion dynamics were not affected by CytoD, it is questionable whether those structures were the main drivers of the mechanical bonds between the cell and the particles.

Instead, in the experiments discussed in chapter 4, it was established that the ζ-potential, a measure of the surface charge of the particles, can have a significant influence on the cell-particle adhesion strength. In particular, plain and carboxylated polystyrene particles acquired from Micromod were shown to adhere very differently to cells and coverslips and the binding rates of both particle types differed by multiple orders of magnitude (sec. 4.4.2). Uncoated carboxylated particles had high negative surface charges (compared to particles from other manufacturers and plain particles from micromod) and adhered very strongly to cells. In the blinking experiments discussed here, carboxylated polystyrene particles functionalized with IgG were used. An interesting question to be addressed in the future is the degree to which surface charges on IgG-coated particles are shielded by the IgG layer on the surface. Futhermore, the degree to which cell-particle adhesion is mediated by unspecific binding and binding of IgG to FcγR is unknown. An approach to address these questions is given in chapter 5.

In general, no indications that the cellular responses were affected by the laser beam in any resolvable manner were observed. The cells pulled the particles out of the optical trap with a similar velocity for stiff and soft traps. Furthermore, the binding kinetics apparently did not depend on the trap stiffness, which could be the case as the particles were pulled away from the cell membrane, especially at the beginning of the experiments.

There are three main uncertainties associated with the determined creep compliances j_0 reported in section 3.3.2.1. Firstly, the creep compliances were calculated assuming that the contact radius converged to the particle radius R. In case the final contact radius was actually smaller, the true creep compliances of the macrophages were also correspondingly lower (eq. 3.22). In future experiments, this assumption could be checked with electron microscopy as described by A. Sabri[308], which offers the necessary resolution to resolve the contact region. Secondly, the calibration of the holographic optical trap was carried out in 75 % v/v aqueous glycerol solution, which has a higher refractive index than the imaging medium used during the cell experiments. As the optical trapping forces generally depend on both the refractive index of the medium and the refractive index of the particles in a highly nonlinear and even non-monotonic manner when $R \approx \lambda$[281], the true absolute values of the compliance can differ by roughly a single digit factor from the values reported in table 3.1. However, the correction is a constant factor affecting all of the measured

amplitudes, which suggests that the relations between the compliances, the temporal evolution of the contact radius $r(t)$, and the power law exponent β are most likely not affected by the refractive index mismatch between the glycerol solution and the imaging medium. Thirdly, the particles did not only move laterally, but also axially during the experiment. This z displacement was not considered in the data evaluation, although the axial displacement was sometimes considerable. This can for example be seen as the particle images in figure 3.7 at $t = 26\,\mathrm{s}$ and $t = 57\,\mathrm{s}$ are considerably different. Therefore, it is likely that the optical forces were lower on average than predicted by the calibration force fields shown in section 3.3.1.5, suggesting that the compliances of the cells were actually a bit higher than indicated by the measurements. Keeping the particles in focus requires a 3D feedback system, which positions the particles during the experiment at a dedicated position in the trap. Such a system is introduced in section 3.4.

Nevertheless, the compliances measured in this work were of the same magnitude as those reported in the literature. Neglecting viscous effects, j_0 can be interpreted as the inverse of the elastic modulus and consequently, the range of measured compliances of $2.8\,\mathrm{kPa}^{-1} < j_0 < 20\,\mathrm{kPa}^{-1}$ roughly corresponds to $50\,\mathrm{Pa} < E < 360\,\mathrm{Pa}$. For example, Bausch et al. reported a shear modulus of about 350 Pa for J774 mouse macrophages[331] and Rotsch et al. measured elastic moduli in the range of a few hundred Pa to a few kPa for rat liver macrophages[332]. Leporatti et al. determined elastic moduli of 290 Pa for lipopolysaccharide-stimulated human macrophages and 830 Pa for resting macrophages[333].

The decrease of the compliance with increasing trap stiffness can most likely be attributed to nonlinear stress stiffening, as the optical forces were higher at higher trap stiffnesses. Stress stiffening is an inherent property of cross-linked actin networks and it arises due to entropic effects[334]. For example, stress stiffening has been observed in in-vitro experiments in actin networks cross-linked with the actin-binding proteins filamin and gelsolin[335]. On the cell level, stress stiffening has been observed for macrophages[333], fibroblasts and epithelial cells[327,336] but strain stiffening is also observed in tissue[337].

The measured power law exponents of untreated macrophages of about $0.2 < \beta < 0.3$ were also in the range which is typically reported for mammalian cells. For example, Fabry et al. measured values of about $0.2 < \beta < 0.3$ for fibroblasts[88]. Balland et al. report values between $0.15 < \beta < 0.26$ for various mammalian cell types and in particular $0.2 < \beta < 0.25$ for macrophages[297]. A very thorough study examining the influence of various drugs was recently conducted by Flormann et al., who reported $\beta \approx 0.1$ for untreated epithelial cells[325].

While no time dependence of j_0 could be resolved in any of the tested conditions, it is possible and even likely that the effective viscoelastic parameters of the probed cell region changed with time as the contact radius increased during the experiments. In general, the depth of the deformation field is approximately equal to the contact radius (chapter 2). Therefore, the depth of the deformation field increased as well, probing deeper regions at later stages of the experiment. By now, it is well established that the actin cortex of mammalian cells is approximately a few hundred nanometers thick[338–341], which is considerably thinner than the particle radius of 1 µm. This is in line with the confocal images acquired with Lifeact-GFP transfected macrophages in this work, where filamentous actin forming the cortex was only observed directly below the membrane (fig. 3.14). It is therefore likely that cytoskeletal structures beneath the cortex, e.g. microtubules and intermediary filaments were probed as well during the later stages of the blinking experiments. Those regions are typically softer than the cortex[341]. Therefore, the model used here, which assumed homogeneous viscoelastic properties, did not fully reflect the rheological geometry of the probed cell regions, especially during the later stages of the experiment.

For example, consider the idealized sketches illustrated in figure 3.15. The cell is idealized as a thin layer resembling the membrane and the actin cortex with viscoelastic properties $j_{0,1}$ and β_1, which is firmly bound to a viscoelastic half space with properties $j_{0,2}$ and β_2. In the following

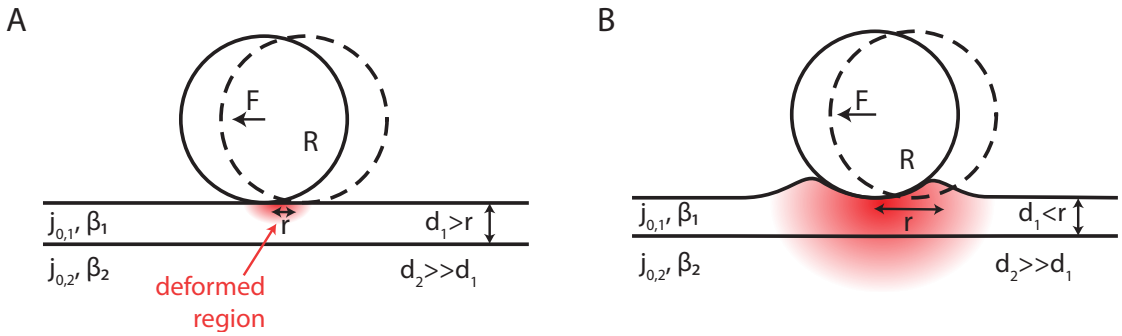

Figure 3.15: Sketch of the changes of the contact geometry during the blinking experiments. Contact geometry of force-strain-experiments, in which an adherent sphere with radius R is stuck on a system of two layers with different thicknesses and different viscoelastic properties. The system consists of a thin layer (thickness d_1) with $j_{0,1}$ and β_1, which is affixed to a thicker layer underneath with parameters $j_{0,2}$ and β_2 assuming a no slip boundary condition. The viscoelastic parameters of both layers are assumed to be different and in particular, $j_{0,1}$ is assumed to be slightly lower than $j_{0,2}$, reflecting the fact that the cortex of mammalian cells is slightly stiffer than the structures below. (A) When the contact radius r is small compared to d_1 and the sphere is pulled to the left, only the thin layer at the top is deformed and probed (red region). (B) In case of $r > d_1$, the deformation field extends to the thick layer below and the measured viscoelastic parameters reflect a combination of both layers' properties.

argument, the assumption that the viscoelastic parameters of both materials are different, yet of roughly the same order of magnitude is implied. This was certainly the case in the experiments as the blinking amplitudes α changed by less than an order of magnitude. In the early phase after the initial binding, when the contact radius r is still small, the deformation field is too small to reach the lower layer (fig. 3.15A) and the measured cellular stiffness mainly reflects the stiffness of the upper layer, i.e. the actin cortex. As the contact radius increases, the depth of the deformation field increases as well and reaches down into deeper regions of the cell. In case the true contact radius increased to roughly the particle radius, it appears likely that the observed decrease of the blinking amplitude resulted from a combination of an increased deformed volume, decreasing the amplitude with time, as well as a gradually increasing influence of regions below the cortex.

It is, however, important to note that both effects, i.e. the increase of the contact area and the deeper sampling depth, which goes along with it, can not be isolated with the present data as both effects inherently happen on the same timescale. In order to resolve the properties of the cortex alone, an approach similar to the experiments presented in chapter 2 could be followed. A combination of differently sized spheres and in particular, smaller spheres with diameter roughly equal to the thickness of the cortex could be used to isolate the properties of the cortex from those of the underlying structures. Difficulties might however arise as such particles are difficult to keep in focus and track automatically. For such an approach and in particular for the mechnical investigation of the phagocytic cup formation, which is driven by the polymerization of cortical actin, the extension of any of the bilayer models described by Mencik et al. and Lüchtefeld et al. to viscoelastic layers could be helpful[341,342].

3.4 Blinking Trap Experiments During Phagocytic Uptake

In this section, the technique described in section 3.3 is advanced with the aim to acquire data of the mechanics of the full phagocytic process, starting with the binding phase and ending with the subsequent transport to the nucleus. As phagocytosis can occur tens of minutes after particle attachment[239], a 3D realtime particle autofocus system was implemented to prevent the particles from leaving the optical trap, enabling prolonged blinking experiments with controlled forces. The optical trap had a lateral size of about 4 µm and trapping forces changed noticeably on a length scale of a few hundred nanometers (fig. 3.5). Thus, the positioning accuracy requirement for such a system is on the order of about 100 nm. Furthermore, phagocytic cup formation is difficult to see with bright field or DIC microscopy. Therefore, Lifeact-GFP transfected cells were used in the experiments to visualize the remodeling of the cortex and to identify cup formation. To simultaneously enable optical trapping, bright field transmission microscopy and fluorescence microscopy, the setup was extended with a set of filters to separate the channels. Due to the high particle localization accuracy requirement and the need for a temporal resolution shorter than 5 s in the fluorescence channel to resolve cup formation, approaches based on moving parts such as shutters or the switching of filters were not an option.

The implemented adaptions to the optical setup are described in section 3.4.1.1. In section 3.4.1.2, a 3D particle tracking algorithm is described, which was used to detect the particle position in real time. The advanced experimental procedure to acquire blinking data during phagocytosis together with the implementation of the 3D feedback loop, which keeps the particle inside the optical trap is described in section 3.4.1.3. The results are presented in section 3.4.2.

3.4.1 Methods

3.4.1.1 Adaptations to the Setup

The setup used for prolonged blinking trap experiments is illustrated in figure 3.16. This configuration enables simultaneous holographic optical trapping to exert modulated forces on the targets (red beam path in fig. 3.16), bright field transmission microscopy for particle localization (grey beam path), and fluorescence microscopy to visualize the cortex of the macrophages (blue and green beam paths). The laser beam path itself was not changed and was used as described in section 3.3.1.4.

For bright field transmission microscopy, the red wavelength regime was used and a long pass filter (RG645; $\lambda > 645$ nm; Schott, Mainz, Germany) was introduced into the bright field illumination path. Bright field transmission microscopy images were acquired with the PCO Pixelfly camera (pco.pixelfly usb, Excelitas PCO GmbH, Kelheim, Germany), which were used to localize the particles during the experiments for the live feedback system. The implementation of the 3D tracking algorithm used to keep the particle in focus during the blinking experiments is described in detail in section 3.4.1.2. Simultaneous high speed data acquisition was done with the IDT NX4-S2 camera. A 20/80 % beamsplitter was introduced into the beam path to direct 80 % of the light to the high speed camera, which required a high intensity for image acquisition. In contrast to the blinking experiments described in section 3.3, DIC microscopy was not used in the measurements performed in this project and in particular, the Wollaston prism inside the objective was removed. The Wollaston prism is built of birefringent crystals and it is designed such that it spatially separates beams of light with perpendicular polarization by a few hundred nanometers inside the sample plane to enable DIC microscopy. The Wollaston prism inside the objective was oriented such that the angle between its ordinary axis and the polarization of the laser beam was roughly 45°. Thus, the laser focus was widened in the sample plane when the Wollaston prism was in the beam path.

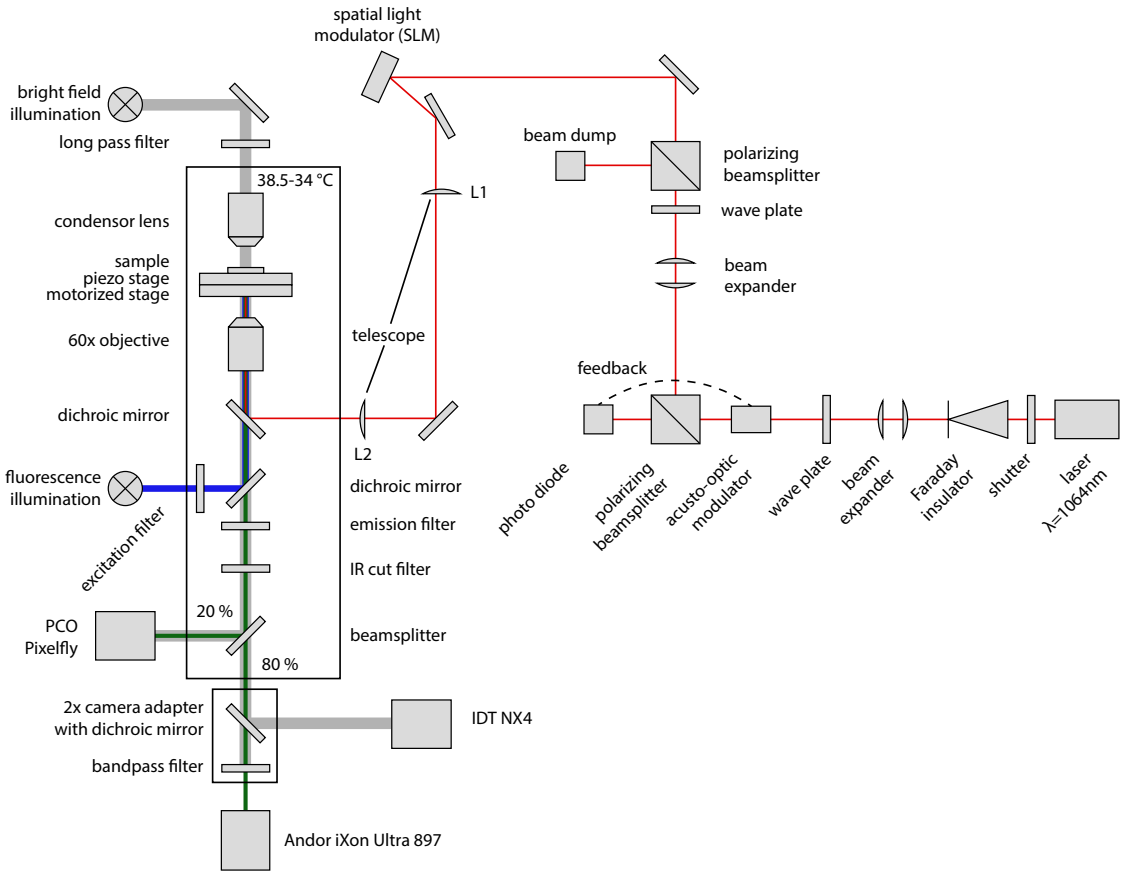

Figure 3.16: Improved optical setup used for prolonged blinking experiments. The configuration enables simultaneous holographic optical trapping (red beam path), transmission microscopy for particle localization (gray beam path), and fluorescence microscopy (excitation: blue beam path, emission: green beam path) to visualize cortical actin. The setup is based on the Nikon Eclipse Ti-E microscope. A detailed description of the imaging setup is provided in the main text in section 3.4.1.1 and a description of the laser beam path used to generate the optical traps is provided in section 3.3.1.4.

Instead, to validate cell morphology and to image the cortex of the macrophages, fluorescence microscopy was used. Fluorescence light from a mercury lamp (Nikon Intensilight C-HGFI; Nikon) was coupled into the beam path via a fluorescence filter cube (GFP-LP; excitation wavelength: 460 - 500 nm, blue beam path in fig. 3.16; dichroic mirror wavelength: 505 nm; emission: long pass filter wavelength: 510 nm, green beam path in fig. 3.16; Nikon). The emission signal was captured with a highly sensitive EMCCD camera (Andor iXon Ultra 897; Andor). To split the bright field and the fluorescence signal for data acquisition, a dichroic mirror (CHROMA zt 605 DCSPXT; $\lambda = 605\,\text{nm}$; Chroma, Bellows Falls, VT, USA) and a band pass filter (Semrock FF01-505/119-25; $445\,\text{nm} < \lambda < 564\,\text{nm}$; SemGroup, Tulsa, Oklahoma, USA) were introduced into the beam path. In the experiments, the intensity of the fluorescence emission signal from the Lifeact-GFP transfected macrophges was far lower than the intensity of the bright field illumination. Therefore, no dedicated filters to block the fluorescence light had to be used in front of the PCO Pixelfly and

the IDT NX4-S2 camera.

To keep the particles inside the optical trap, a piezo stage (PInano PI P-545; Physik Instrumente, Karlsruhe, Germany) was placed on the Nikon microscopy stage to enable precise 3D sample positioning. The piezo stage was addressed by its respective controller (PI nano Piezo Stage Controller PI E-545, Physik Instrumente), which was programmed with the corresponding MATLAB driver. Details about the configuration of the hardware are given in section 3.4.1.3.

3.4.1.2 Implementation of a 3D-Particle Tracking Algorithm

3D realtime particle tracking was implemented with the combination of the 2D particle tracking algorithm introduced in section 3.3.1.5 and a separate z tracking component, which was realized with a convolutional neural network (CNN). The network was trained such that the current z position of a particle is inferred from a tightly cropped image of the particle. To acquire training data, 2 µm-sized particles were sedimented on a coverslip. The sample was placed in the sample mount of the piezo stage and a z-stack was acquired with the PCO pixelfly camera. Training images were acquired with the same conditions used in the cell experiments, i.e. the same filters were inserted into the beam path and image acquisition was done with the PCO pixelfly camera. The camera was used in 2x2 binning mode which, in the blinking experiments, was used to improve the frame rate. Between images, the sample was moved by 100 nm along the axial direction with the piezo stage (fig. 3.17A). A total of 61 images were acquired to achieve a total stack depth of 6 µm. The imaging conditions were varied (e.g. the condensor knob was turned slightly, the voltage of the illumination lamp was changed) to account for slightly variable imaging conditions during the cell experiments. Training data acquisition was done by Johanna Lix. Images of the particles are shown in figure 3.17B. As cells were not present when the training images were acquired, the training images were tightly cropped around the particle (15 pxx15 px, see fig. 3.17B) to minimize the influence of the cells in the blinking experiments on inference accuracy.

The absolute z-position of the particles relative to the focal plane in the bright field channel is not required to achieve high positioning accuracy in the optical trap. Instead, only the displacement relative to the stable trap position is required and thus, an arbitrary reference plane can be chosen. The reference plane $z = 0$ was chosen such that the intensity in the center of the particles (fig. 3.17B, red squares) was highest (fig. 3.17C). This was done on a per-particle basis to account for possibly tilted coverslips during data acquisition (fig. 3.17A).

To simplify the network setup and to speed up the training, the pretrained CNN GoogLeNet[343] was used. The used version of the network had been pretrained with the ImageNet database[344], which consists of images of 1000 categories. The network was adapted to infer the z-position of the particles based on a tightly cropped image of the particle. Therefore, the final fully connected layer of GoogLeNet was replaced with a custom, fully connected layer with an output size equal to the number of planes present in the training data. In figure 3.17D, an abstract sketch of the network is shown. Note that this abstract representation of the network is not representative for the real network. The full structure of GoogLeNet was illustrated by Szegedy et al.[343]. To avoid any bias, the training data was chosen such that an equal number of 6600 particle images for every plane were used for training. An additional 1650 particle images of every plane were used as validation data. Input image data augmentation in the form of random reflection (x and y axis), rotation (0 to 360°), and translation (±3 px) was applied to the training and to the validation data set to regularize the training process[345]. The new network weights were determined by transfer learning[346] without locking the weights of the original network. This was found to be unnecessary for accurate results. Adaptive moment estimation (ADAM)[347] was used to train the network. Training was done on a GPU (Nividia RTX 2070; Nvidia, Santa Clara, California, USA).

A typical output of the network for a sample image is shown in figure 3.17E. The output score

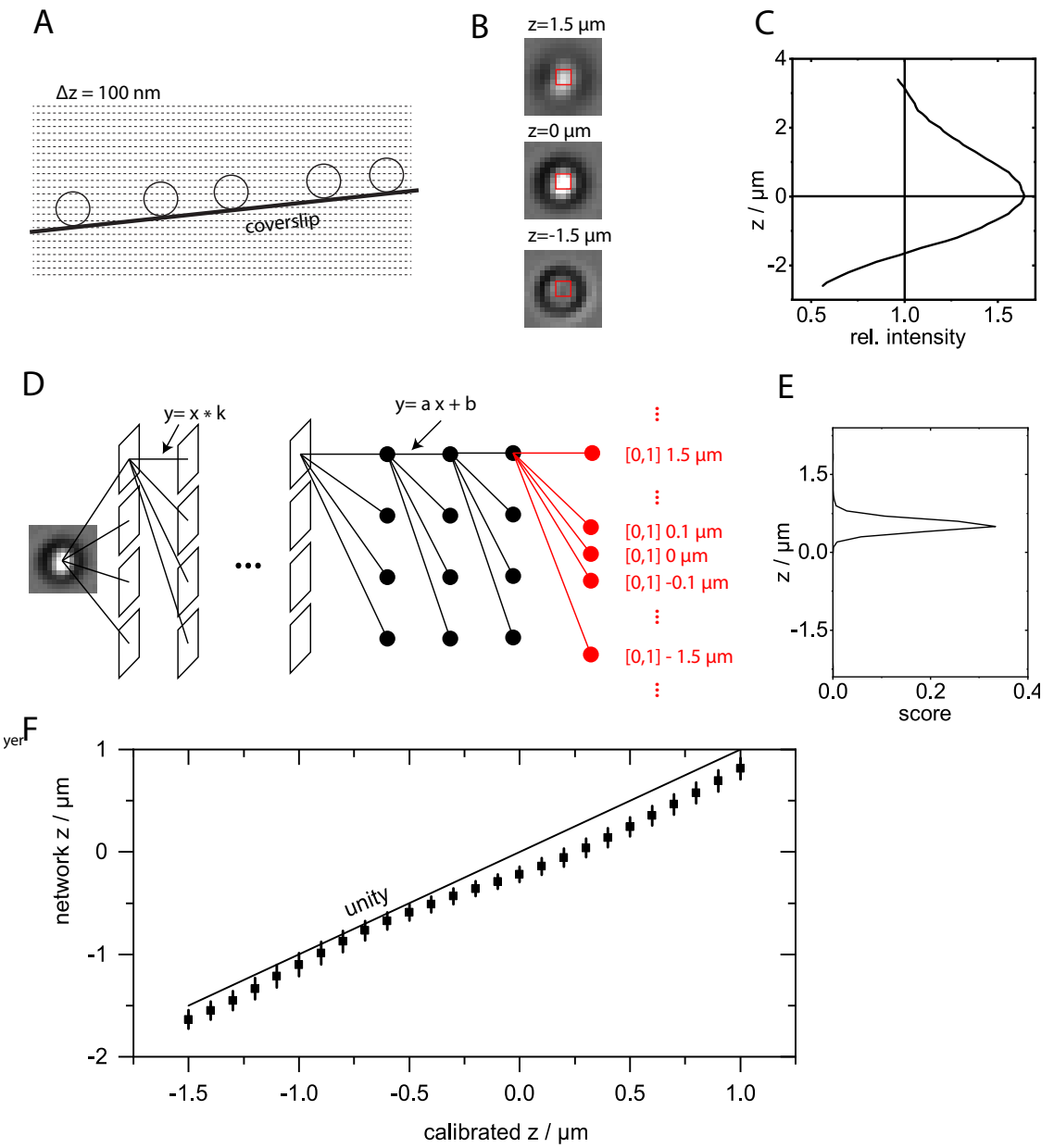

Figure 3.17: Implementation of the axial particle tracking algorithm. (A) Calibration data was acquired by scanning in z-direction through particles with a diameter of 2 µm, sedimented on a coverslip. Between images, the piezo stage was moved by 100 nm. (B) Images of the particles (15x15px), captured at different z-positions. Negative values $z < 0$ indicate that the particle was below the reference plane. To define a reference plane for every particle, the intensity in the center (red squares) of every particle was measured. (C) The plane in which the intensity was highest was defined as the reference plane $z = 0$. (D) The convolutional neural net was trained such that the output of the network was the z-position of the particle. The output scores for every plane ranged from 0 to 1 and the output was normalized, such that the sum of all scores was 1. (E) Output scores of the network for a test data set. The output score peaked near the correct plane. (F) Comparison of the calibrated z-position and the z-position determined by the network. For every plane, 1650 validation images were used. Error bars represent the standard deviation, which was on the order of 100 nm.

peaked at a distinct z-position and output neurons near the correct z plane inferred values greater than 0. To achieve a higher resolution, the output of the network was fitted with a Gaussian function and the mean value was chosen as the best approximation for the z-position of the particle. A comparison of the output of the network to the calibrated z-positions for the validation data set is shown in figure 3.17F. The inferred z-positions were slightly lower than the calibrated z-positions, however, the slope of the calibration curve was close to unity and therefore, relative positioning information could be interred from from particle images. The standard deviation, and thus the localization accuracy, was on the order of 100 nm, which was sufficient for the blinking experiments, given the fact that the particles had a diameter of 2 µm.

The full 3D-tracking algorithm was implemented such that the 2D-particle tracking algorithm based on cross correlation described in section 3.3.1.5 was used to detect the lateral position of the particle. The 2D tracking settings were chosen such that I_{ref} (left image in fig. 3.4) had the same size as the images used to train the axial tracking network described here, i.e. 15 pxx15 px. I_{ref} was then used to infer the z-position of the particle.

3.4.1.3 Prolonged Blinking Trap Experiments

For prolonged blinking experiments, Lifeact-GFP transfected J774 macrophages were cultured, seeded on coverslips and prepared as described in section 3.3.1. The imaging medium was incubated at 37 °C over night to reduce bubble formation. IgG-coated particles (sec. 3.3.1.2) were dispersed in imaging medium directly prior to the experiments to achieve a final concentration of about $25 \times 10^3\,\mathrm{mL}^{-1}$, which roughly corresponded to 5 particles per field of view after sedimentation.

The optical setup described in section 3.4.1.1 was used for imaging. At least 1 h before the experiments, the incubation chamber was heated to 38.5 °C. During the experiments, the heating chamber had to be turned off to minimize vibrations and during one measurement, which lasted for up to 22 min, the temperature in the chamber dropped to about 33 to 34 °C.

The laser power reflected by the SLM was adjusted with the power meter to 300 mW. A 1^{st} order trap was generated, located $(x, y) = (-4/4)$ µm from the 0^{th} order. To maximize the acquisition time of the high speed camera, which ultimately limited the measurement time, binning was set to the highest setting (4x4 px) and the region of interest was chosen just large enough to capture the whole particle (16x16 px). The frame rate was set to 500 Hz, which is just fast enough to capture the particle dynamics during the blinking experiments and the exposure time was set to about 1 ms, which is just slightly shorter than the frame time to minimize phototoxicity. The intensity of the brightfield illumination lamp was adjusted accordingly such that no pixels were overilluminated. With those settings in place, the exposure time of the PCO Pixelfly camera was also adjusted such that no pixels were overilluminated. At the beginning of the experiment, the frame rate of the PCO Pixelfly camera was set to the highest possible value, which was roughly 3 Hz. The fluorescence illumination lamp was turned on and a neutral density filter of 1/512 was set in the excitation beam path to minimize photodamage. The frame rate of the EMCCD camera (Andor iXon Ultra 897, Andor) was set to 0.5 Hz. An exposure time of 1.5 s was chosen, the EM gain was set to 3 at a pixel readout rate of 1 MHz and the multiplier was set to 700. Higher frame times would allow a longer exposure time and thus a lower excitation intensity and less photodamage respectively. However, at considerably longer exposure times, the cells move and thus, motion blur occurs. Thus, cup formation took about 20 s and therefore, a frame rate of about 2 s was required to resolve the dynamic processes of the actin cytoskeleton. Therefore, the chosen setting was a compromise between photodamage and temporal resolution.

Directly before the experiments, the coverslips with the cells were glued to the aluminium holders, immersed in the imaging medium and the holders were sealed with a second coverslip to avoid optical distortions due to the curved water-air interface. The holders were placed on the piezo

stage, which was situated on the microscope stage. Next, a particle was trapped in the 1st order trap and positioned above a macrophage. The heating system of the incubation chamber was turned off and image acquisition was started with all 3 cameras simultaneously. The 3D particle tracking algorithm described in section 3.4.1.2 was used to track the particle in the images acquired by the PCO pixelfly camera. The particle was kept in the optical trap above the cell until the particle had been tracked in at least 80 frames. During this time, the particle diffused freely inside the optical trap and therefore, this time interval was used to define the equilibrium position $(x, y, z) = (0, 0, 0)$ of the optical tap in the images acquired by the PCO Pixelfly camera, which were used as input data for the feedback system. During data analysis, this time frame was also used to define the equilibrium position of the trap in the images acquired with the high speed camera.

The particle was then carefully attached to the cell from the top by moving the objective downwards. After attachment was detected, i.e. after the tracked z position of the particle had changed slightly relative to the focal plane, the automated positioning feedback system and the trap blinking were started. Both systems and the PCO pixelfly camera were controlled with the same computer to synchronize the actions and to avoid piezo stage movement during the blinking events. At the same time, the frame rate of the PCO pixelfly camera was set to 0.5 Hz, which also defined the blinking and the feedback frequency.

The hardware timings are summarized in figure 3.18. In every time step, the 1st order trap was first turned on by switching the supply voltage of the SLM display on. After 600 ms, the 1st order trap was turned off again by switching the supply voltage of the SLM display off. After 600 ms, an image was acquired with the PCO Pixelfly camera, the target particle was tracked and the piezo stage was moved such that the particle was offset by 1 µm along the x-axis, i.e. it was positioned at $(1, 0, 0)$ µm relative to the trap center position. Near this position, the optical force is nearly maximal and thus, the optical force is nearly constant during the blinking events. Details on the trap calibration are given in section 3.4.1.4. Then, the image together with the tracking information was displayed on the screen. As the above-mentioned steps required a variable computation time to complete, a pause was added to precisely control the blinking frequency. The working thread was set to idle and to resume when 2 s had passed since the 1st order trap had been turned on. This implementation ensures that the blinking events can be detected as described in section 3.3.1.7. Then, those steps were repeated. Data acquisition was finally stopped after 22 min, when the internal data storage of the high speed camera was full.

A simpler, uncalibrated implementation of a z-tracking algorithm was used in most experiments shown in section 3.4.2.1 as this version was implemented first. In this simpler implementation, the current intensity in the center of the particle was compared to the median intensity in the center of the particle before attachment (in the experiments, the equlilibrium position of the trap was aligned such that the particle was positioned at roughly $z = -0.75$ µm below the reference plane, fig. 3.17C). To keep the focus, a bang-bang feedback system was implemented. In case the current intensity was too low, the piezo stage was moved upwards by 75 nm and when the current intensity was too high, the stage was moved downwards by 75 nm. With the feedback frequency of 0.5 Hz, this amounts to a maximum feedback speed of 75 nm × 0.5 Hz = 2.3 µm/min, which, in many cases was slower than the axial particle velocity during cup formation. In those cases, particle tracking in the high speed data typically failed during cup formation. Therefore, the calibrated implementation based on neural nets should be used in future experiments.

3.4.1.4 Trap Calibration in Water

In this section, an improved version of the drag force method to calibrate the holographic optical trap is presented. In contrast to the methods described in section 3.3.1.5, trap calibration was not

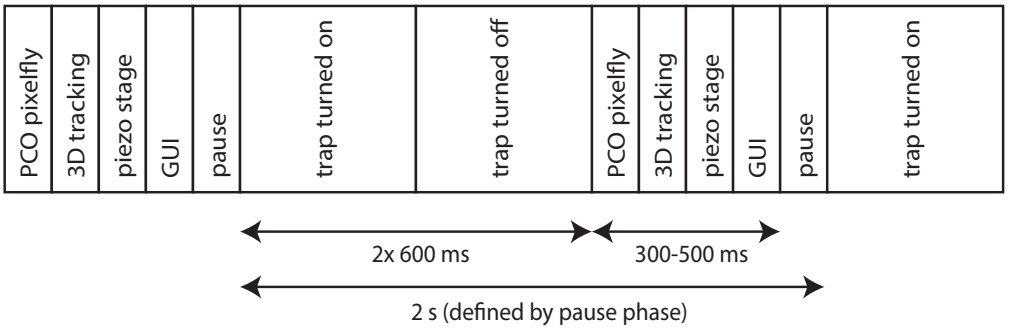

Figure 3.18: Timing of the 3D feedback system. In every period, the 1st order trap was turned on for 600 ms and subsequently turned off for 600 ms by turning the supply voltage of the SLM on and off (fig. 3.6). Then, an image was was acquired with the PCO Pixelfly camera, the particle was tracked, the piezo stage was moved such that the particle was positioned at a defined location relative to the equilibrium position of the optical trap (see main text) and graphics output was displayed on the computer screen. The control thread was set idle to achieve a well-defined blinking frequency of 0.5 Hz.

done in a glycerol solution but in MilliQ water, which has a refractive index similar to 1xPBS or imaging medium[217]. The measurement was done at room temperature at about 20 °C. At this temperature, the viscosity of water is 1 mPas[213]. Furthermore, the Wollaston prism was removed from the objective to mimic the optical conditions of the cell experiments. Whereas the trap was turned off in the experiments described in section 3.3.1.5, this was not done in the experiments described here. In general, the 1st order trap could be turned off either with the shutter or the SLM, the particle could be deflected by stage movement and the trap could be turned on again to observe the relaxation of the particle to the trap center. The shutter was not used to avoid sample shaking. Furthermore, the relaxation back into the trap center position took typically only about 10 ms with the protocol described below, which was shorter than the switching time $\tau_{\mathrm{SLM}} = 17\,\mathrm{ms}$ of the SLM. Thus, particle deflection had to be induced with the trap turned on all the time. This was realized by positioning the sample holder in the piezo stage and by moving the piezo stage rapidly in the x-direction with a commanded velocity of 9.9 mm/s.

With a laser power of 300 mW measured after the SLM, the trap was too strong to deflect the particle with the piezo stage. In general, the stiffness of an optical trap is proportional to the number of photons per unit of time and thus, proportional to the laser power P. Therefore, to weaken the trap, the laser power after the SLM was adjusted to $P = 10\,\mathrm{mW}$. As the 3D feedback system kept the particle inside the optical trap, particle deflection in only one direction, i.e. along the positive x axis had to be calibrated. Optical forces were exerted on the particle up to a particle deflection of about $x = 2\,\mu\mathrm{m}$. As relaxation started during piezo stage movement, the piezo stage had to be moved by about 2.3 to 2.4 µm to deflect the particle by a little less than 2 µm.

At the edge of the trap, the axial trapping stability appeared to dwindle stronger than the lateral trapping stability. The particles were pushed upwards by the scattering force and very often, deflection in the axial direction was noticable during the relaxation even when the particle stayed inside the optical trap. To minimize this, the piezo stage was simultaneously moved by 2.3 µm in the x-direction and 1 µm upwards in the axial direction to compensate the upwards motion introduced by the scattering force. Measurements, in which considerable deflection along the z-axis was noticed were discarded. This was the case in the majority of all measurements.

The experiments were started with the particle positioned 7 µm above the coverslip. Adding the

axial stage motion, relaxation into the trap center position took place 8 µm above the coverslip. The error was estimated to be 1 µm or 13 %. The height above the coverslip was chosen as the relative error of the height above the coverslip was considerably smaller than e.g. 3 µm above the coverslip, as it was where an absolute error of 1 µm amounts to a relative error of 33 %. This setup did, however, assume that the aberrations this deep in the sample were still negligible. In the cell experiments, optical trapping was done above the cells, which were observed to induce some aberrations and those aberrations are difficult to quantify.

Image acquisition was started with the high speed camera at a frame rate of 25 kHz and videos with a total length of 4 s were acquired. Pixel binning was disabled to optimize the localization accuracy. After imaging was started, a command to deflect the particle by $(\Delta x, \Delta y, \Delta z) = (2.3, 0, 1)$ µm was issued to the piezo stage. Data analysis was done as described in section 3.3.1.5. The particle was tracked with the cross correlation algorithm (fig. 3.19A). The relaxation into the trap center position was detected (fig. 3.19A, red) and the instantaneous particle velocity was calculated by deriving the particle position with respect to time. The highest particle velocities during relaxation were on the order of $v = 150\,\mu\mathrm{m\,s^{-1}}$ and thus, the Reynolds number Re was on the order of

$$\mathrm{Re} = \frac{\rho_\mathrm{M} v R}{\eta} = 1 \times 10^{-4} \ll 1,$$

and thus, inertia could be neglected. Here, the density of the medium ρ_M was assumed to be $1000\,\mathrm{kg/m^3}$. The optical force was calculated using equations 3.7 and 3.8. A total of 13 relaxation data sets were acquired and the calculated optical forces were averaged in intervals of 50 nm for $x < 200$ nm and in intervals of 100 nm for $x \geq 200$ nm. The results are plotted in figure 3.19B.

Near the equilibrium position, the linear trap stiffness per laser power $k_\mathrm{x}/P = \mathrm{d}F_\mathrm{opt,x}/\mathrm{dx}$ along the x direction was determined using the equipartition theorem[273]. In thermal equilibrium, a thermal energy of $k_\mathrm{B}T/2$ is associated with each degree of freedom. T is the temperature and k_B is the Boltzmann constant. In a harmonic potential, i.e. in the trap near $x = 0$, the temperature is related to the particle fluctuations by

$$\frac{1}{2} k_\mathrm{B} T = \frac{1}{2} k_\mathrm{x} \sigma^2, \tag{3.27}$$

where $\sigma = \sqrt{< x^2 >}$ is squareroot of the average squared displacement. σ is thus equal to the standard deviation of the particle positions near the equilibrium position (fig. 3.19A, blue), which was determined to be $\sigma = 61$ nm by fitting a Gaussian to the distribution of x (fig. 3.19C). Using equation 3.27, the linear trap stiffness per laser power was calculated to be $k_\mathrm{x}/P = 107\,\mathrm{pN/\mu mW}$. The heuristic fit function

$$\frac{F_\mathrm{opt,x}}{P} = \left(-107\,\mathrm{pN/W} \left(\frac{x}{\mu\mathrm{m}} \right) + 9.9\,\mathrm{pN/W} \left(\frac{x}{\mu\mathrm{m}} \right)^2 - 1390\,\mathrm{pN/W} \left(\frac{x}{\mu\mathrm{m}} \right)^3 \right) \exp\left(- \left(\frac{x}{0.7\,\mu\mathrm{m}} \right)^2 \right) \tag{3.28}$$

was found to nicely reproduce the force response of the trap. For curve fitting, the linear term was fixed at the value determined by the histogram method as noise appeared to be high near the equilibrium position. The fit function 3.28 is plotted together with the experimental data in figure 3.19B. The trap stiffnesses determined by the equipartition theory method and those determined from the step response curve correspond nicely within the range $|x| < 100$ nm, in which the data for the equipartition theorem was acquired. The highest optical force $F_\mathrm{opt,x}/P = 230\,\mathrm{pN/W}$ was measured at $x = 0.85$ µm, which was slightly smaller than the radius $R = 1$ µm of the particles. Linear force scaling was observed for roughly $x < 200$ nm. The trap was far less stiff in the linear regime near the equilibrium position than further outside. This effect has been observed before

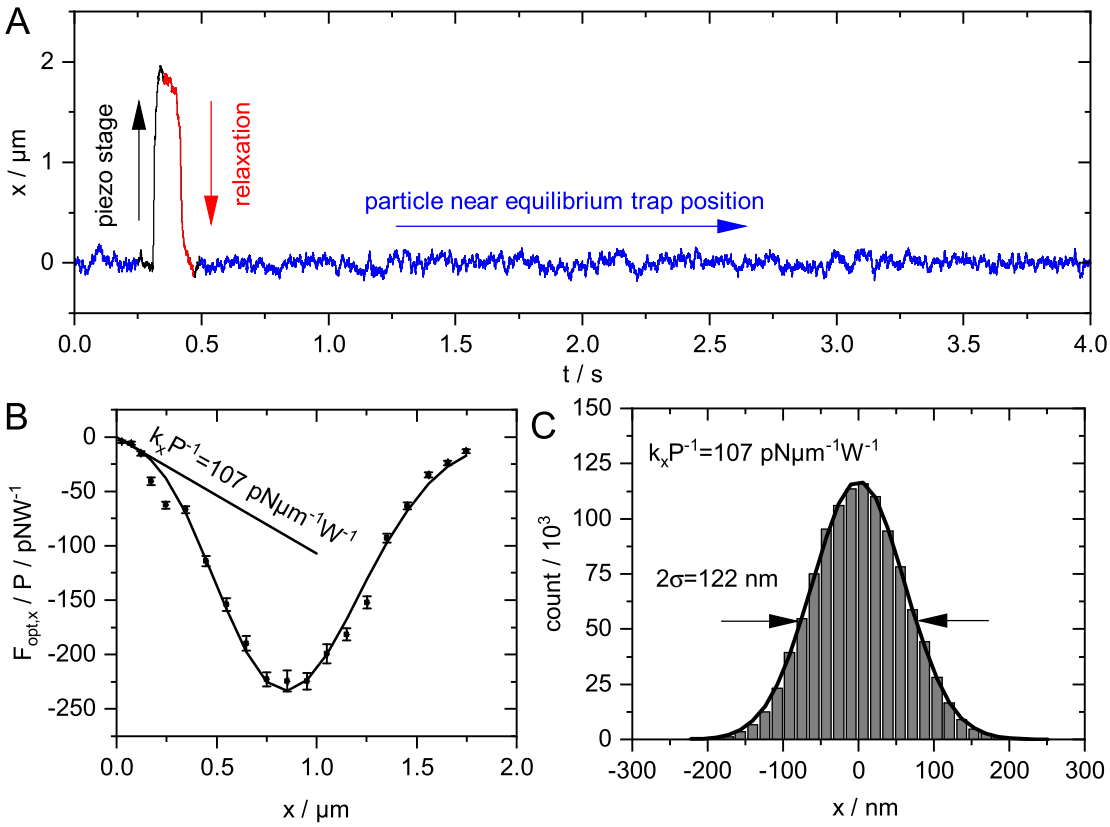

Figure 3.19: Trap calibration in water. (A) A 2 µm-sized particle was trapped inside the 1st order optical trap $(-4/4)$ µm from the 0th order at a laser power of 10 mW. The 60x water immersion objective was used. The piezo stage was used to deflect the particle by about 2 µm in the x-direction (black). The particle relaxed (red) back into the equilibrium position (blue). (B) Optical force normalized to the power after the SLM as a function of the particle deflection x. The optical force was calculated using equations 3.7 and 3.8. The heuristic fit function fitted to F_{opt} is given by equation 3.28. (C) Histogram of the particle positions x in the equilibrium position (blue in panel A). A Gaussian was fitted to the histogram to determine the width of the peak (see main text).

and it can be explained by Mie scattering theory[281,348,349]. In the measurements conducted by K. Berghoff in glycerol[216], the linear range extended to about $x = 500$ nm (sec. 3.3.1.5). There are two possible reasons for this qualitatively different behavior. Firstly, it is possible, that the change of the medium from glycerol to water caused the effect. Secondly, the Wollaston prism, which was in the beam path in the experiments conducted by K. Berghoff, was observed to decrease the beam symmetry in the sample plane and thus, a different trap profile in both experiments is to be expected. The calibration data shown here was therefore not used for the data evaluation presented in section 3.3.

3.4.2 Results

3.4.2.1 Particle Uptake and Cortical Dynamics

In the data acquired by the prolonged blinking experiments, cortical dynamics were analyzed first. The fluorescence intensity of Lifeact-GFP transfected cells was analyzed in all frames in the vicinity of the 2 µm-sized particles to identify the uptake process. In this section, only experiments where uptake was presumably observed are presented. Time series are shown in figures 3.20 and 3.21. For some particles, highly localized actin recruitment was observed in direct vicinity of the particles. Instances where such localized actin recruitment occurred are shown in figure 3.20. Such a localized actin polymerization is consistent with descriptions of FcγR-mediated phagocytic cup formation, where the formation of a thin cup was identified with electron microscopy[96,304,308]. As the particles were opsonized with IgG in the experiments described in this section, such a localized actin recruitment in the direct vicinity of the target particles is referred to as FcγR-mediated phagocytic cup formation from here on. However, it is possible that other phagocytic pathways such as integrin-mediated phagocytosis were also triggered upon the attachment of the particles[72].

In the examples presented here, the onset of cup formation was observed at seemingly random times after attachment. While cup formation started about 110 s after particle attachment in the example presented in figure 3.20A, cup formation was also observed as late as 240 s (fig. 3.20B and 400 s (fig. 3.20C) in other instances. In other examples, no cup formation was observed during the measurement time, i.e. within the first 22 min after attachment. The duration of the local actin recruitment during cup formation was also highly variable. While the particles shown in figures 3.20B and C were engulfed within about 10 to 12 s, cup formation lasted about 20 s in the example shown in figure 3.20A.

From the images, conclusions about the temporal evolution of the cup geometry seem possible. In the example shown in figure 3.20A, actin localizes first in the bottom left region and finishes in the top right region. In contrast, cup formation appears to have been much more symmetric in the case in figure 3.20B, where actin polymerization occurred in a radially symmetric manner.

In other instances, actin polymerization in the vicinity of the particles also occurred, but in contrast to the examples shown in figure 3.20, actin polymerization was not as localized. Instead, considerable membrane ruffling occurred, which extended several micrometers around the particles. Examples of such uptake behavior are presented in figure 3.21. Such uptake morphologies have been associated with other endocytic pathways such as macropinocytosis. In macropinocytosis, actin polymerizes more globally[98]. As a consequence, actin-rich membrane ruffles form, which can extend several micrometers beyond the target and ultimately encompass the target in a seemingly random motion[96,98]. Therefore, when abundant actin-rich ruffling was observed in the vicinity of the target particles, this uptake mechanism is referred to as macropinocytosis below.

In the examples presented here, ruffling in the vicinity of the particle lasted typically a few hundred seconds. In the case of the particle shown in figure 3.21A, ruffling in the direct vicinity of the particle started about 310 s after particle attachment and lasted for about 200 s. While abundant ruffling was observed early, the size of the ruffles diminished and at about 490 s after attachment, actin was located only in the direct vicinity of the target particle, suggesting that the particle was tightly wrapped at this stage. Other examples were membrane ruffling was observed in the vicinity of the particle were less clear. For example, actin-rich ruffles occurred in two distinct phases in the measurement shown in figure 3.21B. Directly after particle attachment, ruffling was observed for about 180 s. Then, ruffling stopped and resumed about 250 s after attachment and continued for another 250 s. In the example presented in figure 3.21C, ruffling started in the vicinity of the particle about 200 s after particle attachment and stopped about 270 s after attachment. Later on, about 530 s after attachment, highly localized f-actin polymerization was observed, resembling phagocytic uptake. Thus, the examples in figures 3.21B and C suggest that terminated membrane

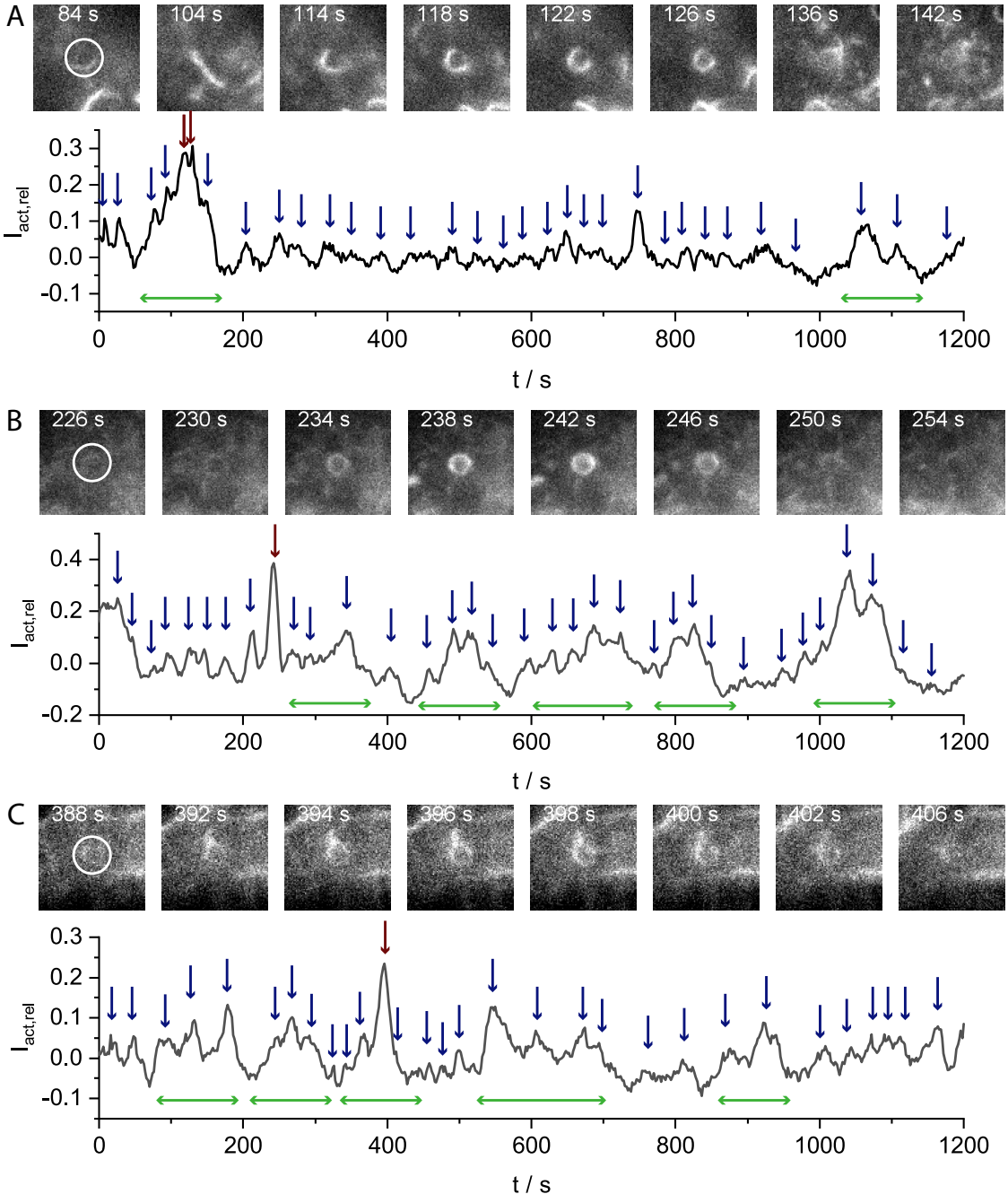

Figure 3.20: Actin dynamics during phagocytic uptake. In panels A, B, and C, three independent measurements are shown. The fluorescence images (11 µm × 11 µm) were acquired during prolonged blinking experiments with 2 µm-sized particles. The fluorescence time traces were calculated by averaging the fluorescence intensity in the direct vicinity of the target particles (white circles, left images) using equation 3.29. Blue arrows mark time points of interim increased actin intensity. Red arrows mark times at which phagocytic cup formation was observed. Green arrows mark times of prolonged actin polymerization. A detailed description is provided in the main text in section 3.4.2.1. The measurement in panel C was carried out by Johanna Lix.

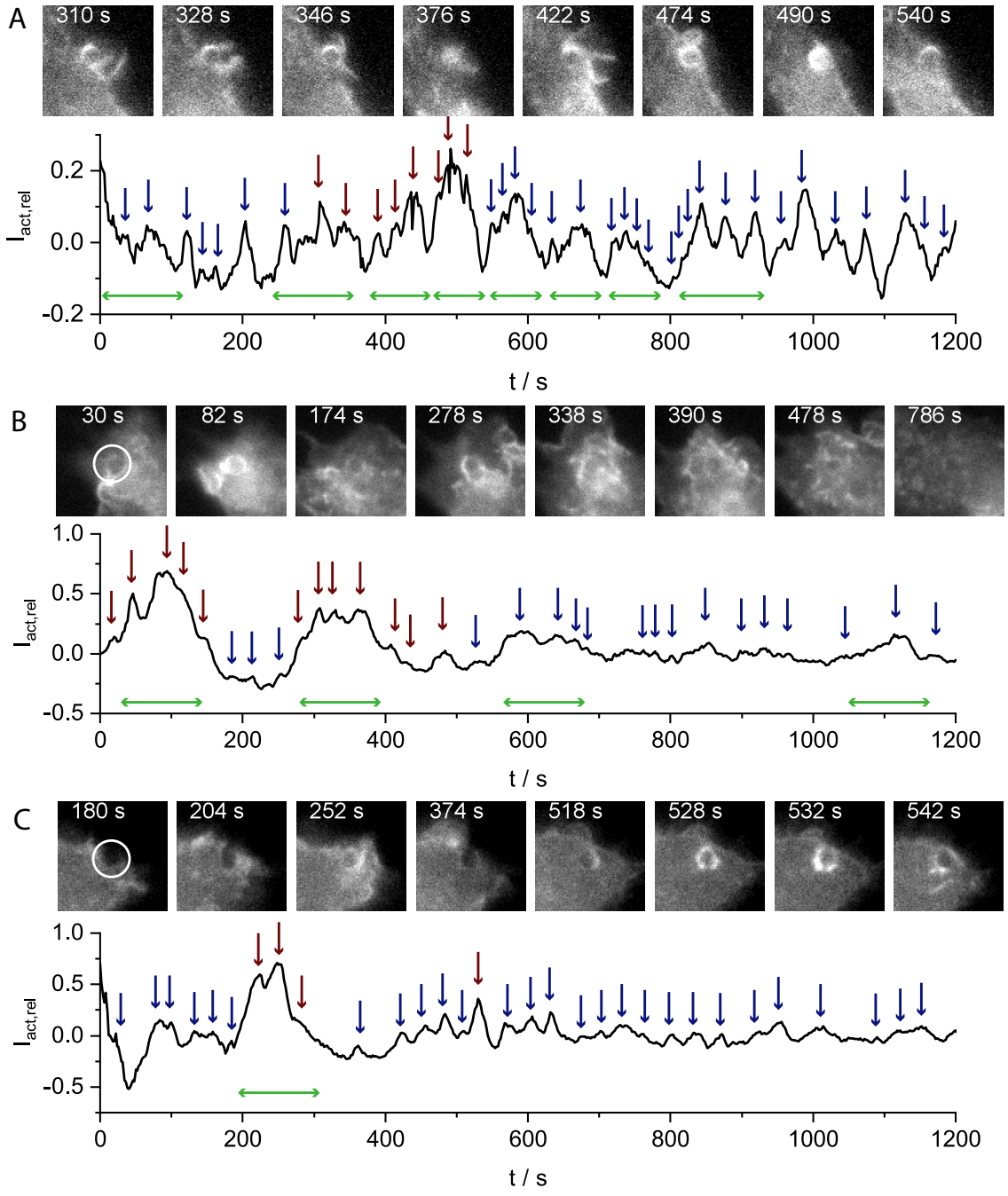

Figure 3.21: Actin dynamics during ruffling in the vicinity of the particle. In panels A, B, and C, three independent measurements are shown. The fluorescence images (11 µm × 11 µm) were acquired during prolonged blinking experiments with 2 µm-sized particles. $I_{\mathrm{act,rel}}$ was calculated by averaging the fluorescence intensity in the direct vicinity of the target particles (white circles, left images) using equation 3.29. Blue arrows mark time points of interim increased actin intensity. Red arrows mark times at which membrane ruffling in the vicinity of the particle and an interim increased fluorescence were observed. Green arrows mark times of prolonged actin polymerization. A detailed description is provided in the main text in section 3.4.2.1.

ruffling alone may not be unequivocal criterion for completed macropinocytosis.

Next, the Lifeact-GFP intensity in the direct vicinity of the phagocytic up was quantified by averaging the fluorescence intensity $I_{\mathrm{act}}(t)$ in the direct vicinity of the target particle (fig. 3.20A, left image, white circle). In some experiments, the intensity varied by more than an order of magnitude within one measurement. To compress the dynamic range, a rolling temporal median filter with a window size of $\pm 100\,\mathrm{s}$ was applied to the data. The relative intensity $I_{\mathrm{act,rel}}$ was defined by:

$$I_{\mathrm{act,rel}} = \frac{I_{\mathrm{act}} - \langle I_{\mathrm{act}} \rangle_{\mathrm{med},\pm 100\,\mathrm{s}}}{\langle I_{\mathrm{act}} \rangle_{\mathrm{med},\pm 100\,\mathrm{s}}} \tag{3.29}$$

where $\langle ... \rangle_{\mathrm{med},\pm 100\,\mathrm{s}}$ denotes the above-mentioned rolling median filter. By definition, $I_{\mathrm{act,ref}}$ is a measure for localized, interim actin polymerization in the vicinity of the target. As the target particles adhered to the cell membrane and as the feedback system counteracted cell motion, $I_{\mathrm{act,ref}}$ was measured in the reference frame of the membrane (in contrast to typical experiments, where fluorescence intensity can only be quantified in the reference frame of the microscope stage). The corresponding time traces $I_{\mathrm{act,ref}}$ are shown in figures 3.20 and 3.21.

During phagocytic cup formation, actin polymerized and therefore, $I_{\mathrm{act,ref}}$ increased temporarily (fig. 3.20, red arrows and fig. 3.21C, right red arrow) The width of the peaks was consistent with the duration of the cup formation identified in the fluorescence images. Generally, the temporal evolution of $I_{\mathrm{act,rel}}$ was vastly different from one cell to the other. While some cells exhibited phases of increased f-actin polymerization, which occurred nearly periodically and lasted for about 75 to 150 s (fig. 3.20B, C and 3.21A, B, green arrows), other cells showed little actin remodeling on this timescale (fig. 3.20A and 3.21C, green arrows). During the times, when macropinocytosis was observed, $I_{\mathrm{act,rel}}$ typically also increased temporarily for roughly 75 to 150 s (fig. 3.21, red arrows).

However, in all cells, actin remodeling occurred quasi-periodically on a much shorter timescale of about 30 to 40 s (fig. 3.20 and 3.21, red and blue arrows) and this timescale was relatively well conserved between cells. In all cases, the period of these oscillations was far longer than the image acquisition period of 2 s and shorter than the median filter window size of 200 s. Interestingly, phagocytic cup formation took about 10 to 20 s, which was roughly equal to or a bit shorter than half of the actin remodeling timescale mentioned above. In both cases, cortical remodeling on both timescales occurred before and after particle internalization.

3.4.2.2 Towards Resolving Uptake Mechanics

During the cell experiments, the optical force on the particles was modulated to measure the viscoelastic properties of the cells. As the bang-bang feedback system used for z tracking was too slow, especially during cup formation, when the instantaneous velocity of the particles often increased, particle tracking of the high speed images was not possible in many of the measurements shown in figures 3.20 and 3.21 (sec. 3.4.1.2). In the measurement acquired in figure 3.20C, the z tracking algorithm based on the convolutional neural net was active. The time traces of the actin signal $I_{\mathrm{act,rel}}(t)$ and that of the displacement $\rho(t)$ are plotted in figures 3.22A, B, and C. In figure 3.22D, an overlay of both time traces during phagocytic cup formation is shown. Time synchronization between both cameras was done manually with a precision of about 5 s. Figure 3.22E shows the position of the piezo stage as a function of time.

About one minute after particle attachment, the automated 3D-feedback system was turned on and the piezo stage compensated the particle motion in three dimensions, keeping it at roughly the same position inside the optical trap. In contrast to the measurement shown in figure 3.8, $\rho(t)$ was thus constant and the particle was positioned roughly 1.2 µm away from the trap center position at the beginning of each blinking event until the end of the measurement (fig. 3.22C, blue arrows).

Thus, the distance from the trap center position was slightly higher than the distance set in the feedback algorithm. A particular reason for this could not be determined. It is however possible that 80 frames at the beginning of the measurement were not enough to accurately determine the equilibrium position of the trap. At $\rho = 1.2\,\mu m$, the optical force at a laser power of 300 mW was roughly 40 pN according to equation 3.28.

Phagocytic cup formation reflected by an actin flash in the vicinity of the particle was observed in the measurement about 400 s after particle attachment. The actin signal was elevated during this time for about 20 s. The piezo stage displacement required to keep the particle inside the optical trap until cup formation was roughly $(\Delta x, \Delta y, \Delta z) = (-0.6, -1.6, 2.3)\,\mu m$, which amounts to a deflection of 2.2 µm in the xy-plane and a total deflection of 3 µm.

Figure 3.20C shows a detailed section of $\rho(t)$ to illustrate the feedback mechanism. The colored arrows denote the timings of the feedback and the blinking implementation. In chronological order, the trap was switched on (red solid arrows) and 600 ms later it was switched off (red dashed arrows). A picture was acquired, the particle was tracked and the feedback was applied, which can be identified by fast, instantaneous particle motion (blue arrows).

A numerical analysis of the individual blinking events to determine j_0 and β was not done in this work. To do so, a precise detection of the individual blinking events, e.g. similar to the methods described in section 3.3.1.7 will be required. Although the background was corrected between blinking events with the feedback mechanism, a correction of the background drift will be necessary to determine j_0 and β from the particle trajectory. This is the case because the slope of $\rho(t)$ reflects cell motion relative to the coverslip and particle motion relative to the cell.

Although such a quantitative analysis was not done in this work, a qualitative analysis of the data is possible as the optical forces at the start of each blinking event were approximately constant during the experiment. After attachment, $\Delta\rho$ during one blinking event was roughly on the order of 50 nm and stayed relatively constant until cup formation (fig. 3.22B). About 400 s after attachment, the amplitude of the cell's step response $\rho(t)$ increased from about $\Delta\rho \approx 50\,nm$ to $\Delta\rho \approx 150$ to 200 nm (fig. 3.22D). As the optical force was roughly constant during the measurement, such an increase of $\Delta\rho$ reflects a softening of the cell. This softening occurred after the actin intensity had peaked.

The motion of the particle relative to the piezo stage coordinate system is encoded in the positions of the piezo stage, which were also recorded during data acquisition. This data may enable the analysis of intracellular transport in the future, which is orchestrated by myosin, dynein, and kinesin motors[154]. In this case, transport relative to the coverslip occurred seemingly erratically. In the first 200 s after particle attachment, the piezo stage had to move very little to keep the particle position stable. From 200 to 400 s, the particle moved mainly in the y direction. Directly during cup formation, no strong particle displacement was observed. Directly after cup formation starting at $t = 400\,s$ however, transport occurred in the xy-plane. Interestingly, the instantaneous velocities before and after internalization were not noticeably different. For example, from $t = 200$ to 400 s, the particle moved by 3 µm, which amounts to an average velocity of about $1\,\mu m\,min^{-1}$ and by 5.4 µm between $t = 400$ and 600 s, which amounts to an average velocity of about $1.5\,\mu m\,min^{-1}$.

3.4.3 Discussion

In this section, the blinking holographic optical tweezer technique was extended to keep the particle in focus, enabling long term blinking measurements while simultaneously visualizing the formation of the phagocytic cup. To simultaneously visualize the formation of the phagocytic cup and enable feedback and optical trapping, filters were introduced into the setup to avoid any moving parts on the optical table.

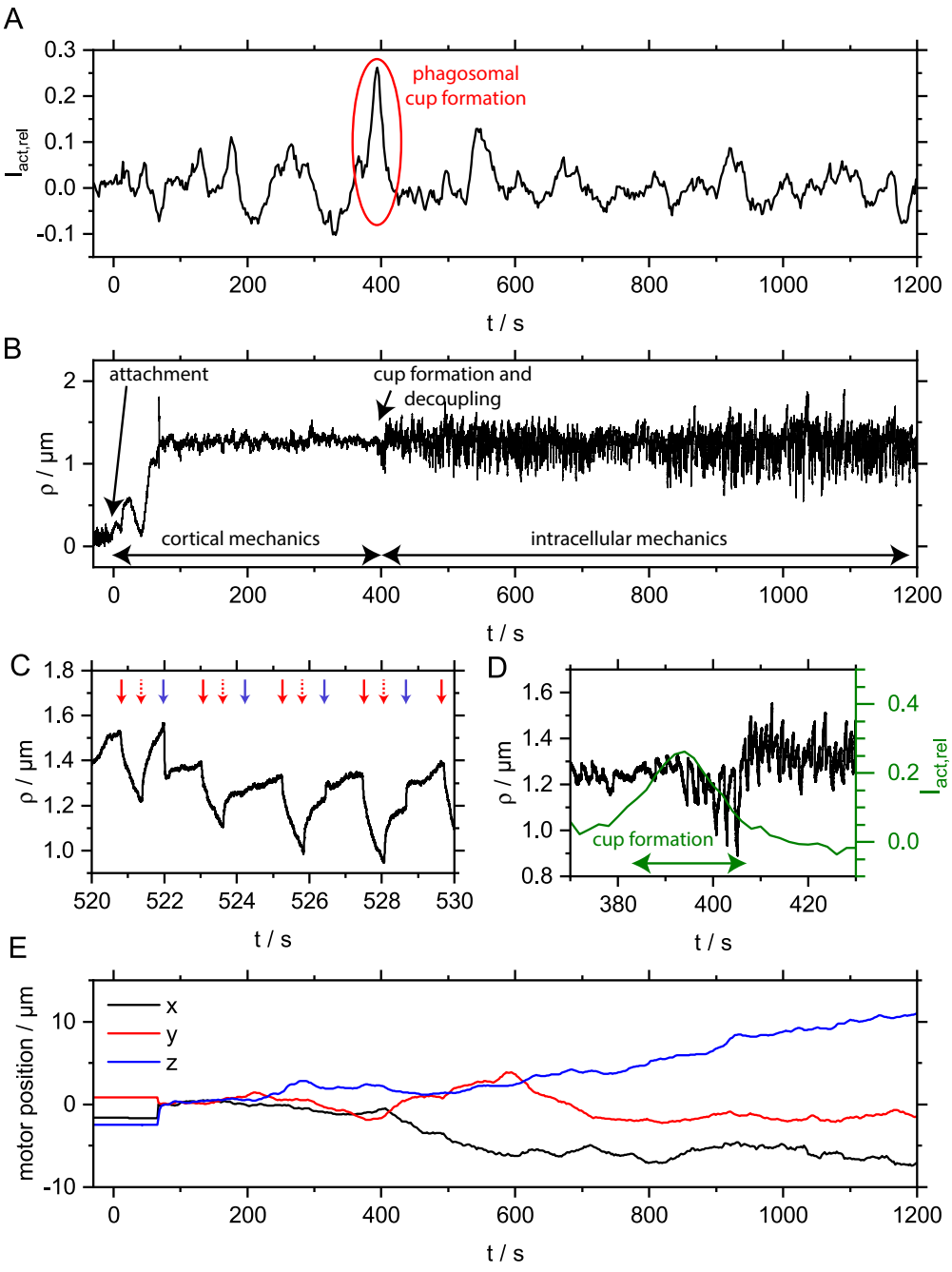

Figure 3.22: Contact mechanics during phagocytosis. (A) The relative actin intensity $I_{\mathrm{act,rel}}(t)$ calculated with equation 3.29 during a prolonged blinking holographic optical tweezers experiment. Phagocytic cup formation occurred between 390 and 400 s after attachment. The corresponding fluorescence images are shown in figure 3.20C. (B) Trajectory $\rho(t)$ of the particle. (C) Timing of the feedback and blinking system (see also fig. 3.18). The trap was turned on (red solid arrows), off (red dashed arrows), and the particle was repositioned with the piezo stage (blue arrows). (D) Overlay of $I_{\mathrm{act,rel}}(t)$ and $\rho(t)$ during cup formation. Time synchronization was done manually with a precision of roughly ±5 s. (E) The corresponding position of the piezo stage. Data acquisition was done by Johanna Lix.

Accurate 3D particle tracking was achieved with a combination of the 2D tracking algorithm based on cross correlation and a convolutional neural net, which enabled axial positioning accuracy on the order of 100 nm. Thus, the particles could be kept inside the optical trap for an extended amount of time, enabling constant optical forces. Furthermore, without the feedback system, focal stacks would be required to reliably image phagocytic cup formation in Lifeact-GFP transfected cells. The acquisition of such a focal stack either reduces the temporal resolution or requires a higher fluorescence excitation intensity, which can cause phototoxicity. Using the 3D feedback system, the acquisition of a focal stack is not necessary, which was demonstrated with uptake experiments.

Preliminary experiments were carried out in the framework of this work to demonstrate the applicability and stability of the setup. It was demonstrated that the visualization of cortical dynamics was possible and that the discrimination of endocytic pathways with different morphologies is theoretically possible. Although a biochemical verification was not done in the framework of this work, tight cup formation resembling FcγR-mediated phagocytosis could be observed. Furthermore, a second uptake mechanism resembling macropinocytosis was observed for IgG-coated particles. In contrast to the tight phagocytic cups, the cells showed extensive membrane ruffling in the region of the target in those cases. However, the distinction between both processes may not always be unequivocal. In the measurement presented in figure 3.20A, there was considerable membrane ruffling before tight cup formation occurred. This is for example visible in the image acquired at $t = 104$ s. Furthermore, in the measurements presented in figures 3.21A and C, membrane ruffling occurred, which was followed by tight cup formation at a later stage. Therefore, clear quantitative criteria may have to be developed in the future to distinguish between both processes. Furthermore, no direct biochemical verification was made in this work to definitively identify the pathways and judgment was made solely based on cortex morphology and dynamics. In future experiments, macropinocytosis could be blocked by treating the cells with the corresponding immunosuppressant drugs. For example, rapamycin[350] or amiloride[351] were previously identified to block macropinocytosis and non-opsonized particles could be used to avoid triggering Fcγ-mediated phagocytosis.

In the fluorescence channel, the present technique revealed quasi-periodic cortical remodeling dynamics in the vicinity of the target. In particular, cortical remodeling was observed in all macrophages with an average periodicity of about 30 to 40 s. Such a quasi-periodic actin remodeling is known in many cell types. For example, wave-like polymerization of actin is known to occur in cell migration in Dictyostelium[352,353], neutrophils[354], keratocytes[355] and fibroblasts[356]. Such wave-like actin organization has been observed to drive membrane protrusions, in particular at the leading edge of migrating cells[355,357–359]. Interestingly, the forces which cells exert on the ECM during migration are characteristic of the cell motility cycle and quasi-periodic undulations on the timescale of roughly one minute were observed, depending on the cell type[80,83,84,93,94].

The mechanism which regulates those waves in the present experiments may be mediated by inositol phospholipids, which are concentrated at the cytosolic surface of cell membranes. Phosphoinositide waves have been shown to regulate cortical and membrane dynamics[360]. It is known that subsequent activation and inactivation of three of these phospholipids can generate oscillatory cortex dynamics with a frequency of a few tens of seconds[361], similar to the faster oscillation frequency observed in this work. Those phospholipids are phosphatidylinositol 4,5-bisphosphate, hereafter called PtdIns(4,5)P_2, phosphatidylinositol (3,4,5)-trisphosphate, hereafter called PI(3,4,5)P_3, and phosphatidylinositol 3,4-bisphosphate, hereafter called PtdIns(3,4)P_2. The reaction kinetics were investigated in detail by Xiong et al., who proposed an activator-inhibitor model for the generation of the observed wave pattern[361,362]. In the reaction, the temporally overlapping interim synthesis of PtdIns(3,4,5)P_3 and PtdIns(4,5)P_2 is quickly followed by the synthesis of PtdIns(3,4)P_2.

PtdIns(4,5)P_2, is known to trigger the activation of the ARP2/3 complex[360,363–365], which me-

diates branched actin polymerization in the phagocytic cup and thus drives membrane protrusion[122,135,137]. PtdIns(4,5)P_2 is also known to promote the dissociation of the actin-severing and capping protein gelsolin[366] and the presence of PtdIns(4,5)P_2 provides additional actin monomers by promoting the dissociation of actin-monomer-profilin-complexes[360,367]. The effects of PtdIns(3,4,5)P_3 polymerization on cortical regulation are similar to those of PtdIns(4,5)P_2, although the effector proteins are often different[360]. PtdIns(3,4)P_2, which is produced after PtdIns(4,5)P_2 and PtdIns(3,4,5)P_3[361], is known to promote cytoskeletal rearrangements such as subsequent podosome formation[368].

These findings were mainly derived from cell migration studies, in which, similar to phagoytosis, Arp2/3 mediated actin polymerization drives membrane protrusions. Furthermore, in both mechanisms, the formation of integrin-mediated adhesion sites behind the leading edge is known, which are believed to prevent actin retrograde flow (sec. 1.2.2.2). In fact, phosphoionosites are known to play a crucial role regulating the cortical machinery during phagocytosis and also during macropinocytosis[369,370]. In particular, propagating phosphoionoside waves have been linked to phagocytic cup formation of rod-shaped particles[371]. Furthermore, wave-like polymerization of actin was observed to be synchronized with PI(4,5)P_2 activity during frustrated phagocytosis in macrophages and it has been hypothesized that these waves are nucleated at Fcγ-R clusters[372,373]. Recently, de Leon et al. proposed a mathematical model of the actin waves observed during frustrated phagocytosis[372,373].

In the present work, the particles were tracked and kept at a constant position in the field of view throughout the measurement and actin polymerization was only quantified locally. Therefore, such traveling cortical actin waves would indeed show up as an oscillatory signal in the fluorescence channel $I_{\mathrm{act,rel}}$, as it was observed in the measurements. In the experiments showing tight phagocytic cup formation (fig. 3.20B, C), it appears as if the amplitude of actin waves propagating in the background was amplified. In those cases, phagocytic cup formation took roughly 15 s, which is approximately half of the period of the actin oscillations in the background, suggesting that cup formation can possibly be regarded as an amplification of the upper half wave. Currently, two models describing the initiation of phagocytosis are under debate. Firstly, the trigger model postulates that cup formation is driven by a burst of FcγR activation. Secondly, the zipper model proposes that cup formation requires subsequent activation of FcγR around the phagocytic target[241,373,374]. The possible wave amplification observed in this work could have been triggered by the binding of Fcγ-R to IgG on the particle surface, supporting the trigger mechanism for the initiation of phagocytosis. A potential test to verify this hypothesis in the future is to fluorescently label PtdIns(4,5)P_2 and cortical actin simultaneously in order to verify that both colocalize in space and time in the cortex and also inside the cup during FcγR-mediated phagocytosis.

The initial, seemingly passive particle binding phase took roughly 100 s, during which the cell-particle contact radius increased. During this time, no indications of any systematic actin polymerization or depolymerization were observed. The mechanism, which triggered phagocytic cup formation appeared to be random to a certain degree. Until the particle in figure 3.20B had been taken up, 8 actin peaks had passed and in the measurement shown in figure 3.20C, 12 actin peaks had passed before cup formation. In other measurements, tight cup formation did not occur and instead, membrane ruffling and possibly macropinocytosis was induced. The picket fence model for phagocytosis appears to be nicely in line with such a random behavior[122,133]. In the picket-fence model, it has been hypothesized that high FcγR mobility is required for receptor clustering and ultimately for signal integration. In case the oscillatory actin signal $I_{\mathrm{act,ref}}$ is solely caused by cortical actin, the measurements acquired here suggest that phases of high and low FcγR mobility may alternate until enough receptor clusters have formed to initiate cup formation. Aside from receptor diffusion, another factor of variance between different particles may be the extent of IgG coating. With secondary antibody staining, K. Berghoff showed that the IgG density achieved

with the present passive adsorption protocol varies considerably from one particle to the next[216]. Therefore, in case IgG is a limiting factor in signal integration in the present experiments, part of the experimental particle-to-particle variance may be explained by the IgG density on the particles. To improve on this, other protocols such as the one suggested by Francis and Heinrich could be tested in the future. The protocol is based on anti-BSA IgG, which is coupled to BSA-coated targets[255]. In contrast to the seemingly random initiation of phagocytic uptake, cup formation itself for such small beads was observed to be highly directed and localized, suggesting a potential trigger mechanism with a threshold. Particle uptake of 2 µm-sized particles took roughly 10 to 20 s and actin polymerization was only observed in the direct vicinity of the targets. This time scale is roughly equal to one half of the above-mentioned actin remodeling time scale, suggesting that the upper half-wave of the actin polymerization cycle may be locally amplified during phagocytosis. A possible test for this hypothesis is to compare the actin fluorescence intensity of the phagocytic cup to the actin fluorescence intensity in the direct vicinity of the cup.

In some cells, actin remodeling appeared to occur also on a longer timescale of about 75 to 150 s. The background of these actin undulations is totally unclear at the present state and can only be speculated about. A possible hint to unravel the background of these undulations is given by the fact that increased actin levels were observed during macropinocytosis, i.e. the times at which the cells also showed extended membrane ruffling in the vicinity of the target particle. Such membrane ruffling has been linked to macrophage activation states[375,376]. During the experiments, the macrophages showed more membrane ruffling, when more IgG-coated particles were added to the samples. Membrane ruffling was however not exclusively associated with cell-particle contact and it is therefore likely that free IgG in the medium caused such membrane ruffling. In this regard, S. Wieland observed the formation of large vacuoles when IgG-coated particles were added to the cells. When the particles were washed, the formation of such vacuoles was significantly reduced, suggesting that the reduction of free IgG in the medium reduced macropinocytosis[377]. To verify whether cortical remodeling on this longer timescale can be induced by the addition of free IgG to the imaging medium, the experiments shown here could be repeated, adding not particles but free IgG at different concentrations to the imaging medium.

The updated blinking technique was demonstrated to be generally capable of resolving cortex mechanics during cup formation. In the experiment shown in figure 3.22, an increase of the blinking amplitude was observed during the second half of cup formation, after $I_{\mathrm{act,ref}}$ had peaked. It must be noted that the refractive index of the cytoplasm of macrophages is slightly higher than that of water and a value of roughly 1.37 has been reported. Thus, the refractive index of the medium surrounding the target changed during cup formation and thus, also the optical forces changed. The observed fourfold increase in the particle amplitude during cup formation can however not be caused by such a slight increase of the refractive index. Instead, it is likely that those amplitude changes indeed reflect changes of the visoelastic properties of the cortex. To verify this hypothesis, precise data analysis taking the background drift of the particle into account is required in the future.

For such a more detailed analysis of the cellular rheology and an analysis of the cellular compliance as well as the power law exponent, adaptations to the mechanical model presented in section 3.3.1.8 may be required. The model assumed that a viscoelastic half space was deformed and that the cell-particle contact radius converged to the particle radius. However, the deformed volume during uptake increases and eventually, the endosome is fully surrounded by the cell, roughly doubling the deformed volume. Therefore, the assumption that the effective contact radius doubles from R to $2R$ may be a reasonable extension to model the contact geometry during endocytic uptake. The corresponding transition timescale can possibly by inferred from the fluorescence images.

An interesting question is the degree to which the mechanical properties of the cup itself were

assessed with the technique. As a thin cup formed around the target, the cup itself was probably not deformed by the blinking trap and thus, also not probed. Considering figure 3.15 and SEM images showing the tight formation of the cup[308], it is more likely that the cortex below the cup was deformed and tested instead. The fact that the blinking amplitude started to decrease while the actin signal was still elevated suggests that cortical decoupling at the base of the cup may have started before cup closure.

3.5 Summary of the Blinking Holographic Optical Tweezers Technique

In this chapter, a technique to measure cellular rheology on the micron length scale was established. The technique is based on blinking holographic optical tweezers, which allow the exertion of optical forces on a target particle attached to a cell. In section 3.3, it was demonstrated that the technique allows the simultaneous measurement of the temporal evolution of the cellular compliance j_0, the power law exponent β, and the contact radius r. Using macrophages treated with different concentrations of CytoD and using traps with different stiffnesses, it was established that the cellular rheology assessed with the technique was mediated by cortical actin. The optical forces, which could be exerted, were on the order of 200 pN. No indications that the laser beam influenced or damaged the cells were observed.

In section 3.4, the blinking holographic optical tweezer setup was extended to enable long term measurements and to simultaneously visualize the endocytic uptake by keeping the particle position relative to the objective constant. Thus, the particle could always be kept in the same focal plane. In this manner, sharp fluorescence images during cup formation could be acquired reliably without any error-prone manual input. Furthermore, the target particles could be kept at roughly the same position inside the optical trap, keeping the optical force at the start of each blinking event constant. This is especially desirable as the rheology of eukaryotic cells is generally nonlinear, as it was observed in this work (sec. 3.3.2.1). Cells can exhibit considerable stress stiffening[237] and strain fluidization[378,379], which may otherwise render the detection of mechanical changes in the cortex difficult.

With these extensions, from the early data presented in this work, it seems possible to discriminate between different uptake pathways by judging the cortical morphology of the cells during uptake. In this work, cortical dynamics during two separate uptake mechanisms, i.e. tight cup formation and uptake via more global membrane ruffling, could be observed. As the simultaneous visualization of the cup formation and cellular rheology is possible with the enhanced setup, the cellular rheology before, during and after internalization can be reliably discriminated, which is not possible with bright field transmission or DIC microscopy alone. In particular, an interesting question to be addressed in the future is whether viscoelastic changes go along with the observed cortical oscillations. Furthermore, after particle internalization, the viscoelasticity in the vicinity of the endosomes can be probed. The technique could, for example, provide data about the mechanical coupling of the endosomes to the microtubule structure, along which endosomes are transported to the nucleus via dynein motor proteins[153]. Furthermore, the mechanics of the transient assembly of filamentous actin around phagosomes[380] could be investigated.

In contrast to magnetic tweezers, optical tweezers offer the possibility to precisely position the target particles and thus, the phagocytic process starting with the binding of membrane receptors to their respective ligands on the target can be initiated in a well defined manner[216]. Therefore, the technique also offers the possibility to deliberately attach the particles to various regions of the cell, e.g. a lamellipodium, the nucleus or regions, in which membrane ruffling occurred even before particle attachment. Recently, Rohrbach et al. demonstrated that it is possible

to detect the binding of individual molecules during the early phase of particle binding using thermal fluctuations[328]. With the data analysis performed in this work, this was, however, not possible. Instead, the binding kinetics were resolved in a more coarse-grained manner by inferring the temporal evolution of the contact radius during particle binding from the cellular step response. The temporal resolution of these contact radius measurements was on the order of 20 s.

The temporal resolution of the individual experiments was defined by the time between two blinking events, which was on the order of 1 s. This should be sufficient to resolve cup formation given the fact that the phagocytic uptake of particles with a diameter of 2 µm took roughly 20 s. Significant improvements to the temporal resolution could be made by modulating the trap intensity with an acousto-optical modulator, which supports switching times in the kilohertz regime. However, this would also require faster signal detection, which is currently limited by the frame rate of the high speed camera. In the implementation described in this work, the temporal resolution for particles detection was 500 Hz. Faster particle localization is possible with a quadrant photodiode, which can give access to particle dynamics with a bandwith in the megahertz regime[381].

The spatial resolution of the rheology measurements was limited to the size of the probe. Thus, the technique provides good resolution on the cell level. However, the resolution will likely not be high enough to measure the cellular viscoelasticity inside the phagocytic cup in a spatially resolved manner. In case cup formation occurs in a tight manner as illustrated in figure 1.2C and as indicated by the fluorescence microscopy images shown in figures 3.20B and C, the cup itself will not be deformed by exerting optical forces on the target particle. Thus, the rheology measured by the current implementation of the technique is likely mediated by or representative of the cortical structure, which mechanically undergirds the phagocytic cup.

To overcome the spatial resolution limit and to resolve the cellular viscoelasticity inside the phagocytic cup, opsonized large polyacrylamide particles with a diameter of roughly 10 µm could be polymerized and attached to the cells. Polyacrylamide has optical properties similar to those of water[74] and thus, such particles do not interfere with the optical trap. A secondary probe could then be attached to certain regions of the phagocytic cup to probe the rheological properties of the cup itself. However, as polyacrylamide particles can not be trapped and attached to the cell membrane in a controlled manner, such experiments are certainly difficult to perform and will require a finite amount of patience.

In general, an adapted filter set could allow the use of a second fluorescent dye to label one additional protein, possibly in the DAPI channel. Possible label targets to investigate phagocytic uptake include IgG[264], FcγR[132], or filamentous actin-associated proteins such as Arp2/3[137], vinculin or integrin[145]. Other interesting label targets are the inositol phospholipids mentioned in section 3.4.3 as well as their corresponding effector proteins. A detailed overview of possible label targets in the inositol phospholipid signaling pathway was given by Xiong et al.[361]. Such an adaptation would however require the switching of the filter cube inside the microscope, which may induce mechanical shaking and thus, invalidate the mechanical blinking data.

4 A Microfluidics Device to Measure Cell-Particle Adhesion

In this chapter, a microfluidic shear flow approach to investigate the adhesion between cells and microplastic particles is presented. The project was done in cooperation with Anja Ramsperger, Simon Wieland, Moritz Lehmann, and Thomas Witzmann. The scanning electron microscopy experiments as well as the cell experiments were done by Simon Wieland. Thomas Witzmann contributed the measurements of the ζ-potential of microparticles and Moritz Lehmann contributed numerical simulations of the flow field around microparticles The microfluidic technique, i.e. the setup and the data analysis was designed and verified by the author of this work. Simon Wieland performed the microfluidic essay and Anja Ramsperger performed the uptake experiments.

Many of the methods and results presented in this section will be published in the following research article:

'Same but different: the choice of model microplastics strongly affects particle-cell interactions ', W. Gross, A. FRM Ramsperger, S. Wieland, M. Lehman, T. Witzmann, S. Gekle, G. Auernhammer, A. Fery, C. Laforsch, H. Kress), in preparation, 2022[382]

If not stated otherwise, all mathematical symbols are redefined in this chapter.

4.1 Microparticle Adhesion and Internalization

4.1.1 Microparticles for Internalization Studies

In studies quantifying particle uptake, the most abundantly used particle material is certainly polystyrene and most studies use spherical polystyrene particles with roughly the same size of a few micrometers[106,246,271,383–385]. However, the absolute uptake efficiencies differ quite drastically between studies. One reason why this may occur is the fact that most laboratories use slightly different opsonization protocols. However, the particles themselves can be produced with a vast variety of different polymerization protocols. For example, different surfactants, initiators or catalyzers can be used to polymerize polystyrene particles, leading to potentially different properties[386–388]. Thus, even studies conducted with untreated particles show remarkably different results. For example, some studies find high uptake efficiencies and even cytotoxic effects with particles purchased from Polysciences (Warrington, PA, USA)[389] and TianJin Baseline Chromtech Research Centre(Tianjin, China)[390], while another study by Stock et al. used microplastic particles purchased from Thermo Fisher Scientific (Waltham, MA, USA) and Kisker Biotech (Steinfurt, Germany) and found only a low uptake efficiency and no adverse effects[391]. Other studies used particles from other manufacturers such as Phosphorex (Hopkinton, MA, USA)[392], Micromod[239,393,394], and MicroParticles (Berlin, Germany)[395]. Recently, Ramsperger et al. showed that plain polystyrene particles from Polysciences and Micromod differed considerably in their monomer content and their surface charge densities[396]. The particles produced by Polysciences showed more cell-particle-interactions than

particles purchased from Micromod[396]. The particles purchased from Polysciences were also internalized more often and the cellular metabolic activity decreased when the cells were exposed to high concentrations of particles from Polysciences, while no such effects were observed for particles from Micromod.

In chapter 3, it was established that internalization is a two stage process. In the first stage, cell-particle contact was established and the contact radius increased with time (sec. 3.3). Only minutes after cell-particle contact was established, phagocytic uptake was observed.. This seemingly random temporal delay indicates that the initiation of the cup formation may generally be largely independent of the initial binding process (sec. 3.4), although cell-particle binding is likely a fundamental necessity for uptake. In this chapter, the role of the cell-particle adhesion strength for particle internalization is investigated. As differences in cell-particle interactions were observed previously for particles from different manufacturers[396], it is likely that the adhesion between the particles and the cells is weaker or stronger, depending on the manufacturer. As such differences were also observed for untreated particles, unspecific adhesion appears to be a major driver of cell-particle adhesion. Unspecific Adhesion can be mediated by electrostatic charges on the surface of the particles. The ζ-potential, i.e. the electrostatic potential at the hydrodynamic slipping plane of the particles, has been hypothesized to be a major factor determining cell-particle adhesion strength[396–398]. A similar observation was made in the experiments described in chapter 2, where it was observed that carboxylated polystyrene particles stuck to coverslips in 1xPBS but not in deionized water, suggesting that electrostatic forces may indeed be one of the major contributors, which mediated particle-coverslip adhesion. Similar observations were also made in the experiments presented in chapter 3. There, it was observed that carboxylated and IgG-opsonized particles stuck firmly to the membrane of macrophages and the contact radius between the cells and the particles appeared to increase with time, independent of cotex mechanics, suggesting that passive adhesion effects may be at play. Thus, the results from previous experiments, both in literature, but also in this work, suggest that cell-particle adhesion may be mediated by particle surface charges. A typical protocol used in internalization essays relies on fixed samples. In such essays, particles are sedimented on cells adhering to a coverslip. The cells are then given some time to internalize the particles and the sample is fixed. Those protocols typically include washing steps, in which non-adherent particles may even be washed away. Thus, there is an undeniable need for a careful calibration of the adhesion in such model systems used for internalization and cytotoxicity studies[399].

4.1.2 Techniques to Quantify Cell-Particle Adhesion

A suitable technique to measure the adhesion strength between cells and extracellular objects both on the single cell and on the single molecule level is atomic force microscopy. For example, one of the major mediators of the adhesion between eukaryotic cells and baceria are bacterial adhesins. The most common of these adhesins of *Escherichia coli* is FimH, which has been shown to form catch bond complexes with mannose in the cell membrane[400]. In contrast to slip bonds, which loosen under tensile stress, catch bonds strengthen under mechanical tension[401]. The high sensitivity of atomic force microscopes ranging down to about 10 pN made it possible to reveal such details about the binding and unbdining kinetics of those bonds between FimH and mannose[402]. However, with an atomic force microscope, the probe has to be glued to a cantilever, which makes every measurement costly and time consuming. Another approach to quantify the adhesion strength is a shear flow essay[403]. In such an approach, a large quantity of particles or bacteria can be tested simultaneously. In the experiments, adherent objects are exposed to a shear flow in a microfluidic chamber and the relative number of detached objects after a given amount of time is quantified. Such experiments have been described for bacteria[403,404] and eukaryotic cells[405]

adhering to coverslips, but also for cell-particle adhesion studies[406–409].

4.1.3 A Microfluidic Shear Flow Essay to Quantify Cell-Particle Adhesion

In order to provide a comprehensive platform to quantify cell-particle adhesion and thus, to calibrate model systems for particle internalization studies, such a microfluidic device was designed and verified in this work. A shear flow essay was conducted to measure the adhesion strength between particles and cells. Inside the microfluidic chamber, a large number of particles adherent to cells and coverslips were exposed to a shear flow and hydrodynamic forces were exerted on the particles to quantify the adhesion strength of all particles simultaneously.

As previous results suggested that the surface properties of particles purchased from various manufacturers can differ drastically, a wide range of nominally identical plain polystyrene particles was purchased from eight different manufacturers. Furthermore, two carboxylated and one amine-functionalized particle type were purchased. The adhesion strength between cells and particles as well as between cells and coverslips was quantified with a microfluidic device. Futhermore, the ζ-potential of all of those particle types was measured to investigate the role of electrostatic charges on cell-particle and cell-coverslip adhesion in a systematic manner.

Inside the microfluidic chamber, particles were allowed to sediment on cells and coverslips. Then a flow was turned on to exert a well-defined hydrodynamic force on the particles. The data was analyzed with automated particle detection and tracking routines. Using artificial intelligence, particles adhering to cell were discriminated from particles adhering to coverslips. In order to quantify the adhesion between the particles and the cells, the binding and unbinding rates, the fraction of irreversible binding events, and the number of particles remaining after the exertion of a hydrodynamic force of 50 pN were quantified. Furthermore, the ζ-potential of the particles was measured and its role in mediating adhesion and particle internalization was investigated. Additionally, the particles were incubated in salt and freshwater to investigate the role of environmental exposure on the ζ-potential, the adhesion strength and on particle internalization into cells.

In section 4.2, the characterization of the microparticles is described. Their surface morphologies were imaged with scanning electron microscopy and their ζ-potential was measured with a zetasizer. The design and the calibration of the flow chambers is described in section 4.3. Finally, the shear flow essays quantifying the particles' adhesion strength as well as the internalization probabilities are presented in section 4.4 of this chapter.

4.2 Microparticle Characterization

4.2.1 Particle Types and Surface Functionalization

In order to investigate the adhesion between different polystyrene microparticles and cells as well was between microparticles and coverslips, particles from 8 different manufacturers were used. An overview over all microparticle types and their respective surface functionalization is given in table 4.1. The abbreviations used in the following for every particle type are also introduced in the table. The particles of 8 types were not surface-modified and as such, designated as 'plain' by the manufacturer. PY-C and MM-C particles were functionalized with carboxyl groups and PY-A particles were functionalized with amine groups. MM particles were additionally incubated for two and four weeks in salt and freshwater by Simon Wieland and Anja Ramsperger to investigate the effects of an eco-corona. Freshwater was obtained from an artificial outdoor pond and salt water was obtained from a marine aquarium facility with a defined salinity of 35 ‰. The particles were incubated in salt and freshwater on a shaker for two and four weeks. Along the way, the water

was exchanged three times per week. Further details on the incubation process were published by Ramsperger et al.[394].

4.2.2 Scanning Electron Microscopy

Scanning electron microscopy was performed by Simon Wieland to characterize the particles' surface morphology and their monodispersity. The microplastic particle stock dispersions were dispersed in deionized water at a concentration of 1 % v/v. 100 µL of these dispersions were each pipetted on a silicon wafer placed on carbon conductive tabs (diameter 12 mm; Plano GmbH, Wetzlar, Germany) and fixed to aluminium stubs (diameter 12 mm; Plano GmbH). In order to fix the eco-corona on the surface of the environmentally exposed particles, Karnovsy's fixative (2 % v/v paraformaldehyde and 2.5 % v/v glutaraldehyde dissolved in 1xPBS) was used. The samples were subsequently dehydrated in an ethanol series (30, 50, 70, 80, and 90 % v/v for 30 min each, followed by 95 % and absolute ethanol for 1 h each. Finally, they were dried in hexamethyldisilazane. The stubs were transferred into a desiccator and coated with a 4 nm thick layer of platinum in a sputter coater (208HR sputter coater; Cressington, Watford, United Kingdom) and imaged using a scanning electron microscope (SEM, FEI Apreo Volumescope; Thermo Fisher Scientific, 5 kV). The particle diameters were measured on the basis of the SEM images.

4.2.3 Measurement of the ζ-Potential

The particles' ζ-potential was measured by Thomas Witzmann (Leibnitz-Institut für Polymerforschung Dresden e.V., Dresden, Germany) with a zetasizer (Zetasizer Nano ZS, Malvern Panalytical, Worcestershire, United Kingdom). The particles were immersed in 0.1 mM KCl at pH 7 and equilibrated at 24 °C for 120 s before the measurements. The results of 3 independent measurements with 50 runs lasting 5 s each were averaged.

4.3 Design and Calibration of the Flow Chamber

4.3.1 Experimental Setup

A sketch of the microfluidic setup to quantify the adhesion strength between the particles and the cells is shown in figure 4.1. The piston of a plastic syringe with an inner radius $R_{\mathrm{piston}} = (6.1 \pm 0.1)\,\mathrm{mm}$ was driven with a high precision linear stage (L511.20DG10; Physik Instrumente, Karlsruhe, Germany) with a defined velocity v_{m} to control the volume flux in the flow chamber. The motor had a maximum velocity of $v_{\mathrm{m,max}} = 6\,\mathrm{mm/s}$ and a maximum drive force of 100 N, which amounted to a maximum pressure of 860 kPa, which could be exerted on the fluid. The syringe was connected to the flow chamber with a tubing system built from polyurethane tubes (PU-S32-85-100, PU-S16-85-100; Piper Filter GmbH, Zwischenahn, Germany). The tubes had an inner diameter of 1.6 and 2.3 mm. Check valves (RVMINI-32, Piper Filter GmbH) were used to drive the flow inside the chamber in one direction, independent of the motors movement direction. The check valves were therefore aligned like diodes in a electronic bridge rectifier. The motor was controlled with a custom-written MATLAB program (MATLAB 2019b; The MathWorks Inc., Natick, MA, USA). A second syringe without a piston was used as a reservoir. The flow chambers were built with a plastic lid (sticky-Slide I Luer, nominal channel height 0.1 mm, nominal width 5 mm, nominal length 48 mm, ibidi GmbH, Gräfelfing, Germany), which was glued to a glass coverslip (24 mm × 60 mm,# 1, Menzel Gläser, Thermo Fisher Scientific Inc., Waltham, MA) with a thin film of epoxy resin (Uhu Endfest Plus; UHU, Bühl, Germany). Care was taken that the resin sealed the channel completely. All parts were connected with luer slip connectors (PP-S32 S32 Y,

Manufacturer	Abbrev.	Product Name	Product Number	Surface Functionalization	Nominal Diameter
Polysciences	PY-A	Polybead Amino Microspheres	17145-5	amine groups	2.96
Polysciences	PY-C	Polybead Carboxylate Microspheres	09850-5	carboxylic groups	3.04
Micromod	MM-C	micromer	01-02-303	carboxylic groups	3
Polysciences	PY	Polybead Microspheres	17134-15	plain	3
Micromod	MM	micromer	01-00-303	plain	3
Microparticles	MG	PS-Forschungspartikel	none	plain	3.03
Kisker Biotech	KI	Polystyrene Microparticles	PPS-3.0	plain	3
Spherotech	ST	none	PP-30-10	plain	3.43
ThermoFisher Scientific	TS	Latex Microspheres	5300A	plain	2.8
Tianjin BaseLine Chromatographic Technology	TJ	Monodispersed polystyrene microspheres	6-1-0300	plain	3
Phosphorex	PX	Polyspherex	11	plain	3.246
Micromod	MM-SW2	micromer	01-00-303	salt water (2 weeks)	3*
Micromod	MM-SW4	micromer	01-00-303	salt water (4 weeks)	3*
Micromod	MM-FW2	micromer	01-00-303	freshwater (2 weeks)	3*
Micromod	MM-FW4	micromer	01-00-303	freshwater (4 weeks)	3*

Table 4.1: **Specifications of all polystyrene particle types used in this study.** Table adapted from Gross et al., in preparation, 2022[382].

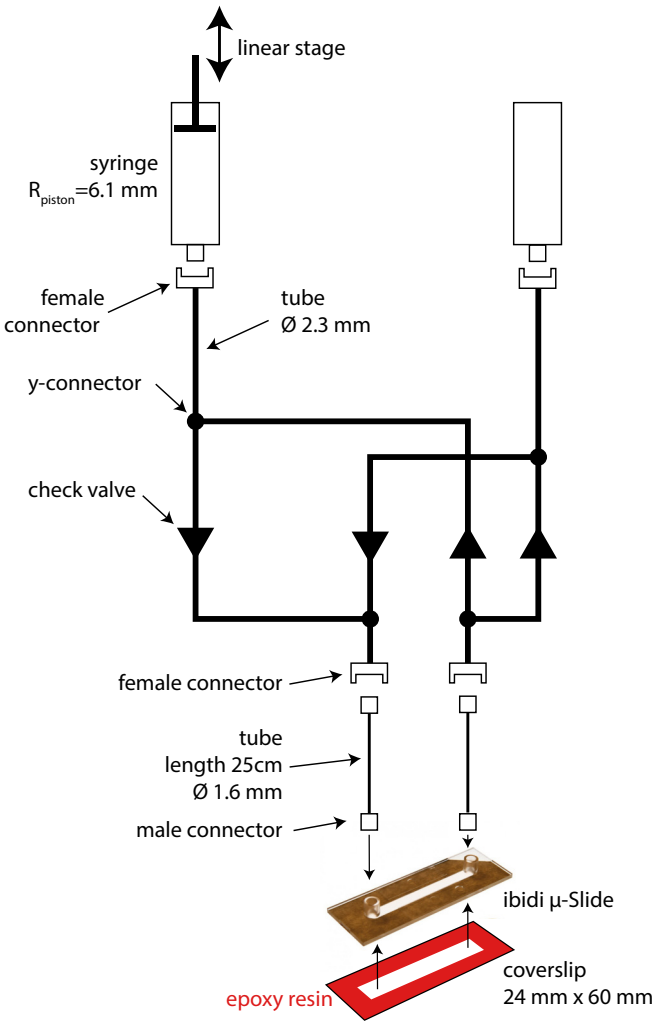

Figure 4.1: Sketch of the microfluidics setup. A high precision linear stage attached to the piston of a syringe was used in combination was check valves to drive the flow inside the flow chamber in one direction, independent of the motor motion direction. Further details about the tubing are given in the main text in section 4.3.1.

PP-LF S32, PP-LMS S15 Piper Filter GmbH, Bad Zwischenahn, Germany). The flow channel was placed on the stage of the Nikon Eclipse Ti-E microscope. The brightfield tranmission microscopy setup illustrated in figure 2.5 was used.

4.3.2 Flow in a Rectangular Channel

In the following sections, the force exerted on a spherical particle located at the bottom of the flow chamber will be derived. For the derivation, an analytical expression of the velocity field of the flow in a rectangular channel is required. The necessary expressions, which assume a stationary, laminar flow, i.e. a Hagen-Poiseuille flow, are introduced in this section. A sketch of the channel

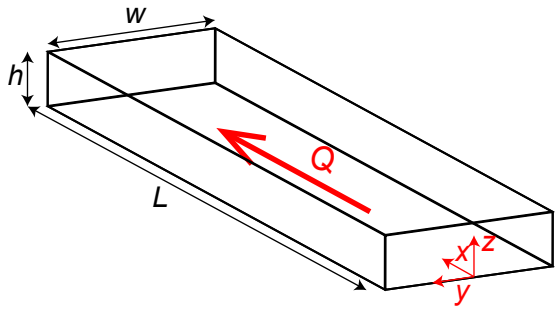

Figure 4.2: Geometry of a rectangular channel with width w, height h, and length L. The fluid flows along the x-axis with a flow rate Q. Figure adapted from Gross et al., in preparation, 2022[382].

geometry is shown in figure 4.2. In a rectangular channel with height h, width w, and length L, the velocity profile $v_\mathrm{x}(y,z)$ is given by[410,411]

$$v_\mathrm{x}(y,z) = \frac{4h^2\Delta p}{\pi^3\eta L}\sum_{\mathrm{n,odd}}^{\infty}\frac{1}{n^3}\left[1-\frac{\cosh\left(n\pi\frac{y}{h}\right)}{\cosh\left(n\pi\frac{w}{2h}\right)}\right]\sin\left(n\pi\frac{z}{h}\right). \tag{4.1}$$

Here, x is the coordinate along the flow direction and y and z are the coordinates defining the plane perpendicular to the flow direction, which satisfy $-w/2 \leq y \leq w/2$ and $0 \leq z \leq h$ and η is the dynamic viscosity. The pressure drop Δp along the x axis due to the viscosity of the fluid is a function of the volume flow rate Q through the channel:[411]

$$\Delta p = \frac{12\eta LQ}{wh^3}\left[1-\sum_{\mathrm{n,odd}}^{\infty}\frac{192h}{n^5\pi^5 w}\tanh\left(n\pi\frac{w}{2h}\right)\right]^{-1}. \tag{4.2}$$

In case $w \gg h$, i.e. when the influence of the boundaries at $y = -w/2$ and $y = w/2$ can be neglected, the velocity profile does not depend on the y-position and equation 4.1 simplifies to

$$v_\mathrm{x}(z) = \frac{\Delta p}{2\eta L}\left(\left(\frac{h}{2}\right)^2-\left(z-\frac{h}{2}\right)^2\right). \tag{4.3}$$

Similarly, equation 4.2 simplifies to[411]

$$\Delta p = \frac{12\eta LQ}{wh^3}. \tag{4.4}$$

4.3.3 Hydrodynamic Force Exerted on the Particles

In order to estimate the hydrodynamic drag force F_h on a sedimented particle with radius R located in the center of the channel, Stoke's law can be used. In general, the velocity at the bottom of the channel satisfies the no-slip boundary condition and, neglecting the spherical particle, it increases linearly as a function of the z-position in the direct vicinity of the bottom of the channel (fig. 4.3).

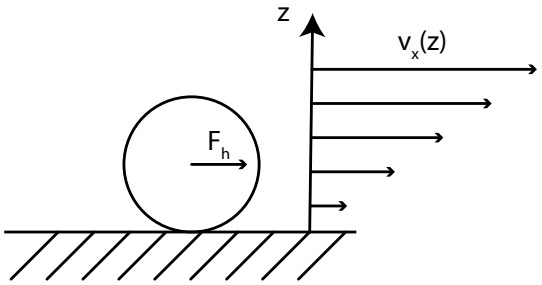

Figure 4.3: Estimation of the hydrodynamic force on a particle located at the bottom of a flow chamber. Neglecting the influence of the sphere, the gradient $\mathrm{d}v_\mathrm{x}/\mathrm{dz}$ is approximately constant near $z = 0$. The hydrodynamic force F_h on the particle can be approximated with Stokes law, assuming that the particle is hit with with an approach velocity $v_\mathrm{x}\,(z = R)$.

According to equation 4.3, the averaged velocity in the interval $0 \leq z \leq 2R$ is thus equal to the velocity $v_\mathrm{x}\,(z = R)$, which is given by

$$v_\mathrm{x}\,(z = R) = \frac{\Delta p}{2\eta L}\left(\left(\frac{h}{2}\right)^2 - \left(R - \frac{h}{2}\right)^2\right) \tag{4.5}$$

$$= 6Q\frac{R\,(h - R)}{wh^3}. \tag{4.6}$$

Neglecting the influence of the interaction between the sphere and the boundary, equation 4.6 can be used to estimate the hydrodynamic force on a sedimented particle. In an infinitely large and homogeneous flow field, the hydrodynamic force F_h exerted on a sphere with radius R is given by Stoke's law:

$$F_\mathrm{h} = 6\pi\eta R v_\mathrm{x}. \tag{4.7}$$

In order to approximate the hydrodynamic force on a particle located at the bottom of a rectangular channel, equation 4.6 is inserted into Stoke's law to yield

$$F_\mathrm{h} \approx 36\pi\eta Q\frac{R^2\,(h - R)}{wh^3}. \tag{4.8}$$

In the experiments, the force on the particle was slightly higher for two reasons. Firstly, as the sphere was in direct contact with the bottom wall, the effective approach velocity was higher than the velocity given by equation 4.6. Secondly, the channels used in this work did not have a perfectly rectangular shape. Instead, the channels were slightly thinner at $y = -w/2$ and $y = w/2$ than in the center at $z = 0$. Compared to the velocity profile in a rectangular channel, the velocity was therefore slightly higher in the channel center than predicted by equation 4.8. Both of those effects were accounted for by two correction factors C_1 and C_2:

$$F_\mathrm{h} \approx 36C_1C_2\pi\eta Q\frac{R^2\,(h - R)}{wh^3}. \tag{4.9}$$

The correction factor C_1 accounting for the proximity to the bottom surface was determined by Moritz Lehmann with boundary element simulations. When $R \ll h \ll w$, C_1 is given by[382]:

$$C_1(R) = 0.002\,56\left(\frac{R}{\mu\mathrm{m}}\right)^2 + 0.069\,62\frac{R}{\mu\mathrm{m}} + 1.507\,57 \tag{4.10}$$

which, for $R = 1.5\,\mu m$, evaluates to $C_1 = 1.61$. The correction factor C_2, correcting for the non-rectangular shape of the channels, is derived in the following section.

4.3.4 Flow in a Parabolic Channel

In this section, the correction factor C_2 for the flow profile in a channel with an inhomogeneous height profile $h = h(y)$ is derived. In a rectangular channel, the flow rate Q is found by integrating the flow velocity $v_x(x, z)$ (eq. 4.1):

$$Q(h, w, L) = \int_{y=-w/2}^{w/2} dy \int_{z=0}^{h} dz\ v_x(y, z). \tag{4.11}$$

Integration yields[411]

$$Q(h, w, L) = \frac{h^3 w \Delta p}{12\eta L}\left[1 - \sum_{n,odd}^{\infty} \frac{192h}{n^5\pi^5 w}\tanh\left(n\pi\frac{w}{2h}\right)\right]. \tag{4.12}$$

For a very wide channel, i.e. $h/w \approx 0$, i.e. when the walls at $y = -w/2$ and $y = w/2$ can be neglected, equation 4.12 simplifies to

$$Q \approx \frac{h^3 w \Delta p}{12\eta L}. \tag{4.13}$$

As described in section 4.3.3, the channel height near the side walls was a few micrometers lower than in the center. As the coverslips used for the experiments were very flat, the inhomogeneous height profile most likely originated from the plastic lid or from an inhomogeneous glue distribution. In general, the height profile could be well described by a parabolic profile of the form

$$h(y) = h_0 + \gamma y + \delta y^2. \tag{4.14}$$

where γ and δ are two arbitrary parameters. Typically, the channels were between $h_0 = 150$ and $200\,\mu m$ high in the center and 10 to $20\,\mu m$ thinner near the edges, which corresponded to $|\gamma| \leq 3 \times 10^{-3}$ and $\delta \approx -2.5\,m^{-1}$.

The total flow rate Q through a channel with such a parabolic height profile can be approximated by the sum of infinitesimally small flow rates dQ, flowing through thin sections of the channel with width dy and height $h(y)$. As the height changes only slightly with respect to y and as the channels used in the experiments were very wide (e.g. $w = 5\,mm$, $h \approx 175\,\mu m$, $w/h \approx 0.04$), the velocity gradients $dv_x(y, z)/dy$ were considered to be negligible for the correction term and dQ was derived from the solution of a wide, rectangular channel given by equation 4.13:

$$dQ = \frac{h(y)^3 \Delta p}{12\eta L} dy. \tag{4.15}$$

Integration yields:

$$Q = \int_{y=-w/2}^{w/2} \frac{h(y)^3 \Delta p}{12\eta L} dy. \tag{4.16}$$

The effective height h_{eff} of the parabolic channel can be identified comparing equations 4.13 and 4.16:

$$h_{eff} = \left(\frac{1}{w}\int_{y=-w/2}^{w/2} h(y)^3\, dy\right)^{1/3} \tag{4.17}$$

$$= \left[h_0^3 + \frac{1}{4}h_0^2\delta w^2 + \frac{1}{4}h_0\gamma^2 w^2 + \frac{3}{80}h_0\delta^2 w^4 + \frac{3}{80}\gamma^2\delta w^4 + \frac{1}{488}\delta^3 w^6\right]^{1/3}. \tag{4.18}$$

Inserting h_{eff} into equation 4.2, the pressure drop Δp_{par} inside a parabolic channel is increased compared to a channel with an homogeneous height h_0:

$$\Delta p_{\mathrm{par}}\left(h_{\mathrm{eff}}\right) \approx \frac{12\eta LQ}{w h_{\mathrm{eff}}^3}\left[1 - \sum_{\mathrm{n,odd}}^{\infty} \frac{192\, h_{\mathrm{eff}}}{n^5\pi^5 w}\tanh\left(n\pi\frac{w}{2h_{\mathrm{eff}}}\right)\right]^{-1}. \tag{4.19}$$

The velocity profile $v_{\mathrm{x,par}}\left(y,z\right)$ in the parabolic channel can then be approximated by adapting equation 4.1:

$$v_{\mathrm{x,par}}\left(y,z\right) \approx \frac{4h\left(y\right)^2 \Delta p_{\mathrm{par}}\left(h_{\mathrm{eff}}\right)}{\pi^3\eta L} \sum_{\mathrm{n,odd}}^{\infty} \frac{1}{n^3}\left[1 - \frac{\cosh\left(n\pi\frac{y}{h(y)}\right)}{\cosh\left(n\pi\frac{w}{2h(y)}\right)}\right]\sin\left(n\pi\frac{z}{h\left(y\right)}\right). \tag{4.20}$$

Firstly, this approximation accounts for the increased pressure drop. Secondly, it ensures that the velocity at the channel boundaries is 0. A verification that $v\left(y,z\right)$ is a good model for the flow field inside the channels is provided in section 4.3.5. Comparing equations 4.1 and 4.20, the velocity in the center of the parabolic channel is increased by a factor of

$$\frac{v_{\mathrm{x,par}}\left(y=0,z\right)}{v_{\mathrm{x}}\left(0,z\right)} \approx \frac{\Delta p_{\mathrm{par}}\left(h_{\mathrm{eff}}\right)}{\Delta p\left(h_0\right)} \tag{4.21}$$

compared to a rectangular channel with height h_0. As the force on a particle is proportional to the velocity in the channel, the correction factor C_2 accounting for the parabolic height profile can be identified to be

$$C_2 \approx \frac{\Delta p_{\mathrm{par}}\left(h_{\mathrm{eff}}\right)}{\Delta p\left(h_0\right)}. \tag{4.22}$$

In the experiments, h_{eff} was small compared to the channel width and consequently, C_2 simplifies to

$$C_2 \approx \frac{h_0^3}{h_{\mathrm{eff}}^3}. \tag{4.23}$$

For a typical channel with a height $h_0 = 165\,\mu\mathrm{m}$, this resulted in an effective height of about $155\,\mu\mathrm{m}$. With equation 4.23, this amounts to $C_2 = 1.2$ or to a 20 % increase of the hydrodynamic force due to the parabolic height profile.

4.3.5 Validation of the Flow Profile in the Parabolic Channel

The flow profile $v_{\mathrm{x}}(y,z)$ in the parabolic channel was measured as a function of the flow rate to verify that the flow velocity is well predicted by equation 4.20. A highly diluted dispersion of carboxylated polystyrene tracer particles with a diameter of $1\,\mu\mathrm{m}$ (Micromod) in MilliQ water with a final concentration of about $2 \times 10^5\,\mu\mathrm{L}^{-1}$ was used to visualize the flow velocity (figure 4.4). The particles were dispersed in MilliQ water because particle-coverslip adhesion was observed to be highly reduced in MilliQ water compared to 1xPBS (see also sec. 2.2.1.3 and 2.2.2), keeping the number of free particles approximately constant during the experiment. To minimize sedimentation during the experiments, the particles were chosen just large enough such that they can be easily resolved, i.e. slightly larger than the wavelength of visible light. Nevertheless, the particles sedimented noticeably and thus, the first measurements were conducted near $z = h$, measuring from the top to the bottom. The stock particle dispersion was highly diluted to avoid ambiguities during particle tracking and thus, to maximize tracking accuracy and reliability. The dispersion

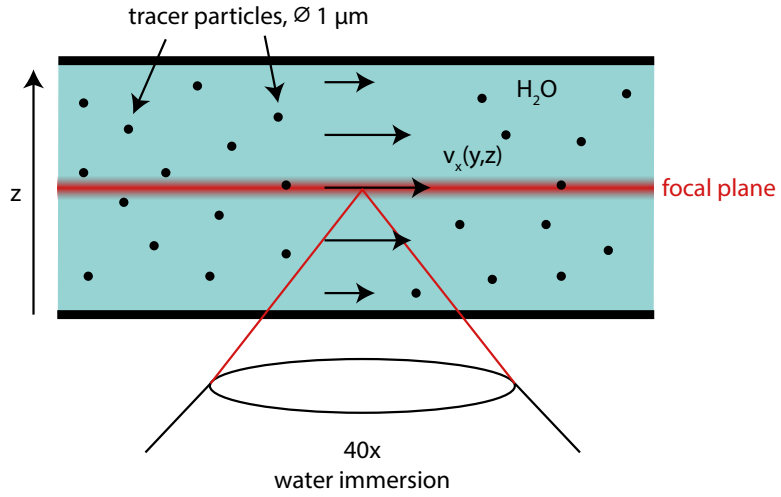

Figure 4.4: Sketch of the flow chamber calibration experiments. Polystyrene particles with a diameter of 1 µm were immersed in water an flushed through the channel. The particle motion was imaged in different focal planes and at various positions (x, y). Imaging was done with the 40x objective and the high speed camera with frame rates of up to 2000 Hz.

was filled into the tubing system as described in section 4.3.1 and pumped through the channel. The motor velocity v_m was set according to

$$v_\mathrm{m} = \frac{Q}{\pi R^2_\mathrm{piston}} \tag{4.24}$$

to achieve a flow rate of 0.2 µl/s. The particles were imaged with the 40x objective, which was chosen as it provided a reasonably small focal depth due to its high numerical aperture of 1.15 and a reasonably large field of view. Images were acquired at different positions (y, z) with the IDT NX4-S2 high-speed camera at frame rates of up to $f = 2$ kHz, which was the limit of the camera in full frame mode without pixel binning.

The images were preprocessed with a spatial band pass filter. The band pass was implemented by filtering the raw images with a Gaussian filter with a width of 0.5 µm, resulting in an image $I_>$ of mainly long range image features such as vignetting effects. Noise in the original images was removed by filtering the original images with a gaussian filter with a width of one pixel (i.e. 0.16 µm, resulting in an image $I_<$ of the particles and the long range image features. The band pass filtered image I_bp showing only the particles was then calculated by subtracting both images:

$$I_\mathrm{bp}\,(i,j,t) = I_<\,(i,j,t) - I_>\,(i,j,t)\,. \tag{4.25}$$

Here, i and j denote the indices of a pixel in the images acquired at time t. The time series of those bandpass filtered images was then filtered with a pixel-wise rolling median filter in time to isolate all stationary image features:

$$I_\mathrm{med}\,(i,j,t) = < I_\mathrm{part}\,(i,j,t) >_\mathrm{med,5}\,. \tag{4.26}$$

Here, $< \ldots >_\mathrm{med,5}$ denotes the rolling median filter in time calculated for every pixel from time $t - 5/f$ to $t + 5/f$. The filtered images, which were used for particle detection showing only moving

particles were then calculated with:

$$I_{\text{filtered}}(i,j,t) = I_{\text{bp}}(i,j,t) - I_{\text{med}}(i,j,t). \tag{4.27}$$

The particles were detected in I_{filtered} with a custom-written peak finding routine based on the version published by Style et al.[51] and tracked with a Matlab implementation of the particle tracking algorithm originally published by Crocker and Grier[51,412]. The code was implemented in MATLAB 2019b. For every position (y, z) inside the channel, the velocities obtained from 50 to 100 particle trajectories were averaged. As the focal depth of the objective was a few micrometers deep, particle trajectories located in planes a few micrometers below and above the focal plane were picked up as well by the imaging and by the particle tracking algorithm. Near the channel center at $z = h/2$, this effect could lead to a slight underestimation of the flow velocity as v_{x} was highest at $z = h/2$. At all other z-positions, the influence of those particles located below the focal plane should negate the influence of those particles located above the focal plane and the errors should cancel each other out.

The results are shown in figure 4.5. Within the margin of error, the measured flow field $v_{\text{x}}(x, z)$ was in excellent agreement with the theoretical prediction $v_{\text{x,par}}(y, z)$ predicted from the motor velocity v_{m} using equations 4.19, 4.20, and 4.24, demonstrating that the theory derived in section 4.3.4 was suitable to predict the flow field in a channel with a parabolic height profile $h(y)$. However, the measured velocities were up to 7 % lower than the theoretical prediction at almost all y and z positions. An overestimation of R_{piston} could have been the cause of these deviations. Furthermore, the assumption that the flow field $v_{\text{x,par}}$ inside the parabolic channel can be approximated with equation 4.20 could also be the reason for the systematic deviations.

Furthermore, linear scaling between the flow rate and the flow velocity was validated by measuring the flow velocity in the channel center at $y = 0$ and $z = h/2$ for flow rates between 0.2 and $2\,\mu\text{l}\,\text{s}^{-1}$. For example, non-linear scaling could have occurred, when the pressure gradient inside the check valves was not high enough to properly close them at low flow rates. The frame rate of the high speed camera was adjusted to different frame rates depending on the flow rate. The camera was fast enough to capture the particle motion with sufficient temporal resolution for particle tracking up to a flow rate of $Q = 2\,\mu\text{l}\,\text{s}^{-1}$, which corresponded to about $v_{\text{x}} = 3\,\text{mm}\,\text{s}^{-1}$. The results are shown in figure 4.6, demonstrating that the flow velocity scaled linearly with the flow rate inside the channels and that the flow velocities could be predicted from equations 4.19, 4.20, and 4.24. As both the shape and the magnitude of v_{x} were in excellent agreement with $v_{\text{x,par}}$ derived in section 4.3.4, the correction factor C_2 was used to correct the forces exerted on the particles in the parabolic channels.

4.4 Quantification of the Particles' Adhesion Strength

4.4.1 Methods

4.4.1.1 Microfluidics Experiments

In order to quantify the adhesion strength between microplastic particles and cells as well as coverslips, murine J774 macrophages were seeded inside the channels. Cells were cultured as described in section 3.3.1.1. In order to prepare the cells for the channels, the cells were scraped off the cell culture flasks prior to the experiments, centrifuged at 150 g at 20 °C for 2 min and the supernatant was removed. They were re-suspended in 600 µL of cell culture medium (sec. 3.3.1.1). 200 µL of cell suspension was used for every channel and the channels were incubated at 37 °C in 5 % CO_2 for 1 h until the cells adhered to the coverslip at the bottom of the chamber.

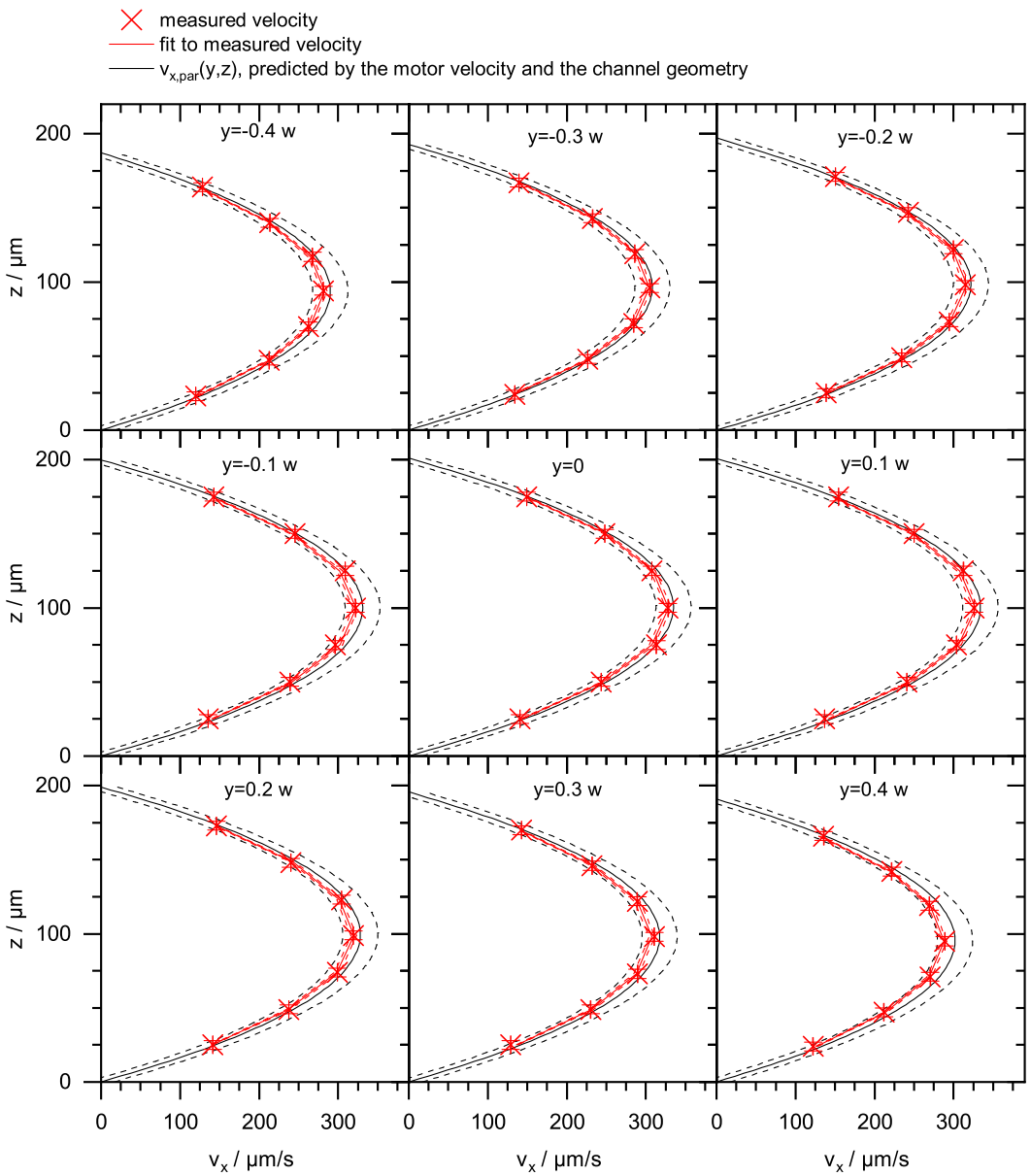

Figure 4.5: Velocity profile $v_x(y, z)$ inside a channel with a parabolic height profile. The flow rate was set to 0.2 µl/s, which corresponded to $v_m = 1.69\,\mu m\,s^{-1}$. The channel was $h_0 = (201 \pm 2)\,\mu m$ high in the center and approximately 15 µm thinner near the side walls, which corresponded to $\gamma = 0.95 \times 10^{-3}$ and $\delta = -3.0\,m^{-1}$. Every data point (red crosses) represents the mean velocities obtained from 50 to 100 particle trajectories and the corresponding error bars represent the standard deviation. Red lines represent fits of equation 4.20, in which the velocity in the channel center was used as the only free parameter. Errors of the fit were determined with Monte-Carlo simulations considering the errors of the measured velocity v_x. Black lines indicate the flow profile $v_{x,par}$ predicted from the motor velocity v_m using equations 4.19, 4.20, and 4.24. The errors of $v_{x,par}$ were determined with Gaussian error propagation considering the errors of w, h, y, z, R_{piston}, and v_m (black dashed lines). Figure adapted from Gross et al., in preparation, 2022[382].

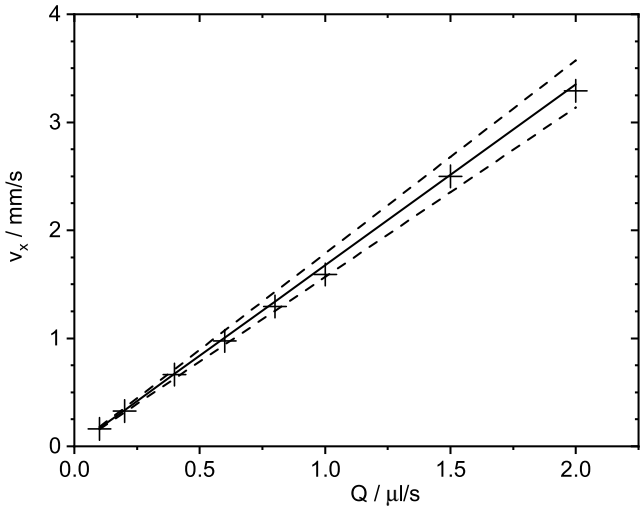

Figure 4.6: Velocity $v_\mathrm{x}\,(y = 0, z = h/2)$ in the channel center as a function of the flow rate Q. Crosses represent the measured velocities $v_\mathrm{x}\,(y = 0, z = h/2)$. The line represents the flow velocity $v_{\mathrm{x,par}}$ calculated from equations 4.19, 4.20, and 4.24. The predictions' errors were determined with Gaussian error propagation considering the errors of w, h, y, z, R_piston, and v_m. Figure adapted from Gross et al., in preparation, 2022[382].

Imaging medium (Minimum Essential Medium, Thermo Fisher Scienfitic Inc.) was supplemented with 5 % HEPES (Thermo Flisher Scientific Inc.) as a pH buffer and 1 % penicillin-streptomycin. The medium was incubated at 37 °C for at least 12 h to get rid of dissolved gasses, with tended to form air bubbles in the flow system during the experiment otherwise. Microparticles were added to the solution directly prior to the microfluidic experiments. Live cell imaging was performed on the inverted microscope (Nikon Eclipse Ti-E, Nikon) with a 10x objective (CFI Plan Fluor DL 10x, Nikon, $NA = 0.3$). A CCD camera (pco.pixelfly usb; PCO AG, Kehlheim, Germany) was used for image acquisition with a frame rate of 1 Hz. The microscope, the tubing and the syringes were placed inside the custom-built incubation chamber described in section 2.2.2 and kept at 37 °C during the experiments. The camera and the precision stage were controlled with a custom-written MATLAB program (MATLAB 2019b, The MathWorks Inc., Natick, MA, USA).

At the start of each experiment, the camera acquisition was started. Each experiment consisted of three phases. In the first phase, a low flow was briefly applied to flush the particles into the flow chamber (fig. 4.7A) and the flow was turned off again. In the second phase, the particles were allowed to sediment for 10 min (fig. 4.7B). During this sedimentation phase, a combination of image analysis and particle tracking was used to reveal the binding and unbinding kinetics between particles and cells and between particles and coverslips when no force was exerted. The sedimentation data analysis is described in detail in section 4.4.1.2.

After the sedimentation phase, the flow was turned on, which defined the start of the rupture phase (fig. 4.7C). The motor velocity was chosen such that the hydrodynamic force on the particles was $F_\mathrm{h} = (50 \pm 5)\,\mathrm{pN}$ in all cases. The error was estimated from the relative error of the velocity field, which was about 10 % (fig. 4.5). Equations 4.9 and 4.24 were used to calculate the corresponding motor velocity v_m:

$$v_\mathrm{m} = \frac{1}{\pi R_\mathrm{piston}^2} \frac{F_\mathrm{h} w h^3}{36 C_1 C_2 \pi \eta R^2 (h - R)}. \tag{4.28}$$

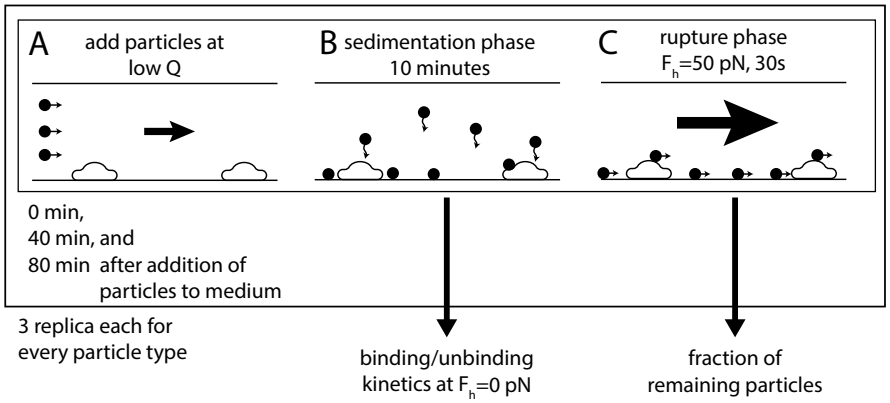

Figure 4.7: Sketch of the microfluidic experiments. The particles were added 0, 40, and 80 min before the experiment to the medium. (A) At the beginning of an experiment, the particles were flushed into the chamber at a low flow rate. (B) The particles were allowed to sediment and adhere for 10 min (sedimentation phase). (C) The flow was turned on with the flow rate necessary to exert a hydrodynamic force of (50 ± 5) pN on the particles (rupture phase). Three replica of every experiment at every time point were performed for every particle type. Thus, a total of 9 experiments was conducted with every particle type. The particles' binding and unbinding kinetics were analyzed during the sedimentation phase. In the rupture phase, the fraction of remaining particles after the exertion of $F_\mathrm{h} = 50$ pN for 30 s was analyzed.

The dynamic viscosity η of the medium was assumed to be equal to the viscosity of water at 37 °C, which is 0.7 mPas[213,413]. As the channel geometry and consequently also C_2 differed slightly from channel to channel, the height profile $h\,(y)$ of every channel was measured before each experiment. $h\,(y)$ was measured in the experiments by focusing on the top and bottom channel surfaces with the 10x objective. The measured height was corrected using equation 2.3.2 and the assumptions, that the refractive index of air is 1.0 and that the refractive index of the medium is equal to that of water ($n_\mathrm{w} = 1.33$[217]) were used. A typical height profile resulted in a correction factor C_2 of ≈ 1.2.

Thus, for a typical channel geometry with $h_0 = 165\,\mu\mathrm{m}$, $w = 5$ mm, and $L = 48$ mm, the flow rate corresponding to $F_\mathrm{h} = 50$ pN was approximately $20\,\mu\mathrm{l\,s^{-1}}$, which corresponded to $v_\mathrm{m} = 0.1$ mm/s. According to equation 4.4, this amounted to a pressure drop of $\Delta p \approx 350$ Pa $= 3.5$ mbar inside the chamber. In this case, the velocity at $z = R$ was approximately $v_\mathrm{x}(z = R) = 1.3$ mm/s and in the middle of the channel, the velocity was approximately $v_\mathrm{x}(z = h/2) = 35$ mm/s according to equations 4.3 and 4.6. With respect to the sphere, the Reynolds number was given by:

$$\mathrm{Re} = \frac{\rho R v_\mathrm{x}(z = R)}{\eta} = 3 \times 10^{-3}. \tag{4.29}$$

With respect to the channel geometry, the Reynolds number can be defined by:

$$\mathrm{Re} = \frac{\rho D v_\mathrm{x}(z = h/2)}{\eta} = 16, \tag{4.30}$$

where the hydraulic diameter $D = 2hw/(h + w)$ of the chamber was used as the characteristic length scale[414]. In general, the critical Reynolds number in tubes is difficult to assess as it depends, among others, on the aspect ratio[415,416]. For rectangular channels with an aspect ratio similar to

the one used in this work, critical Reynolds numbers are typically reported to be above 1000[414,415]. During all calibration experiments and during all cell experiments, straight particle trajectories were observed far away from the cells, indicating laminar flow in the channels. The data analysis of the rupture phase is described in detail in section 4.4.1.3.

In general, it is possible that components in the imaging medium adhered to the particle surfaces, altering the cell-particle and cell-coverslip binding kinetics over time. Furthermore, it is possible that sticky particles adhered to the syringe, the tubing or the check valves, which could have altered the average adhesion behavior of the particle ensemble in case the individual particles of one particle type were not identical. For this reason, identical experiments were performed 0, 40, and 80 min after the particles were added to the imaging medium and for each time point, 3 independent replica of the experiment were carried out (fig. 4.7).

After each experiment, the channels were cleaned for reuse. Any remaining cells and particles were removed by cleaning the channels with trypsin, deionized water and 70 % ethanol for 10 min each. The imaging medium was discarded and the tubing was thoroughly flushed with deionized water and 70 % ethanol to remove any remaining particles in the system. The tubes and the channels were reused only with the same particle type.

4.4.1.2 Analysis of the Sedimentation Phase

The particle trajectories during the sedimentation phase were analyzed in order to quantify the transition kinetics between bound and unbound particle states. The particles were therefore detected by calculating the 2-dimensional cross correlation images of the acquired images and a reference image of a particle (sec. 3.3.1.5). The cross correlation image peaked at the particle locations. These local maxima were detected with a custom written peak finding algorithm. Subpixel resolution was achieved by fitting a 2 dimensional Gaussion peak function of the form

$$g(x,y) = A \exp\left(-\frac{(x-x_0)^2 + (y-y_0)^2}{2\sigma^2}\right) \tag{4.31}$$

to the peaks in the cross correlation images. A is the amplitude, σ is the peak's width, and x_0 and y_0 are the subpixel particle coordinates. The particles were then tracked with the tracking algorithm uTrack (version 2.3), which is generally capable of resolving overlapping trajectories[417–419]. As the particle trajectories overlapped in many cases, the uTrack algorithm yielded far better results than the tracking algorithm published by Crocker and Grier[51,412].

The discrimination between the bound and the unbound state was done on the basis of the instantaneous particle velocity $(v_\mathrm{x}, v_\mathrm{y})$. The instantaneous particle velocity was calculated by deriving the position vector with respect to time. A symmetric, rolling median filter in time was applied to the absolute value of the velocity $v = \sqrt{v_\mathrm{x}^2 + v_\mathrm{y}^2}$. The median filter was used to eliminate noise. The filter width was chosen to be $\pm 15\,\mathrm{s}$, which corresponded to 31 subsequent frames. In the unbound state, the particle velocity was generally higher and it was dominated by diffusion and convection. In contrast, in the bound state, the velocity was far lower and it was presumably dominated by effects such as cell motion (fig. 3.7), stage drift, and particle localization errors.

Both motion state regimes did not overlap considerably. Thus, a velocity threshold v_thresh was introduced to distinguish between the bound and the unbound state. The number of motion state changes as a function of v_thresh is shown in figure 4.8 for a highly adherent (MM-C), a slightly-adherent (TS), and a non-adherent (MG) particle type. Non-adherent particles such as MG diffused in the sample and typically had velocities, which were higher than $v_\mathrm{thresh} = 0.3\,\mu\mathrm{m\,s^{-1}}$. Consequently, the number of state changes was low for $v_\mathrm{thresh} < 0.3\,\mu\mathrm{m\,s^{-1}}$. Adherent particles such as MM-C were in the bound state most of the time and thus, their measured velocity was typically

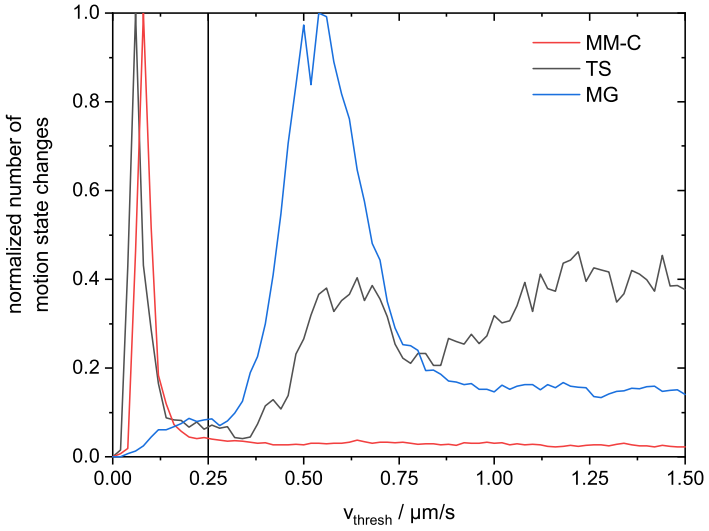

Figure 4.8: Particle motion state changes as a function of the velocity threshold. The number of motion state changes is plotted exemplarily for a highly adherent (MM-C), a slightly-adherent (TS), and a non-adherent (MG) particle type. No discrimination between particles located near coverslips and particles located near cells was made. The black vertical line indicates the velocity threshold v_{th}, for which the number of motion state changes was minimal for all particle types. Figure adapted from Gross et al., in preparation, 2022[382].

below $0.2\,\mu\mathrm{m\,s^{-1}}$. Consequently, the number of state changes was low for $v_{\mathrm{thresh}} > 0.2\,\mu\mathrm{m\,s^{-1}}$. TS particles often switched between the bound and the unbound state and consequently, the number of state changes was low for $0.2\,\mu\mathrm{m\,s^{-1}} < v_{\mathrm{thresh}} < 0.3\,\mu\mathrm{m\,s^{-1}}$. Consequently, velocities in this range were neither characteristic for the bound nor for the unbound state and both regimes could be separated by $v_{\mathrm{thresh}} = 0.25\,\mu\mathrm{m\,s^{-1}}$, at which the total number of state changes was minimal. Particles where thus defined to be bound when

$$\left\langle \sqrt{v_{\mathrm{x}}^2 + v_{\mathrm{y}}^2} \right\rangle_{\mathrm{med},\pm 15\,\mathrm{s}} < v_{\mathrm{thresh}} = 0.25\,\mu\mathrm{m\,s^{-1}} \tag{4.32}$$

and unbound otherwise. Multiple particles' velocities and their respective motion states are shown as a function of time in figure 4.9, highlighting the two distinctive motion states.

Even though the tracker could generally resolve overlapping particle trajectories, tracking errors were still observed. For instance, such tracking errors lead to an overestimation of the binding and unbinding rates, which occurred when an unbound particle diffused next to a bound particle and the tracking algorithm confused both particles. As there were typically hundreds of particle trajectories available from every measurement, the trajectories were filtered with the following, strict conditions to remove such tracking errors.

- Particle trajectories, which did not start during the sedimentation phase, were excluded from the analysis. This way, particles, which were bound before the experiment started were excluded.
- Particles, which were already bound in the first tracked frame were clearly not tracked properly throughout the measurement. Thus, they were excluded from the analysis.

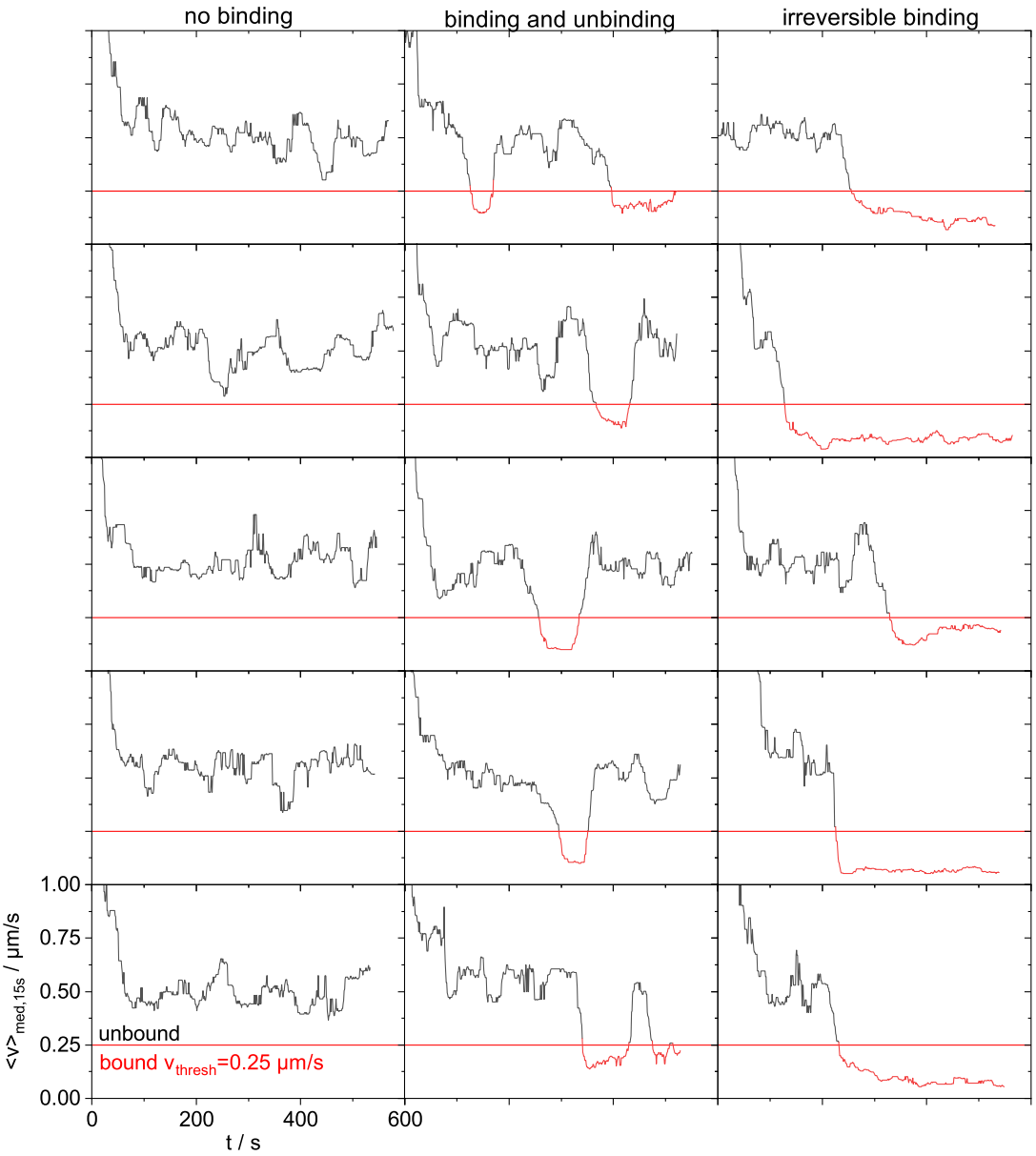

Figure 4.9: Median filtered instantaneous particle velocities and their respective motion state. The velocity was filtered with a rolling median filter in time with a width of $\pm 15\,\mathrm{s}$ to reduce noise. The particles were defined to be in the bound state (red), when their velocity was below $v_{\mathrm{thresh}} = 0.25\,\mu\mathrm{m\,s^{-1}}$ and in the unbound state (black), when their velocity was above v_{thresh}. Some particles never bound (left column), others bound and detached (center column) and others bound and never detached again until the end of the the sedimentation phase. Figure adapted from Gross et al., in preparation, 2022[382].

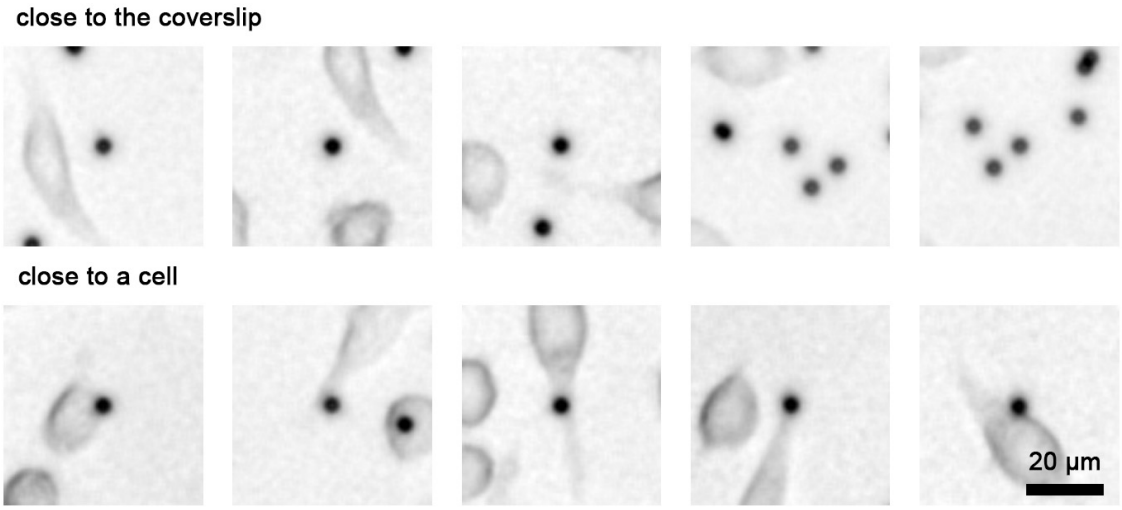

Figure 4.10: Exemplary training images used for the classification of the location state. The images were used as training and validation data for transfer learning of GoogLeNet. The network was trained to classify whether the particle in the middle of each image was close to a coverslip (upper row) or close to a cell (bottom row). Figure adapted from Gross et al., in preparation, 2022[382].

- Trajectories, which ended more than 5 s before the end of the sedimentation phase were also excluded from the data analysis. In this way, further tracking errors are excluded as tracking errors resulted in premature trajectory termination.
- In order to remove particle clusters, particles, which were closer than 4.5 µm to another particle for more than 30 s, were also excluded from the data analysis.

The cells did not form a monolayer and therefore, the particles sedimented both on cells and on coverslips randomly. In order to automate the detection of the particle location state, which determined whether a particle was close to a cell or close to a coverslip, the pretrained convolutional neural net GoogLeNet[343] was used. The implementation was done similar to the implementation used for the 3D particle tracking algorithm (sec. 3.4.1.2). A version of the network was used, which had been pretrained with the ImageNet database[344], which consists of images of 1000 categories. The network was adapted to distinguish between particles near cells and particles near coverlips by replacing the final layer of GoogLeNet with a custom, fully connetected layer with an output size of 2, representing the two particle location states. Subimages with a size of $52 \times 52\,\mu m^2$ with the particle to be classified located in the center of the subimage were used as input images for the network. The crop size for the subimages was chosen such that the cells around the particles were clearly visible. The subimages were scaled to match the input size of GoogLeNet. 1560 subimages of particles close to a cell and 1560 subimages of particles close to a coverslip were manually classified and used as training data and 400 subimages of particles close to a cell. 400 subimages of particles close to a coverslip were manually classified and used as validation data. Examples of such manually classified subimages are shown in figure 4.10.

Input data augmentation[345] in the form of random reflection (x and y axis), rotation (0 to 360°), scale (0.5 to 2), slight shear of up to 15° and translation (±3 px) was applied to the training and to the validation data set to regularize the training process. The new network weights were

determined by transfer learning[346] without locking the weights of the network trained with the ImageNet database. This was found to be unnecessary for accurate results. The adaptive moment estimation (ADAM) algorithm[347] was used to train the network. When applied to the validation data set, particles manually classified to be close to the coverslip were classified identically by the trained network in 96.6 % of all cases. Particles close to the coverslip were classified identically in 96.3 % of all cases. Differences mainly occurred in edge cases where the classification of the particle location state was limited by the optical resolution and thus also difficult to classify manually.

Examples of the final classification result of the motion state and the location state are shown in figure 4.11. All images were captured at the end of the sedimentation phase. At this point in time, MM-C and ST particles had all bound to coverslips and cells. On the contrary, MM particles had bound neither to cells nor to coverslips, while some of the sedimented PX particles had bound to cells and to coverslips.

The particles' binding kinetics were quantified according to the sketches illustrated in figure 4.12. Whenever a particle switched from the bound to the unbound state, an unbinding event was registered and whenever a particle switched from the unbound to the bound state, a binding event was registered (fig. 4.12A). The corresponding rates were defined such that a low k_{on} and a high k_{off} correspond to weak adhesion and vice versa. In particular binding rate $k_{\mathrm{on,cell}}$ was defined as the number of binding events near a cell $N_{\mathrm{binding,cell}}$ divided by the total time $T_{\mathrm{unbound,cell}}$ the particles were unbound and near a cell (fig. 4.12B):

$$k_{\mathrm{on,cell}} = \frac{N_{\mathrm{binding,cell}}}{T_{\mathrm{unbound,cell}}}. \tag{4.33}$$

The unbinding rate $k_{\mathrm{off,cell}}$ was defined analogously as the number of unbinding events $N_{\mathrm{unbinding,cell}}$ divided by the total time $T_{\mathrm{bound,cell}}$ the particles were bound to a cell:

$$k_{\mathrm{off,cell}} = \frac{N_{\mathrm{unbinding,cell}}}{T_{\mathrm{bound,cell}}}. \tag{4.34}$$

The binding rate to coverslips $k_{\mathrm{on,coverslip}}$ and the unbinding rate $k_{\mathrm{off,coverslip}}$ were defined analogously.

Even particles shipped in one batch from one manufacturer behaved differently and some of the particles appeared to be more adhesive than others in the same batch (sec. 4.4.1.3). With the definition introduced above, k_{on} and k_{off} represent the bulk behavior of any particle type. The values are, however, not necessarily representative for every individual particle. The filter timescale of 31 s used to discriminate the bound from the unbound state limited the temporal resolution of the experiment. As a consequence, the upper limit of the rates that can be resolved by the method is given by $1/31\,\mathrm{s} \approx 3 \times 10^{-2}\,\mathrm{s}^{-1}$. Furthermore, the focal depth of the objective of about 5 µm also lead to an upper limit for the rates, as the particles were already detected and tracked before they were fully sedimented on the coverslip. The corresponding timescale could be estimated by solving equation 2.6 for Δt. The focal depth was estimated by $\Delta z = 5\,\mu\mathrm{m}$, and with the viscosity of the medium of $\eta = 0.7\,\mathrm{mPas}$ and a particle density of polystyrene $\rho_{\mathrm{PS}} = 1055\,\mathrm{kg/m^3}$ (sec. 2.2.1.2). This amounts to a time difference of $\Delta t \approx 30\,\mathrm{s}$ between the time point, when the particles appeared in focus and the time point, when they reached the coverslip. This sedimentation effect therefore amounted to an upper boundary for k_{on} of $1/30\,\mathrm{s} \approx 3 \times 10^{-2}\,\mathrm{s}^{-1}$. Thus, particles with $k_{\mathrm{on}} > 3 \times 10^{-2}\,\mathrm{s}^{-1}$ bound instantly and the binding kinetics of particle types with $k_{\mathrm{on}} > 3 \times 10^{-2}\,\mathrm{s}^{-1}$ could not be discriminated. In theory, the lower boundaries for k_{on} and k_{off} are given by the total time, the particles were tracked, i.e. if N particles were tracked for T_{track} seconds each, the lower rate limit was given by $1/(N * T_{\mathrm{Track}})$. In practice, tracking errors could artificially increase the observed rates. This could happen for example when a bound particle was mistaken for an

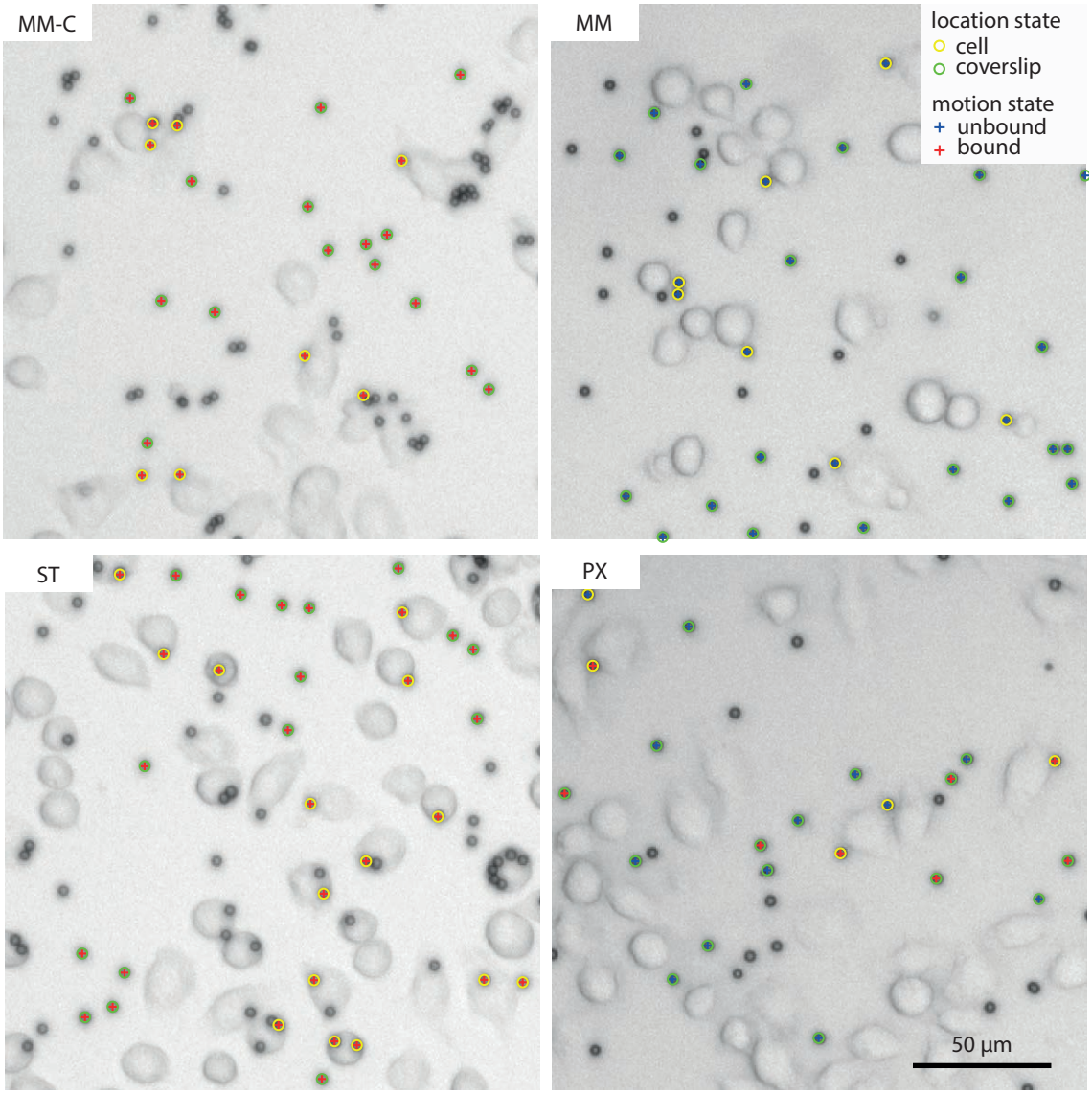

Figure 4.11: Results of the classification of the motion state and the location state at the end of the sedimentation phase for four measurements with different particle types. Unmarked particles were either not detected, not tracked or their trajectories were excluded from the analysis as described in section 4.4.1.2. MM-C and ST particles had all bound to coverslips and cells. MM particles had neither bound to cells nor to coverslips. PX particles were a bit more adherent and at the end of the measurement, a few particles had bound to cells and to coverslips. Data acquisition: Simon Wieland.

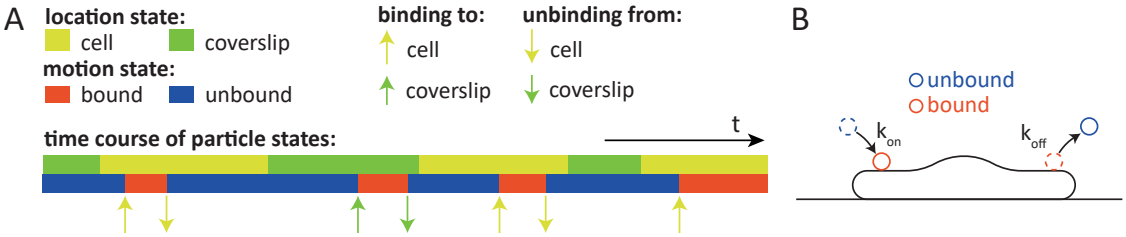

Figure 4.12: Sketch of the binding and unbinding kinetics during the sedimentation phase. (A) The location state and the motion state of the particles were analyzed to detect binding events to (up arrows) and unbinding events from (down arrows) cells (yellow arrows) and coverslips (green arrows). (B) The characteristic binding rate k_{on} and the unbinding rate k_{off} were used to quantify the adhesive strength to cells and coverslips. A low k_{on} and a high k_{off} correspond to slow binding and fast unbinding and therefore to a weak adhesion. On the contrary, a high k_{on} and a low k_{off} correspond to fast binding and slow unbinding and therefore to strong adhesion. A mathematical definition of the rates is given in the main text. Figure adapted from Gross et al., in preparation, 2022[382].

unbound particle. Consequently, the lower resolution limit of the method was difficult to quantify as it did depend on the particle density. The lowest measured rates were, however, on the order of $1 \times 10^{-4}\,\mathrm{s}^{-1}$ (sec. 4.4.2.3) and therefore, it is safe to assume that the lower resolution limit of the method was roughly equal to or lower than $1 \times 10^{-4}\,\mathrm{s}^{-1}$.

It was observed that some of the particles never unbound after a binding event (fig. 4.9, right column). In order to quantify this effect, the fraction of irreversible binding events p_{irrev} was defined as the number of binding events, which happened at least 200 s before the end of the sedimentation phase and after which the respective particle never unbound, divided by the total number of biding events.

In each experiment, typically a few hundred particle trajectories were analyzed and the binding and unbinding rates as well as the fraction of irreversible binding events were averaged over 9 independent experiments.

Statistical analysis was done with R studio (version 4.0.2, 2020-06-22) with the packages 'car', 'carData', 'rstatix' and 'multcompView'. Significance testing between different particle types was done by conducting a Shapiro-Wilk test (test for normal distribution) and a Levene test (test for homogeneity of variances). If one of both tests was significant, a Kruskal-Wallis test with a Games Howell post hoc test was conducted to check for differences between different particle types. An ANOVA with a Tukey post hoc test was performed otherwise.

4.4.1.3 Analysis of the Rupture Phase

The rupture phase was analyzed in a different manner. As the uTrack algorithm, which was used to analyze the sedimentation phase, failed in almost all cases in the moment the flow was turned on, the data analysis was conducted in an alternative manner. Instead, moving particles were removed from the acquired image time series by filtering the time series with a rolling median filter in time with a window size of ±3 consecutive images as described in section 4.3.5. Particle detection and location state classification was then carried out as described in section 4.4.1.2. The particle detection threshold was carefully chosen such that clustered particles were discarded. This was possible as the cross correlation image peak of clustered particles was lower than that of isolated particles due to the influence of neighboring particles. That way, clusters were eliminated from the data analysis. The analysis results are shown in figure 4.13. The fraction of particles

remaining on cells $p_{\mathrm{rem,cells}}$ was defined as the fraction of particles still attached to a cell after 30 s of $F_{\mathrm{hyd}} = (50 \pm 5)$ pN (fig. 4.13, right column) compared to the number of particles attached to the cells at end of the sedimentation phase (fig. 4.13, left column). The fraction of particles remaining on coverslips $p_{\mathrm{rem,coverslips}}$ was defined analogously.

4.4.1.4 Internalization Experiments

Internalization experiments with all particle types were performed by Anja Ramsperger as described[394,396]. Briefly, J774 macrophages were cultured as described in section 3.3.1.1. Prior to the experiments, the cells were scraped off the bottom surfaces of the cell culture flasks. The cell dispersion was centrifuged at 200 g for 2 min at 20 °C and resuspended in 5 ml of cell culture medium. The cells were then counted using a haemocytometer (Neubauer improved, Brand, Wertheim, Germany) and seeded on round coverslips (diameter: 18 mm, #1; Menzel Gläser, Braunschweig, Germany) in 12-well plates (CellStar; Greiner Bio-One, Frickenhausen, Germany) in 1 ml of cell culture medium each. The cells were allowed to sediment and adhere at standard cell culture conditions (37 °C, 5 % CO_2, humidified) overnight. 50 000 cells per ml were seeded in each well to yield 40 000 cells per coverslip. About 10 000 cells were lost as not all cells adhered to the coverslips or were lost at later stages during the sample preparation.

In order to reduce particle uptake during the sedimentation phase and thus to achieve comparable results between different particle types, the 12-well plates were placed on ice for one hour. The particles were dispersed in 1xPBS to yield 150 000 beads per coverslip for every particle type and they were added to the cells. Three coverslips were prepared for every particle type, which amounted to a total of 45 coverslips. The culture medium on the coverslips was replaced with the particle dispersion. After 1 h of sedimentation, the cells were incubated under standard cell culture conditions (37 °C, 5 % CO_2) for 2 h. The coverslips were washed three times with 1xPBS to remove particles, which were not bound to the cells and the cells were fixed with 4 % paraformaldehyde. Actin filaments inside the cells were labeled with Alexa Fluor Phalloidin 488 (Invitrogen, Carlsbad, USA), which forms tight complexes with filamentous actin and stabilizes the filaments[420,421].

The number of particle-cell interactions and the area covered by the macrophages was quantified on every coverslip in 5 regions of interest (ROI) with an area of 0.29 mm^2 using a DMI 6000 microscope (Leica, Wetzlar, Germany) equipped with a 63x oil immersion objective (HCX PL APO 63x oil objective , $NA = 1.30$) and a spinning disc unit (CSU-X1, Yokogawa, Musashino, Japan). Image acquisition was done with an EMCCD camera (Evolve 512, Photometrics, Tucson, Arizona including a 1.2x magnification lens). In order to distinguish between internalized particles and particles attached to the cell membrane, confocal z-stacks of fluorescently labeled cells with an axial distance of 200 nm were acquired with a 100 x oil immersion objective ($NA = 1.40$) together with a DIC image used to localize the cell-particle interactions. Alexa Fluor 488 was excited with a 488 nm laser with a power of 50 mW (Sapphire 488; Coherent, Santa Clara, California, USA) and the spinning disc speed was set to 5000 rpm for image acquisition. In order to quantify the number of cell-particle interactions in the ROIs, DIC images were acquired and analyzed in Fiji ImageJ (version 1.53c). In order to evaluate whether a particle was internalized or not, the confocal z-stacks were used. Particles fully surrounded by the actin cortex of the macrophages were classified to be internalized. The conditional internalization probability $p_{\mathrm{int,cond}}$ was defined as the number of internalized particles divided by the number of particle-cell interactions. It described the conditional probability that a particle, which was attached to a cell, was also internalized. However, the absolute internalization probability was the product of the binding probability and the probability that a bound particle is internalized. Therefore, the absolute internalization probability $p_{\mathrm{int,abs}}$ was defined as the product of the fraction of remaining particles p_{rem} and the conditional

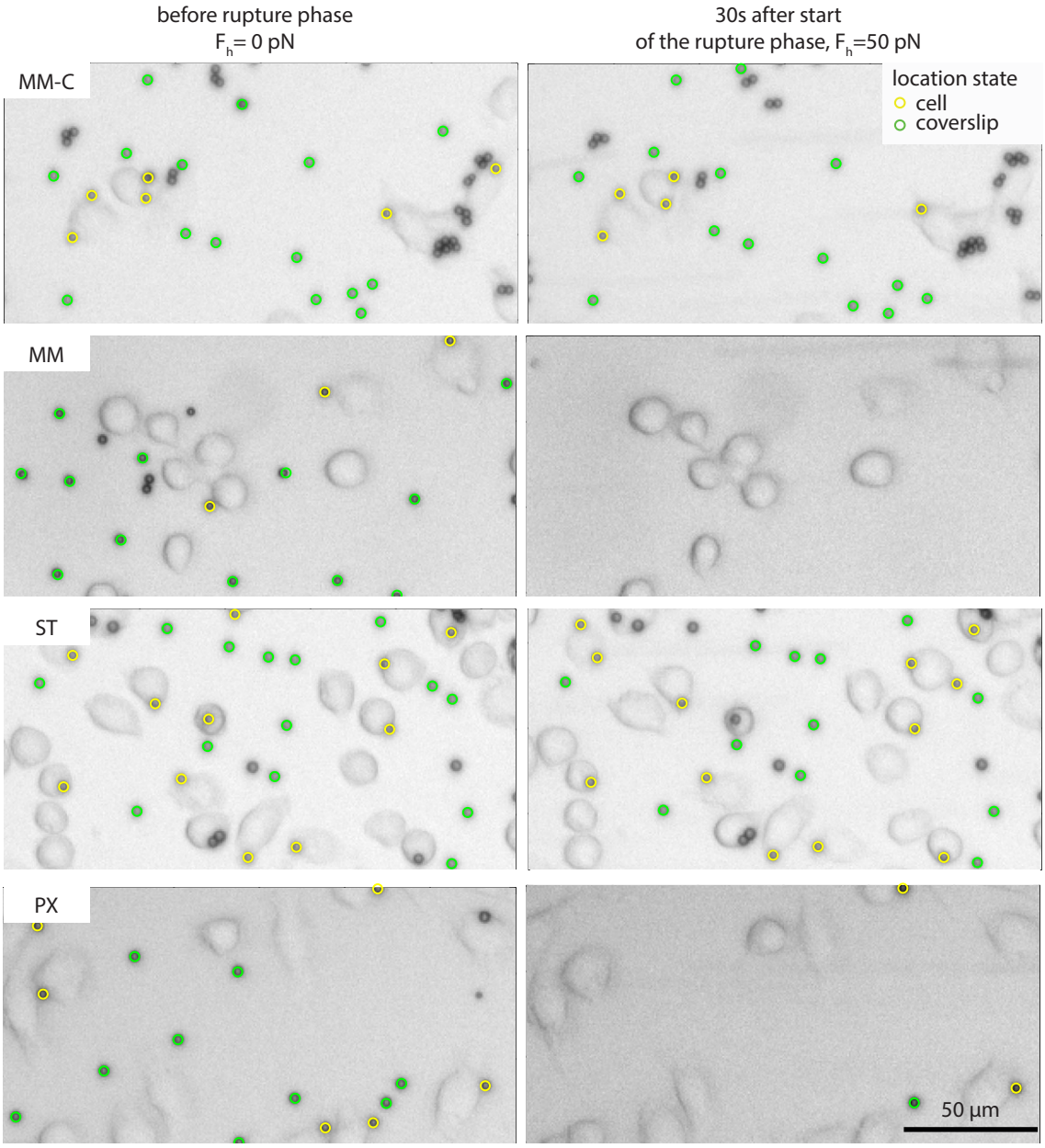

Figure 4.13: Results of the location state classification in the rupture phase analysis for four measurements with different particle types. The images in the left column were taken at the end of the sedimentation phase and the images in the right column were taken 30 s after the start of the sedimentation phase. Unmarked particles were not used for data analysis e.g. because they were not bound or because they were part of a particle cluster (sec. 4.4.1.3). MM-C and ST particles were neither ruptured from cells nor from coverslips in almost all cases. PX particles were a bit more adherent and at the end of the measurement, a few particles were still attached to cells and to coverslips. In contrast, all MM particles were ruptured from the cells and from the coverslips. Data acquisition: Simon Wieland.

Particle Type	Nominal Diameter /µm	Measured Diameter (SEM) / µm	ζ-potential /mV
PY-A	2.96	3.00 ± 0.24	29.1 ± 0.6
PY-C	3.04	2.92 ± 0.02	-91.8 ± 2.0
MM-C	3	2.98 ± 0.03	-38.1 ± 0.1
PY	3	3.00 ± 0.02	-86.7 ± 0.4
MM	3	2.97 ± 0.03	-4.5 ± 0.4
MG	3.03	3.03 ± 0.05	-7.7 ± 0.9
KI	3	2.95 ± 0.03	-6.6 ± 0.3
ST	3.43	3.42 ± 0.28	-91.3 ± 2.4
TS	2.8	2.85 ± 0.02	-11.1 ± 0.4
TJ	3	3.38 ± 0.09	-35.8 ± 1.7
PX	3.246	2.89 ± 0.90	-8.5 ± 0.1
MM-SW2	3	2.98 ± 0.11	-5.6 ± 0.3
MM-SW4	3	3.00 ± 0.07	-9.4 ± 1.7
MM-FW2	3	3.03 ± 0.04	-11.3 ± 1.5
MM-FW4	3	3.01 ± 0.08	-15.5 ± 3.1

Table 4.2: **Diameter and ζ-potential of all polystyrene microparticle types.** The values of both quantities indicate mean ± standard deviation. Table adapted from Gross et al., in preparation, 2022[382]. Data: Simon Wieland and Thomas Witzmann.

internalization probability $p_{\text{int,cond}}$:

$$p_{\text{int,abs}} = p_{\text{int,cond}} \cdot p_{\text{rem}}. \tag{4.35}$$

4.4.2 Results

4.4.2.1 Particle Morphology

SEM images of all particle types are shown in figure 4.14. The surface morphologies of different particle types were different. While PY-A, PY-C, PY, MG, and ST particles had the roughest surfaces of all particle types with irregularities with a size of approximately 100 nm, MM-C, MM, KI and TS particles had pretty smooth surfaces and a high sphericity. Those particles exposed to salt water (MM-SW2 and MM-SW4) and those particles exposed to freshwater (MM-FW2 and MM-FW4) were heterogeneously coated with a layer likely consisting of biomolecules and organic debris (eco-corona). The diameters measured with SEM are presented in table 4.2. TS particles had the smallest diameter with (2.85 ± 0.02) µm and ST and TJ particles had the largest diameters with 3.42 ± 0.28 and (3.38 ± 0.09) µm. All other particle types had diameters of about 3.0 µm. Compared to MM particles which had a diameter of (2.97 ± 0.03) µm, the diameter of environmentally exposed particles was slightly higher and varied more, indicating that the eco-corona was inhomogeneously thick. In general, the measured particle diameters differed only little from the nominal diameters given by the manufacturers. While the measured diameters of PY-C, TJ, and PX particles deviated by 4, 12, and 11 % from the nominal diameter, the deviation was smaller than 2 % for all other particle types.

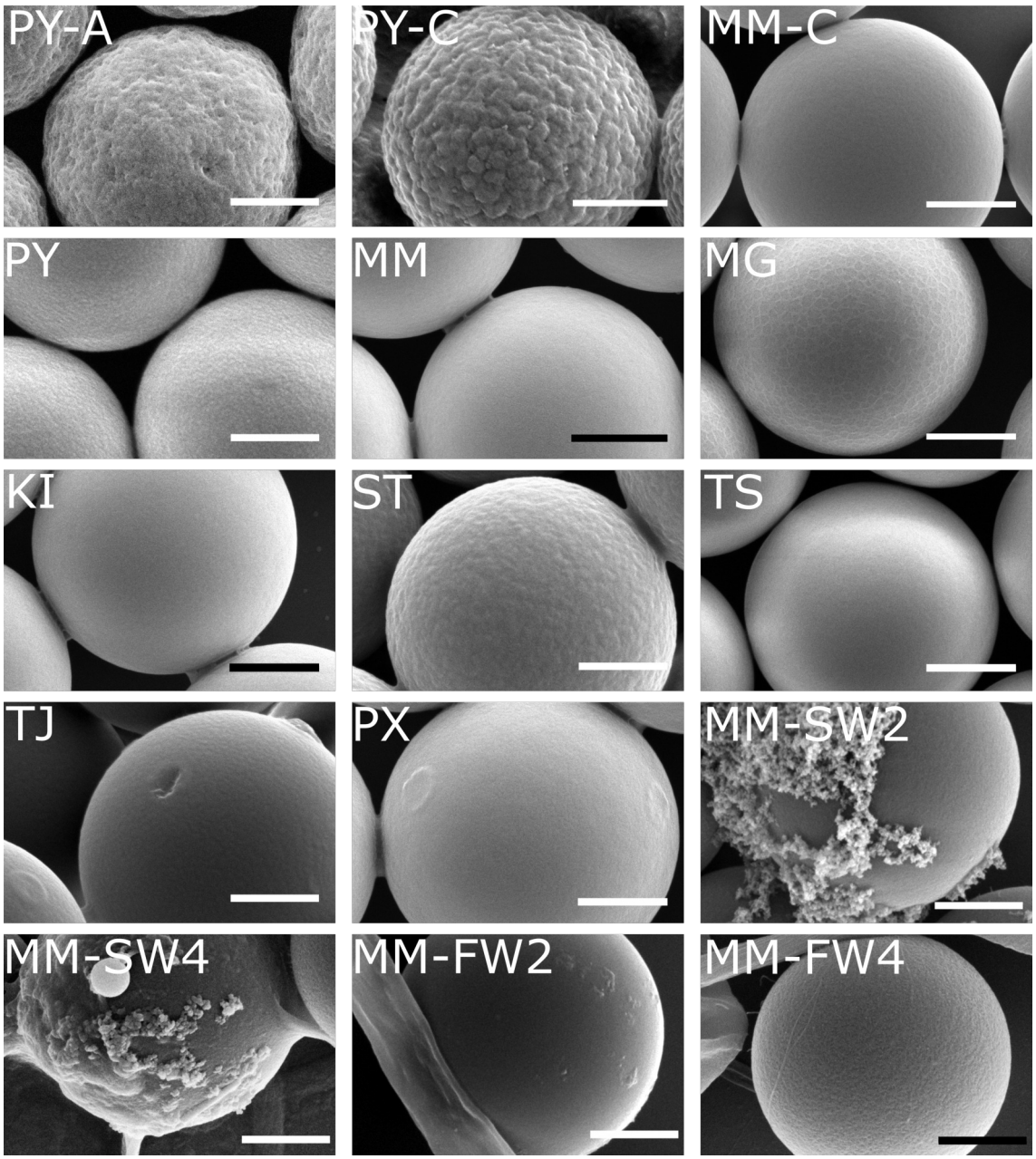

Figure 4.14: SEM images of different polystyrene particle types and with different surface functionalization. The specifications and abbreviations of all particles used in this work are given in table 4.1. While MM-C, MM, KI, and TS particles had rather smooth surfaces, PY-A, PY-C, PY, MG, and ST particles had rough and irregular surfaces. PX particles had some elevations and TJ particles had some elevations and indentations. Those particles exposed to salt water (MM-SW2 and MM-SW4) had elevations which were presumably salt crystals which precipitated during the drying process. The particles exposed to freshwater (MM-FW2 and MM-FW4) had rather smooth surfaces with few elevations. Scale bars: 1 µm. Data: Simon Wieland. Figure adapted from Gross et al., in preparation, 2022[382].

4.4.2.2 ζ-Potential

The particles' ζ-potential is also given in table 4.2. PY-C, PY, and ST particles had the lowest ζ-potentials (-91.8 ± 2.0, -86.7 ± 0.4, and (-91.3 ± 2.4) mV). MM-C and TJ had medium ζ-potentials (-38.1 ± 0.1 and (-35.8 ± 1.7) mV). The ζ-potential of all other particle types was on the order of or below −10 mV (MM: (-4.5 ± 0.4) mV, MG: (7.7 ± 0.9) mV, KI: (-6.6 ± 0.3) mV, TS: (-11.1 ± 0.4) mV, PX: (-8.5 ± 0.1) mV). PY-A particles were the only particle type with a positive ζ-potential with (29.1 ± 0.6) mV). After incubation in salt and freshwater, the ζ-potential had decreased compared to pristine MM particles, which was measured to be (-4.5 ± 0.4) mV. After two and four weeks of salt water incubation, the ζ-potential of MM-SW2 and MM-SW4 particles was -5.6 ± 0.3 and (-9.4 ± 1.7) mV respectively and after two and four weeks of freshwater incubation, the ζ-potential had dropped to -11.3 ± 1.5 and (-15.5 ± 3.1) mV respectively. As the ζ-potential after four weeks of incubation was lower than that after two weeks of incubation, the results indicate that the accumulation of the eco-corona continued after two weeks of incubation.

4.4.2.3 Binding Kinetics Without Any Applied Force

k_{on}, k_{off}, as well as p_{irrev} were determined as described in section 4.4.1.2. First, the time dependence of the binding kinetics was analyzed. k_{on}, k_{off}, and p_{irrev} 0, 40, and 80 min after the addition of the particles to the imaging medium are shown in appendix 6.2 in figure 6.1. In most cases, no significant time dependence ($p < 0.05$) was detected. Only in rare cases, the results indicated that the particles tended to adhere slightly less the longer they were immersed in imaging medium. In particular, $k_{off,cells}$ of PY-A, PY-C, and MM-C particles increased slightly with time (fig. 6.1C on page 169) and $p_{irrev,cells}$ decreased for PX and MM-SW2 particles (fig. 6.1E on page 169). In general, only minor effects were visible and the data from all three time points was pooled. The pooled results of the binding kinetics are shown in figure 4.15. The results of the statistical analysis are shown in table 4.3.

The binding kinetics of different particle types varied significantly depending on the particle type and their surface functionalization. $k_{on,cells}$ varied between $(8.1 \pm 0.8) \times 10^{-4}\,s^{-1}$ (MM) and $2.5 \times 10^{-2}\,s^{-1}$ (PY-C and MM-C) (fig. 4.15A) and $k_{off,cells}$ varied between $(1.5 \pm 0.1) \times 10^{-4}\,s^{-1}$ (PY) and $2.5 \times 10^{-2}\,s^{-1}$ (MM) (fig. 4.15D). Particles which bound quickly to cells also bound quickly to coverslips and vice versa (fig. 4.15A,D). Similarly, particles which unbound quickly from cells also unbound quickly from coverslips (fig. 4.15A,D).

Particle-cell adhesion was, however, generally slightly stronger than particle-coverslip adhesion. For example, $k_{on,cells}$ of MM particles was $(8.1 \pm 0.8) \times 10^{-4}\,s^{-1}$ and $k_{on,coverslips}$ was lower with $(2.5 \pm 0.4) \times 10^{-4}\,s^{-1}$ for the same particle type. Similarly, $k_{off,cells}$ of MM particles was $(2.5 \pm 0.8) \times 10^{-2}\,s^{-1}$ and $k_{off,coverslips}$ was slightly higher with $(4 \pm 1)\,s^{-1}$. However, both rates differed by no more than one order of magnitude between cells and coverslips and the choice of the particle type had a bigger influence on the rates. $p_{irrev,cells}$ varied between (32 ± 11) % (MM) and (99 ± 1) % (PY-C) and $p_{irrev,coverslips}$ varied between (37 ± 8) % (TJ) and (97 ± 1) % (PY-C, MM-C) for coverslips (fig. 4.15G). In general, particle types such as PY-A, PY-C, MM-C, and ST which had relatively high binding rates compared to the other particle types also had low unbinding rates and a high fraction of irreversible binding events. On the contrary, particle types such as MM, MG, and KI, which had low binding rates also had high unbinding rates and a low fraction of irreversible binding events.

MM particles incubated in fresh or saltwater adhered stronger to cells and to coverslips than plain MM particles. While plain MM-particles bound to cells and coverslips only in rare cases, particles with an eco-corona adhered more strongly. $k_{on,cells}$ increased by about one order of magnitude from $(8.1 \pm 0.8) \times 10^{-4}\,s^{-1}$ (MM) to $(8.0 \pm 0.9) \times 10^{-3}\,s^{-1}$ (MM-SW2) and to $(8.1 \pm 1.0) \times 10^{-3}\,s^{-1}$ (MM-FW2). $k_{off,cells}$ decreased from $(2.5 \pm 0.2) \times 10^{-2}\,s^{-1}$ (MM) to $(1.4 \pm 0.1) \times 10^{-2}\,s^{-1}$ (MM-

SW2) and to $(1.1 \pm 0.1) \times 10^{-2}\,\mathrm{s}^{-1}$ (MM-FW2). Correspondingly, $k_{\mathrm{on,coverslip}}$ increased from $(2.5 \pm 0.4) \times 10^{-4}\,\mathrm{s}^{-1}$ (MM) to $(3.6 \pm 0.5) \times 10^{-3}\,\mathrm{s}^{-1}$ (MM-SW2) and to $(1.8 \pm 0.2) \times 10^{-3}\,\mathrm{s}^{-1}$ (MM-FW2). $k_{\mathrm{off,coverslip}}$ decreased from $(4.3 \pm 1.0) \times 10^{-2}\,\mathrm{s}^{-1}$ (MM) to $(2.0 \pm 0.2) \times 10^{-2}\,\mathrm{s}^{-1}$ (MM-SW2) and to $(1.9 \pm 0.2) \times 10^{-2}\,\mathrm{s}^{-1}$ (MM-FW2). Incubation in fresh and saltwater for four weeks had a similar effect on the binding and unbinding rates.

The adhesion between particles and cells and between particles and coverslips depended strongly on $|\zeta|$ (fig. 4.15 B,C, E,F,H,I). Particle types with a high $|\zeta|$ generally adhered strongly to cells and coverslips, which was reflected by high binding rates, low unbinding rates and in general also by a high fraction of irreversible binding events. On the contrary, particle types with a low $|\zeta|$ generally adhered weakly to cells and coverslips, which was reflected by low binding rates, high unbinding rates and in general also by a low fraction of irreversible binding events. For example, MG particles, which had $|\zeta| = 7.7\,\mathrm{mV}$, had $k_{\mathrm{on,cells}} = (2.3 \pm 0.3) \times 10^{-3}\,\mathrm{s}^{-1}$, $k_{\mathrm{off,cells}} = (1.6 \pm 0.2) \times 10^{-2}\,\mathrm{s}^{-1}$, and $p_{\mathrm{irrev,cells}} = (42 \pm 3)\,\%$. In contrast, PY particles, which had $|\zeta| = 86.7\,\mathrm{mV}$ had $k_{\mathrm{on,cells}} = (2.2 \pm 0.1) \times 10^{-2}\,\mathrm{s}^{-1}$, $k_{\mathrm{off,cells}} = (1.5 \pm 0.1) \times 10^{-4}\,\mathrm{s}^{-1}$, and $p_{\mathrm{irrev,cells}} = (99 \pm 1)\,\%$.

4.4.2.4 Adhesion Strength Probed with a Hydrodynamic Shear Force

The fraction of remaining particles p_{rem} after the exertion of $F_{\mathrm{h}} = (50 \pm 5)\,\mathrm{pN}$ for 30 s was determined as described in section 4.4.1.3. As it was the case for the binding and unbinding rates, the fraction of remaining particles was measured for particles which were added to the imaging medium 0, 40, and 80 min before the start of the measurement. The time-dependent results are shown in appendix 6.3 in figure 6.2 on page 170. While the fraction of particles remaining on cells and coverslips decreased slightly with time for TS, TJ, and PX particles, the decrease was only significant for KI particles bound to cells (ANOVA, $p = 0.02$). No time dependence was observed in all other cases. The data acquired at all three time points was therefore pooled for all particle types.

$p_{\mathrm{rem,cells}}$ and $p_{\mathrm{rem,coverslips}}$ varied significantly, depending on the particle type (fig. 4.16 and tab. 4.3). The lowest $p_{\mathrm{rem,cells}}$ was measured for MM particles with $(3 \pm 1)\,\%$, indicating that the vast majority of MM particles was flushed away. After 30 s of flushing, the highest $p_{\mathrm{rem,cells}}$ was measured for PY-C particles with $(105 \pm 2)\,\%$. These particles were only rarely ruptured from the cells and in some cases, particles even bound to the cells during the rupture phase (fig. 4.16A). As it was the case for the binding kinetics, the adhesion to coverslips was slightly weaker than the adhesion to cells. Still, particles which bound strongly to cells generally also bound strongly to coverslips (fig. 4.16A). For example, $p_{\mathrm{rem,cells}}$ of MM particles was $(3 \pm 1)\,\%$ and $p_{\mathrm{rem,coverslips}}$ was $(1.0 \pm 0.6)\,\%$. The largest deviation was found for PY-A particles, where $p_{\mathrm{rem,cells}}$ was $(103 \pm 2)\,\%$ which was considerably higher than $p_{\mathrm{rem,coverslips}} = (41 \pm 9)\,\%$.

Particles with an eco-corona (MM-FW2, MM-FW4, MM-SW2, MM-SW4) bound more strongly to cells and coverslips. For example, $p_{\mathrm{rem,cells}} = (24 \pm 6)\,\%$ of MM-SW2 particles remained bound on cells and $(18 \pm 3)\,\%$ of MM-FW2 remained bound, while plain MM particles remained bound in only $(1.0 \pm 0.6)\,\%$ of all cases. Similarly, $p_{\mathrm{rem,coverslips}}$ increased from $(1.0 \pm 0.6)\,\%$ (MM) to $(2.5 \pm 0.4)\,\%$ (MM-SW2) and to $(2.3 \pm 0.3)\,\%$ (MM-FW2). The results for particles incubated for 4 weeks in fresh and saltwater were similar.

The adhesion between particles and cells and particles and coverslips depended strongly on $|\zeta|$ as indicated by $p_{\mathrm{rem,cells}}$ (fig. 4.16B) and $p_{\mathrm{rem,coverslips}}$ (fig. 4.16C). In general, particles with a high $p_{\mathrm{rem,cells}}$ and a high $p_{\mathrm{rem,coverslip}}$ also had a high $|\zeta|$ and particles with a low $p_{\mathrm{rem,cells}}$ and a low $p_{\mathrm{rem,coverslip}}$ also had a low $|\zeta|$. For instance, MM-particles, which had the lowest $|\zeta|$ of 4.5 mV compared to other particle types also had a low $p_{\mathrm{rem,cells}}$ of only $(3 \pm 1)\,\%$ and a low $p_{\mathrm{rem,coverslips}}$ of only $(0.96 \pm 0.60)\,\%$. On the contrary, PY-C particles which had the highest $|\zeta|$ of 91.8 mV had a much higher $p_{\mathrm{rem,cells}} = (105 \pm 2)\,\%$ (i.e. the number of adherent particles even increased slightly

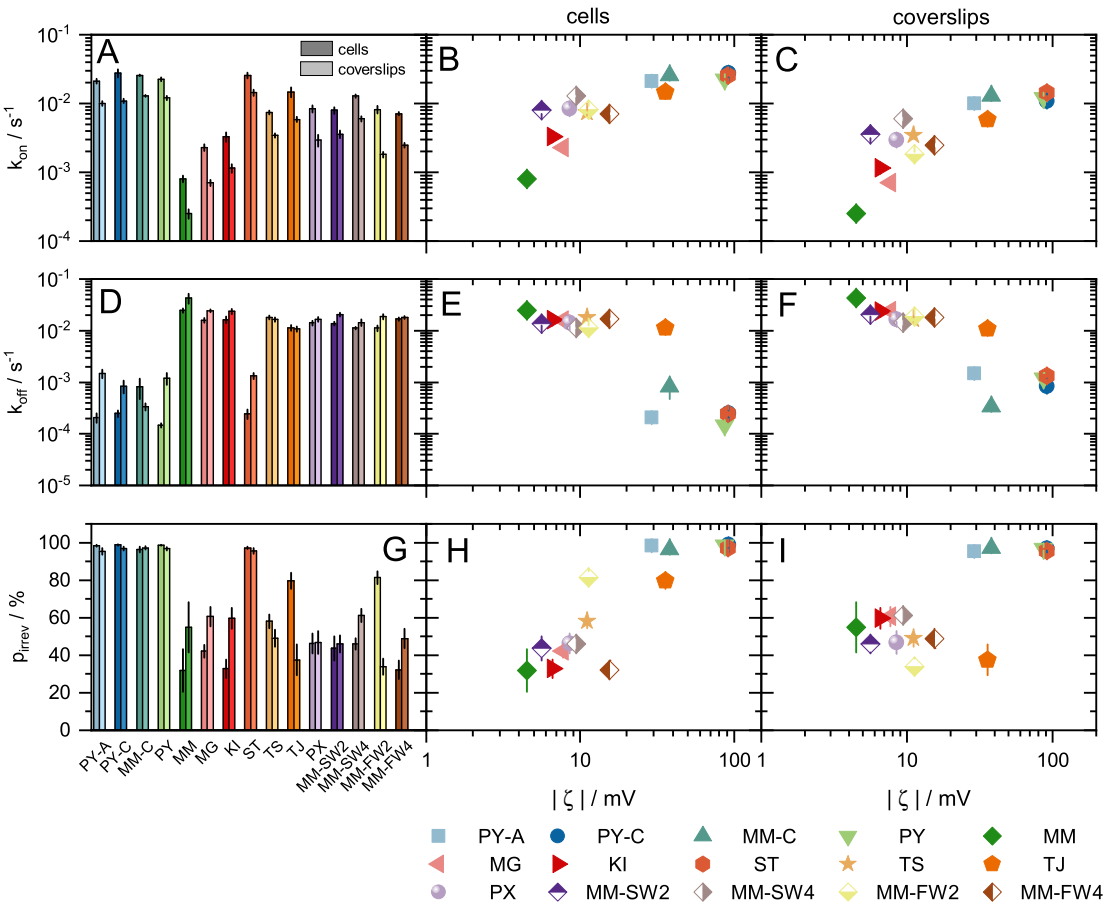

Figure 4.15: Particle binding and unbinding kinetics without any applied hydrodynamic force. (A) Comparison of the binding rates $k_{on,cells}$ (dark colors) and $k_{on,coverslips}$ (light colors) of different particle types. (B) Binding rates $k_{on,cells}$ and C() $k_{on,coverslips}$ as a function of the ζ-potential. (D) Comparison of the unbinding rates $k_{off,cells}$ (dark colors) and $k_{off,coverslips}$ (light colors) of different particle types. (E) Unbinding rates $k_{off,cells}$ and (F) $k_{off,coverslips}$ as a function of the ζ-potential. G) Comparison of $p_{irrev,cells}$ (dark colors) and $p_{irrev,coverslips}$ (light colors) for different particle types. (H) $p_{irrev,cells}$ for different particle types and (I) $p_{irrev,coverslips}$ as a function of the ζ-potential. A detailed description is given in the main text in section 4.4.2.3. Error bars represent the standard error of mean calculated from 9 individual experiments each (fig. 4.7). Figure adapted from Gross et al., in preparation, 2022[382].

Particle Type	PY-A	PY-C	MM-C	PY	MM	MG	KI	ST	TS	TJ	PX	MM FW2	MM FW4	MM SW2	MM SW4
$k_{\text{on,cells}}$	F	CF	F	F	D	E	DE	F	ABE	ABC EF	AB	AB	AC	B	B
$k_{\text{on,coverslip}}$	H	H	H	H	F	G	EFG	H	ACD	D	ABCD EFG	ABC	AD	BE	BC
$k_{\text{off,cells}}$	B	B	B	B	A	A	A	B	A	A	A	A	A	A	A
$k_{\text{off,coverslips}}$	C	C	C	C	ABC	A	ABC	C	AB	B	AB	A	AB	AB	A
$p_{\text{irrev,cells}}$	CE	E	CDE	CE	ABC DE	AB	A	CE	BCD E	D	AB	AB	AB	CD	AB
$p_{\text{irrev,coverslips}}$	C	C	C	C	ABC	AB	ABC	C	AB	AB	AB	AB	A	B	AB
$p_{\text{rem,cells}}$	A	A	A	A	B	BCD	BD	A	BCD	BCD	BCD	BCD	D	BCD	C
$p_{\text{rem,coverslips}}$	AB	A	A	A	C	C	C	A	BC	C	C	C	BC	C	BC

Table 4.3: **Significance testing of binding kinetics and fraction of remaining particles.** Significance testing between different particle types was done by conducting a Shapiro-Wilk test (test for normal distribution) and a Levene test (test for homogeneity of variances). If one of both tests was significant, a Kruskal-Wallis test with a Games Howell post hoc test was conducted to check for differences between different particle types. An ANOVA with a Tukey post hoc test was performed otherwise. The data is presented according to the guidelines suggested by Piepho[422]: In every row, different letters denote groups of particles types, between which significant differences with $p < 0.05$ were detected. For example, in the first row, $k_{\text{on,cells}}$ of PY-A was significantly different from MM, MG, KI, TS, PX, MM-FW2, MM-FW4, MM-SW2, and MM-SW4. No significant differences existed e.g. between PY-A, PY-C, MM-C, PY, ST, and TJ. Table adapted from Gross et al., in preparation, 2022[382].

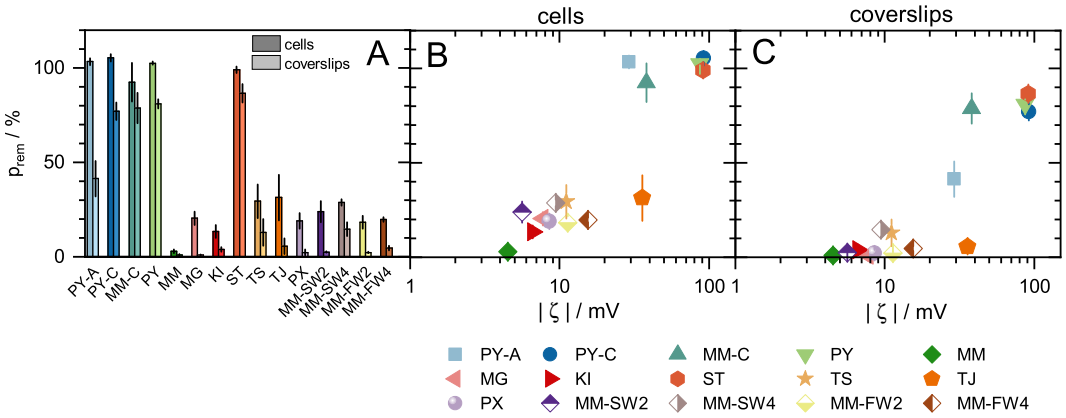

Figure 4.16: Fraction of remaining particles p_{rem} after the exertion of a hydrodynamic shear force of (50 ± 5) pN **for** 30 s**.** (A) Comparison of $p_{\mathrm{rem,cells}}$ (dark colors) and $p_{\mathrm{rem,coverslips}}$ (light colors). (B) $p_{\mathrm{rem,cells}}$ and (C) $p_{\mathrm{rem,coverslips}}$ as a function of $|\zeta|$. A detailed description of the data is given in the main text in section 4.4.2.4. Error bars represent the standard error of mean calculated from 9 individual experiments each (fig. 4.7). Data: Simon Wieland. Figure adapted from Gross et al., in preparation, 2022[382].

during flushing) and a much higher $p_{\mathrm{rem,coverslips}}$ of $(77 \pm 5)\,\%$.

4.4.2.5 Internalization Probability

The conditional internalization probability $p_{\mathrm{int,cond}}$ measured as described in section 4.4.1.4 is shown in figure 4.17A for all different particle types. As it was the case for the parameters characterizing the adhesion strength, $p_{\mathrm{int,cond}}$ also depended strongly on the particle type. The lowest conditional internalization probability was found for TS and MM-C, of which 13 ± 2 and $(19 \pm 1)\,\%$ of all attached particles were internalized (fig. 4.17A). The highest conditional internalization probability was found for MG and PY-A particles, of which 77 ± 2 and $(77 \pm 1)\,\%$ of all attached particles were internalized. Of all other particle types, internalization probabilities in between those values were measured. For example, 55 ± 3 and $(49 \pm 2)\,\%$ of all adherent TJ and PX particles were internalized. Interestingly, particles functionalized with amine groups (PY-A, $p_{\mathrm{int,cond}} = (77 \pm 1)\,\%$) were internalized considerably more often than particles from the same manufacturer functionalized with carboxylic groups (PY-C, $p_{\mathrm{int,cond}} = (31 \pm 1)\,\%$), which in turn were internalized slightly more often than plain particles (PY, $p_{\mathrm{int,cond}} = (27 \pm 1)\,\%$) from the same manufacturer (Polysciences).

Incubation in fresh and saltwater slightly increased the probability, that adherent MM particles were internalized. While $p_{\mathrm{int,cond}}$ was $(38 \pm 3)\,\%$ for MM particles, it increased to $(42 \pm 4)\,\%$ after two weeks of fresh water incubation (MM-FW2) and to $(46 \pm 4)\,\%$ after two weeks of salt water incubation (MM-SW2). In contrast to the parameters characterizing the adhesion between the particles and the cells, $p_{\mathrm{int,cond}}$ did not correlate with $|\zeta|$ as shown in figure 4.17A.

The absolute internalization probability $p_{\mathrm{int,abs}}$ ranged from $(1.1 \pm 0.4)\,\%$ (MM) to $(80 \pm 2)\,\%$ (PY-A) (fig. 4.17B). $p_{\mathrm{int,abs}}$ of all other particles types was between these vales. For example, $p_{\mathrm{int,abs}}$ was 18 ± 3, 33 ± 2, and $(40 \pm 2)\,\%$ for MM-C, PY-C, and ST particles. As it was the case for $p_{\mathrm{int,cond}}$, $p_{\mathrm{int,abs}}$ also increased after incubation in fresh and saltwater, however not only by a few percent but by about one order of magnitude. While $p_{\mathrm{int,cond}} = (1.1 \pm 0.4)\,\%$ was measured

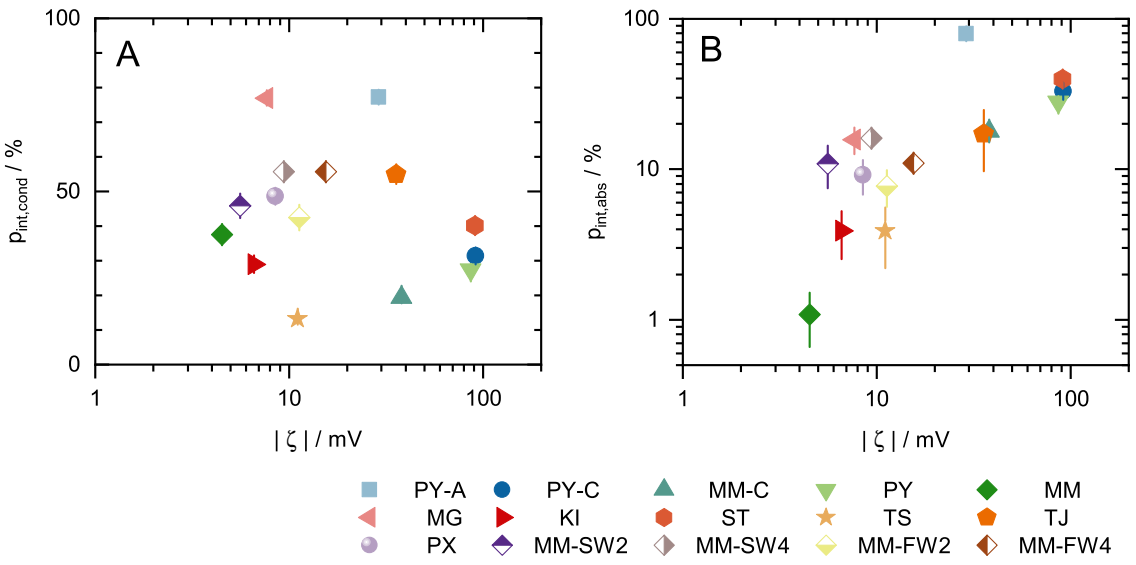

Figure 4.17: (A) Conditional and (B) absolute internalization probabilities $p_{int,cond}$ and $p_{int,abs}$ as a function of the $|\zeta|$-potential. While $p_{int,cond}$ does not systematically depend on $|\zeta|$, $p_{int,abs}$ is generally higher for particles with a higher $|\zeta|$-potential. Data: Anja Ramsperger. Figure adapted from Gross et al., in preparation, 2022[382].

for plain MM particles, $p_{int,cond}$ increased to 7 ± 2 (MM-FW2) and $(11 \pm 3)\,\%$ (MM-SW2).

In contrast to $p_{int,cond}$, $p_{int,abs}$ was also correlated with $|\zeta|$ as shown in figure 4.17B. For example, MM particles, which had the lowest $|\zeta|$ of 4.5 mV, also had the lowest $p_{int,abs}$ of $(1.1 \pm 0.4)\,\%$. PY-C particles, which had the highest $|\zeta|$ of 91.8 mV, had one of the highest absolute internalization probabilities of $(33 \pm 2)\,\%$.

However, aside from the ζ-potential, other unknown parameters seem to influence $p_{int,abs}$ as well. For example, PY-A particles had a $|\zeta|$ of 29.1 mV and a $p_{int,abs}$ of $(80 \pm 3)\,\%$. PY-C had a higher $|\zeta|$ than PY-A of 91.8 mV and a lower $p_{int,abs}$ of $(33 \pm 2)\,\%$, which is in contrast to the general trend that a higher $|\zeta|$ correlates with a higher $p_{int,abs}$.

4.4.3 Discussion

In this section, a microfluidic essay to investigate the adhesion between cells and extracellular objects was implemented. As a model system, the particle-cell and the particle-coverslip adhesion strength was investigated for 14 different particle types. In the method, four analysis parameters, namely the binding rate k_{on}, the unbinding rate k_{off}, the fraction of irreversible binding events p_{irrev}, as well as the fraction particles p_{rem} remaining after a shear flow of 50 pN for 30 s were developed. Using the method, the binding and unbinding kinetics of typically few hundred particles could be investigated simultaneously. Thus, a broad overview over a large ensemble of binding and unbinding events could be generated quickly. However, the method does neither provide the temporal and spatial resolution nor the control over the attachment process, which the blinking holographic optical tweezer technique offers. Using the blinking holographic optical tweezer technique, it was demonstrated that the temporal evolution of the contact radius could be resolved, which was not possible here. In order to discriminate between a bound and an unbound state during the

sedimentation phase, a rolling median filter with a window size of 31 s had to be applied to the instantaneous particle velocity. Thus, the highest rates, which could be resolved, were on the order of $3 \times 10^{-2}\,\mathrm{s}^{-1}$. For the shear flow essay, a theory describing the flow field in a channel with a quadratic profile was developed and validated. In the cell experiments, the flow was set such that the hydrodynamic force exerted on the particles was 50 pN. To calculate the force, the particles were assumed to be situated on a flat surface. Although this assumption may be roughly correct in all cases, there were certainly particles for which this assumption was rather coarse. For example, particles, which were located at the side of the cell streamed against were possibly rather pushed into the cells while particles on top of the cells were rather sheared off. Furthermore, the rupture mechanism itself could not be resolved. Aside from the shear force, it is also possible that the torque lead to a rolling motion, which ultimately separated the particles from the cells. Although the working point of the hydrodynamic force is not known for a particle bound to a hard wall, the lever arm with respect to the attachment point was certainly on the order of the particle radius, which was 1.5 µm. This amounted to a total torque of 75 pNµm, which acted on the attachment point at the base of the particles.

Comparing the different particle types, a clear correlation between all four adhesion strength parameters (k_{on}, k_{off}, p_{irrev}, and p_{rem}) and the ζ-potential was observed, i.e. particles with a high $|\zeta|$ adhered stronger to cells and to coverslips. This indicates that local electrostatic forces between the particles and the cells as well as between the particles and the coverslips are one of the major mediators of the observed adhesion effects. Interestingly, the ζ-potential of all plain particle types purchased from different manufacturers varied by more than one order of magnitude from −91.3 mV (ST) to −4.5 mV (MM). Such differences can originate from different polymerization protocols. For the production of such particles a wide range of different protocols is available[386,387,423–425] and in particular, different stabylizers but also polymerization starters and catalyzers could for example lead to different surface charges[396]. As details of the processes are typically undisclosed by the manufacturers, nominally identical particle types can have very different electrostatic surface properties and the present study highlights the necessity to carefully choose the supplier for adhesion and uptake studies.

The fact that cell-particle adhesion was observed for particle types with a positive (amine-functionalized; PY-A) and with a negative ζ-potential (plain, carboxylated; all other particle types), both in this work, but also in the literature appears to be a contradiction at first glance[426–428]. However, even though the cell surface is negatively charged on average[429], spatially resolved measurements with scanning ion conductance microscopy have revealed that the charge distribution on the cell surface is not only inhomogeneous but even the sign of the charge density on the surface can differ locally[430,431]. Such membrane charge inhomogeneities could therefore mediate unspecific binding of both negatively as well as positively charged particles.

The observation of apparently irreversible binding events suggests that the particle dispersions were, at least in part, inhomogeneous, i.e. the surface properties differed between the individual particles of one type or even locally on the particle surfaces. Aside from particle-to-particle inhomogeneities, it is possible that local membrane charge inhomogeneities on the cell membrane as described above were the reason why more irreversible particle-cell binding events than expected were observed. In fact, surface charge inhomogeneities have recently been revealed for MM particles by Ramsperger et al.[396]. These inhomogeneities were also observed within the framework of this work. For example, the unbinding rate of MM particles from cells was $k_{\mathrm{off,cells}} = 2.5 \times 10^{-2}\,\mathrm{s}^{-1}$, which corresponded to an average dwell time of about $k_{\mathrm{off,cells}}^{-1} = 40\,\mathrm{s}$. Assuming homogeneity, $1 - \exp(-k_{\mathrm{off}} t) = 99\,\%$ of all bonds should not have been released after 200 s. However, after $p_{\mathrm{irrev,cells}} = 32\,\%$ of all binding events, no subsequent unbinding event was observed for at least 200 s. A similar behavior was also observed for particle-coverslip binding events of MM particles (fig. 4.15). In contrast, the charge density of PY particles has been shown to be similar on all

particles and homogeneously distributed on the surface[396]. PY had $k_{\mathrm{off,cell}} = 1.5 \times 10^{-4}\,\mathrm{s}^{-1}$, which corresponded to an average dwell time of $6.6 \times 10^{3}\,\mathrm{s}$. In this case, $1 - \exp(-k_{\mathrm{off}} t) = 97\,\%$ of all bonds should have released after 200 s. In the experiment, $p_{\mathrm{irrev,cell}} = 99\,\%$ of all of all bonds had not released after 200 s, suggesting that the PY-particle dispersion was rather homogeneous.

As the cell experiments were carried out in imaging medium, the formation of a protein corona on the particle surface within a few tens of seconds is likely. Such a protein corona can form on a timescale of about 30 s[432]. As the formation of such a protein corona can alter the charge density on the particle surface[389,396,433,434] and enable specific binding between the proteins and membrane receptors, different adhesion strengths are very likely to be observed in different media with the same particle types[396,428]. The temporal resolution of the experiments described in this chapter was not high enough to validate the timescale for the formation of such a protein corona, which is about two orders of magnitude faster than the temporal resolution of the microfluidics experiments described in this work. The data acquired in this work indicates that the formation of a protein corona was likely finished after 40 min as the particle-cell and particle-coverslip adhesion strength did not change on that timescale (appendix 6.2 and 6.3). However, the data obtained in this work provides two clues. It suggests that unspecific adhesion mediated by surface charge is indeed a main driver of particle-cell and particle-coverslip adhesion and that specific ligand-receptor binding is not as important, at least not during the early binding phase. Firstly, particle-coverslip adhesion (in which case specific binding of proteins to membrane receptors is not possible) and particle-cell adhesion had very similar strengths for almost all particle types as indicated by k_{on}, k_{off}, and p_{rem}. Secondly, a major role of electrostatic forces in particle-coverslip binding was also suggested by the data obtained with the PAA system, in which biological material was not even present (sec. 2.2.1.3). In the PAA system, it was observed that the particle-coverslip adhesion of carboxylated particles was altered considerably by changing the salt concentration of the surrounding medium (compare fig. 2.8 on page 32 and fig 2.9 on page 33). Yet, the change of the ζ-potential of the particles upon immersion in different media possibly also containing serum and the influence of the ensuing protein corona on the adhesion is still an interesting pathway for future experiments[396]. It is, however, possible that differences in the protein corona can explain the observed differences in the adhesion behavior and of $p_{\mathrm{int,cond}}$ of particles with a similar ζ-potential.

As a control experiment, the microfluidic experiments could be carried out in 1xPBS in the future to avoid the formation of a protein corona altogether. Furthermore, the influence of specific binding, for example the binding of IgG to FcγR[328] was not investigated in this work. If possible, an adaptation of the IgG coating protocol described in section 3.3.1.2 to weakly adherent particle types such as MM could be an interesting approach for future experiments to investigate the role of IgG-FcγR mediated binding. The observed formation of an eco-corona on the surface of MM particles highlights that the surface charge on these particles was generally sufficient for the adsorption of proteins[394]. When coated particles detach, it is generally not clear whether the bond between the particle and the coating or the bond between the coating and the cell is ruptured, rendering the precise interpretation of k_{off} and p_{rem} difficult. The binding rate k_{on} serves as a helpful consistency check to confirm that indeed the adhesion between the ligand and the cell is probed. An additional technique such as secondary antibody staining[154] or raman spectroscopy[394] is, however, necessary to verify the coating independently.

Environmental exposure can lead to the formation of an eco-corona, also altering the particles' biochemical surface properties. Such an eco-corona is formed by the adsorption of extracellular substances containing, among others, polysaccarides, proteins, glycolipids, amino and nucleic acids[394,435–439]. As it was demonstrated in this work, the formation of such an eco-corona on MM particles was observed to be correlated with a decreased ζ-potential by a few mV, and in turn also with an increased adhesion strength. In detail, the ζ-potential decreased by a few mV depending on whether the particles were incubated in salt or freshwater and depending on the incubation

time. In turn, $k_{\mathrm{on,cells}}$ and $k_{\mathrm{on,coverslips}}$ both increased by about one order of magnitude compared to uncoated MM particles and in contrast to the above-mentioned protein corona, the adhesion strength of particles incubated for 4 week was slightly higher than that of particles incubated for 2 weeks in fresh and saltwater, suggesting that the formation of the eco-corona was not finished after two weeks. It is likely that these differences in the electrostatic and also the adhesion properties were mediated by different functional groups and different densities of functional groups on the particle surfaces. While no significant differences in the unbinding rates were observed, $p_{\mathrm{rem,cells}}$ was slightly higher for eco-corona coated particles, indicating stronger adhesion forces. However, the binding rate differences between eco-corona coated particles and uncoated MM particles were still smaller than the differences of the binding rates between plain particles from different manufacturers. Therefore, the data obtained in this work supports previous findings that unspecific binding due to surface charges are a major driver of early particle-cell adhesion[426,440].

In general, particles with a rough surface generally also have a higher surface area at a given particle radius. As the contact area between the cells and the particles can therefore be larger, rough particles should adhere stronger to cells. Such surface roughness effects were, however, not observed in the experiments conducted in this work, and it was not even possible to resolve differences for particles with similar ζ-potentials. For example, MG, KI and PX particles all had a ζ-potential of about $-7\,\mathrm{mV}$ (tab. 4.2). While KI and PX particles had slightly smoother surfaces than MG particles, the observed adhesion strength was very similar for all three particle types (fig. 4.14). This also held true for particles with a more negative ζ-potential. PY-C, PY and ST particles all had a ζ-potential of about $-90\,\mathrm{mV}$ (tab. 4.2). While PY-C particles had a very rough surface, the surface of ST particles was slightly smoother and the surface of PY particles was smoothest among these three particles types (fig. 4.14). Their adhesion strength, characterized by k_{on}, k_{off}, p_{irrev}, and p_{rem} was, however, very similar. Therefore, although the particles' surface morphology differed considerably and some particles types had a much rougher surface than others, no systematic correlation between the the particles' surface roughness and the particle-cell and particle-coverslip adhesion was observed. Instead, surface charges appeared to be the main mediator of particle-cell and particle-coverslip adhesion as suggested above. This is in line with the findings in chapter 3, where the initial particle-cell binding phase appeared to be independent of actin polymerization and thus also independent of focal adhesion or podosome formation.

In this work, the internalization of uncoated particles was quantified with the conditional probability $p_{\mathrm{int,cond}}$ describing whether or not a bound particle is internalized. $p_{\mathrm{int,cond}}$ depended strongly on the particle type, however, it did not correlate with the ζ-potential of the particles (fig. 4.17). While unspecific particle-vesicle-contact can lead to spontaneous lipid membrane wrapping[441], internalization of extracellular objects, for example, by phagocytosis[122] or macropinocytosis[98] generally requires the binding of ligands to membrane receptors[96] (see also sec 1.2.1). Although specific antibodies such as IgG were not added in the microfluidic experiments, a protein corona on the particle surface as discussed above could, for example, induce specific binding to membrane receptors. A phagocytic pathway that could be involved in the uptake of non-IgG-coated particles is integrin-mediated phagocytosis, which has been shown to be triggered by various ECM proteins[97,104] such as collagen[442,443], fibronectin[120], and laminin, which were likely present in the medium due to the presence of cells[444]. Furthermore, internalization via scavenger-receptor mediated phagocytosis is also possible[123], which, in contrast to Fc receptor mediated phagocytosis does not require opsonin binding[101]. Scavenger receptor mediated phagocytosis has been attributed to the uptake of, among others[101,123], plain polystyrene particles[445], and lipoproteins[446]. Interestingly, $p_{\mathrm{int,cond}} = 19\,\%$ of all bound unopsonized MM-C particles had been internalized. Previously, K. Berghoff measured with secondary antibody staining that about 50 % of IgG-coated MM-C particles with a diameter of $2\,\mu\mathrm{m}$ were taken up[216]. This finding suggests that roughly 60 % of all internalized IgG-coated

MM-C particles were taken up via FcγR-mediated phagocytosis (neglecting the fact that particles with a diameter of 3 µm were used in this work). For the remaining 40 % of all uptake events of those particles, the mechanism remains elusive by now.

Although the precise mechanism by which particle internalization occurred was not determined within the framework of this thesis, important implications ensue from the different adhesion characteristics of different particle types. Judging from figure 4.17B, the absolute probability whether or not a particle in contact with a cell is taken up appears to be mainly driven by the initial adhesion phase, which appears to be governed by the ζ-potential of the particle. In fact, adhesion effects can reduce $p_{\mathrm{int,abs}}$ relative to $p_{\mathrm{int,rel}}$ by more than one order of magnitude (MM and KI particles, fig. 4.17). As a consequence, care must be taken in uptake efficiency studies as adhesion and internalization effects are two separate processes, which seem to be driven by entirely different mechanisms. In order to evaluate the uptake probability of a given phagocytic target, however, both effects must be considered. This is especially important if the protocol contains any washing steps, during which weakly adherent and non-internalized particles may be washed away.

5 Synthesis: Implications for Future Studies on the Mechanics of Phagocytosis

In this work, three techniques to investigate the mechanical interactions between cells and their environment were developed.

In chapter 2, the elastic modulus and the Poisson ratio of hydrophilic and hydrophobic thin elastic substrates was measured. The technique is based on millimeter-sized steel spheres and it can be used in future mechanosensitivity studies to characterize soft polymer films, which are commonly used to model the mechanical environment of cells.

The blinking holographic optical tweezer technique presented in chapter 3 was designed to measure the visoelastic properties of cells during the full endocytic process by exerting optical forces on an endocytic target particle. Furthermore, the technique was demonstrated to be capable of resolving the early cell-particle binding kinetics. It was extended to simultaneously visualize the cortical morphology during the rheology measurements. In future experiments, this information can be used to discriminate phagocytic cup formation from other endocytic processes such as macropinocytosis. Furthermore, both the cortical density and the cortical rheology can potentially be correlated. For example, a high actin intensity and a high compliance could for example indicate a loosely cross-linked actin network while a low actin intensity and a low compliance could indicate a highly cross-linked network.

Finally, in chapter 4, a microfluidics device was designed, which can exert well-defined hydrodynamic forces on particles and potentially also on cells in future experiments. In this work, it was used to quantify the adhesion strength between particles and cells. The technique is suitable to resolve the binding kinetics between cells and extracellular objects as well as the forces required to disrupt cell-particle adhesion bonds.

Although all three methods have a wide range of applications for studies on mechanosensitivity, micromanipulation, cellular force measurement as well as the investigation of cellular adhesion, in this chapter, follow-up experiments which tie up many loose ends regarding the investigation of the endocytic pathways, and in particular, phagocytosis are discussed as, in combination, all three techniques represent a powerful tool set to investigate these cellular processes.

During the initial binding of the particles, an interesting question to be answered in the future is the degree, to which the mechanical binding between the phagocytic targets and the macrophages is mediated by unspecific binding due to electrostatic forces and by specific binding mediated by transmembrane proteins such as integrins, which can bind to fibronectin, or even Fcγ, which binds to IgG. In chapter 4, it was demonstrated that unspecific adhesion can mediate the binding of unopsonized particles to the cell membrane. To isolate the influence of opsonization by IgG or fibronectin, particle types, which, in their uncoated state, exhibit very low unspecific adhesion are required. In particular, MM particles, are a potential candidate for such a study. Firstly, MM particles showed very little adhesion to cells, as demonstrated in chapter 4. Secondly, they have been shown to adsorb an eco corona on their surface when incubated in salt or freshwater (sec. 4.2). Thus, MM particles could potentially also be coated with IgG or integrin with a similar passive adsorption protocol and the binding strength of those opsonized particles could be compared to the binding strength of unopsonized particles, either with the microfluidic device or by attaching the particles to the cells with the holographic optical traps.

Before the start of phagocytic cup formation, receptor-ligand binding and signal integration occurs. During this phase, oscillatory cortex dynamics were observed below the target particles in the experiments presented in section 3.4. While such oscillations were observed on all cells, the initiation of phagocytic uptake appeared to be in phase with the propagation of those waves in the background, suggesting that these cortical waves may be amplified locally during cup formation. A potential mechanism, which may drive those waves is the inositol phospholipid pathway, which was discussed in section 3.4.3. The verification of this mechanism may provide a potential resolution to the riddle, how phagocytic uptake is initiated. The mechanism could be tested by labeling the respective phospholipids to verify that oscillations with the same frequency and phase are present in the lipid concentrations.

The findings presented in section 3.4 suggest that there may be a threshold in the IgG-FcγR signaling pathway, above which phagocytic uptake is triggered. The initiation of the cup formation was, in some cases, observed a few minutes after the initial cell-particle contact, while in other cases, no uptake was observed at all. In those cases, in which phagocytosis was triggered and tight cup formation was started, no interruptions of the cup formation were noticable. This suggests that a signaling threshold may potentially be crossed in a random manner, however, once it has been crossed, a similar signal strength from the Fcγ receptors as before may be sufficient to keep cup formation going. In this regard, the elucidation of the underlying mechanism is interesting, which could potentially include a self-reinforcing component. In order to unravel the working mechanisms of such a trigger, particles could be opsonized with different IgG densities. The particles could subsequently be attached to the cells with the holographic optical tweezers setup. A potential and promising readout parameter is the number of actin oscillation periods, which occurred after particle binding and before cup formation. Such experiments, however, will require precise control of the IgG density on the particle surface. Suitable methods to achieve such a high control were for example recently published by Francis et al.[255]. Furthermore, in order to account for different receptor densities in different cells, it may be useful to fluorescently label FcγR clusters[132].

Further unknowns, which can be addressed with the feedback system presented in chapter 3.4 are the endocytic pathways, with which both opsonized as well as unopsonized particles are actually taken up. For example, Konrad Berghoff measured an uptake efficiency of roughly 50 % for IgG-coated MM-C particles[216], while in section 4.4.2.5, a conditional uptake probability of 18 % was measured for uncoated MM-C particles with a similar protocol, suggesting that uptake of MM-C particles occurred without any IgG coating. This suggests that IgG coated particles may not necessarily solely be taken up by phagocytosis alone and other pathways may be active as well. In fact, both macropinocytosis as well as tight cup formation were both observed in the vicinity of IgG-coated particles in the experiments presented in section 3.4. An elucidation of the respective uptake pathway efficiencies using the holographic optical tweezer method may provide a clarification for the underlying mechanism. In order to differentiate between both pathways, different particle types could be attached to the cells and the uptake mechanisms could be discriminated by differences in the cortical uptake morphology.

In this regard, in the experiments conducted in section 3.4, it was observed that free IgG in the imaging medium triggered extensive membrane ruffling, which was presumably correlated with a periodic reorganization of cortical actin on a timescale of about 75 to 150 s. In case macropinocytic uptake can be stimulated in this manner, precise control over the amount of free IgG will be required in case the uptake efficiencies of different endocytic pathways are to be resolved. This may potentially require the development of a new opsonization protocol, which guarantees stable binding of IgG. On the contrary, free IgG could also be used in order to deliberately stimulate macropinocytosis. A verification of the macropinocytic pathway could be done by its respective inhibitors, namely rapamycin[350] or amiloride[351].

Furthermore, in chapter 4, it was observed that the conditional internalization probability of

unopsonized microparticles varied drastically from about 15 (TS) to about 80 % (MG and PY-A). Therefore, depending on the particle type, the uptake efficiency of unopsonized particles can even be higher than that of opsonized particles. However, in the fixation protocols, the uptake mechanism itself was not resolved as the cells were fixed and imaged after internalization had occurred. It is for example possible that chemical substances in the MG or PY-A particles not present in other model systems triggered the activation of the macrophages or extended membrane ruffling, followed by the subsequent uptake via phagocytosis or macropinocytosis.

The holographic optical tweezer method was also demonstrated to be capable of resolving the dynamics of the cup formation. Therefore, the technique is a powerful tool, which will potentially yield data for more precise models of the mechanics and the dynamics of the phagocytic cup formation. The elucidation of the cellular viscoelastic parameters during cup formation and during the decoupling from the cortex is of high interest for such a deeper mechanical understanding of the process. However, the data analysis presented in this work will have to be updated for this purpose. The guidelines presented in sections 3.3.3 and 3.4.3 may be a convenient starting point. In order to isolate the viscoelastic properties of the relatively thin cortex, the use of smaller particles may be suitable to limit the depth of the deformation field as discussed in section 3.4.3.

Furthermore, the elastic films polymerized in this work may serve as a substrate to investigate the mechanical forces exerted on the target during phagocytosis. In studies on mechanosensitivity and in TFM essays, the surface of those films is typically coated with ECM proteins such as fibronectin via chemical cross-linkers[50] in order to facilitate cell adhesion. The films could additionally be coated with IgG to initiate frustrated phagocytosis, i.e. the phagocytic spreading of a cell on an object too large to be engulfed by a single cell. In such an experiment, the forces, which are exerted on the film (i.e. the target) could be investigated in a spatially and temporally resolved manner using traction force microscopy. Additionally, the role of the molecular clutch mechanism discussed in section 1.2.2.2 could be investigated by studying the protrusion speed of the leading edge of the phagocytic cup on films with different stiffnesses and films coated with different concentrations of fibronectin or IgG.

Although the closure of the cup and the subsequent decoupling of the phagosome from the cortex can not be investigated in such a frustrated phagocytosis system, the holographic optical tweezers technique is perfectly suitable to resolve the process and thus, it can provide mechanical data for future mechanical models, which can cover this late stage of phagocytosis as well.

The blinking holographic optical tweezers technique can potentially also resolve the viscoelastic properties of the cells during the transport of the endosomes, i.e. the phagosomes and the macropinosomes, to the nucleus. This transport is typically orchestrated by dynein motors, which move along microtubules. Typically, the phagosomes are transported by more than one motor protein and possibly also along multiple microtubules at the same time[154]. Thus, the acquisition of blinking data during the transport phase could provide information about the mechanical coupling of the endosomes to the microtubule network and possibly also resolve the number of active motors in case the transport can be stalled with the optical forces[377]. A potentially interesting analysis parameter is the power law exponent β, which could serve as an indicator for a stronger coupling to the elastic microtubule network, when more motors are bound. Furthermore, the method also provides access to the transport dynamics of the phagosome, which are available in the form of the piezo stage coordinates. For example, the power law exponent β could for example be correlated with the transport speed of the endosomes. As the endocytic pathway is generally known in the holographic optical tweezers technique, present differences between phagosomes and macropinosomes could potentially even be resolved.

6 Appendices

6.1 Laboratory Protocols

6.1.1 Coverslip Activation for Polyacrylamide Films

Following the next steps, you'll prepare 25 coverslips to covalently bind to polyacrylamide gels. These steps should be performed before polymerization. The protocol is an adapted version of the protocol shown by Kraning-Rush et al.[50]. The first section of the protocol was originally implemented by Andrea Hanold and is used to clean the coverslips. In the second section, the coverslips are coated with NaOH*,* $3-$APTMS*, and glutaraldehyde to chemically activate the coverslip surfaces. A summary of this protocol is given in the main text (section 6.1.1).*

Reagents:

For cleaning the coverslips:

- 7X-O-Matic laboratory detergent
  MP Biomedicals, LCC, # 76674-49
  or:
  Alconox detergent (Alconox Ltd.)
  dissolved at a concentration of 1 % w/v in dH2O (according to the instructions on the package)
- milliQ water (dH2O)
- 10 % HCl
  CAS 7647-01-0
  e.g. Sigma # 84421-1L
  Hazards: May be corrosive to metals. Causes severe skin burns and eye damage. May cause respiratory irritation
  Handling: Avoid breathing vapours. Wear protective gloves/ protective clothing/ eye protection/ face protection. If in eyes: Rinse cautiously with water for several minutes. Remove contact lenses, if present and easy to do. Continue rinsing. Immediately call a poison center or doctor/ physician.
- 0.2 M Ethylenediaminetetraacetic acid (EDTA)
  CAS 6381-92-6
  e.g. Sigma # E5134-500G
- 90 % ethanol for storage (EtOH)

For activating the coverslips:

- 1 ml 0.1 N NaOH
  CAS 1310-73-2
  e.g. Hedinger

- ≈ 300 µl 3-aminopropyl-trimethoxysilane (3-APTMS)
  CAS 13822-56-5
  e.g. 97 %, Sigma-Aldrich stock solution # 281778-5ML
  Hazards: Causes skin irritation, auses serious eye damage
  Handling: Gloves, eyeshields, hood, avoid skin contact
- deionized water (dH2O)
- gluteraldehyde
  CAS 111-30-8
  e.g. 8 %, Sigma-Aldrich stock solution # G7526-10ML
  Hazards: Harmful by inhalation and if swallowed, irritating to respiratory system and skin, risk of serious damage to eyes, may cause sensitization by inhalation and skin contact, very toxic to aquatic organisms
  Handling: gloves, eyeshields, hood
  Storage temperature: −20 °C
- RainX
  Caro Care Care International # 80122200
- Fluorescent microparticles
  e.g. Life Tech carboxylated fluorescent microparticles, diameter 0.2 µm , # F8810, F8811
- Isopropanol (3-Propanol):
  CAS: 67-63-0

Consumables:

- 25 Coverslips (22x40 mm, #1),
  e.g. Karl Hecht Gmbh, # 10003741
- 25 Coverslips (round, 15 mm, # 1)
  e.g. Menzel Gläser, Thermo Fisher Scientific
- Pasteur pippettes
- Kimwipes
- canned air
- drying beads
  e.g. NeoLab # 1-7031 (with color indicator)

Equipment:

- beakers
- sonicator bath
- fume hood
- coverslip holders

Methods

The following steps describe the cleaning of the coverslips before activation (from Andrea Hanold). This can be done with many coverslips at once and must not be done directly prior to activation.

1. Place the coverslips in the coverslip holders.
2. Place the holder in a beaker with dH2O and 1 % v/v 7X-O-Matic or the prepared Alconox solution.
3. Sonicate for 10 min.
4. Rinse with dH2O and place in dH2O in anonther beaker - sonicate for 10 min.
5. Dry the coverslips with canned air.
6. Add 10 % HCl to coverslips and sonicate for 10 min.
7. Rinse with dH2O and place in dH2O in anonther beaker - sonicate 10 min.
8. Dry the coverslips with canned air.
9. Add 0.2 M EDTA to coverslips and sonicate for 10 min.
10. Rinse with dH2O and take out each coverslip seperately from the holder with forceps (while wearing gloves) and place into dH2O in anonther beaker - sonicate 10 min.
11. Dry the coverslips with canned air.
12. Place coverslips in a jar with 90 % EtOH for storage.

The following steps describe the activation of the lower coverslip which is not removed after polymerization.

1. Take the coverslips out of the 90 % EtOH and let them dry completely.
2. Prepare the coverslips (22x40 mm) on lens cleaning tissue.
3. Work with three coverslips at a time in all further coating steps. Apply a drop (12 µl) of 0.1 N NaOH to the coverslips. NaOH should be spread quickly by rolling a pasteur pipette over both coverslips. Let the coverslips dry for 10 - 20 min.
4. In the fume hood, apply 15 µl 3-APTMS to each coverslip. Quickly spread the drop by rolling a Pasteur-Pipette over the coverslip. Be quick as APTMS will dry rapidly.
5. Discard gloves and allow the coverslips to dry for 5 min (up to 10 min since fully dried layers of 3-APTMS are difficult to remove). Meanwhile, for each coverslip, prepare one Petri-dish, filled with dH2O.
6. Place the coverslips in the Petri-dishes and rinse them briefly. Shake the holders to dislodge the 3-APTMS layer.
7. Rinse 2 more times with dH2O in the sample holders. Incubate 5 min between each rinse.
8. In the fume hood, prepare 0.5 % aqueous gluteraldehyde solution (from 8 % stock solution, Sigma-Aldrich). Therefore mix 375 µl of stock solution with 5.625 ml dH2O. You'll need ≈0.20 ml for each 22x40 mm coverslip. Ensure thorough mixing.

9. Prepare one piece of parafilm on the workbench in the fume hood. Pipette a 0.20 ml drop of 0.5 % gluteraldehyde-solution for each coverslip onto the Parafilm. Invert the coverslips on the drops and incubate for 30 min.
10. Remove coverslips from the Parafilm. Dispose gluteraldehyde waste in specified containers. Place coverslips in Petri dishes again and rinse them 3 times with dH2O in the sample holders, incubating for 5 min after each rinse.
11. Remove coverslips from the Petri dishes and place them on a paper for cleaning optical glasses inside the fume hood. Let them dry for $\approx 30 - 40$ min.
12. Mark the uncoated side of the coverslip with the capital letter 'L', readable from the coated side.

From here, the coverslips can be stored for over a month, preferably under desiccation (you can use desiccant beads).
A second coverslip (round, diameter 15 mm) for covering the gel during the polymerization can be prepared in the following way:

- Preparation of hydrophobic coverslips coated with RainX:
  1. Using a cotton swab, cover the coverslip surface with a drop of RainX and let it dry for at least 5 min. Using a Kimwipe, remove excess RainX from the surface.
  2. Remove dust and debris from the coverslips using canned air. This is particularly important because these coverslips cover the surface where your cells will be!
- Preparation of coverslips coated with microparticles (enables higher resolution during TFM) due to out of focus light minimization (centrifugal acceleration optimized for particles with a diameter of 0.2 µm).
  1. Place 100 µl of microparticle stock solution in an Eppendorf tube.
  2. Centrifuge the solution at 2500 g for 30 min.
  3. Replace the supernatant with 100 µl of isopropanol.
  4. Vortex the eppi briefly and sonicate for 10 min (turn on sweep-mode on the device). Ensure that the water in the bath is cold. Temperatures above 30 °C were observed to lead to particle clustering. Warning: The bath heats up during extended operation. You may add a bit of ice to cool the bath down.
  5. Centrifuge the solution at 2500 g for 30 min.
  6. Replace the supernatant with 100 µl of isopropanol.
  7. Vortex the eppi briefly and sonicate for 10 min (turn on sweep-mode on the device).
  8. Place the solution in a PCR-tube (200 µl) with a thin wall.
  9. Sonicate for 10 min (turn on sweep-mode on the device).
  10. Place the solution in an Eppendorf tube.
  11. Centrifuge the solution at 7000 g for 1 min to centrifuge down larger clusters and move the solution to a new Eppendorf tube. Be careful not to touch the clusters at the bottom of the old tube.
  12. Place 3 µl of the solution on a round coverslip and swipe the droplet over the whole coverslip with a rectangular cover slip. Allow the isopropanol to evaporate.
  13. Test the particle density on the coverslips at the microscope before gel polymerization.

Troubleshooting

- If the coverslips turn orange or red after applying gluteraldehyd, the coverslips where not thoroughly rinsed after 3-APTMS treatment. These coverslips should be discarded.
- Using 100 % ethanol instead of isopropanol resulted in large particle clusters.

6.1.2 Polymerization of Thin Polyacrylamide Films

Following the next steps, you'll prepare 6 polyacrylamide films with a thickness of a few tens of micrometers, which are covalently bound to a previously prepared coverslip. The protocol itself is an adapted version of the protocol published by Kraning-Rush et al.[50]. Acrylamide can be substituted by N-isopropylacrylamide to polymerize temperature-responsive polymer films with otherwise comparable properties. Porous polyacrylamide films can be produced by adding $CaCO_3$ *power during the polymerization. After polymerization, the powder can be dissolved in* HCl*. A summary of this protocol is given in the main text (section 6.1.2)*
SAFETY NOTE: All work with acrylamide monomers should be done with gloves, eyeshields, and under the fume hood.

Reagents:

- milliQ water (dH2O)
- 40 % aqueous acrylamide solution (AA)
  CAS 79-06-1
  Sigma-Aldrich, # A4058-100ML
  Hazards: Harmful if swallowed. Toxic in contact with skin. Causes skin irritation. May cause an allergic skin reaction. Causes serious eye irritation. Fatal if inhaled. May cause allergy or asthma symptoms or breathing difficulties if inhaled. May cause genetic defects. May cause cancer. Suspected of damaging fertility or the unborn child. Harmful to aquatic life.
  Handling: Eyeshields, gloves (Meditrade # 1283 are suitable for 60 min), fume hood
  Storage: 2 - 8 °C for up to 1 year to prevent oxidation
- 20 % aqueous N-isopropylacrylamide solution (NIPA)
  CAS 2210-25-5
  Sigma-Aldrich # 731129
  Hazards: Harmful if swallowed. Toxic in contact with skin. Causes skin irritation. May cause an allergic skin reaction. Causes serious eye irritation. Fatal if inhaled. May cause allergy or asthma symptoms or breathing difficulties if inhaled. May cause genetic defects. May cause cancer. Suspected of damaging fertility or the unborn child. Harmful to aquatic life.
  Handling: Eyeshields, gloves (Meditrade # 1283 are suitable for 60 min), fume hood
  Storage: 2 - 8 °C for up to 1 year to prevent oxidation
- 2 % aqueous N,N'-methylene-bis-acrylamide solution (BIS)
  CAS 110-26-9
  Sigma-Aldrich, # 66675-100ML
  Hazards: Harmful to aquatic life. Causes serious eye irritation. Harmful if swallowed. Causes skin irritation. Toxic in contact with skin. May cause an allergic skin reaction. Fatal if inhaled. May cause allergy or asthma symptoms or breathing difficulties if inhaled. May cause

genetic defects. Suspected of damaging fertility or the unborn child. May cause cancer.
Handling: Eyeshields, gloves (Meditrade # 1283 are suitable for 60 min), fume hood
Storage: 2 - 8 °C for up to 1 year to prevent oxidation

- N,N,N,N-Tetramethylethylenediamine (TEMED)
  Thermo Fisher Scientific Nr. 17919
  CAS 110-18-9
  Hazards: Flammable liquid and vapor, causes severe eye burns, causes respiratory tract and skin burns, harmful if inhaled or swallowed, may be harmful if absorbed through skin, can cause target organ damage
  Handling: Eyeshields, gloves, fume hood
  Storage: Store under inert gas. Air and moisture sensitive. Protect from sunlight. Keep away from oxidizing materials.

- crystalline Ammonium Persulfate (APS)
  Thermo Fisher Scientific # BP179-100
  CAS 7727-54-0
  Hazards: Oxidizer: Contact with combustible/organic material may cause fire. Harmful if swallowed. Causes eye, skin and respiratory tract irritation. May cause allergic respiratory and skin reaction.
  Handling: Eyeshields, gloves
  Storage: Store at dry, well ventilated place. Solution storeable at −20 °C for up to 1 year, do not store aqueous solution at room temperature.

- florescent, carboxylated microparticles
  diameter 200 nm
  excitation 505 nm
  emission 515 nm)
  Life Technologies, F-8811 or F-8810
  $c = 4.6 \times 10^{12}\,\mathrm{ml}^{-1}$ (keeping them in PBS induces cluster formation; keep the time in PBS solution as short as possible)
  only for performing TFM/steel sphere characterization of the elastic properties of the film

- 1xPBS (≈ 0.5 l) and 10xPBS (2 ml) as a buffer (concentrations in 10xPBS are 2.0 g KCl, 80.0 g NaCl, 14.4 g Na_2HPO_4 und 2.4 g KH_2PO_4 in 1 l dH2O)

- calcium carbonate powder ($CaCO_3$)
  e.g. Sigma # 239216
  CAS 471-34-1
  particle size 1 to 3 µm

- 1 % aqueous HCl solution
  e.g. prepared from 25 % v/v stock solution
  VWR chemicals # 20257.296P
  CAS 7647-01-0
  Hazards: Corrosive to metals. Causes severe skin burns and eye damage. May cause respiratory irritation.
  Handling: Eyeshields, gloves, fume hood

Consumables:

- 6 coverslips, activated with 3-APTMS and 0.5 % gluteraldehyde (size 22x40 mm)
- 6 coverslips, coated with RainX or another suitable hydrophobic coating (round, 15 mm diameter)

Equipment:

- fume hood
- exsiccator
- sonicator bath
- centrifuge (15 000 g)

Methods

1. During all the next steps, exposure of the microparticles to light should be minimized. Use aluminum foil or dim the lights! Wash the fluorescent bead stock solution in deionized water three times in dH2O by centrifuging at 15 000 g for 5 min and replacing the supernatant with dH2O. Sonicate the solution for 10 minutes and vortex the solution for 10 s. Repeat sonication and vortexing for two more times. Meanwhile, you can go on with the monomer solution.
2. In a container, mix AA, NIPA, BIS, dH2O and 10x PBS according to the following table for every ml of monomer solution needed. This ensures that the final concentration is 1xPBS!

AA/%	NIPA /	BIS/%	40 % AA /µl	20 % NIPA /µl	2 % BIS µl	dH_2O /µl	10xPBS/µl
10.0	0.0	0.10	253	0.0	50.7	594	101
10.0	0.0	0.060	253	0.0	30.4	614	101
10.0	0.0	0.030	253	0.0	15.2	629	101
3.00	0.0	0.1	76.0	0.0	50.7	771	101
0.00	10.0	0.1	0.0	506	50.6	341	101

3. Mix thoroughly by pipetting up and down before performing the next step. Be careful not to induce bubbles.
4. As a catalyst, add 0.5 µl (1/2000 v/v final concentration) of TEMED for AA gels and 1.0 µl (1/1000 v/v) for NIPA gels. Your total volume should be 1 ml right now.
5. Mix thoroughly again by pipetting up and down.
6. Optional: Degas the solution for 30 minutes (AA) or 45 minutes (NIPA) using an exsiccator. For AA films, degassing led to nonlinear elasticity in the past (see the author's master's thesis[156]). For NIPA films, this was not observed (sec. 2.2.6 in this work).
7. Take 247.6 µl of the previously prepared monomer solution and fill it in an Eppendorf tube.
8. Freshly prepare a 10 % w/v APS solution in dH2O. If using a previously prepared APS solution, it should have been stored at −20 °C as the activity of APS diminishes rather quickly in H_2O at room temperature.

9. Optional: At this stage, $CaCO_3$ can be added to the monomer solution to prepare porous films.

$CaCO_3$ / % v/v	$CaCO_3$ / mg
3.0	20
10	68
20	140

Important: When $CaCO_3$ is added to the solution, fluorescent particles should not be added in the next step because the particles will stick to $CaCO_3$ as well. Instead, to label the surface, the gels can be immersed in a 1 % v/v solution of the microparticles in 1xPBS for 30 min after the polymerization is completed. Alternatively, the round coverslip coated with RainX can be immersed in a similar microparticle solution for 30 min prior to polymerization. The coverslip should be air-dried before polymerization in this case.

10. Add 2.1 µl of bead dispersion, diluted in dH2O as prepared in the first step. In order to prepare films without microparticles, add 2.1 µl of dH2O. Ensure thorough mixing.

11. Before going on, prepare all materials you'll need in the next steps as the addition of APS starts the polymerization and the solution will get viscous rapidly.
    - Pipettes and tips
    - APS
    - large activated coverslips
    - small round coverslips
    - Using sticky tape, pin 10 pasteur-pipettes to the workbench at a distance larger than the diameter of the round coverslip.

    Make sure, the solution is at room temperature. Optimally, polymerization should occur at 23 - 25 °C.

12. In order to initiate polymerization, add 1.25 µl of 10 % APS solution to the mixture to achieve a final APS concentration of 1/200. For NIPA gels, double the amount of APS solution to a final concentration of 1/100 v/v. Mix thoroughly, pipetting the solution up and down for 3 times. Be careful not to introduce bubbles. Set your stopwatch to zero!

13. On each small coverslip, place 9 µl of solution quickly for a final average height of 30 µm. These gels are suitable for TFM. By adjusting the volume of the drop, you can alter the height of the final gel. For thicker gels of approximately 50 - 150 µm, which are suitable for the steel sphere method for measuring the elastic modulus, use 15 µl. Note that the volume of the film shrinks during polymerization. Thus the height can not be calculated from the volume pipetted on the coverslip. The final height of the film also depends on the details of the coverslip handling.
    For NIPA films, the final thickness will be a lot smaller than that of AA films. Use 50 µl of monomer solution per coverslip to achieve a final thickness of 80 to 90 µl and consider using stainless steel spacers to control the thickness of the film.

14. The activated side of the large coverslips should face down to be in contact with the gel. Lower the large coverslips on top using forceps or your hands (fig. 2.3) until the liquid touches the large coverslip. Be careful not to introduce bubbles so that the gel is perfectly attached to the activated surface. Furthermore, O_2 affects the extent of the polymerization.[50]

15. Place the inverted sandwiches onto the fixed pasteur pipettes. Polymerizing the gels upside down will cause the microparticles to settle down and be more dense on the final surface.

16. Cover the set up with a box as an incubation chamber. Use wet kimwipes to increase the air humidity inside to 80 % to prevent wrinkling when the polymerized film is immersed in 1xPBS. Use aluminum foil to prevent bleaching of the microparticles.

17. Polymerizing the gel takes 45 min for degassed AA solutions. Use 120 min for non-degassed AA solutions. The edges of the gel should begin to recede beneath the coverlip. NIPA films should be polymerized in a sealed box in N_2 atmosphere for 3 h.

18. After polymerization has completed, carefully remove the round coverslip using forceps. Be careful not to break the glass. Check the appearance of the gels. They should not appear turbid.

19. Optional: In order to disssolve the $CaCO_3$ particles, immerse the films in 1 % HCl for 1.5 h under gentle agitation. Treatment with higher concentrations of HCl can lead to detachment of the gels from the coverslips. Gaseous CO_2 should slowly escape from the films without any bloating.

20. Wash the gels twice for 15 minutes in 1xPBS in separate petri dishes to get rid of any remaining monomers which might affect your cells later in the process. In case the gels were immersed in HCl, add another washing step.

The gels are now ready to be functionalized with proteins or used otherwise. When storing the gels for some time, always make sure that they are soaked in the same buffer they were polymerized in (1xPBS) to prevent them from running dry and to prohibit osmotic swelling.

Troubleshooting

- If you notice pieces of dirt at the bottom of the gel which are fluorescent using the GFP-L (Ex: 460 - 500 nm, Em: $\geq$ 510 nm) and TX RED (Ex: 540 - 580 nm, Em: $\geq$ 600 $-$ 660 nm) filter cubes, you din't rinse the coverslips well enough during the activation of the rectangular coverslip. Make sure the APTMS-layer has properly detached from the coverslip before exposing it to gluteraldehyde.

- In case the NIPA films do not polymerize, try to increase the concentration of APS and TEMED and try to degas the monomer solution prior to polymerization. The polymerization time can also be increased.

6.2 Time Dependence of the Binding Kinetics and the Fraction of the Irreversible Binding Events

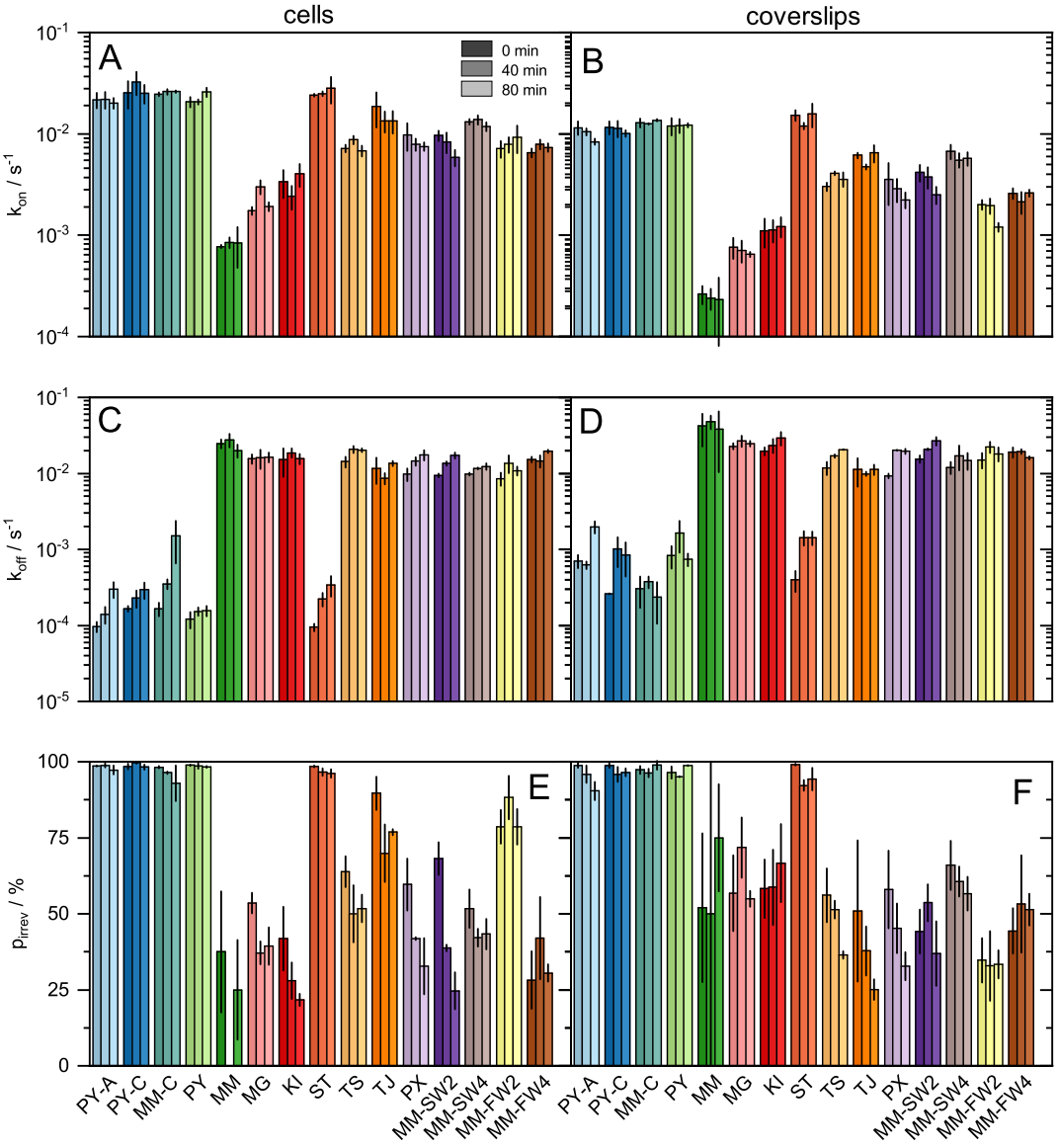

Figure 6.1: Time dependent particle binding and unbinding kinetics without any applied hydrodynamic force. A) Comparison of the binding rates $k_{on,cells}$ and B) $k_{on,coverslips}$ 0 min (light colors), 40 min (medium colors), and 80 min (dark colors) after the addition of the particles to the imaging medium. C) Unbinding rates $k_{off,cells}$ and D) $k_{off,coverslips}$ for the three different time points. E) Comparison of the fraction of irreversible binding events to cells and to F) coverslips for the three different time points. Error bars represent the standard error of mean calculated from 3 individual experiments each (fig. 4.7). The figure is discussed in section 4.4.2.3. Figure adapted from Gross et al., in preparation, 2022[382].

6.3 Time Dependence of the Fraction of Remaining Particles

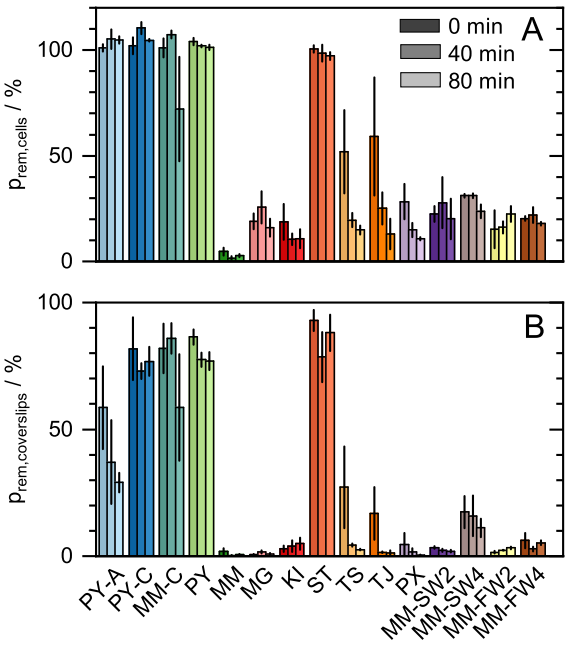

Figure 6.2: Time dependency of the fraction of remaining particles. A) Comparison of $p_{\mathrm{rem,cells}}$ 0 min (light colors), 40 min (medium colors), and 80 min (dark colors) after the addition of the particles to the imaging medium. B) Comparison of $p_{\mathrm{rem,coverslips}}$ 0 min (light colors), 40 min (medium colors), and 80 min (dark colors) after the addition of the particles to the imaging medium. Error bars represent the standard error of mean calculated from 3 individual experiments each (fig. 4.7). The figure is discussed in section 4.4.2.4. Figure adapted from Gross et al., in preparation, 2022[382].

Bibliography

[1] C. Milsom and S. Rigby. *Fossils at a Glance*. Wiley-Blackwell, 2010.

[2] C. M. Vidal et al. "Age of the oldest known Homo sapiens from eastern Africa". *Nature* 601.7894 (2022), 579–583.

[3] E. Bianconi et al. "An estimation of the number of cells in the human body". *Annals of Human Biology* 40.6 (2013), 463–471.

[4] R. Dawkins and Y. Wong. *The Ancestor's Tale: A Pilgrimage to the Dawn of Life*. Weidenfeld & Nicolson, 2017.

[5] J. D. Watson and F. H. C. Crick. "Molecular Structure of Nucleic Acids: A Structure for Deoxyribose Nucleic Acid". *Nature* 171.4356 (1953), 737–738.

[6] I. Ezkurdia et al. "Multiple evidence strands suggest that there may be as few as 19 000 human protein-coding genes". *Human Molecular Genetics* 23.22 (2014), 5866–5878.

[7] S. Westland, Q. Pan, and S. Lee. "A review of the effects of colour and light on non-image function in humans". *Coloration Technology* 133.5 (2017), 349–361.

[8] J. R. Sellers. "Myosins: a diverse superfamily". *Biochimica et Biophysica Acta (BBA) - Molecular Cell Research* 1496.1 (2000), 3–22.

[9] J. Garcia-Anoveros and D. P. Corey. "The molecules of mechanosensation". *Annual Review of Neuroscience* 20.1 (1997), 567–594.

[10] B. Alberts et al. *Molekularbiologie der Zelle*. Wiley-VCH, 2004.

[11] E. A. Miao et al. "TLR5 and Ipaf: dual sensors of bacterial flagellin in the innate immune system". *Seminars in Immunopathology* 29.3 (2007), 275–288.

[12] H. Kumar, T. Kawai, and S. Akira. "Pathogen Recognition by the Innate Immune System". *International Reviews of Immunology* 30.1 (2011), 16–34.

[13] H. Sakano et al. "Identification and nucleotide sequence of a diversity DNA segment (D) of immunoglobulin heavy-chain genes". *Nature* 290.5807 (1981), 562–565.

[14] R. Pelanda and R. M. Torres. "Central B-Cell Tolerance: Where Selection Begins". *Cold Spring Harbor Perspectives in Biology* 4.4 (2012), a007146–a007146.

[15] W. R. Frontera and J. Ochala. "Skeletal Muscle: A Brief Review of Structure and Function". *Calcified Tissue International* 96.3 (2014), 183–195.

[16] I. Rayment et al. "Three-dimensional structure of myosin subfragment-1: a molecular motor". *Science* 261.5117 (1993), 50–58.

[17] A. F. Huxley and R. Niedergerke. "Structural Changes in Muscle During Contraction: Interference Microscopy of Living Muscle Fibres". *Nature* 173.4412 (1954), 971–973.

[18] H. Huxley and J. Hanson. "Changes in the Cross-Striations of Muscle during Contraction and Stretch and their Structural Interpretation". *Nature* 173.4412 (1954), 973–976.

[19] J. D. Powers et al. "The Sliding Filament Theory Since Andrew Huxley: Multiscale and Multidisciplinary Muscle Research". *Annual Review of Biophysics* 50.1 (2021), 373–400.

[20] G. Anastasi et al. "Integrins, muscle agrin and sarcoglycans during muscular inactivity conditions: an immunohistochemical study." *European journal of histochemistry : EJH* 50 (2006), 327–336.

[21] J. T. Finer, R. M. Simmons, and J. A. Spudich. "Single myosin molecule mechanics: piconewton forces and nanometre steps". *Nature* 368.6467 (1994), 113–119.

[22] B. Geiger and K. M. Yamada. "Molecular Architecture and Function of Matrix Adhesions". *Cold Spring Harbor Perspectives in Biology* 3.5 (2011), a005033–a005033.

[23] P. W. Oakes et al. "Geometry Regulates Traction Stresses in Adherent Cells". *Biophysical Journal* 107.4 (2014), 825–833.

[24] A. Harris, P. Wild, and D. Stopak. "Silicone rubber substrata: a new wrinkle in the study of cell locomotion". *Science* 208.4440 (1980), 177–179.

[25] J. Lee et al. "Traction forces generated by locomoting keratocytes". *The Journal of Cell Biology* 127.6 (1994), 1957–1964.

[26] J. Lee. "The Use of Gelatin Substrates for Traction Force Microscopy in Rapidly Moving Cells". *Methods in Cell Biology*. Elsevier, 2007, 295–312.

[27] F. Bosveld et al. "Mechanical Control of Morphogenesis by Fat/Dachsous/Four-Jointed Planar Cell Polarity Pathway". *Science* 336.6082 (2012), 724–727.

[28] M. Murrell et al. "Forcing cells into shape: the mechanics of actomyosin contractility". *Nature Reviews Molecular Cell Biology* 16.8 (2015), 486–498.

[29] Z. Sun, S. S. Guo, and R. Fässler. "Integrin-mediated mechanotransduction". *Journal of Cell Biology* 215.4 (2016), 445–456.

[30] P. Pandya, J. L. Orgaz, and V. Sanz-Moreno. "Actomyosin contractility and collective migration: may the force be with you". *Current Opinion in Cell Biology* 48 (2017), 87–96.

[31] J. Z. Kechagia, J. Ivaska, and P. Roca-Cusachs. "Integrins as biomechanical sensors of the microenvironment". *Nature Reviews Molecular Cell Biology* 20.8 (2019), 457–473.

[32] T. Arimori et al. "Structural mechanism of laminin recognition by integrin". *Nature Communications* 12.1 (2021), 4012.

[33] J. Heino. "Cellular Signaling by Collagen-Binding Integrins". *Advances in Experimental Medicine and Biology*. Springer Netherlands, 2014, 143–155.

[34] B.-H. Luo, C. V. Carman, and T. A. Springer. "Structural Basis of Integrin Regulation and Signaling". *Annual Review of Immunology* 25.1 (2007), 619–647.

[35] S. Linder. "Podosomes at a glance". *Journal of Cell Science* 118.10 (2005), 2079–2082.

[36] J. D. Humphrey, E. R. Dufresne, and M. A. Schwartz. "Mechanotransduction and extracellular matrix homeostasis". *Nature Reviews Molecular Cell Biology* 15.12 (2014), 802–812.

[37] S. V. Plotnikov et al. "Force Fluctuations within Focal Adhesions Mediate ECM-Rigidity Sensing to Guide Directed Cell Migration". *Cell* 151.7 (2012), 1513–1527.

[38] A. Elosegui-Artola, X. Trepat, and P. Roca-Cusachs. "Control of Mechanotransduction by Molecular Clutch Dynamics". *Trends in Cell Biology* 28.5 (2018), 356–367.

[39] A. Elosegui-Artola et al. "Rigidity sensing and adaptation through regulation of integrin types". *Nature Materials* 13.6 (2014), 631–637.

[40] L. B. Case and C. M. Waterman. "Integration of actin dynamics and cell adhesion by a three-dimensional, mechanosensitive molecular clutch". *Nature Cell Biology* 17.8 (2015), 955–963.

[41] A. Elosegui-Artola et al. "Mechanical regulation of a molecular clutch defines force transmission and transduction in response to matrix rigidity". *Nature Cell Biology* 18.5 (2016), 540–548.

[42] V. Swaminathan and C. M. Waterman. "The molecular clutch model for mechanotransduction evolves". *Nature Cell Biology* 18.5 (2016), 459–461.

[43] H. Wolfenson, B. Yang, and M. P. Sheetz. "Steps in Mechanotransduction Pathways that Control Cell Morphology". *Annual Review of Physiology* 81.1 (2019), 585–605.

[44] M. R. Mofrad. "Rheology of the Cytoskeleton". *Annual Review of Fluid Mechanics* 41.1 (2009), 433–453.

[45] D. A. Fletcher and R. D. Mullins. "Cell mechanics and the cytoskeleton". *Nature* 463.7280 (2010), 485–492.

[46] J. Tao et al. "Cell mechanics: a dialogue". *Reports on Progress in Physics* 80.3 (2017), 036601.

[47] A. M. Handorf et al. "Tissue Stiffness Dictates Development, Homeostasis, and Disease Progression". *Organogenesis* 11.1 (2015), 1–15.

[48] D. Ghosh and M. R. Dawson. "Microenvironment Influences Cancer Cell Mechanics from Tumor Growth to Metastasis". *Advances in Experimental Medicine and Biology*. Springer International Publishing, 2018, 69–90.

[49] O. Chaudhuri et al. "Effects of extracellular matrix viscoelasticity on cellular behaviour". *Nature* 584.7822 (2020), 535–546.

[50] C. M. Kraning-Rush et al. "Quantifying Traction Stresses in Adherent Cells". *Methods in Cell Biology*. Elsevier, 2012, 139–178.

[51] R. W. Style et al. "Traction force microscopy in physics and biology". *Soft Matter* 10.23 (2014), 4047–4055.

[52] D. J. Papachristou et al. "Signaling networks and transcription factors regulating mechanotransduction in bone". *BioEssays* 31.7 (2009), 794–804.

[53] R. J. McMurray, M. J. Dalby, and P. M. Tsimbouri. "Using biomaterials to study stem cell mechanotransduction, growth and differentiation". *Journal of Tissue Engineering and Regenerative Medicine* 9.5 (2014), 528–539.

[54] A. J. Engler et al. "Matrix Elasticity Directs Stem Cell Lineage Specification". *Cell* 126.4 (2006), 677–689.

[55] C.-M. Lo et al. "Cell Movement Is Guided by the Rigidity of the Substrate". *Biophysical Journal* 79.1 (2000), 144–152.

[56] A. Engler et al. "Substrate Compliance versus Ligand Density in Cell on Gel Responses". *Biophysical Journal* 86.1 (2004), 617–628.

[57] P. C. Georges and P. A. Janmey. "Cell type-specific response to growth on soft materials". *Journal of Applied Physiology* 98.4 (2005), 1547–1553.

[58] S. Féréol et al. "Sensitivity of alveolar macrophages to substrate mechanical and adhesive properties". *Cell Motility and the Cytoskeleton* 63.6 (2006), 321–340.

[59] P. Moshayedi et al. "Mechanosensitivity of astrocytes on optimized polyacrylamide gels analyzed by quantitative morphometry". *Journal of Physics: Condensed Matter* 22.19 (2010), 194114.

[60] C. A. Mullen et al. "The Effect of Substrate Stiffness, Thickness, and Cross-Linking Density on Osteogenic Cell Behavior". *Biophysical Journal* 108.7 (2015), 1604–1612.

[61] A. Balgude. "Agarose gel stiffness determines rate of DRG neurite extension in 3D cultures". *Biomaterials* 22.10 (2001), 1077–1084.

[62] L. A. Flanagan et al. "Neurite branching on deformable substrates." *Neuroreport* 13 (2002), 2411–2415.

[63] S. Kumar et al. "Viscoelastic Retraction of Single Living Stress Fibers and Its Impact on Cell Shape, Cytoskeletal Organization, and Extracellular Matrix Mechanics". *Biophysical Journal* 90.10 (2006), 3762–3773.

[64] B. Geiger, J. P. Spatz, and A. D. Bershadsky. "Environmental sensing through focal adhesions". *Nature Reviews Molecular Cell Biology* 10.1 (2009), 21–33.

[65] R. J. Pelham and Y.-l. Wang. "Cell locomotion and focal adhesions are regulated by substrate flexibility". *Proceedings of the National Academy of Sciences* 94.25 (1997), 13661–13665.

[66] T. Kawano and S. Kidoaki. "Elasticity boundary conditions required for cell mechanotaxis on microelastically-patterned gels". *Biomaterials* 32.11 (2011), 2725–2733.

[67] P. Roca-Cusachs, R. Sunyer, and X. Trepat. "Mechanical guidance of cell migration: lessons from chemotaxis". *Current Opinion in Cell Biology* 25.5 (2013), 543–549.

[68] R. Sunyer et al. "Collective cell durotaxis emerges from long-range intercellular force transmission". *Science* 353.6304 (2016), 1157–1161.

[69] B. J. DuChez et al. "Durotaxis by Human Cancer Cells". *Biophysical Journal* 116.4 (2019), 670–683.

[70] K. A. Beningo and Y.-l. Wang. "Fc-receptor-mediated phagocytosis is regulated by mechanical properties of the target". *Journal of Cell Science* 115.4 (2002), 849–856.

[71] N. G. Sosale et al. "Cell rigidity and shape override CD47's "self"-signaling in phagocytosis by hyperactivating myosin-II." *Blood* 125 (2015), 542–552.

[72] V. Jaumouille, A. X. Cartagena-Rivera, and C. M. Waterman. "Coupling of $\beta 2$ integrins to actin by a mechanosensitive molecular clutch drives complement receptor-mediated phagocytosis". *Nature Cell Biology* 21.11 (2019), 1357–1369.

[73] D. Vorselen, R. L. D. Labitigan, and J. A. Theriot. "A mechanical perspective on phagocytic cup formation". *Current Opinion in Cell Biology* 66 (2020), 112–122.

[74] D. Vorselen et al. "Microparticle traction force microscopy reveals subcellular force exertion patterns in immune cell–target interactions". *Nature Communications* 11.1 (2020), 20.

[75] D. Vorselen et al. "Phagocytic 'teeth' and myosin-II 'jaw' power target constriction during phagocytosis". *eLife* 10 (2021), e68627.

[76] A. K. Harris, D. Stopak, and P. Wild. "Fibroblast traction as a mechanism for collagen morphogenesis". *Nature* 290.5803 (1981), 249–251.

[77] X. Yu et al. "Measurement of the traction force of biological cells by digital holography". *Biomedical Optics Express* 3.1 (2011), 153–159.

[78] A. D. L. Pena et al. "Quantifying cellular forces: Practical considerations of traction force microscopy for dermal fibroblasts". *Experimental Dermatology* 30 (2020), 74–83.

[79] M. Dembo et al. "Imaging the traction stresses exerted by locomoting cells with the elastic substratum method". *Biophysical Journal* 70.4 (1996), 2008–2022.

[80] J. C. del Alamo et al. "Spatio-temporal analysis of eukaryotic cell motility by improved force cytometry". *Proceedings of the National Academy of Sciences* 104.33 (2007), 13343–13348.

[81] S. V. Plotnikov et al. "High-Resolution Traction Force Microscopy". *Methods in Cell Biology*. Elsevier, 2014, 367–394.

[82] B. Sabass et al. "High Resolution Traction Force Microscopy Based on Experimental and Computational Advances". *Biophysical Journal* 94.1 (2008), 207–220.

[83] B. Sabass et al. "Force generation by groups of migrating bacteria". *Proceedings of the National Academy of Sciences* 114.28 (2017), 7266–7271.

[84] E. Bastounis et al. "The SCAR/WAVE complex is necessary for proper regulation of traction stresses during amoeboid motility". *Molecular Biology of the Cell* 22.21 (2011), 3995–4003.

[85] L. E. Hind, M. Dembo, and D. A. Hammer. "Macrophage motility is driven by frontal-towing with a force magnitude dependent on substrate stiffness". *Integrative Biology* 7.4 (2015), 447–453.

[86] N. Schierbaum, J. Rheinlaender, and T. E. Schäffer. "Combined atomic force microscopy (AFM) and traction force microscopy (TFM) reveals a correlation between viscoelastic material properties and contractile prestress of living cells". *Soft Matter* 15.8 (2019), 1721–1729.

[87] N. Q. Balaban et al. "Force and focal adhesion assembly: a close relationship studied using elastic micropatterned substrates". *Nature Cell Biology* 3.5 (2001), 466–472.

[88] B. Fabry et al. "Focal Adhesion Kinase Stabilizes the Cytoskeleton". *Biophysical Journal* 101.9 (2011), 2131–2138.

[89] J. C. Chang, Y. Liu, and T. Chou. "Reconstruction of Cell Focal Adhesions using Physical Constraints and Compressive Regularization". *Biophysical Journal* 113.11 (2017), 2530–2539.

[90] P. Rajagopalan et al. "Direct Comparison of the Spread Area, Contractility, and Migration of balb/c 3T3 Fibroblasts Adhered to Fibronectin- and RGD-Modified Substrata". *Biophysical Journal* 87.4 (2004), 2818–2827.

[91] C. Müller and T. Pompe. "Distinct impacts of substrate elasticity and ligand affinity on traction force evolution". *Soft Matter* 12.1 (2016), 272–280.

[92] S. Pok and J. G. Jacot. "Work and Tension: New Evidence that Adherent Cells of the Same Area Do the Same Work Independent of Stiffness and Focal Adhesions". *Biophysical Journal* 107.4 (2014), 798–799.

[93] N. Hersch et al. "The constant beat: cardiomyocytes adapt their forces by equal contraction upon environmental stiffening". *Biology Open* 2.3 (2013), 351–361.

[94] J.-P. Rieu et al. "Periodic traction in migrating large amoeba of Physarum polycephalum". *Journal of The Royal Society Interface* 12.106 (2015), 20150099.

[95] M. Ouyang et al. "Sensing Traction Force on the Matrix Induces Cell-Cell Distant Mechanical Communications for Self-Assembly". *ACS Biomaterials Science & Engineering* 6.10 (2020), 5833–5848.

[96] J. A. Swanson. "Shaping cups into phagosomes and macropinosomes". *Nature Reviews. Molecular Cell Biology* 9.8 (2008), 639–649.

[97] A. Torres-Gomez, C. Cabañas, and E. M. Lafuente. "Phagocytic Integrins: Activation and Signaling". *Frontiers in Immunology* 11 (2020), 738.

[98] M. C. Kerr and R. D. Teasdale. "Defining Macropinocytosis". *Traffic* 10.4 (2009), 364–371.

[99] D. M. Underhill and H. S. Goodridge. "Information processing during phagocytosis". *Nature Reviews Immunology* 12.7 (2012), 492–502.

[100] O. Elomaa et al. "Cloning of a novel bacteria-binding receptor structurally related to scavenger receptors and expressed in a subset of macrophages". *Cell* 80.4 (1995), 603–609.

[101] D. M. E. Bowdish and S. Gordon. "Conserved domains of the class A scavenger receptors: evolution and function". *Immunological Reviews* 227.1 (2009), 19–31.

[102] P. Maderna and C. Godson. "Phagocytosis of apoptotic cells and the resolution of inflammation". *Biochimica et Biophysica Acta (BBA) - Molecular Basis of Disease* 1639.3 (2003), 141–151.

[103] A. G. Dupuy and E. Caron. "Integrin-dependent phagocytosis – spreading from microadhesion to new concepts". *Journal of Cell Science* 121.11 (2008), 1773–1783.

[104] R. S. Flannagan, V. Jaumouille, and S. Grinstein. "The Cell Biology of Phagocytosis". *Annual Review of Pathology: Mechanisms of Disease* 7.1 (2012), 61–98.

[105] S. Gordon and A. Plüddemann. "Macrophage Clearance of Apoptotic Cells: A Critical Assessment". *Frontiers in Immunology* 9 (2018), 127.

[106] J. A. Champion, A. Walker, and S. Mitragotri. "Role of Particle Size in Phagocytosis of Polymeric Microspheres". *Pharmaceutical Research* 25.8 (2008), 1815–1821.

[107] G. Cannon and J. Swanson. "The macrophage capacity for phagocytosis". *Journal of Cell Science* 101.4 (1992), 907–913.

[108] A. Aderem and D. M. Underhill. "Mechanisms of Phagocytosis in Macrophages". *Annual Review of Immunology* 17.1 (1999), 593–623.

[109] L. Buonaguro et al. "Baculovirus-Derived Human Immunodeficiency Virus Type 1 Virus-Like Particles Activate Dendritic Cells and Induce Ex Vivo T-Cell Responses". *Journal of Virology* 80.18 (2006), 9134–9143.

[110] S. M. Schmidt et al. "Uptake of calcium phosphate nanoshells by osteoblasts and their effect on growth and differentiation". *Journal of Biomedical Materials Research Part A* 87A.2 (2008), 418–428.

[111] S. A. Freeman and S. Grinstein. "Phagocytosis: How Macrophages Tune Their Non-professional Counterparts". *Current Biology* 26.24 (2016), R1279–R1282.

[112] K. S. Ravichandran and U. Lorenz. "Engulfment of apoptotic cells: signals for a good meal". *Nature Reviews Immunology* 7.12 (2007), 964–974.

[113] M. R. Elliott and K. S. Ravichandran. "Clearance of apoptotic cells: implications in health and disease". *The Journal of Cell Biology* 189.7 (2010), 1059–1070.

[114] E. Metchnikoff. *Lectures on the Comparative Pathology of Inflammation, translated from the French by F. A. Starling and E. H. Starling, with a new introduction by Arthur M. Silverstein.* Dover Publications, 1968.

[115] S. Gordon. "Phagocytosis: The Legacy of Metchnikoff". *Cell* 166.5 (2016), 1065–1068.

[116] M. Rabinovitch. "Professional and non-professional phagocytes: an introduction". *Trends in Cell Biology* 5.3 (1995), 85–87.

[117] A. J. Rees. "Monocyte and Macrophage Biology: An Overview". *Seminars in Nephrology* 30.3 (2010), 216–233.

[118] J. J. Lim, S. Grinstein, and Z. Roth. "Diversity and Versatility of Phagocytosis: Roles in Innate Immunity, Tissue Remodeling, and Homeostasis". *Frontiers in Cellular and Infection Microbiology* 7 (2017), 191.

[119] F. Nimmerjahn and J. V. Ravetch. "Fcγ receptors as regulators of immune responses". *Nature Reviews Immunology* 8.1 (2008), 34–47.

[120] S. D. Blystone et al. "Integrin alpha v beta 3 differentially regulates adhesive and phagocytic functions of the fibronectin receptor alpha 5 beta 1." *Journal of Cell Biology* 127.4 (1994), 1129–1137.

[121] S. D. Blystone et al. "Integrin beta 3 cytoplasmic tail is necessary and sufficient for regulation of alpha 5 beta 1 phagocytosis by alpha v beta 3 and integrin-associated protein." *Journal of Cell Biology* 130.3 (1995), 745–754.

[122] S. A. Freeman and S. Grinstein. "Phagocytosis: receptors, signal integration, and the cytoskeleton". *Immunological Reviews* 262.1 (2014), 193–215.

[123] S. Gordon. "Phagocytosis: An Immunobiologic Process". *Immunity* 44.3 (2016), 463–475.

[124] S. Jaiswal et al. "CD47 Is Upregulated on Circulating Hematopoietic Stem Cells and Leukemia Cells to Avoid Phagocytosis". *Cell* 138.2 (2009), 271–285.

[125] S. B. Willingham et al. "The CD47-signal regulatory protein alpha (SIRPa) interaction is a therapeutic target for human solid tumors". *Proceedings of the National Academy of Sciences* 109.17 (2012), 6662–6667.

[126] T. Fujiwara et al. "Phospholipids undergo hop diffusion in compartmentalized cell membrane". *Journal of Cell Biology* 157.6 (2002), 1071–1082.

[127] R. S. Flannagan et al. "Dynamic macrophage "probing" is required for the efficient capture of phagocytic targets". *Journal of Cell Biology* 191.6 (2010), 1205–1218.

[128] A. Kusumi et al. "Dynamic Organizing Principles of the Plasma Membrane that Regulate Signal Transduction: Commemorating the Fortieth Anniversary of Singer and Nicolson's Fluid-Mosaic Model". *Annual Review of Cell and Developmental Biology* 28.1 (2012), 215–250.

[129] P. K. Mattila, F. D. Batista, and B. Treanor. "Dynamics of the actin cytoskeleton mediates receptor cross talk: An emerging concept in tuning receptor signaling". *The Journal of Cell Biology* 212.3 (2016), 267–280.

[130] D. Krapf. "Compartmentalization of the plasma membrane". *Current Opinion in Cell Biology* 53 (2018), 15–21.

[131] V. Jaumouille et al. "Actin Cytoskeleton Reorganization by Syk Regulates Fcγ Receptor Responsiveness by Increasing Its Lateral Mobility and Clustering". *Developmental Cell* 29.5 (2014), 534–546.

[132] J. Lin et al. "TIRF imaging of Fc gamma receptor microclusters dynamics and signaling on macrophages during frustrated phagocytosis". *BMC Immunology* 17 (2016), 5.

[133] S. M. Mylvaganam, S. Grinstein, and S. A. Freeman. "Picket-fences in the plasma membrane: functions in immune cells and phagocytosis". *Seminars in Immunopathology* 40.6 (2018), 605–615.

[134] D. M. Mosser and J. P. Edwards. "Exploring the full spectrum of macrophage activation". *Nature Reviews Immunology* 8.12 (2008), 958–969.

[135] J. D. Rotty et al. "Arp2/3 Complex Is Required for Macrophage Integrin Functions but Is Dispensable for FcR Phagocytosis and InVivo Motility". *Developmental Cell* 42.5 (2017), 498–513.e6.

[136] E. Colucci-Guyon et al. "A Role for Mammalian Diaphanous-Related Formins in Complement Receptor (CR3)-Mediated Phagocytosis in Macrophages". *Current Biology* 15.22 (2005), 2007–2012.

[137] R. C. May et al. "Involvement of the Arp2/3 complex in phagocytosis mediated by FcγR or CR3". *Nature Cell Biology* 2.4 (2000), 246–248.

[138] S. Tollis et al. "The zipper mechanism in phagocytosis: energetic requirements and variability in phagocytic cup shape". *BMC Systems Biology* 4.1 (2010), 149.

[139] G. Kaplan. "Differences in the Mode of Phagocytosis with Fc and C3 Receptors in Macrophages". *Scandinavian Journal of Immunology* 6.8 (1977), 797–807.

[140] L. A. Allen and A. Aderem. "Molecular definition of distinct cytoskeletal structures involved in complement- and Fc receptor-mediated phagocytosis in macrophages." *Journal of Experimental Medicine* 184.2 (1996), 627–637.

[141] A. B. Hall et al. "Requirements for Vav Guanine Nucleotide Exchange Factors and Rho GTPases in FcγR- and Complement-Mediated Phagocytosis". *Immunity* 24.3 (2006), 305–316.

[142] S. A. Freeman and S. Grinstein. "Phagocytosis: Mechanosensing, Traction Forces, and a Molecular Clutch". *Current Biology* 30.1 (2020), R24–R26.

[143] V. Jaumouille and C. M. Waterman. "Physical Constraints and Forces Involved in Phagocytosis". *Frontiers in Immunology* 11 (2020), 1097.

[144] S. Greenberg, K. Burridge, and S. C. Silverstein. "Colocalization of F-actin and talin during Fc receptor-mediated phagocytosis in mouse macrophages." *Journal of Experimental Medicine* 172.6 (1990), 1853–1856.

[145] S. A. Freeman et al. "Integrins Form an Expanding Diffusional Barrier that Coordinates Phagocytosis". *Cell* 164.1-2 (2016), 128–140.

[146] Y. Gao and Y. Yu. "Macrophage Uptake of Janus Particles Depends upon Janus Balance". *Langmuir* 31.9 (2015), 2833–2838.

[147] N. Araki et al. "Phosphoinositide-3-kinase-independent contractile activities associated with Fcγ-receptor-mediated phagocytosis and macropinocytosis in macrophages". *Journal of Cell Science* 116.2 (2003), 247–257.

[148] S. R. Barger, N. C. Gauthier, and M. Krendel. "Squeezing in a Meal: Myosin Functions in Phagocytosis". *Trends in Cell Biology* 30.2 (2020), 157–167.

[149] R. Levin, S. Grinstein, and J. Canton. "The life cycle of phagosomes: formation, maturation, and resolution". *Immunological Reviews* 273.1 (2016), 156–179.

[150] S. M. Ferguson and P. D. Camilli. "Dynamin, a membrane-remodelling GTPase". *Nature Reviews Molecular Cell Biology* 13.2 (2012), 75–88.

[151] F. Marie-Anais et al. "Dynamin-Actin Cross Talk Contributes to Phagosome Formation and Closure". *Traffic* 17.5 (2016), 487–499.

[152] C. Rosales and E. Uribe-Querol. "Phagocytosis: A Fundamental Process in Immunity". *BioMed Research International* 2017 (2017), 1–18.

[153] S. Keller, K. Berghoff, and H. Kress. "Phagosomal transport depends strongly on phagosome size". *Scientific Reports* 7.1 (2017), 17068.

[154] S. Keller. "Abhängigkeit des phagosomalen Transports von der Größe des Phagosoms". *PHD thesis, University of Bayreuth* (2019).

[155] S. Saroussi and N. Nelson. "The little we know on the structure and machinery of V-ATPase". *Journal of Experimental Biology* 212.11 (2009), 1604–1610.

[156] W. Gross. "Implementierung von Zugkraftmikroskopie mithilfe von Polyacrylamidgelen". *Master's Thesis, University of Bayreuth* (2014).

[157] W. Gross and H. Kress. "Simultaneous measurement of the Young's modulus and the Poisson ratio of thin elastic layers". *Soft Matter* 13.5 (2017), 1048–1055.

[158] W. Gross and H. Kress. "Optimization of experimental parameters for the mechanical characterization of thin elastic films". *Journal of Physics Communications* 3.5 (2019), 055021.

[159] M. Dembo and Y.-L. Wang. "Stresses at the Cell-to-Substrate Interface during Locomotion of Fibroblasts". *Biophysical Journal* 76.4 (1999), 2307–2316.

[160] M. T. Frey et al. "Microscopic Methods for Measuring the Elasticity of Gel Substrates for Cell Culture: Microspheres, Microindenters, and Atomic Force Microscopy". *Methods in Cell Biology*. Elsevier, 2007, 47–65.

[161] C. E. Kandow et al. "Polyacrylamide Hydrogels for Cell Mechanics: Steps Toward Optimization and Alternative Uses". *Methods in Cell Biology*. Elsevier, 2007, 29–46.

[162] K. S. Boochoon et al. "The influence of substrate elastic modulus on retinal pigment epithelial cell phagocytosis". *Journal of Biomechanics* 47.12 (2014), 3237–3240.

[163] P. Madhusudanan, G. Raju, and S. Shankarappa. "Hydrogel systems and their role in neural tissue engineering". *Journal of The Royal Society Interface* 17.162 (2020), 20190505.

[164] B. Strachota, J. Hodan, and L. Matějka. "Poly(N-isopropylacrylamide)–clay hydrogels: Control of mechanical properties and structure by the initiating conditions of polymerization". *European Polymer Journal* 77 (2016), 1–15.

[165] H. Guo et al. "Thermoresponsive Toughening in LCST-Type Hydrogels: Comparison between Semi-Interpenetrated and Grafted Networks". *Macromolecules* 49.24 (2016), 9568–9577.

[166] C. Li, Z. Hu, and Y. Li. "Poisson's ratio in polymer gels near the phase-transition point". *Physical Review E* 48.1 (1993), 603–606.

[167] P. Kujawa et al. "Temperature-Sensitive Properties of Poly(N-isopropylacrylamide) Mesoglobules Formed in Dilute Aqueous Solutions Heated above Their Demixing Point". *Macromolecules* 39.22 (2006), 7686–7693.

[168] L. Li et al. "Fabrication of Thermoresponsive Polymer Gradients for Study of Cell Adhesion and Detachment". *Langmuir* 24.23 (2008), 13632–13639.

[169] R. Pelton. "Poly(N-isopropylacrylamide) (PNIPAM) is never hydrophobic". *Journal of Colloid and Interface Science* 348.2 (2010), 673–674.

[170] S. Hirotsu. "Elastic anomaly near the critical point of volume phase transition in polymer gels". *Macromolecules* 23.3 (1990), 903–905.

[171] P. Voudouris et al. "Micromechanics of temperature sensitive microgels: dip in the Poisson ratio near the LCST". *Soft Matter* 9.29 (2013), 7158.

[172] M. Yamato et al. "Signal transduction and cytoskeletal reorganization are required for cell detachment from cell culture surfaces grafted with a temperature-responsive polymer". *Journal of Biomedical Materials Research* 44.1 (1999), 44–52.

[173] K. Nishida et al. "Functional bioengineered corneal epithelial sheet grafts from corneal stem cells expanded ex vivo on a temperature-responsive cell culture surface". *Transplantation* 77.3 (2004), 379–385.

[174] Z. Tang, Y. Akiyama, and T. Okano. "Temperature-Responsive Polymer Modified Surface for Cell Sheet Engineering". *Polymers* 4.3 (2012), 1478–1498.

[175] B. Trappmann et al. "Extracellular-matrix tethering regulates stem-cell fate". *Nature Materials* 11.7 (2012), 642–649.

[176] A. Ulbricht et al. "Cellular Mechanotransduction Relies on Tension-Induced and Chaperone-Assisted Autophagy". *Current Biology* 23.5 (2013), 430–435.

[177] J. R. D. Soiné et al. "Measuring cellular traction forces on non-planar substrates". *Interface Focus* 6.5 (2016), 20160024.

[178] M. Murrell, R. Kamm, and P. Matsudaira. "Substrate Viscosity Enhances Correlation in Epithelial Sheet Movement". *Biophysical Journal* 101.2 (2011), 297–306.

[179] C. M. Cesa et al. "Micropatterned silicone elastomer substrates for high resolution analysis of cellular force patterns". *Review of Scientific Instruments* 78.3 (2007), 034301.

[180] D. Calvet, J. Y. Wong, and S. Giasson. "Rheological Monitoring of Polyacrylamide Gelation: Importance of Cross-Link Density and Temperature". *Macromolecules* 37.20 (2004), 7762–7771.

[181] O. Okay and W. Oppermann. "Polyacrylamide-Clay Nanocomposite Hydrogels: Rheological and Light Scattering Characterization". *Macromolecules* 40.9 (2007), 3378–3387.

[182] K. Izdihar et al. "Structural, Mechanical, and Dielectric Properties of Polydimethylsiloxane and Silicone Elastomer for the Fabrication of Clinical-Grade Kidney Phantom". *Applied Sciences* 11.3 (2021), 1172.

[183] R. Jana, H. Bhunia, and G. Nando. "An investigation into the mechanical properties and curing kinetics of blends of low-density polyethylene and polydimethyl siloxane rubber". *Thermochimica Acta* 302.1-2 (1997), 1–9.

[184] Y. Konku-Asase, A. Yaya, and K. Kan-Dapaah. "Curing Temperature Effects on the Tensile Properties and Hardness of γ-Fe2O3 Reinforced PDMS Nanocomposites". *Advances in Materials Science and Engineering* 2020 (2020), 1–11.

[185] O. Okay, S. B. Sariisik, and S. D. Zor. "Swelling behavior of anionic acrylamide-based hydrogels in aqueous salt solutions: Comparison of experiment with theory". *Journal of Applied Polymer Science* 70.3 (1998), 567–575.

[186] M. Y. Kizilay and O. Okay. "Effect of swelling on spatial inhomogeneity in poly(acrylamide) gels formed at various monomer concentrations". *Polymer* 45.8 (2004), 2567–2576.

[187] Y. Lai and Y. Hu. "Probing the swelling-dependent mechanical and transport properties of polyacrylamide hydrogels through AFM-based dynamic nanoindentation". *Soft Matter* 14.14 (2018), 2619–2627.

[188] M. H. Esteki et al. "A new framework for characterization of poroelastic materials using indentation". *Acta Biomaterialia* 102 (2020), 138–148.

[189] H. R. Hertz. "Über die Berührung fester elastischer Körper und über die Härte". *Journal für die reine und angewandte Mathematik* 92 (1882), 156–171.

[190] E. K. Dimitriadis et al. "Determination of Elastic Moduli of Thin Layers of Soft Material Using the Atomic Force Microscope". *Biophysical Journal* 82.5 (2002), 2798–2810.

[191] R. Long et al. "Effects of Gel Thickness on Microscopic Indentation Measurements of Gel Modulus". *Biophysical Journal* 101.3 (2011), 643–650.

[192] S. Huth, S. Sindt, and C. Selhuber-Unkel. "Automated analysis of soft hydrogel microindentation: Impact of various indentation parameters on the measurement of Young's modulus". *PLOS ONE* 14.8 (2019), e0220281.

[193] W. Hayes et al. "A mathematical analysis for indentation tests of articular cartilage". *Journal of Biomechanics* 5.5 (1972), 541–551.

[194] Y. Cao, D. Ma, and D. Raabe. "The use of flat punch indentation to determine the viscoelastic properties in the time and frequency domains of a soft layer bonded to a rigid substrate". *Acta Biomaterialia* 5.1 (2009), 240–248.

[195] F. Rico et al. "Probing mechanical properties of living cells by atomic force microscopy with blunted pyramidal cantilever tips". *Physical Review E* 72.2 (2005), 021914.

[196] A. J. Engler et al. "Microtissue Elasticity: Measurements by Atomic Force Microscopy and Its Influence on Cell Differentiation". *Methods in Cell Biology*. Elsevier, 2007, 521–545.

[197] K. Franze et al. "Spatial mapping of the mechanical properties of the living retina using scanning force microscopy". *Soft Matter* 7.7 (2011), 3147–3154.

[198] T. Boudou et al. "An extended modeling of the micropipette aspiration experiment for the characterization of the Young's modulus and Poisson's ratio of adherent thin biological samples: Numerical and experimental studies". *Journal of Biomechanics* 39.9 (2006), 1677–1685.

[199] S. A. Maskarinec et al. "Quantifying cellular traction forces in three dimensions". *Proceedings of the National Academy of Sciences* 106.52 (2009), 22108–22113.

[200] U. Chippada, B. Yurke, and N. A. Langrana. "Simultaneous determination of Young's modulus, shear modulus, and Poisson's ratio of soft hydrogels". *Journal of Materials Research* 25.03 (2010), 545–555.

[201] H. Jin and J. L. Lewis. "Determination of Poisson's Ratio of Articular Cartilage by Indentation Using Different-Sized Indenters". *Journal of Biomechanical Engineering* 126.2 (2004), 138–145.

[202] M. S. Hall et al. "Mapping Three-Dimensional Stress and Strain Fields within a Soft Hydrogel Using a Fluorescence Microscope". *Biophysical Journal* 102.10 (2012), 2241–2250.

[203] D. Koch et al. "Strength in the Periphery: Growth Cone Biomechanics and Substrate Rigidity Response in Peripheral and Central Nervous System Neurons". *Biophysical Journal* 102.3 (2012), 452–460.

[204] J. G. Jacot et al. "A simple microindentation technique for mapping the microscale compliance of soft hydrated materials and tissues". *Journal of Biomedical Materials Research Part A* 79A.3 (2006), 485–494.

[205] V. Peschetola et al. "Time-dependent traction force microscopy for cancer cells as a measure of invasiveness". *Cytoskeleton* 70.4 (2013), 201–214.

[206] Y. Li, Z. Hu, and C. Li. "New method for measuring poisson's ratio in polymer gels". *Journal of Applied Polymer Science* 50.6 (1993), 1107–1111.

[207] T. Boudou et al. "An extended relationship for the characterization of Young's modulus and Poisson's ratio of tunable polyacrylamide gels." *Biorheology* 43 (6 2006), 721–728.

[208] Z. I. Kalcioglu et al. "From macro- to microscale poroelastic characterization of polymeric hydrogels via indentation". *Soft Matter* 8.12 (2012), 3393–3398.

[209] S. Girardo et al. "Standardized microgel beads as elastic cell mechanical probes". *Journal of Materials Chemistry B* 6.39 (2018), 6245–6261.

[210] J. C. del Alamo et al. "Three-Dimensional Quantification of Cellular Traction Forces and Mechanosensing of Thin Substrata by Fourier Traction Force Microscopy". *PLoS ONE* 8.9 (2013), e69850.

[211] J. D. Aplin and R. Hughes. "Protein-derivatised glass coverslips for the study of cell-to-substratum adhesion". *Analytical Biochemistry* 113.1 (1981), 144–148.

[212] J. Zhang and A. Wang. "Study on superabsorbent composites. IX: Synthesis, characterization and swelling behaviors of polyacrylamide/clay composites based on various clays". *Reactive and Functional Polymers* 67.8 (2007), 737–745.

[213] R. C. Weast and M. Astle. *CRC Handbook of Chemistry and Physics*. 61st ed. CRC Press Inc., 1980.

[214] A. Lasslett. "Principles and applications of differential interference contrast light microscopy". *Microscopy and Analysis* 20.5 (2006), S9–S11.

[215] L. Gebhardt. "Implementierung Fluoreszenz-basierter Mikrothermometrie zur Untersuchung von Zellen in Temperaturgradienten". *Master's Thesis, University of Bayreuth* (2015).

[216] K. Berghoff. "Entwicklung einer Arbeitsstation zur optischen Mikromanipulation und Charakterisierung des Einflusses von Aktin auf die Zellmechanik der Phagozytose". *PHD thesis, University of Bayreuth* (2018).

[217] K. Chaitavon, S. Sumriddetchkajorn, and J. Nukeaw. "Highly sensitive refractive index measurement with a sandwiched single-flow-channel microfluidic chip". *RSC Advances* 3.19 (2013), 6981–6984.

[218] M. L. Byron and E. A. Variano. "Refractive-index-matched hydrogel materials for measuring flow-structure interactions". *Experiments in Fluids* 54.2 (2013), 1456.

[219] B. W. Garner et al. "Refractive Index Change Due to Volume-Phase Transition in Polyacrylamide Gel Nanospheres for Optoelectronics and Bio-photonics". *Applied Physics Express* 2 (2009), 057001.

[220] J. E. Jonkman et al. "[18] Resolution in optical microscopy". *Methods in Enzymology*. Elsevier, 2003, 416–446.

[221] J. Schindelin et al. "Fiji: an open-source platform for biological-image analysis". *Nature Methods* 9.7 (2012), 676–682.

[222] X. Peng et al. "A method to determine Young's modulus of soft gels for cell adhesion". *Acta Mechanica Sinica* 25.4 (2009), 565–570.

[223] G. N. Greaves et al. "Poisson's ratio and modern materials". *Nature Materials* 10.11 (2011), 823–837.

[224] W. H. Press et al. *Numerical Recipes 3rd Edition: The Art of Scientific Computing*. Cambridge University Press, 2007.

[225] A. Ochs. "Phagozytoseexperimente mithilfe von Zugkraftmikroskopie: Referenzmessungen und Weiterentwicklung der Methode". *Master's thesis, University of Bayreuth* (2021).

[226] T. Yeung et al. "Effects of substrate stiffness on cell morphology, cytoskeletal structure, and adhesion". *Cell Motility and the Cytoskeleton* 60.1 (2004), 24–34.

[227] P. H. Mott and C. M. Roland. "Limits to Poisson's ratio in isotropic materials". *Physical Review B* 80.13 (2009), 132104.

[228] H. J. Naghash and O. Okay. "Formation and structure of polyacrylamide gels". *Journal of Applied Polymer Science* 60.7 (1996), 971–979.

[229] E. Hecht. *Optics, 4th edition*. Addison-Wesley, 2001.

[230] J. Seo and L. P. Lee. "Effects on wettability by surfactant accumulation/depletion in bulk polydimethylsiloxane (PDMS)". *Sensors and Actuators B: Chemical* 119.1 (2006), 192–198.

[231] K. L. Johnson, K. Kendall, and A. D. Roberts. "Surface Energy and the Contact of Elastic Solids". *Proceedings of the Royal Society A: Mathematical, Physical and Engineering Sciences* 324.1558 (1971), 301–313.

[232] R. W. Style et al. "Surface tension and contact with soft elastic solids". *Nature Communications* 4.1 (2013), 2728.

[233] R. W. Style et al. "Elastocapillarity: Surface Tension and the Mechanics of Soft Solids". *Annual Review of Condensed Matter Physics* 8.1 (2017), 99–118.

[234] S. Dogru et al. "Poisson's ratio of PDMS thin films". *Polymer Testing* 69 (2018), 375–384.

[235] P. C. Nalam et al. "Nano-rheology of hydrogels using direct drive force modulation atomic force microscopy". *Soft Matter* 11.41 (2015), 8165–8178.

[236] M. L. Lombardi et al. "Traction force microscopy in Dictyostelium reveals distinct roles for myosin II motor and actin-crosslinking activity in polarized cell movement". *Journal of Cell Science* 120.9 (2007), 1624–1634.

[237] P. Kollmannsberger and B. Fabry. "Linear and Nonlinear Rheology of Living Cells". *Annual Review of Materials Research* 41.1 (2011), 75–97.

[238] D. Lee et al. "Three-Dimensional Confocal Microscopy Indentation Method for Hydrogel Elasticity Measurement". *Langmuir* 31.35 (2015), 9684–9693.

[239] K. Berghoff et al. "Using blinking optical tweezers to study cell rheology during initial cell-particle contact". *Biophysical Journal* 120.16 (2021), 3527–3537.

[240] D. M. Richards. "Receptor Models of Phagocytosis: The Effect of Target Shape". *Advances in Experimental Medicine and Biology*. Springer International Publishing, 2020, 55–70.

[241] F. M. Griffin et al. "Studies on the mechanism of phagocytosis. I. Requirements for circumferential attachment of particle-bound ligands to specific receptors on the macrophage plasma membrane." *Journal of Experimental Medicine* 142.5 (1975), 1263–1282.

[242] M. Herant. "Mechanics of neutrophil phagocytosis: experiments and quantitative models". *Journal of Cell Science* 119.9 (2006), 1903–1913.

[243] J. S. van Zon et al. "A mechanical bottleneck explains the variation in cup growth during FcγR phagocytosis". *Molecular Systems Biology* 5.1 (2009), 298.

[244] E. A. Francis and V. Heinrich. "Integrative experimental/computational approach establishes active cellular protrusion as the primary driving force of phagocytic spreading by immune cells". *bioRxiv* (2022), 2022.03.01.482589.

[245] D. M. Richards and R. G. Endres. "Target shape dependence in a simple model of receptor-mediated endocytosis and phagocytosis". *Proceedings of the National Academy of Sciences* 113.22 (2016), 6113–6118.

[246] J. A. Champion and S. Mitragotri. "Shape Induced Inhibition of Phagocytosis of Polymer Particles". *Pharmaceutical Research* 26.1 (2008), 244–249.

[247] Z. Lu et al. "Effect of particle shape on phagocytosis of CdTe quantum dot–cystine composites". *MedChemComm* 1.1 (2010), 84.

[248] G. Sharma et al. "Polymer particle shape independently influences binding and internalization by macrophages". *Journal of Controlled Release* 147.3 (2010), 408–412.

[249] D. M. Richards and R. G. Endres. "How cells engulf: a review of theoretical approaches to phagocytosis". *Reports on Progress in Physics* 80.12 (2017), 126601.

[250] Y. Zhao et al. "Phagocytosis of Escherichia coli biofilm cells with different aspect ratios: a role of substratum material stiffness". *Applied Microbiology and Biotechnology* 101.16 (2017), 6473–6481.

[251] J. A. Champion and S. Mitragotri. "Role of target geometry in phagocytosis". *Proceedings of the National Academy of Sciences* 103.13 (2006), 4930–4934.

[252] D. Paul et al. "Phagocytosis Dynamics Depends on Target Shape". *Biophysical Journal* 105.5 (2013), 1143–1150.

[253] S. Rudt and R. Müller. "In vitro phagocytosis assay of nano- and microparticles by chemiluminescence. III. Uptake of differently sized surface-modified particles, and its correlation to particle properties and in vivo distribution". *European Journal of Pharmaceutical Sciences* 1.1 (1993), 31–39.

[254] M. H. Bakalar et al. "Size-Dependent Segregation Controls Macrophage Phagocytosis of Antibody-Opsonized Targets". *Cell* 174.1 (2018), 131–142.e13.

[255] E. Francis et al. "Mechanisms of frustrated phagocytic spreading of human neutrophils on antibody-coated surfaces". *bioRxiv* (2022), 2022.02.18.481104.

[256] M. Herant. "Mechanics of neutrophil phagocytosis: behavior of the cortical tension". *Journal of Cell Science* 118.9 (2005), 1789–1797.

[257] M. Irmscher et al. "A method for time-resolved measurements of the mechanics of phagocytic cups". *Journal of The Royal Society Interface* 10.82 (2013), 20121048–20121048.

[258] D. Cox et al. "Requirements for Both Rac1 and Cdc42 in Membrane Ruffling and Phagocytosis in Leukocytes". *Journal of Experimental Medicine* 186.9 (1997), 1487–1494.

[259] A. D. Hoppe and J. A. Swanson. "Cdc42, Rac1, and Rac2 Display Distinct Patterns of Activation during Phagocytosis". *Molecular Biology of the Cell* 15.8 (2004), 3509–3519.

[260] Y. Ikeda et al. "Rac1 switching at the right time and location is essential for Fcγ receptor-mediated phagosome formation". *Journal of Cell Science* 130.15 (2017), 2530–2540.

[261] J. Swanson et al. "A contractile activity that closes phagosomes in macrophages". *Journal of Cell Science* 112.3 (1999), 307–316.

[262] F. Castellano, P. Chavrier, and E. Caron. "Actin dynamics during phagocytosis". *Seminars in Immunology* 13.6 (2001), 347–355.

[263] M. Horsthemke et al. "Multiple roles of filopodial dynamics in particle capture and phagocytosis and phenotypes of Cdc42 and Myo10 deletion". *Journal of Biological Chemistry* 292.17 (2017), 7258–7273.

[264] E. Nelsen et al. "Combined Atomic Force Microscope and Volumetric Light Sheet System for Correlative Force and Fluorescence Mechanobiology Studies". *Scientific Reports* 10.1 (2020), 8133.

[265] R. E. Roberts, S. Dewitt, and M. B. Hallett. "Membrane Tension and the Role of Ezrin During Phagocytosis". *Advances in Experimental Medicine and Biology*. Springer International Publishing, 2020, 83–102.

[266] M. Irmscher. "Mechanics of the contact interface between cells and functionalized surfaces". *PHD thesis, Eindhoven University of Technology* (2013).

[267] J. A. Cooper. "Effects of cytochalasin and phalloidin on actin". *The Journal of Cell Biology* 105.4 (1987), 1473–1478.

[268] U. B. Nair et al. "Crystal Structures of Monomeric Actin Bound to Cytochalasin D". *Journal of Molecular Biology* 384.4 (2008), 848–864.

[269] S. T. Souza et al. "Macrophage adhesion on fibronectin evokes an increase in the elastic property of the cell membrane and cytoskeleton: an atomic force microscopy study". *European Biophysics Journal* 43.12 (2014), 573–579.

[270] F. Castellano, P. Montcourrier, and P. Chavrier. "Membrane recruitment of Rac1 triggers phagocytosis". *Journal of Cell Science* 113.17 (2000), 2955–2961.

[271] M. Yoshida and J. E. Babensee. "Molecular aspects of microparticle phagocytosis by dendritic cells". *Journal of Biomaterials Science, Polymer Edition* 17.8 (2006), 893–907.

[272] A. Ashkin. "Acceleration and Trapping of Particles by Radiation Pressure". *Physical Review Letters* 24.4 (1970), 156–159.

[273] K. C. Neuman and S. M. Block. "Optical trapping". *Review of Scientific Instruments* 75.9 (2004), 2787–2809.

[274] E. R. Dufresne and D. G. Grier. "Optical tweezer arrays and optical substrates created with diffractive optics". *Review of Scientific Instruments* 69.5 (1998), 1974–1977.

[275] J. E. Curtis, B. A. Koss, and D. G. Grier. "Dynamic holographic optical tweezers". *Optics Communications* 207.1-6 (2002), 169–175.

[276] N. J. Jenness et al. "Three-dimensional parallel holographic micropatterning using a spatial light modulator". *Optics Express* 16.20 (2008), 15942–15948.

[277] R. D. Leonardo, F. Ianni, and G. Ruocco. "Computer generation of optimal holograms for optical trap arrays". *Optics Express* 15.4 (2007), 1913.

[278] S. H. Jones, M. D. King, and A. D. Ward. "Determining the unique refractive index properties of solid polystyrene aerosol using broadband Mie scattering from optically trapped beads". *Physical Chemistry Chemical Physics* 15.47 (2013), 20735–20741.

[279] H. Kress, E. Stelzer, and A. Rohrbach. "Measuring and adjusting the trapping position in optical tweezers". *DGaO Proceedings*. DGaO, 2005.

[280] X. Zhao et al. "Optical Fiber Tweezers: A Versatile Tool for Optical Trapping and Manipulation". *Micromachines* 11.2 (2020), 114.

[281] T. A. Nieminen et al. "Optical tweezers: Theory and modelling". *Journal of Quantitative Spectroscopy and Radiative Transfer* 146 (2014), 59–80.

[282] A. Rohrbach and E. H. K. Stelzer. "Optical trapping of dielectric particles in arbitrary fields". *Journal of the Optical Society of America A* 18.4 (2001), 839.

[283] A. Rohrbach, H. Kress, and E. H. K. Stelzer. "Reply to comment on "Trapping force, force constant, and potential depths for dielectric spheres in the presence of spherical aberrations"". *Applied Optics* 43.9 (2004), 1827–1829.

[284] A. Rohrbach. "Stiffness of Optical Traps: Quantitative Agreement between Experiment and Electromagnetic Theory". *Physical Review Letters* 95.16 (2005), 168102.

[285] R. Simmons et al. "Quantitative measurements of force and displacement using an optical trap". *Biophysical Journal* 70.4 (1996), 1813–1822.

[286] N. Malagnino et al. "Measurements of trapping efficiency and stiffness in optical tweezers". *Optics Communications* 214.1-6 (2002), 15–24.

[287] C. Bustamante, Z. Bryant, and S. B. Smith. "Ten years of tension: single-molecule DNA mechanics". *Nature* 421.6921 (2003), 423–427.

[288] G. Sitters et al. "Optical Pushing: A Tool for Parallelized Biomolecule Manipulation". *Biophysical Journal* 110.1 (2016), 44–50.

[289] C. Bustamante et al. "Single-Molecule Studies of Protein Folding with Optical Tweezers". *Annual Review of Biochemistry* 89.1 (2020), 443–470.

[290] A. E.-M. Clemen et al. "Force-Dependent Stepping Kinetics of Myosin-V". *Biophysical Journal* 88.6 (2005), 4402–4410.

[291] M. J. Schnitzer and S. M. Block. "Kinesin hydrolyses one ATP per 8-nm step". *Nature* 388.6640 (1997), 386–390.

[292] A. Gennerich et al. "Force-Induced Bidirectional Stepping of Cytoplasmic Dynein". *Cell* 131.5 (2007), 952–965.

[293] L. Pozzo et al. "Studying taxis in real time using optical tweezers: Applications for Leishmania amazonensis parasites". *Micron* 40.5-6 (2009), 617–620.

[294] H. Kress et al. "Cell stimulation with optically manipulated microsources". *Nature Methods* 6.12 (2009), 905–909.

[295] K. Berghoff et al. "Application of optical tweezers for biochemical and thermal cell stimulation". *Light Robotics: Structure-Mediated Nanobiophotonics*. Elsevier, 2017, 385–410.

[296] S. Suresh et al. "Connections between single-cell biomechanics and human disease states: gastrointestinal cancer and malaria". *Acta Biomaterialia* 1.1 (2005), 15–30.

[297] M. Balland et al. "Power laws in microrheology experiments on living cells: Comparative analysis and modeling". *Physical Review E* 74.2 (2006).

[298] M. Fällman et al. "Yersinia pseudotuberculosis inhibits Fc receptor-mediated phagocytosis in J774 cells". *Infection and Immunity* 63.8 (1995), 3117–3124.

[299] D. J. Hackam et al. "Rho is Required for the Initiation of Calcium Signaling and Phagocytosis by Fcγ Receptors in Macrophages". *Journal of Experimental Medicine* 186.6 (1997), 955–966.

[300] H. Kress et al. "Control of relative radiation pressure in optical traps: Application to phagocytic membrane binding studies". *Physical Review E* 71.6 (2005), 061927.

[301] T. Becker, A. Volchuk, and J. E. Rothman. "Differential use of endoplasmic reticulum membrane for phagocytosis in J774 macrophages". *Proceedings of the National Academy of Sciences* 102.11 (2005), 4022–4026.

[302] A. Haas. "The Phagosome: Compartment with a License to Kill". *Traffic* 8.4 (2007), 311–330.

[303] H. Kress et al. "Filopodia act as phagocytic tentacles and pull with discrete steps and a load-dependent velocity". *Proceedings of the National Academy of Sciences* 104.28 (2007), 11633–11638.

[304] J. Lam et al. "Baseline Mechanical Characterization of J774 Macrophages". *Biophysical Journal* 96.1 (2009), 248–254.

[305] J. Riedl et al. "Lifeact: a versatile marker to visualize F-actin". *Nature Methods* 5.7 (2008), 605–607.

[306] X. Zhang et al. "Transdermal delivery of water-soluble fluorescent antibody mediated by fractional Er:YAG laser for the diagnosis of lupus erythematosus in mice". *Lasers in Surgery and Medicine* 51.3 (2018), 268–277.

[307] D. Karlsson, G. Zacchi, and A. Axelsson. "Electronic Speckle Pattern Interferometry: A Tool for Determining Diffusion and Partition Coefficients for Proteins in Gels". *Biotechnology Progress* 18.6 (2002), 1423–1430.

[308] A. Sabri. "Cellular decision making during phagocytosis". *Master's Thesis, University of Bayreuth* (2015).

[309] K. C. Neuman et al. "Characterization of Photodamage to Escherichia coli in Optical Traps". *Biophysical Journal* 77.5 (1999), 2856–2863.

[310] J. Liesener et al. "Multi-functional optical tweezers using computer-generated holograms". *Optics Communications* 185.1 (2000), 77–82.

[311] J. Leach et al. "Interactive approach to optical tweezers control". *Applied optics* 45.5 (2006), 897–903.

[312] A. Ashkin. "Forces of a single-beam gradient laser trap on a dielectric sphere in the ray optics regime". *Biophysical Journal* 61.2 (1992), 569–582.

[313] E. Fällman and O. Axner. "Influence of a glass-water interface on the on-axis trapping of micrometer-sized spherical objects by optical tweezers". *Applied Optics* 42.19 (2003), 3915–3926.

[314] N.-S. Cheng. "Formula for the Viscosity of a Glycerol-Water Mixture". *Industrial & Engineering Chemistry Research* 47.9 (2008), 3285–3288.

[315] J. P. Lewis. "Fast Template Matching". *Vision Interface* 95 (1995), 120–123.

[316] D. Padfield. "Masked FFT registration". *2010 IEEE Computer Society Conference on Computer Vision and Pattern Recognition*. IEEE, 2010.

[317] J. H. H. Brenner. *Low Reynolds number hydrodynamics*. Springer Netherlands, 1983.

[318] M. Tanase, N. Biais, and M. Sheetz. "Magnetic Tweezers in Cell Biology". *Methods in Cell Biology*. Vol. 83. Elsevier, 2007, 473–493.

[319] H. Faxén. "Der Widerstand gegen die Bewegung einer starren Kugel in einer zähen Flüssigkeit, die zwischen zwei parallelen ebenen Wänden eingeschlossen ist". *Annalen der Physik* 373.10 (1922), 89–119.

[320] H. Faxen. "Die Bewegung einer starren Kugel langs der Achse einesmit zaeher Fluessigkeit gefuellten Rohres". *Arkiv for Matematik, Astronomi och Fysik* 17.27 (1923), 1–28.

[321] K. Svoboda et al. "Direct observation of kinesin stepping by optical trapping interferometry". *Nature* 365.6448 (1993), 721–727.

[322] S. C. Baicu and M. J. Taylor. "Acid-base buffering in organ preservation solutions as a function of temperature: new parameters for comparing buffer capacity and efficiency". *Cryobiology* 45.1 (2002), 33–48.

[323] A. C. Pipkin. *Lectures on Viscoelasticity Theory*. Springer New York, 1986.

[324] F. M. Hecht et al. "Imaging viscoelastic properties of live cells by AFM: power-law rheology on the nanoscale". *Soft Matter* 11.23 (2015), 4584–4591.

[325] D. Flormann et al. "Oscillatory Microrheology, Creep Compliance and Stress Relaxation of Biological Cells Reveal Strong Correlations as Probed by Atomic Force Microscopy". *Frontiers in Physics* 9 (2021), 711860.

[326] B. Fabry et al. "Scaling the Microrheology of Living Cells". *Physical Review Letters* 87.14 (2001), 148102.

[327] P. Kollmannsberger, C. T. Mierke, and B. Fabry. "Nonlinear viscoelasticity of adherent cells is controlled by cytoskeletal tension". *Soft Matter* 7.7 (2011), 3127–3132.

[328] A. Rohrbach et al. "Measuring Stepwise Binding of Thermally Fluctuating Particles to Cell Membranes without Fluorescence". *Biophysical Journal* 118.8 (2020), 1850–1860.

[329] J. C. Mills et al. "Apoptotic Membrane Blebbing Is Regulated by Myosin Light Chain Phosphorylation". *The Journal of Cell Biology* 140.3 (1998), 627–636.

[330] P. Cai et al. "Quantifying Cell-to-Cell Variation in Power-Law Rheology". *Biophysical Journal* 105.5 (2013), 1093–1102.

[331] A. R. Bausch, W. Möller, and E. Sackmann. "Measurement of Local Viscoelasticity and Forces in Living Cells by Magnetic Tweezers". *Biophysical Journal* 76.1 (1999), 573–579.

[332] C. ROTSCH. "AFM imaging and elasticity measurements on living rat liver macrophages". *Cell Biology International* 21.11 (1997), 685–696.

[333] S. Leporatti et al. "Elasticity and adhesion of resting and lipopolysaccharide-stimulated macrophages". *FEBS Letters* 580.2 (2005), 450–454.

[334] M. L. Gardel et al. "Elastic Behavior of Cross-Linked and Bundled Actin Networks". *Science* 304.5675 (2004), 1301–1305.

[335] K. Kasza et al. "Actin Filament Length Tunes Elasticity of Flexibly Cross-Linked Actin Networks". *Biophysical Journal* 99.4 (2010), 1091–1100.

[336] K. Kasza et al. "Filamin A Is Essential for Active Cell Stiffening but not Passive Stiffening under External Force". *Biophysical Journal* 96.10 (2009), 4326–4335.

[337] J. Luo et al. "Biomimetic Strain-Stiffening Hydrogel with Crimped Structure". *Advanced Functional Materials* 31.43 (2021), 2104139.

[338] M. P. Clausen et al. "Dissecting the actin cortex density and membrane-cortex distance in living cells by super-resolution microscopy". *Journal of Physics D: Applied Physics* 50.6 (2017), 064002.

[339] P. Chugh and E. K. Paluch. "The actin cortex at a glance". *Journal of Cell Science* 131.14 (2018), jcs186254.

[340] R. Kumar, S. Saha, and B. Sinha. "Cell spread area and traction forces determine myosin-II-based cortex thickness regulation". *Biochimica et Biophysica Acta (BBA) - Molecular Cell Research* 1866.12 (2019), 118516.

[341] I. Lüchtefeld et al. "Elasticity spectra as a tool to investigate actin cortex mechanics". *Journal of Nanobiotechnology* 18.1 (2020), 147.

[342] J. Mencik et al. "Determination of elastic modulus of thin layers using nanoindentation". *Journal of Materials Research* 12.9 (1997), 2475–2484.

[343] C. Szegedy et al. "Going deeper with convolutions". *2015 IEEE Conference on Computer Vision and Pattern Recognition (CVPR)*. IEEE, 2015.

[344] O. Russakovsky et al. "ImageNet Large Scale Visual Recognition Challenge". *International Journal of Computer Vision* 115.3 (2015), 211–252.

[345] C. Shorten and T. M. Khoshgoftaar. "A survey on Image Data Augmentation for Deep Learning". *Journal of Big Data* 6.1 (2019), 60.

[346] H. Ravishankar et al. "Understanding the Mechanisms of Deep Transfer Learning for Medical Images". *Deep Learning and Data Labeling for Medical Applications*. Springer International Publishing, 2016, 188–196.

[347] D. P. Kingma and J. Ba. "Adam: A Method for Stochastic Optimization". *arXiv* (2014), 1412.6980.

[348] M. Jahnel et al. "Measuring the complete force field of an optical trap". *Optics Letters* 36.7 (2011), 1260–1262.

[349] J. C. Wilcox et al. "Improved calibration of the nonlinear regime of a single-beam gradient optical trap". *Optics Letters* 41.10 (2016), 2386–2389.

[350] H. Hackstein et al. "Rapamycin inhibits macropinocytosis and mannose receptor-mediated endocytosis by bone marrow-derived dendritic cells". *Blood* 100.3 (2002), 1084–1087.

[351] A. von Delwig et al. *Arthritis Research & Therapy* 8.4 (2006), R93.

[352] T. Bretschneider et al. "Dynamic Actin Patterns and Arp2/3 Assembly at the Substrate-Attached Surface of Motile Cells". *Current Biology* 14.1 (2004), 1–10.

[353] G. Gerisch et al. "Mobile Actin Clusters and Traveling Waves in Cells Recovering from Actin Depolymerization". *Biophysical Journal* 87.5 (2004), 3493–3503.

[354] O. D. Weiner et al. "An Actin-Based Wave Generator Organizes Cell Motility". *PLoS Biology* 5.9 (2007), e221.

[355] E. L. Barnhart et al. "An Adhesion-Dependent Switch between Mechanisms That Determine Motile Cell Shape". *PLoS Biology* 9.5 (2011). Ed. by J. B. Alberts, e1001059.

[356] G. L. Ryan et al. "Excitable Actin Dynamics in Lamellipodial Protrusion and Retraction". *Biophysical Journal* 102.7 (2012), 1493–1502.

[357] M. G. Vicker. "Eukaryotic Cell Locomotion Depends on the Propagation of Self-Organized Reaction–Diffusion Waves and Oscillations of Actin Filament Assembly". *Experimental Cell Research* 275.1 (2002), 54–66.

[358] M. Machacek and G. Danuser. "Morphodynamic Profiling of Protrusion Phenotypes". *Biophysical Journal* 90.4 (2006), 1439–1452.

[359] M. Machacek et al. "Coordination of Rho GTPase activities during cell protrusion". *Nature* 461.7260 (2009), 99–103.

[360] G. D. Paolo and P. D. Camilli. "Phosphoinositides in cell regulation and membrane dynamics". *Nature* 443.7112 (2006), 651–657.

[361] D. Xiong et al. "Frequency and amplitude control of cortical oscillations by phosphoinositide waves". *Nature Chemical Biology* 12.3 (2016), 159–166.

[362] H. Meinhardt and A. Gierer. "Applications of a Theory of Biological Pattern Formation Based on Lateral Inhibition". *Journal of Cell Science* 15.2 (1974), 321–346.

[363] R. Rohatgi, H.-y. H. Ho, and M. W. Kirschner. "Mechanism of N-Wasp Activation by Cdc42 and Phosphatidylinositol 4,5-Bisphosphate". *Journal of Cell Biology* 150.6 (2000), 1299–1310.

[364] R. Rohatgi et al. "Nck and Phosphatidylinositol 4,5-Bisphosphate Synergistically Activate Actin Polymerization through the N-WASP-Arp2/3 Pathway". *Journal of Biological Chemistry* 276.28 (2001), 26448–26452.

[365] T. D. Pollard and G. G. Borisy. "Cellular Motility Driven by Assembly and Disassembly of Actin Filaments". *Cell* 112.4 (2003), 453–465.

[366] H. Q. Sun et al. "Gelsolin, a Multifunctional Actin Regulatory Protein". *Journal of Biological Chemistry* 274.47 (1999), 33179–33182.

[367] I. Lassing and U. Lindberg. "Specific interaction between phosphatidylinositol 4,5-bisphosphate and profilactin". *Nature* 314.6010 (1985), 472–474.

[368] L. Gozzelino et al. "PI(3,4)P2 Signaling in Cancer and Metabolism". *Frontiers in Oncology* 10 (2020), 360.

[369] D. J. Gillooly, A. Simonsen, and H. Stenmark. "Phosphoinositides and phagocytosis". *Journal of Cell Biology* 155.1 (2001), 15–18.

[370] R. Levin, S. Grinstein, and D. Schlam. "Phosphoinositides in phagocytosis and macropinocytosis". *Biochimica et Biophysica Acta (BBA) - Molecular and Cell Biology of Lipids* 1851.6 (2015), 805–823.

[371] G. Gerisch et al. "Self-organizing actin waves as planar phagocytic cup structures". *Cell Adhesion and Migration* 3.4 (2009), 373–382.

[372] T. A. Masters, M. P. Sheetz, and N. C. Gauthier. "F-actin waves, actin cortex disassembly and focal exocytosis driven by actin-phosphoinositide positive feedback". *Cytoskeleton* 73.4 (2016), 180–196.

[373] M. A. A. P. de León, B. Félix, and H. G. Othmer. "A phosphoinositide-based model of actin waves in frustrated phagocytosis". *Journal of Theoretical Biology* 527 (2021), 110764.

[374] F. M. Griffin and S. C. Silverstein. "Segmental response of the macrophage plasma membrane to a phagocytic stimulus". *Journal of Experimental Medicine* 139.2 (1974), 323–336.

[375] J. P. Lim et al. "Sorting nexin 5 (SNX5) selectively regulates dorsal ruffle-mediated macropinocytosis in primary macrophages". *Journal of Cell Science* 128.23 (2015), 4407–4419.

[376] N. D. Condon et al. "Macropinosome formation by tent pole ruffling in macrophages". *Journal of Cell Biology* 217.11 (2018), 3873–3885.

[377] S. Wieland. "Entwicklung einer Methode zur Messung von Transportkräften kleiner Organellen in Zellen". *Bachelor's Thesis, University of Bayreuth* (2017).

[378] P. Bursac et al. "Cytoskeletal remodelling and slow dynamics in the living cell". *Nature Materials* 4.7 (2005), 557–561.

[379] X. Trepat et al. "Universal physical responses to stretch in the living cell". *Nature* 447.7144 (2007), 592–595.

[380] D. Liebl and G. Griffiths. "Transient assembly of F-actin by phagosomes delays phagosome fusion with lysosomes in cargo-overloaded macrophages". *Journal of Cell Science* 122.16 (2009), 2935–2945.

[381] R. Huang et al. "Direct observation of the full transition from ballistic to diffusive Brownian motion in a liquid". *Nature Physics* 7.7 (2011), 576–580.

[382] W. Gross et al. “Same but different: the choice of model microplastics strongly affects the outcome of particle-cell interactions”. *In Preparation* (2022).

[383] A. Magenau et al. “Phagocytosis of IgG-Coated Polystyrene Beads by Macrophages Induces and Requires High Membrane Order”. *Traffic* 12.12 (2011), 1730–1743.

[384] E. Diler et al. “Influence of external calcium and thapsigargin on the uptake of polystyrene beads by the macrophage-like cell lines U937 and MH-S”. *BMC Pharmacology and Toxicology* 15.1 (2014), 16.

[385] Z. Liang et al. “Impaired macrophage phagocytosis of bacteria in severe asthma”. *Respiratory Research* 15.1 (2014), 72.

[386] C. K. Ober, K. P. Lok, and M. L. Hair. “Monodispersed, micron-sized polystyrene particles by dispersion polymerization”. *Journal of Polymer Science: Polymer Letters Edition* 23.2 (1985), 103–108.

[387] A. M. Telford et al. “Micron-sized polystyrene particles by surfactant-free emulsion polymerization in air: Synthesis and mechanism”. *Journal of Polymer Science Part A: Polymer Chemistry* 51.19 (2013), 3997–4002.

[388] H. Kawaguchi. “Functional polymer microspheres”. *Progress in Polymer Science* 25.8 (2000), 1171–1210.

[389] J. Rudolph et al. “Noxic effects of polystyrene microparticles on murine macrophages and epithelial cells”. *Scientific Reports* 11.1 (2021), 15702.

[390] L. Pan et al. “Polystyrene microplastics-triggered mitophagy and oxidative burst via activation of PERK pathway”. *Science of The Total Environment* 781 (2021), 146753.

[391] V. Stock et al. “Uptake and effects of orally ingested polystyrene microplastic particles in vitro and in vivo”. *Archives of Toxicology* 93.7 (2019), 1817–1833.

[392] S. D. Merkley et al. “Polystyrene microplastics induce an immunometabolic active state in macrophages”. *Cell Biology and Toxicology* 38.1 (2021), 31–41.

[393] K. Isoda et al. “Influence of 50-nm polystyrene particles in inducing cytotoxicity in mice co-injected with carbon tetrachloride, cisplatin, or paraquat”. *Die Pharmazie* 67.8 (2012), 712–714.

[394] A. F. R. M. Ramsperger et al. “Environmental exposure enhances the internalization of microplastic particles into cells”. *Science Advances* 6.50 (2020), eabd1211.

[395] C. Lu, P. W. Kania, and K. Buchmann. “Particle effects on fish gills: An immunogenetic approach for rainbow trout and zebrafish”. *Aquaculture* 484 (2018), 98–104.

[396] A. Ramsperger et al. “Supposedly identical microplastic particles substantially differ in their material properties influencing particle-cell interactions and cellular responses”. *Journal of Hazardous Materials* 425 (2022), 127961.

[397] S. Jeon et al. “Surface Charge-Dependent Cellular Uptake of Polystyrene Nanoparticles”. *Nanomaterials* 8.12 (2018), 1028.

[398] S. Wieland et al. “From properties to toxicity: Comparing microplastics to other airborne microparticles”. *Journal of Hazardous Materials* 428 (2022), 128151.

[399] C. Yong, S. Valiyaveettil, and B. Tang. “Toxicity of Microplastics and Nanoplastics in Mammalian Systems”. *International Journal of Environmental Research and Public Health* 17.5 (2020), 1509.

[400] P. Klemm and M. A. Schembri. “Bacterial adhesins: function and structure”. *International Journal of Medical Microbiology* 290.1 (2000), 27–35.

[401] W. E. Thomas, V. Vogel, and E. Sokurenko. “Biophysics of Catch Bonds”. *Annual Review of Biophysics* 37.1 (2008), 399–416.

[402] M. Mathelié-Guinlet et al. “Force-clamp spectroscopy identifies a catch bond mechanism in a Gram-positive pathogen”. *Nature Communications* 11.1 (2020), 5431.

[403] W. E. Thomas et al. “Shear-dependent ‘stick-and-roll’ adhesion of type 1 fimbriated Escherichia coli”. *Molecular Microbiology* 53.5 (2004), 1545–1557.

[404] W. E. Thomas et al. “Bacterial Adhesion to Target Cells Enhanced by Shear Force”. *Cell* 109.7 (2002), 913–923.

[405] M. Irmscher et al. “The influence of inhomogeneous adhesion on the detachment dynamics of adhering cells”. *European Biophysics Journal* 42.6 (2013), 419–426.

[406] H. S. Sakhalkar et al. “Leukocyte-inspired biodegradable particles that selectively and avidly adhere to inflamed endothelium in vitro and in vivo”. *Proceedings of the National Academy of Sciences* 100.26 (2003), 15895–15900.

[407] X. Zou et al. "PSGL-1 derived from human neutrophils is a high-efficiency ligand for endothelium-expressed E-selectin under flow". *American Journal of Physiology-Cell Physiology* 289.2 (2005), C415–C424.

[408] P. Decuzzi et al. "Flow chamber analysis of size effects in the adhesion of spherical particles." *International journal of nanomedicine* 2.4 (2007), 689–696.

[409] A. M. Smith, B. Prabhakarpandian, and K. Pant. "Generation of Shear Adhesion Map Using SynVivo Synthetic Microvascular Networks". *Journal of Visualized Experiments* 87 (2014), e51025.

[410] N. A. Mortensen, F. Okkels, and H. Bruus. "Reexamination of Hagen-Poiseuille flow: Shape dependence of the hydraulic resistance in microchannels". *Physical Review E* 71.5 (2005), 057301.

[411] H. Bruus. *Theoretical Microfluidics*. Oxford University Press, 2008.

[412] J. C. Crocker and D. G. Grier. "Methods of Digital Video Microscopy for Colloidal Studies". *Journal of Colloid and Interface Science* 179.1 (1996), 298–310.

[413] C. J. Seeton. "Viscosity–temperature correlation for liquids". *Tribology Letters* 22.1 (2006), 67–78.

[414] F. Vignati et al. "Numerical Simulations of the flow field within a 1:10 Aspect Ratio duct at intermediate Re". *Journal of Physics: Conference Series* 1599.1 (2020), 012044.

[415] T. Tatsumi and T. Yoshimura. "Stability of the laminar flow in a rectangular duct". *Journal of Fluid Mechanics* 212.1 (1990), 437–449.

[416] R. R. Kerswell and A. Davey. "On the linear instability of elliptic pipe flow". *Journal of Fluid Mechanics* 316 (1996), 307–324.

[417] K. Jaqaman et al. "Robust single-particle tracking in live-cell time-lapse sequences". *Nature Methods* 5.8 (2008), 695–702.

[418] K. T. Applegate et al. "plusTipTracker: Quantitative image analysis software for the measurement of microtubule dynamics". *Journal of Structural Biology* 176.2 (2011), 168–184.

[419] M. R. Ng et al. "Substrate stiffness regulates cadherin-dependent collective migration through myosin-II contractility". *Journal of Cell Biology* 199.3 (2012), 545–563.

[420] P. Dancker et al. "Interaction of actin with phalloidin: Polymerization and stabilization of F-actin". *Biochimica et Biophysica Acta (BBA) - Protein Structure* 400.2 (1975), 407–414.

[421] H. Faulstich et al. "Probing the phalloidin binding site of actin". *FEBS Letters* 318.3 (1993), 218–222.

[422] H.-P. Piepho. "Letters in Mean Comparisons: What They Do and Don't Mean". *Agronomy Journal* 110.2 (2018), 431–434.

[423] J.-S. Song, F. Tronc, and M. A. Winnik. "Two-Stage Dispersion Polymerization toward Monodisperse, Controlled Micrometer-Sized Copolymer Particles". *Journal of the American Chemical Society* 126.21 (2004), 6562–6563.

[424] J. Lee et al. "Synthesis of highly monodisperse polystyrene microspheres via dispersion polymerization using an amphoteric initiator". *Journal of Colloid and Interface Science* 298.2 (2006), 663–671.

[425] J. L. Ma and X. H. Zhang. "Preparation of Polystyrene Microspheres by Suspension Polymerization". *Advanced Materials Research* 233-235 (2011), 2215–2218.

[426] S. Honary and F. Zahir. "Effect of Zeta Potential on the Properties of Nano-Drug Delivery Systems - A Review (Part 1)". *Tropical Journal of Pharmaceutical Research* 12.2 (2013), 255–264.

[427] N. Ma et al. "Influence of Nanoparticle Shape, Size, and Surface Functionalization on Cellular Uptake". *Journal of Nanoscience and Nanotechnology* 13.10 (2013), 6485–6498.

[428] V. Forest, M. Cottier, and J. Pourchez. "Electrostatic interactions favor the binding of positive nanoparticles on cells: A reductive theory". *Nano Today* 10.6 (2015), 677–680.

[429] A. Singh, B. Kasinath, and E. Lewis. "Interaction of polycations with cell-surface negative charges of epithelial cells". *Biochimica et Biophysica Acta (BBA) - Protein Structure and Molecular Enzymology* 1120.3 (1992), 337–342.

[430] P. Happel, D. Thatenhorst, and I. Dietzel. "Scanning Ion Conductance Microscopy for Studying Biological Samples". *Sensors* 12.11 (2012), 14983–15008.

[431] D. Perry et al. "Surface Charge Visualization at Viable Living Cells". *Journal of the American Chemical Society* 138.9 (2016), 3152–3160.

[432] S. Tenzer et al. "Rapid formation of plasma protein corona critically affects nanoparticle pathophysiology". *Nature Nanotechnology* 8.10 (2013), 772–781.

[433] M. Lundqvist et al. "Nanoparticle size and surface properties determine the protein corona with possible implications for biological impacts". *Proceedings of the National Academy of Sciences* 105.38 (2008), 14265–14270.

[434] K. Partikel et al. "Serum type and concentration both affect the protein-corona composition of PLGA nanoparticles". *Beilstein Journal of Nanotechnology* 10 (2019), 1002–1015.

[435] P. Stoodley et al. "Biofilms as Complex Differentiated Communities". *Annual Review of Microbiology* 56.1 (2002), 187–209.

[436] N. G. Cogan. "The role of the biofilm matrix in structural development". *Mathematical Medicine and Biology* 21.2 (2004), 147–166.

[437] T. J. Stewart et al. "Characterization of extracellular polymeric substances (EPS) from periphyton using liquid chromatography-organic carbon detection–organic nitrogen detection (LC-OCD-OND)". *Environmental Science and Pollution Research* 20.5 (2012), 3214–3223.

[438] G. Pulido-Reyes et al. "Bio-nano interface and environment: A critical review". *Environmental Toxicology and Chemistry* 36.12 (2017), 3181–3193.

[439] T. S. Galloway, M. Cole, and C. Lewis. "Interactions of microplastic debris throughout the marine ecosystem". *Nature Ecology & Evolution* 1.5 (2017), 0116.

[440] T. Silva et al. "Particle size, surface charge and concentration dependent ecotoxicity of three organo-coated silver nanoparticles: Comparison between general linear model-predicted and observed toxicity". *Science of The Total Environment* 468-469 (2014), 968–976.

[441] H. T. Spanke et al. "Wrapping of Microparticles by Floppy Lipid Vesicles". *Physical Review Letters* 125.19 (2020), 198102.

[442] W. Lee, J. Sodek, and C. McCulloch. "Role of integrins in regulation of collagen phagocytosis by human fibroblasts". *Journal of Cellular Physiology* 168.3 (1996), 695–704.

[443] L. C. Abraham et al. "Phagocytosis and remodeling of collagen matrices". *Experimental Cell Research* 313.5 (2007), 1045–1055.

[444] P. J. Coopman et al. "Integrin alpha 3 beta 1 participates in the phagocytosis of extracellular matrix molecules by human breast cancer cells." *Molecular Biology of the Cell* 7.11 (1996), 1789–1804.

[445] S. Kanno, A. Furuyama, and S. Hirano. "A Murine Scavenger Receptor MARCO Recognizes Polystyrene Nanoparticles". *Toxicological Sciences* 97.2 (2007), 398–406.

[446] C. Neyen et al. "Macrophage Scavenger Receptor A Mediates Adhesion to Apolipoproteins A-I and E". *Biochemistry* 48.50 (2009), 11858–11871.

List of Figures

9 List of Publications

9.1 Key Publications

- W. Gross und H. Kress: 'Simultaneous measurement of the Young's modulus and the Poisson ratio of thin elastic layers', Soft Matter, 13, 1048-1055, 2017
- W. Gross und H. Kress: 'Optimization of experimental parameters for the mechanical characterization of thin elastic films', J. Phys. Commun., 3, 055021, 2019
- K. Berghoff[1], W. Gross[1], M. Eisentraut, H. Kress: 'Using Blinking Optical Tweezers to Study Cell Rheology During Initial Cell-Particle Contact', Biophys. J., 120, 3527-3537, 2021
- S. Wieland[1], A. FRM Ramsperger[1], W. Gross[1], M. Lehman, T. Witzmann , A. Caspari, M. Obst, S. Gekle, G. Auernhammer, A. Fery, C. Laforsch[2], H. Kress[2]: 'Nominally identical microplastic models differ greatly in their particle-cell interactions', Nat. Commun., 15, 922, 2024

[1] Joint first authors
[2] Joint senior authors

9.2 Further Publications

- S. Hartmann, G. Wittko, F. Schock, W. Gross, F. Lindner, W. Köhler and K. Morozov 'Thermophobicity of liquids: Heats of transport in mixtures as pure component properties - The case of arbitrary concentration', J. Chem. Phys. 141, 134503, 2014
- K. Berghoff, S. Keller, W. Gross, L. Gebhardt, H. Kress: 'Application of optical tweezers for biomechanical and thermal cell stimultion', In: Light Robotics: Structure-Mediated Nanobiophotonics, Amsterdam, Oxford: Elsevir, 385-410, 2017
- C. Zahn, S. Keller, M. Toro-Nahuelpan, P. Dorscht, W. Gross, M. Laumann, S. Gekle, W. Zimmermann, D. Schüler, H. Kress: 'Measurement of the magnetic moment of single Magnetospirillum gryphiswaldense cells by magnetic tweezers', Sci. Rep., 7, 3558, 2017
- A. Ramsperger, V. Narayana, W. Gross, J. Mohanraj, M. Thelakkat, A. Greiner, H. Schmalz, H. Kress[1], C. Laforsch[1]: 'Environmental exposure enhances the internalization of microplastic particles into cells', Sci. Adv., 6, eabd1211, 2020
- S. Wieland, C. Steininger, D. E. Gitschier, M. M. Kaiser, W. Gross, C. Laforsch, A. G. Hendricks, H. Kress: 'Many dynein teams collectively generate high forces during the transport of large organelles', in preparation
- A. FRM Ramsperger, W. Gross, B. Firmke, C. Laforsch[1], H. Kress[1]: 'Environmental exposure of microplastic particles induces inflammatory responses in murine macrophages', in preparation

[1] Joint senior authors

9.3 Conference Contributions as Presenting Author

- W. Gross and H. Kress: 'Traction Force Microscopy during Phagocytosis', DPG Spring Meeting, Berlin, 2015
- W. Gross and H. Kress: 'Traction Force Microscopy during Phagocytosis', DPG Spring Meeting, Regensburg, 2016
- W. Gross, F. Zecherle, K. Weidner-Hertrampf, and H. Kress: 'Macrophages are sensitive to substrate elasticity during phagocytosis', Biophysical Society Meeting, New Orleans, USA, 2017
- W. Gross and H. Kress, 'Simultaneous measurement of the Young‘s modulus and the Poisson ratio of thin elastic layers', DPG Spring Meeting, Berlin, 2018
- W. Gross and H. Kress: 'Traction Force Microscopy during Phagocytosis', DPG Spring Meeting, Regensburg, 2019
- W. Gross, K. Berghoff, M. Eisentraut, H. Kress: 'Investigation of Contact Dynamics and Cell Rheology During Early Phagocytic Binding', Biophysical Society Meeting, San Francisco, USA, 2022

10 Eidesstattliche Versicherung

Hiermit versichere ich an Eides statt, dass ich die vorliegende Arbeit selbstständig verfasst und keine anderen als die von mir angegebenen Quellen und Hilfsmittel verwendet habe.

Weiterhin erkläre ich, dass ich die Hilfe von gewerblichen Promotionsberatern bzw. –vermittlern oder ähnlichen Dienstleistern weder bisher in Anspruch genommen habe, noch künftig in Anspruch nehmen werde.

Zusätzlich erkläre ich hiermit, dass ich keinerlei frühere Promotionsversuche unternommen habe.

Bayreuth, den

Wolfgang Groß